PROBING THE INITIAL STATE OF HEAVY-ION COLLISIONS WITH ISOLATED PROMPT PHOTONS

FLORIAN JONAS

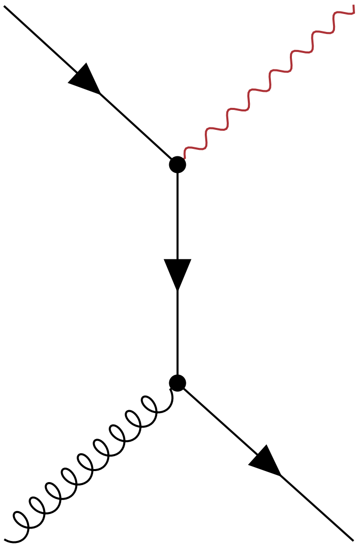

DISSERTATION

AG ANDRONIC
INSTITUT FÜR KERNPHYSIK
WESTFÄLISCHE WILHELMS-UNIVERSITÄT
MÜNSTER

– 2023 –

EXPERIMENTELLE PHYSIK

PROBING THE INITIAL STATE OF HEAVY-ION COLLISIONS WITH ISOLATED PROMPT PHOTONS

Inaugural-Dissertation
zur Erlangung des Doktorgrades (Dr. rer. nat.)
der Naturwissenschaften im Fachbereich Physik
der Mathematisch-Naturwissenschaftlichen Fakultät
der Westfälischen Wilhelms-Universität Münster

vorgelegt von
Florian Jonas
aus Hamm

– 2023 –

Dekan:
Prof. Dr. Rudolf Bratschitsch

Erster Gutachter:
Prof. Dr. Christian Klein-Bösing

Zweiter Gutachter:
Prof. Dr. Anton Andronic

Tag der mündlichen Prüfung:

Tag der Promotion:

ACKNOWLEDGMENTS

I would like to thank all the people who have been by my side during this ongoing journey through particle physics. First and foremost, I want to thank Christian and Anton. You have created an excellent working group with a great social *and* physics climate and always had an open ear for problems and interesting discussions. It is no surprise I stayed in the same group from my bachelor until now. I extend my gratitude to all the people I worked with in Münster over the years. I also owe a huge thank you to Constantin! I thank you for bringing me to CERN and enabling this fruitful collaboration between ORNL and Münster (also thanks to Christian and Anton). You have been a mentor and inspiration for me during the years, and you never grew tired of appearing with "a brand new idea" in the office that you had during the night that required immediate investigation. I don't recall the number of figures I produced for our discussions, but surely it must be in the hundreds. I want to use the opportunity to extend my thanks to the whole group at ORNL, that not only agreed to support a German PhD student stationed at CERN, but also integrated me into their nice group on the other side of the big ocean. I am thankful for the guidance and also the opportunity to travel to the US.

I am forever grateful for all the people that I have collaborated with during my time at CERN and elsewhere. Many of them have become more than colleagues - they have become friends! Mike, it feels like I know you since forever, even though we are only physically in the same place since about a year at CERN. I highly value your opinions and out-of-the-box thinking for all physics related topics and beyond. It never ceases to amaze me what questions are floating around your mind. You never missed an opportunity for morning coffee in building 587, often coupled with an excited exclamation of the question "Have you seen this new Trajectum plot that I am working on?". It is not surprising to me that you have also become a close friend – always available for adventures and nice dinners.

My time at CERN was spent in building 587, which I shared together with amazing occupants. I want to thank Fredi for believing in me since I have been a summer student at CERN and always providing guidance, a good chat and critique for my plotting style. Nico, it was amazing to share an office with you for such a long time and to call you my friend! Thank you for all the time we spent at and outside of work together. A big "Thank You" goes also to Markus! I admire your deep knowledge in a vast array of topics, which you were always happy to share with me. Thank you for all the chats, coffees, the biking we did together and your friendship! I also want to thank Raymond. You have become a good friend, and we could always run our thoughts and ideas by each other. I am especially grateful for the trips we did together around France!

During my time at CERN I had the pleasure to work a lot on the EMCal detector – either during physical access or when working on our software. My thanks go out to Martin, Alex, Gustavo, Joshua and Markus! You are and have been doing an amazing job, and it is a pleasure to work with you! As reflected in the division of this work into multiple parts, my second focus was on the future FoCal detector, where I was fortunate enough to be part of multiple test-beam activities and simulation developments. I would like to thank all the people I met along the way, in particular Constantin, Ionut, Marco, Max and Peter for all the interesting discussions.

I also want to thank Jens and Joshua, with whom I collaborated especially closely during my PhD. Thank you for all your help, Zoom calls, physics discussions, non-physics discussions and conferences we visited together, but most importantly: your friendship. In addition, I want to thank Hannah. We started out as summer students in the same office back in the day and look at where we are now! Caitie, I did not want to dedicate a whole paragraph to you, however, you have become a friend and I also feel a little pressured by the fact that you mentioned me explicitly in your acknowledgments of your recently defended PhD thesis. It was a pleasure sharing my office with you whenever you visited CERN, and I wish you all the best for your future! I also owe thanks to Daniel and Hendrik. I know our journeys in physics together have parted since a while, but we remain in touch, and I am happy about that. Hendrik: You were an inspiration to me since I was a Bachelor student in Münster. Scrolling through this work you will also find that I often reference and build on your work – maybe you find some pleasure in that.

Last but not least, I want to thank my family and my girlfriend! Without your support and love none of this would have been possible! I know that watching me spend late nights discussing mystical "prompt photons" or spending months to obtain some boxes plotted around data points must have been quite a strange sight, but you always supported and somehow understood my passion. From the bottom of my heart: Thank you!

CONTENTS

II Measurement of isolated prompt photon production in pp and p-Pb collisions at $\sqrt{s_{\mathrm{NN}}} = 8$ and 8.16 TeV with ALICE

III Outlook: Isolated prompt photon measurements with the Forward Calorimeter (FoCal)

IV Summary & Conclusions

V Appendix

1

INTRODUCTION

Unconventionally, I want to begin this thesis not with an historical account of the field of particle physics, but rather give a personal account of my fascination with this field, which is the driving force of my past studies in physics and ultimately the motivation for this work. My fascination for particle physics was always driven by the contrasts it contains. First there is a contrast in scale: The object of interest are as small as one can get when it comes to physical objects: Fundamental particles that are not only the most basic constituents of matter but also the mediators for the fundamental forces in nature. The experiments to study these particles on the other hand are large, where hadron colliders such as the LHC are pushing the boundaries of engineering and showcase humanities ability to collaborate in order to build the largest machines known to mankind, giving us access to the world of fundamental particles; following an urge to understand what makes up the world on the most fundamental level. The large size of the experiments goes beyond the mere size of the experimental apparatus and extends to the scientific community: Experiments are often comprised of thousands of scientists from around the world that are collaborating to achieve a common goal, which to me was always inspiring, fascinating and motivating.

A difference of scale can also be observed for the physics itself that is involved: The theory of the strong interaction (QCD) – which is of key importance for this work – behaves drastically different “up close” than it does at “at a distance”. This literal scale dependence makes QCD an interesting and challenging theory, requiring novel theoretical approaches and experimental techniques to access and understand the variety of interesting phenomena that arise as a consequence of this scale dependence. The unprecedented energy densities reached in heavy-ion collisions at the LHC offer unique insights into the behaviour of QCD in extreme conditions, such as e.g. the formation of a new state of matter – the so-called Quark-Gluon Plasma – which existed in our early universe mere microseconds after the Big Bang. The ALICE detector, which is the dedicated heavy-ion experiment at the LHC, is at the forefront of such explorations.

This work presents the measurement of isolated prompt photon production in pp and p–Pb collisions at $\sqrt{s_{\mathrm{NN}}} = 8\,\mathrm{TeV}$ and $8.16\,\mathrm{TeV}$ with the ALICE experiment. Prompt photons are produced directly in the hard scattering of incoming partons in the earliest stages of a collision. This allows prompt photons to serve as a probe for partons inside the colliding nucleons that enter the hard scattering process. How exactly the momentum of different partons is distributed inside the nucleon prior to the collision is not known from first principles, and is commonly encoded in so-called Parton Distribution Functions (PDFs) that rely on input from a vast amount of experimental data. Precise determination of these distributions is crucial, as they are an essential ingredient for the theoretical description of a wide range of particles produced in the hard scattering process. Since prompt photos are dominantly produced by the Compton scattering process $g\mathrm{q} \rightarrow \gamma\mathrm{q}$, they are sensitive the gluon PDF, which is of key importance for hard scatterings at LHC energies. Furthermore, photons do not carry a so-called colour charge and therefore do not participate in the strong interaction, allowing them to traverse the evolution of the collision unaffected by final state effects. This makes them a particularly robust probe, carrying unaltered information from the moment of their production until their detection in the experimental apparatus.

The presented experimental findings on isolated prompt photon production in pp and p–Pb collisions aim to provide experimental constraints for the aforementioned gluon distributions and test our theoretical understanding of prompt photon production within perturbative QCD. Furthermore, one of the key questions explored in this work is how these parton distributions inside the nucleon change when the nucleon itself is part of a bigger structure, e.g. a lead nucleus, where previous experimental findings indicate a suppression of the gluon PDF due to an effect known as gluon shadowing. Such modifications can be probed experimentally using the nuclear modification factor R_{pA}, which quantifies changes of the prompt photon production cross section in p–Pb collisions with respect to the scaled reference cross section measured in pp collisions. The presented R_{pA} of isolated prompt photon production at $\sqrt{s_{\mathrm{NN}}} = 8.16\,\mathrm{TeV}$ aims to explore these effects in a phasespace where gluon shadowing is expected to be sizeable – extending the low transverse momentum coverage of a previous measurement of this observable by a factor of two. Furthermore, this work explores future measurements of prompt photon production at forward rapidities using the ALICE Forward Calorimeter (FoCal). Prompt photons produced at forward rapidities are especially sensitive to very soft gluons that carry only a small momentum fraction x of the proton's total momentum. Measurements in this low-x region are motivated by the observation of a steeply increasing gluon probability density for decreasing x. This growth can not continue indefinitely and one expects a regime of saturated gluons, where this growth is tamed by gluon fusion. No experimental evidence for this gluon saturated matter is currently available, and its discovery would be a landmark in our understanding of the strong interaction. The measurement of isolated prompt photon production with the ALICE FoCal have the potential to make meaningful contributions in the experimental search for these phenomena. This work showcases detailed performance studies using simulations of the collision events and the FoCal detector in order to parametrize key performance metrics such as expected prompt photon reconstruction efficiency, purity and energy resolution. Furthermore, the findings are combined with perturbative QCD calculations to estimate the potential impact of a measurement of isolated prompt photon production with the FoCal on existing nuclear PDFs.

Part I

THEORETICAL AND EXPERIMENTAL PREREQUISITES

2

THEORETICAL BACKGROUND

This chapter discusses the theoretical prerequisites required for this work, beginning with the Standard Model, which embodies our understanding of elementary particles and their interactions. A special focus is put on the strong interaction, which is introduced in Sec. 2.1.3. High-energy hadronic collision are discussed in Sec. 2.2, with an emphasis on the initial state of the collision, i.e. the Parton Distribution Functions (PDFs) describing the colliding projectiles. The collision of heavy-ions is elaborated in Sec. 2.3, outlining modifications in the initial-state as well as the formation of the Quark-Gluon Plasma (QGP). Finally, isolated prompt photon production – the focus of this work – is described in detail in Sec. 2.4, including a discussion of existing experimental data on their production.

2.1 THE STANDARD MODEL

Particle physics, while dealing with very small objects, is trying to answer very big questions: What is our universe made of on the most fundamental level, and what are the laws of nature that govern how these constituents interact which each other? Our best answer to these questions to date is the standard model of particles physics. Finalized in the mid-seventies, it provides a unified picture of fundamental particles that interact with each other through three forces, which are themselves described by an exchange of fundamental particles. This development is a result of a struggle spanning multiple decades in the 20th century to bring structure to a whole zoo of discovered particles and phenomena, requiring great efforts from theorists and experimentalists alike. Since its formulation, it has been tested with remarkable precision and can be seen as one of the greatest achievements of modern physics [1, 2].

2.1.1 *Overview*

Fig. 2.1 shows an overview of the elementary particles that make up the standard model. One distinguishes between two types of elementary particles: Fermions and Bosons. Fermions are the fundamental constituents that comprise the matter content of our universe and consist of 6 quarks and 6 leptons. They can be further grouped into three families/generations, where the particles from the second and third generation only differ from the first generation in their heavier mass. The 6 quarks (up, down, charm, strange, top and bottom) each carry a colour and electro-weak charge, whereas the leptons (e,μ,τ and their corresponding neutrinos ν_e,ν_μ,ν_τ) only carry an electroweak charge. Interactions between these particles are described by three fundamental forces: The electromagnetic force, strong force and weak force. Gravity is negligible on the small scales of fundamental particles and is not part of the standard model. The three fundamental forces are mediated by the exchange of so-called gauge boson: The electromagnetic force is mediated by the exchange of a photon, the strong force by the gluons and the weak force by the three bosons W^+,W^- and Z.

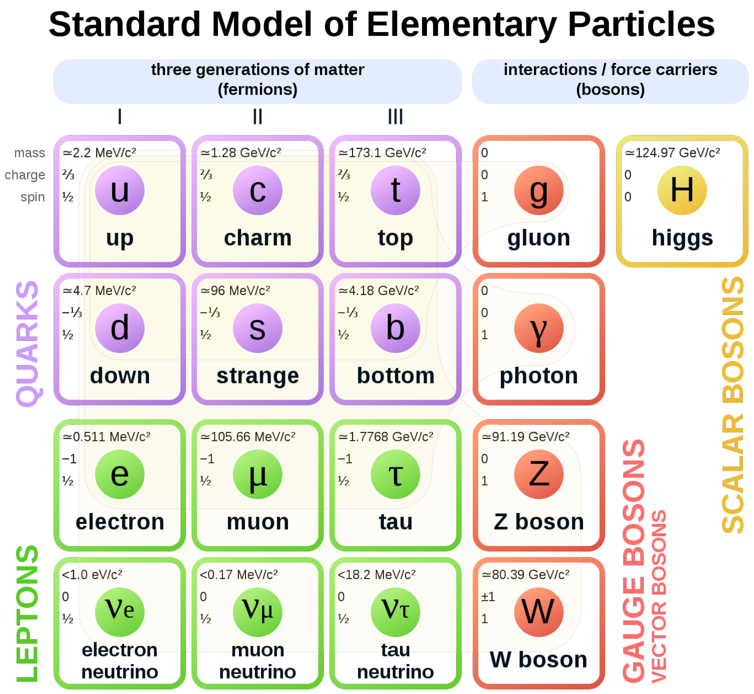

Figure 2.1: The elementary particles of the standard model [3].

Each of these interactions is described by a Quantum Field Theory (QFT) [4, 5], that provides the mathematical framework to understand and quantify the interactions found in the standard model. In essence, in QFT every particle is viewed as an excitation of a quantum field, which is defined over all space and time. How and if a force is mitigated is determined by the properties of the boson and the QFT that is associated with the given interaction. For the electromagnetic interaction the corresponding theory is known as Quantum Electro Dynamics (QED) and the strong interaction is described by Quantum Chromodynamics (QCD). Weak interactions are usually described within electro-weak theory, which allows a unified description of the electromagnetic- and weak force.

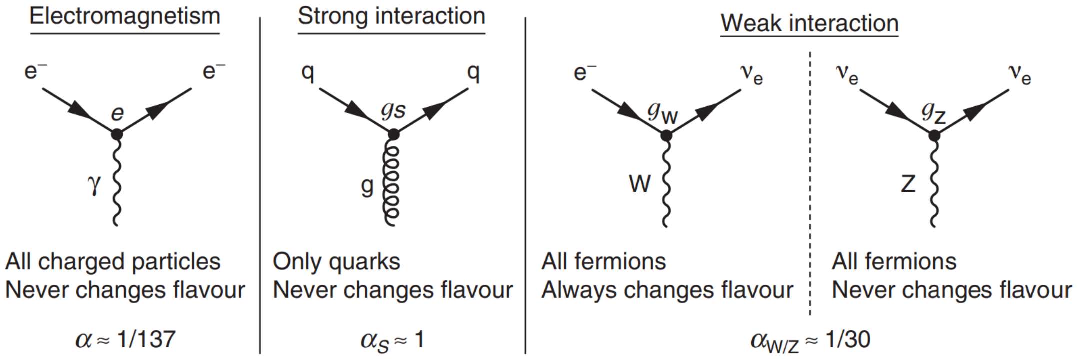

Figure 2.2: Interaction vertices of the three fundamental forces. The interaction strength g at each vertex is expressed as the dimensionless constant $\alpha \propto g^2$ [1]. The given values merely serve guidance for the strength of each interaction, and $\alpha_S \approx 1$ is only valid for low momentum transfers (see Fig. 2.5).

An overview of the three fundamental forces, i.e. the coupling of their gauge bosons to the fermions is illustrated in Fig. 2.2, which shows the so-called interaction vertices of the standard model. The gauge bosons couple to a given fermion only if it carries the charge of the associated interaction and the strength of the coupling is determined by a coupling constant g, which is usually expressed as a dimensionless constant $\alpha \propto g^2$.

2.1.2 *Quantum Electrodynamics (QED)*

Magnetic and electrical forces have long been known in classical physics and were unified by Maxwell to a single force – the electromagnetic force – in 1873 [6]. However, in the early 1900s it became clear that this classical picture of electromagnetic interactions as waves produced by the interacting charged particles themselves was unable to explain observed black-body radiation at small wavelengths. This started the development of quantum mechanics and finally – after a few decades of overcoming theoretical hurdles – resulted in the formulation of QED and a Nobel Prize for Tomonaga, Schwinger and Feynman in 1965 [7–9].

Particles carrying electric charge (see Fig. 2.1) interact via the exchange of a massless virtual boson – the photon (γ) – with spin 1. The Lagrangian describing this interaction of charged spin-1/2 fields ψ (e.g. electrons) with the electromagnetic field is given by:

$$\mathcal{L}_{\text{QED}} = \underbrace{-m_e\bar{\psi}_e\psi_e}_{\substack{\text{propagation of}\\ \text{charged particle}}} \underbrace{-\bar{\psi}_e\gamma^\nu\left[\partial_\nu + ieA_\mu\right]\psi_e}_{\substack{\text{interaction with}\\ \text{photon}}} \underbrace{-\frac{1}{4}F_{\mu\nu}F^{\mu\nu}}_{\substack{\text{propagation of}\\ \text{photon}}}, \tag{2.1}$$

where A_μ the electromagnetic vector potential and

$$F_{\mu\nu} = \partial_\mu A_\nu - \partial_\nu A_\mu \tag{2.2}$$

the electromagnetic field tensor [10]. The first term describes the propagation of a free charged particle of mass m, whereas the interaction of the charged particle with the electromagnetic field (the gauge field A_μ, i.e. the photon) is contained in the second term. Finally, the free electromagnetic field (free photon) is described in the term $-\frac{1}{4}F_{\mu\nu}F^{\mu\nu}$. One refers to the electromagnetic field as a gauge field (or the photon as a gauge boson) since it assures the global and local U(1) symmetry[1] of QED (i.e. conservation of fermion number and electromagnetic current). The Lagrangian does not contain a mass term for the gauge boson – the photon is a massless particle – and the range of the electromagnetic interaction is therefore characterized by an infinite range. Adding a mass for the photon would break U(1) symmetry, showcasing again the powerful connection between symmetries and interactions – a connection which is the essence in the development of any QFT.

The theory of QED is not analytically solvable and relies on perturbation theory to calculate electromagnetic interactions [5]. In practice, physicist often use so-called Feynman diagrams which are a visual representation of a given interaction that can be converted to mathematical expressions by following a set of rules. The Feynman diagrams of QED can all be constructed as a combination of the interaction vertex shown in Fig. 2.2. When calculating cross-sections in QED for a given process, the diagram

---

[1] When saying "assures U(1) symmetry" one means that when applying transformation from the U(1) to A_μ and ψ (i.e. rotations), the Lagrangian does not change.

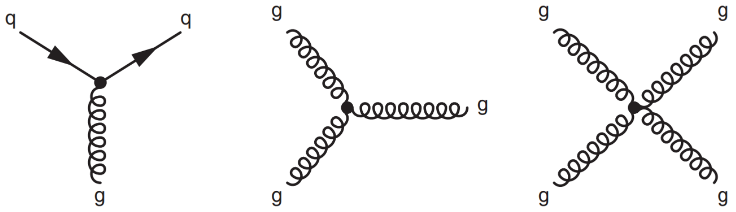

Figure 2.3: Interaction vertices of gluons and quarks in QCD [1]. The three-gluon (middle) and four-gluon vertices (right) represent the self-coupling of the gauge bosons of QCD and cannot be found in QED.

with the fewest number of interaction vertices is usually the biggest contribution and referred to as the Leading Order (LO). An infinite number of diagrams of higher orders exists for the same process, each entering the sum of all possible Feynman diagrams with $\alpha^{N_{\text{vertex}}}$. Since the interaction strength $\alpha \approx 1/137$ at each vertex is small[2], the series quickly converges and one achieves a precision of $\mathcal{O}(1\,\%)$ considering only LO diagrams when calculating QED processes [1].

2.1.3 *Quantum Chromodynamics (QCD)*

The QFT describing the strong interaction is QCD [4, 11]. Where QED is symmetric with respect to the U(1) symmetry group, the underlying symmetry of QCD is SU(3) symmetry. The gauge bosons of the strong interaction are 8 massless gluons, which couple to the colour charge. However, while the photon does not carry any electric charge, the gluons themselves carry a colour charge and can therefore interact with other gluons. This self-interaction gives the theory of QCD some unique (and theoretically challenging) properties, that allow for a variety of interesting phenomena, which will be discussed in the following.

The Lagrangian of QCD, which describes the interaction of quark fields $\psi_{q,a}$ and the gluon gauge fields A^c_ν is given by:

$$\mathcal{L}_{\text{QCD}} = \underbrace{-\sum_q m_q \bar{\psi}_{q,a}\psi_{q,a}}_{\substack{\text{propagation}\\ \text{of quarks}}} \underbrace{-\sum_q \bar{\psi}_{q,a}\gamma^\nu\left[\partial_\nu - ig_s A^c_\mu \mathbf{t_c}\right]\psi_{q,a}}_{\text{interaction term}} \underbrace{-\frac{1}{4}F^c_{\mu\nu}F^{\mu\nu}_c}_{\substack{\text{propagation}\\ \text{of gluon}}}, \tag{2.3}$$

where $\sum_q$ denotes the summation over all $n = 6$ quark fields corresponding to the 6 quark flavours q that are shown in Fig. 2.1. The index a denotes the colour-index running from $a = 1$ to $N_c = 3$ corresponding to the three colours often denoted with red, green and blue. The gluon colour-index $C = 1 \ldots 8$ corresponds to the 8 different gluons, each carrying a pair of colour and anti-colour, as will be discussed later. The reason one finds exactly 8 gluon fields, is again due to symmetry considerations: Where QED required the introduction of one gauge field – the photon – in order to ensure invariance with respect to U(1) symmetry, the 8 gluon gauge fields ensure invariance with respect to SU(3) colour symmetry for QCD. The 3×3 matrices $\mathbf{t_c}$ shown in Eq. 2.3 are the so-called Gell-Mann matrices, which are the generators of SU(3) colour symmetry.

---

[2] As discussed later in more detail for QCD, the coupling strength depends on the scale, e.g. momentum transfer Q^2. For QED, this scale dependence is small and one observes slightly smaller coupling strengths for small Q^2 due to the creation of virtual e^+e^- pairs.

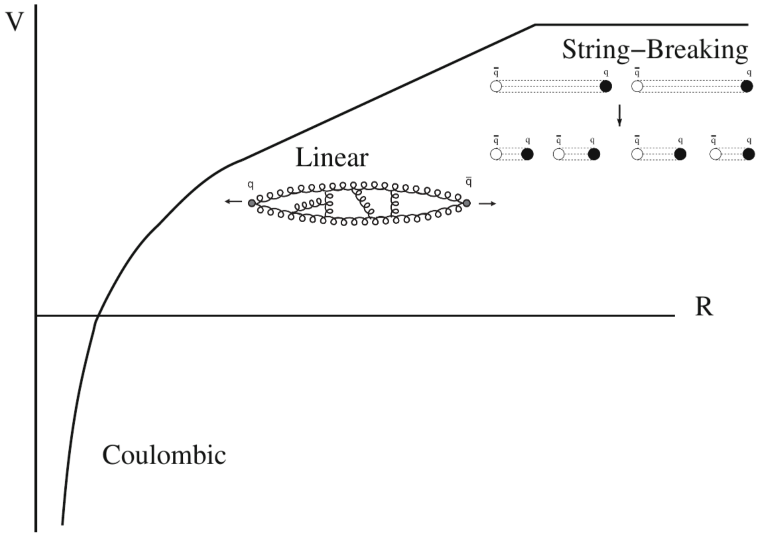

Figure 2.4: Qualitative illustration of the potential V between two quarks in QCD as a function of their separation distance R. A colour-flux tube is illustrated at the linear part of the potential, as well as the mechanism of string breaking which is becoming energetically favourable at large distances. Figure adapted from Ref. [1] and [12].

As can be seen in direct comparison of $\mathcal{L}_{\mathrm{QCD}}$ with $\mathcal{L}_{\mathrm{QED}}$ introduced in Eq. 2.1, both Lagrangians are very similar in their structure, mostly differing in the extensions for the 3 colours, 6 quark flavours and 8 gluon gauge fields in QCD. Furthermore, the electric charge $-e$ in $\mathcal{L}_{\mathrm{QED}}$ is replaced by the strong coupling strength g_s. However, the key difference to QED becomes evident when looking at the gluonic field tensor:

$$F^c_{\mu\nu} = \partial_\mu A^c_\nu - \partial_\nu A^c_\mu - g_s f^c_{\mathrm{AB}} A^{\mathrm{A}}_\mu A^{\mathrm{N}}_\nu , \tag{2.4}$$

which has to be compared to Eq. 2.2. The additional final term is describing the aforementioned self-interaction of gluons (see Fig. 2.3 middle and right) where f^c_{AB} denotes the structure function of QCD. This factor enters because the Gell-Mann matrices $\mathbf{t_c}$ do not commute, i.e.:

$$[\mathbf{t_A}, \mathbf{t_B}] = i f^c_{\mathrm{AB}} \mathbf{t}_{\mathrm{C}} . \tag{2.5}$$

This makes QCD a so-called non-Abelian gauge theory.

COLOUR CONFINEMENT Up to this point, it was described in detail how quarks and gluons interact with each other, where the interaction is described by QCD. Both, quarks and gluons are objects carrying colour charge: The gluons carry a pair of colour and anti-colour, where the combination is such that it is resulting in a non-zero net colour charge. The gluons can couple to other object carrying a non-zero colour charge, such as the quarks which carry a single colour charge of either red, blue or green. However, even though the gluons and quarks are fundamental fields of QCD, no free quarks or gluons have been observed so far. This absence of "free" colour charged particle states is referred to as colour confinement [12]. In nature, one finds quarks in bound states called hadrons which carry a net colour charge of zero. One distinguishes between baryons and mesons, where the former are bound states of three quarks (e.g. proton with uud) and the latter consist of two quarks (e.g. π^+ with u$\bar{\mathrm{d}}$). It is important to note that even though a good qualitative understanding of the concept of colour confinement and how it is manifesting itself in high-energy particle collisions exists, there is so far no analytic proof of confinement as a feature of QCD. This showcases very nicely that there is still a lot to learn about the inner workings of non-albelian gauge theories and more explicitly QCD at long distance scales.

One common qualitative approach to describe confinement, is via colour flux tubes (or strings), that illustrate the relation of gluon self-interaction with confinement: When two quarks are separated, they interact through the exchange of virtual gluons that form a colour charge field between the two quarks. Due to the fact that these exchanged gluons can interact strongly with each other too, one can imagine this field being squeezed into a tube, where the cross-section of the tube is almost constant for increasing distances R between the quarks. Therefore, the energy stored in the tube rises linearly with separation distance and an infinite energy would be needed to separate two quarks an infinite distance. The non-relativistic QCD potential between a quark and anti-quark can be written as [1]:

$$V_{q\bar{q}} = -\frac{4}{3}\frac{\alpha_s}{R} + \kappa R, \tag{2.6}$$

where one finds $\kappa \approx 1\,\mathrm{GeV/fm}$ from experimental studies of bound $\mathrm{c\bar{c}}$ and $\mathrm{b\bar{b}}$ states [13]. This is illustrated in Fig. 2.4, showing the qualitative features of the static potential between two quarks in QCD, including a sketch of a flux tube at the linear rising part of the potential. However, in reality the energy stored in the field will not rise indefinitely with increasing R, and it becomes energetically favourable to break the flux tube and create new $\mathrm{q\bar{q}}$ pairs. This process of “string breaking” is illustrated in the top right part of Fig. 2.4. The process continues until all formed $\mathrm{q\bar{q}}$ pairs have sufficiently low energies to form bound hadronic states, and therefore quarks and gluons are observed as jets of hadrons in high-energy collisions.

THE RUNNING OF α_S AND ASYMPTOTIC FREEDOM The coupling strength of the interactions in QED and QCD mentioned in the previous paragraphs is not constant, but rather depends on the scale, e.g. the momentum transfer Q^2, of a given process. This dependence is rather weak for electromagnetic interactions, where the coupling strength is slightly smaller for larger distances (small Q^2), due to the creation of virtual e^+e^- pairs that partially shield the charges of the interacting particles. However, this scale dependence is very pronounced for QCD and opposite to what is observed in QED, i.e. the coupling strength becomes less for small distances (large Q^2). The drastic change of the coupling constant α_s as a function of Q^2 is commonly referred to as *“the running of α_s”* and its decrease for large Q^2 is known as *asymptotic freedom* [1, 11].

At LO, the dependence of α_s on the momentum transfer Q^2 can be described by:

$$\alpha_s(Q^2) = \frac{12\pi}{(33 - 2N_f)\ln\left(Q^2/\Lambda^2_{\mathrm{QCD}}\right)}, \tag{2.7}$$

where N_f is the number of quark flavours relevant at the given momentum scale Q^2 and Λ_{QCD} is the QCD scale parameter. This perturbatively defined description of the coupling α_s diverges at the scale $\Lambda_{\mathrm{QCD}} \approx 200\,\mathrm{MeV}$[3], meaning that for momentum

---

[3] Exact values depend on how many quark flavours N_f were used in the calculation, where values range from $\Lambda_{\mathrm{QCD}} = (89.6 \pm 6.0)$ MeV for $N_f = 6$ to (332 ± 17) MeV for $N_f = 3$ [11].

transfers smaller than Λ_{QCD} processes can no longer be described within perturbative QCD (pQCD). In this regime, α_s is too large for interactions to be treated as small perturbations of the free theory and one has to rely on non-perturbative methods to perform calculations. The tool mainly used for calculations in this regime is Lattice QCD [11], where space-time is treated as a discrete lattice rather than continuous. However, while Lattice QCD allows for unprecedented insights, e.g. for confinement and the calculation of hadron properties, it is computationally expensive, and its precision is mainly limited by computational resources and algorithm efficiency.

Fig. 2.5 compiles a summary of experimental findings of the scale dependence of α_s [11]. The shown measurements cover a wide momentum range spanning almost 2 TeV and are found to be consistent with QCD predictions using the world average of α_s at $Q^2 = m_Z^2$:

$$\alpha_s(m_Z^2) = 0.1179 \pm 0.0010, \qquad (2.8)$$

where m_Z is the Z boson mass commonly used as a reference scale. As illustrated in the legend, a variety of different experimental techniques can be used to determine α_s, differing in precision and the Q scale probed. The coupling constant is not a physical observable itself, but rather enters other physically measurable quantities through predictions made by pQCD. Therefore, theoretical uncertainties enter these measurements and the highest order considered for the respective calculations is stated in brackets for each measurement. An overview of recent efforts in the determination of α_s can e.g. be found in Ref. [14].

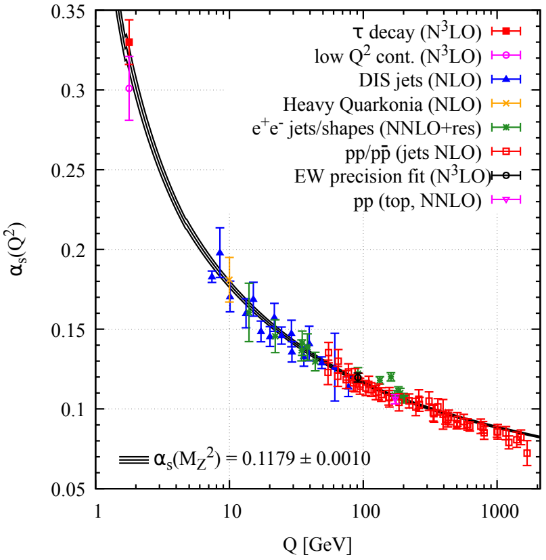

Figure 2.5: Summary of experimental findings on the energy scale Q dependence of the strong coupling constant α_s [11].

2.2 HADRON-HADRON COLLISIONS

Hadron-hadron colliders, such as the Large Hadron Collider (LHC), allow to test our understanding of particle physics at unprecedented energies that are unachievable with circular e^+e^- colliders. Reaching these high energies was e.g. crucial in the search for the Higgs boson, where very high mass scales needed to be accessed. Furthermore, since hadron-hadron collisions involve the scattering of quarks and gluons that carry colour charge, they offer a great test-bed for pQCD. However, theoretically describing hadron-hadron collisions and providing meaningful predictions for particle production is complicated: Hadrons are composite objects with a complex structure that is furthermore time-dependent, where the valenz quarks are surrounded by dynamic clouds of partons constantly changing through the creation of virtual $q\bar{q}$ pairs, as well as the emission and absorption of gluons [15]. An illustration of this complex structure within a proton can be seen in Fig. 2.6. Furthermore, since pQCD can only be applied for the scattering of quasi-free partons with sufficiently large momentum transfers Q (see Sec. 2.1.3), the initial collision state of bound QCD objects cannot be described within pQCD in any case – independent of the aforementioned structural complexity. The challenges continue in the final state of the collision where particle production through the hadronization of partons is also out of reach for pQCD.

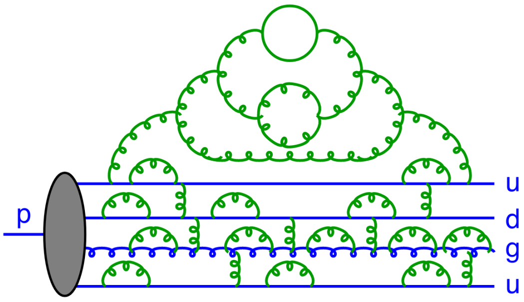

Figure 2.6: Illustration of the complex substructure of a proton [15].

This section outlines the concepts used to describe hadron-hadron collisions, overcoming the aforementioned challenges. First, important kinematic variables are defined, which are needed when describing collision systems. Then the approach of factorization is introduced, which allows to treat the perturbatively solvable hard scattering of two partons independently of the non-perturbative regimes of initial- and final state. The description of the initial state through the use of so-called PDFs is described in more detail in the following section. Finally, the discussion of hadron-hadron collisions is extended to heavy-ion collisions, which is important since also p–Pb collisions are studied in this work.

2.2.1 *Kinematic variables*

The energy E and momentum $\mathbf{p}$ of a particle can be described in a single vector known as the four-vector momentum p, which is given in natural units $c = \hbar = 1$ as

$$p = (E, \mathbf{p}) = (E, p_x, p_y, p_z) \tag{2.9}$$

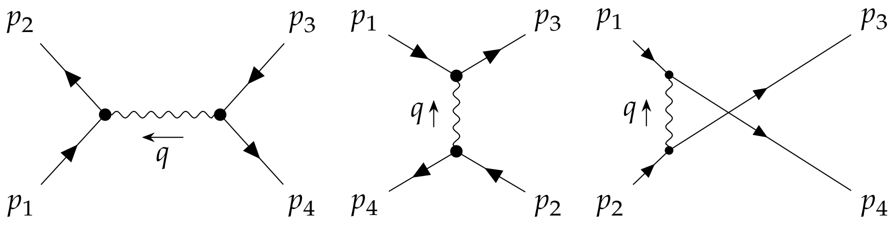

(a) s-channel (b) t-channel (c) u-channel

Figure 2.7: Feynman diagrams showing the different channels of a 2 → 2 process.

When describing any 2 → 2 process with initial state four-vector momenta p_1, p_2 and the final state momenta p_3, p_4, the centre-of-mass (cm) energy is given by the square-root of the Lorentz invariant Mandelstam variable s:

$$\sqrt{s} = \sqrt{(p_1 + p_2)^2} = \sqrt{(p_3 + p_4)^2} \quad \text{where} \quad p^2 = E^2 - \mathbf{p}^2 \tag{2.10}$$

which e.g. in the case of two colliding particles with the same momentum in opposite directions $\mathbf{p_1} = \mathbf{p}$ and $\mathbf{p_2} = -\mathbf{p}$ simplifies to:

$$\sqrt{s} = \sqrt{(p_1 + p_2)^2} = \sqrt{(E_1 + E_2)^2 - (\mathbf{p} - \mathbf{p})^2} = E_1 + E_2 \tag{2.11}$$

The cm energy is a crucial quantity in particle collisions, since it states the total energy in the cm frame which is available for particle production. Furthermore, the fact that it is invariant under Lorentz transformations allows for easy comparison between different reference frames [1, 16]. Two additional invariant Mandelstam variables t and u exist to describe momentum transfers in 2 → 2 processes:

$$\begin{aligned} t &= (p_1 - p_3)^2 = (p_2 - p_4)^2 \\ u &= (p_1 - p_4)^2 = (p_2 - p_3)^2 \end{aligned} \tag{2.12}$$

The three Mandelstam variables are associated with the three possible types of 2 → 2 processes, which are shown in Fig. 2.7: The s-channel describes the annihilation of the two incoming particles, whereas the t-channel describes the scattering process. The u-channel is a scattering process only relevant for identical final state particles [1]. For each channel, the respective Mandelstam variable is equal to the squared four-vector momentum q^2 of the exchanged bosons, which is related to hard scattering scale $Q = -q^2$, as introduced in Sec. 2.1.3.

When looking at kinematic properties of particles created/participating in collisions, it is common to separate them into longitudinal and transverse components. The transverse momentum p_T is defined as:

$$p_\mathrm{T} = \sqrt{p_x^2 + p_y^2} \tag{2.13}$$

where the z-axis is chosen to coincide with the axis of the colliding beams, simply referred to as the beam axis. This separation is motivated by the fact that particles created in the collision itself are mainly produced in the transverse direction, whereas remnants of the beam particles are produced in direction of the respective beam particle, i.e. have a larger longitudinal momentum. Analogous to the transverse momentum, the transverse mass m_{T} is defined as:

$$m_{\mathrm{T}}^2 = E^2 - p_Z^2 = m^2 + p_{\mathrm{T}}^2, \tag{2.14}$$

where $m = E^2 - \mathbf{p}^2$ is the invariant mass of the particle.

Hadron-hadron collisions take place in the cm frame of the two colliding beam particles, however, this reference frame does not necessarily coincide with the cm frame of the incoming beam particles. One has to consider a Lorentz boost along the beam axis – a consequence of special relativity which is not negligible for the high velocities found in particle collisions. It is therefore desirable to express physical quantities in a form that is invariant with respect to Lorentz transformations, i.e. they stay the same in all reference frames. For example, the aforementioned transverse momentum and mass are invariant with respect to a Lorentz boost along the beam axis. The longitudinal part of a particles kinematic condition is commonly described using the rapidity y, which is given by:

$$y = \frac{1}{2}\ln\left(\frac{E + p_z}{E - p_z}\right) \tag{2.15}$$

Even though this dimensionless quantity still depends on the frame of reference, this dependence is simple and one obtains the rapidity y' in a system boosted by y_{Boost} via:

$$y' = y + y_{\mathrm{Boost}}, \tag{2.16}$$

where y is the rapidity in the reference frame. As a direct consequence, differences between rapidities Δy are Lorentz invariant and therefore no knowledge about the boost of a system is needed when describing rapidity differences of two probes. In order to determine the rapidity of a particle experimentally, knowledge of the longitudinal momentum p_z as well as the energy E are required, which is often not easily available. Therefore, one often uses the pseudorapidity η, which only depends on the readily available angle ϑ between a particle and the beam axis, and is defined as:

$$\eta = \frac{1}{2}\ln\left(\frac{|p| + p_z}{|p| - p_z}\right) = -\ln(\tan(\vartheta/2)) \tag{2.17}$$

Comparing Eq. 2.15 and 2.15 one finds that the pseudorapidity coincides with the rapidity for $|p| \approx E$, which is the case for vanishing masses or sufficiently large momenta. Photons, which are the main probe studied in this work can therefore be described with $\eta = y$ due to their vanishing rest mass.

2.2.2 *Factorization*

As outlined in the introduction of this section, calculating cross-sections of QCD processes in hadron-hadron collisions is challenging, since not all aspects of the collision can be treated within pQCD. While scattering of free partons can be described perturbatively for sufficiently large energy scales (small α_s), these requirements are not fulfilled for the initial and final state of the collision that both involve partons bound in hadronic states. In order to still be able to obtain predictions for such cross-sections, one has to make use of so-called *factorization theorems* [17], which allow to separate the different energy scales of the collision in a systematic way. Through factorization one then obtains a cross-section which is a convolution of perturbatively treatable hard parton-parton scatterings and process independent descriptions of the non-perturbative regimes in the initial and final state. Such independent treatment of the different regimes is possible, since the hard scatterings occur on a much shorter timescale than the processes in the initial and final state: Since hadrons are bound objects, the fluctuations inside it must be smaller than the confinement scale $\Lambda_{\text{QCD}} \approx 200\,\text{MeV}$ and most virtual fluctuations inside the hadron occur on a timescale of $\approx 1/\Lambda_{\text{QCD}}$. The scattering partons interact on a much shorter timescale $1/Q \ll 1/\Lambda_{\text{QCD}}$ and therefore "see" a frozen-in-time snapshot of the initial state [15].

The nature of such a factorization and the objects involved are exemplified in the cross-section $\sigma_{NN\to h+X}$ of a process of two colliding nucleons N which produce a hadron h:

$$\frac{\mathrm{d}^3\sigma_{NN\to h}}{\mathrm{d}p^3} = \sum_{a,b,c} \underbrace{f_a(x_a,\mu_f^2) \otimes f_b(x_b,\mu_f^2)}_{\text{PDFs}} \otimes \underbrace{\frac{\mathrm{d}^3\sigma_{ab\to c+X}}{\mathrm{d}\hat{p}^3}}_{\text{partonic cross-section}} \otimes \underbrace{D_{c\to h}(z,\mu_f^2)}_{\text{fragmentation}}\,. \tag{2.18}$$

As illustrated by the brackets in Eq. 2.18[4], the cross-section can be seen as a convolution of three main parts:

PDF The initial state of the interaction is described by Parton Distribution Functions (PDFs) $f_i(x_{ai},\mu_f^2)$, which give the probability density to find a parton of flavour/type i (here parton a and b) in the respective colliding hadron as a function of the momentum fraction x_i, where the hadron is probed at a factorization scale μ_f. PDFs cannot be calculated perturbatively and need to be constrained by fits to data. Providing such constraints is one of the key motivations for the measurements presented in this work and therefore a more detailed discussion of PDFs is given in Sec. 2.2.3.

PARTONIC CROSS-SECTION The partonic cross-section $\sigma_{ab\to c+X}$ describes the hard scattering of two partons a and b that produce an outgoing parton c. Due to the sufficiently large momentum transfers involved, it can be calculated within pQCD up to a given order, commonly Next-to-Leading Order (NLO) or Next-to-next-to-leading order (NNLO). The probability to find the incoming partons a and b is fully contained within the PDFs and therefore the cross-section describes the production of parton c, given that a and b were contained in the colliding hadrons.

FRAGMENTATION FUNCTION The fragmentation function $D_{c\to h}(z,\mu_f^2)$ relates the outgoing parton c to a bound hadronic state h that can be observed in the detector [11]. Explicitly, it gives a measure for the probability density that a hadron h carrying a momentum fraction z of the parton is produced. Like the PDF, the fragmentation function cannot be calculated a priori, and requires input from experimental data. While the PDF described the non-perturbative regime of the initial state, the fragmentation function is associated with the hadronization process in the final-state which is outlined in Sec. 2.1.3.

All three elements (PDF, partonic cross-section and fragmentation function) have a dependence on the probed scale μ_f. Even though the choice of this scale is arbitrary,

---

[4] Integrals over $x_{a,b}$ and z have been omitted for visual clarity.

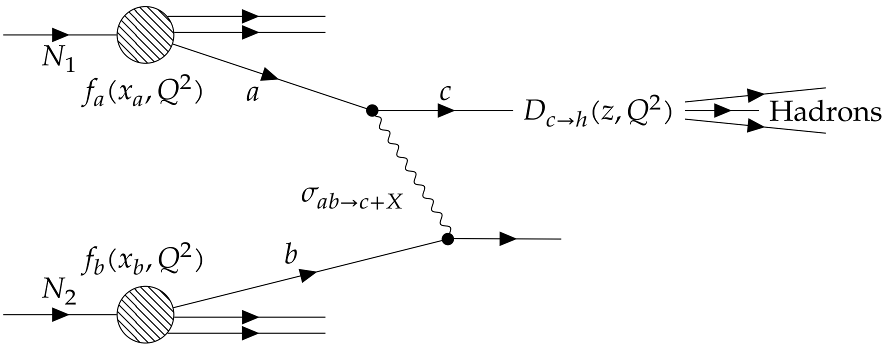

Figure 2.8: Illustration of the factorization theorem for a process $NN \to h + X$.

one commonly chooses the momentum transfer $\mu_f = Q$ or the centre-of-mass energy $\mu_f = \sqrt{s}$ for s-channel processes as a common scale for the calculation. This choice is guided by the fact that Eq. 2.18 contains both the long-distance and short-distance behaviour of the process, and therefore a choice needs to be made that is reasonable in both regimes. For example, since the hard scattering process happens on a timescale $1/Q$, it would be unreasonable to use a much shorter scale that would then include fluctuations in the PDF happening faster than the actual physical process of interest. The uncertainty arising from the choice of scale is usually estimated by varying the scale by a factor 2 around the nominal scale in both directions.

Finally, the generic process $NN \to h + X$ which was discussed in this section is illustrated in a Feynman-like diagram in Fig. 2.8, showcasing the different elements of the factorization.

2.2.3 *Parton Distribution Functions*

As mentioned in the previous section, PDFs give the probability density to find a given parton a within a nucleon/nucleus; absorbing the initial state of composite bound objects that are out of reach for perturbative treatment in parametrizations for each parton species. Explicitly, the PDF corresponds to the density of partons at a given momentum fraction x, integrated over all transverse momenta up to an arbitrary factorization scale μ_f, which is commonly chosen to coincide with the momentum transfer Q of the scattering process [18]. While the PDFs cannot be calculated a priori and have to be obtained by global fits to experimental data, their evolution with μ_f is treatable within pQCD using so-called evolution equations such as DGLAP [19] and BFKL [20]. This means that once a PDF is constrained by experimental data in a certain region of x and Q, the evolution equations can be used to extrapolate the PDF to other regions in phase space.

Precise knowledge of PDFs is crucial, since uncertainties on the PDF propagate to the uncertainties of theory predictions for physics observables, which ultimately enter a variety of measurements performed at the LHC: The PDF uncertainties e.g. played an important role in the discovery of the Higgs boson and are also the dominant systematic uncertainty for precision measurements of fundamental parameters of the standard model, such as the W boson mass [21]. In addition to being an important ingredient for various measurements, PDFs themselves represent our knowledge of the substructure of protons and neutrons: The ongoing endeavour of constraining PDFs over a wide phase space in x and Q directly corresponds to probing the proton in different regimes and testing our understanding of QCD evolution over scales spanning several orders of magnitude.

DETERMINATION OF PARTON DISTRIBUTIONS A PDF is modelled using some form of parametrization for each parton species, that usually fulfils some minimal theoretical constraints such as e.g. energy conservation or the positivity of hadronic observables [22]. These parametrizations come with a number of free parameters, which have to be optimized in order to best describe the available experimental data. Assuming the validity of factorization (see. Sec. 2.2.2), the parametrizations are used to perform theoretical calculations of various observables (jet productions, DIS etc.), which can then be compared to the available experimental data. The free parameters of the parametrization are then optimized using a given figure of merit, commonly χ^2, which encodes the differences between theoretical predictions and corresponding measurements, taking into account experimental uncertainties, as well as correlations between experimental uncertainties [23]. As the theoretical calculations have to be performed for many possible sets of free parameters, computational speed is essential, which is why NLO calculations are often performed using pre-computed grids or K-factors [23]. The x and Q^2 region in which the PDF is constrained by the data, as well as the sensitivity to different parton species (valence quarks, sea quarks gluons etc.) depends on the measured physical process.

Experimental data is mainly provided by Deep Inelastic Scattering (DIS) measurements, where the quark densities are probed directly through the scattering of leptons on nucleons via the exchange of a virtual photon, W or Z boson. This type of measurements allows to directly constrain each quark flavour and furthermore the gluon PDF can be constrained indirectly through the DGLAP evolution of Q^2. In addition, measurements of the Drell–Yan (DY) process and $W^\pm/Z^0$ production in hadronic collisions complement DIS measurements and offer a clean probe that does not involve any fragmentation or hadronisation of the final-state observables. Compared to DIS, DY measurements at colliders probe a larger Q^2 and also give better constraints to the sea-quark densities $\bar{u}(x)$ and $\bar{d}(x)$, especially for $x \gtrsim 0.1$ [18]. Measurements of hadronic observables such as jet production, offer high constraining power for the gluon density. In particular, measurements of inclusive jet, dijet and trijet production at the LHC allowed providing constraints for quarks and gluons at $x \gtrsim 0.005$, as well as the possibility to measure the strong coupling $\alpha_s(Q)$ in the TeV regime [21]. The measurement of isolated photon production, which is the topic of this thesis, allows to probe the gluon density at low-x, which will be covered in more detail in Sec 2.4. For a comprehensive overview of the processes relevant to PDF analyses as well as their kinematic coverage please refer to e.g. Tab 18.1 in Ref. [11] and Fig. 1 in Ref. [22].

The determination of PDFs is mainly carried out by six groups: MMHT [25], NNPDF [24], CT(EQ) [26], HERAPDF [27], ABMP [28] and JR [29]. The PDFs provided by each group differ in their "Ansatz" for the parametrization of the PDF, choice of experimental data included during the fitting as well as the fitting procedure itself.

Fig. 2.9 shows the recently published NNPDF4.0 NNLO proton PDF [24], given as a function of x for different parton species, evaluated at $Q = 3.2\,\text{GeV}$ and $Q = 100\,\text{GeV}$, illustrating the complex substructure of the proton: The up- and down valence quarks u_v and d_v are the dominant contribution at large x, where one finds $u_v \approx 2 \cdot d_v$, as

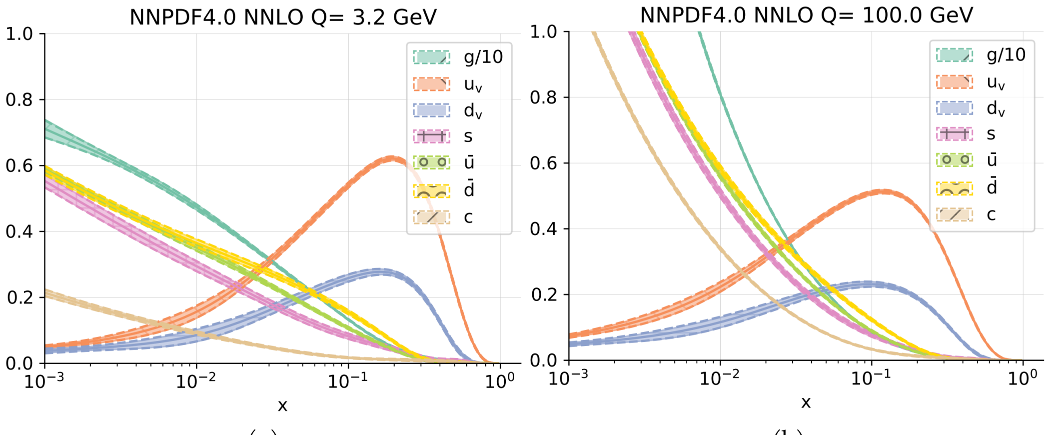

(a) (b)

Figure 2.9: NNPDF4.0 NNLO proton PDF [24] as a function of momentum fraction x, evaluated at two different scales $Q = 3.2\,\text{GeV}$ (left) and $Q = 100\,\text{GeV}$ (right). Each colour represents the PDF of a different parton species, as indicated in the legend.

naively expected for a proton which consists of the valence quark combination *uud*. Since the valence quarks constantly interact with each other via the exchange of gluons and therefore exchange momentum, one finds a smeared-out distribution rather than a delta function, which would be expected for none-interacting point like constituents. In addition to the valence quarks, one finds a sea of gluons and virtual quark- anti-quark pairs, with mostly low-momentum fractions (increase for low x). This is due to the fact that in QCD gluons of large momenta are suppressed by the $1/q^2$ gluon propagator, and therefore also the sea quark contributions originating from $g \to q\bar{q}$ are suppressed in a similar manner. Overall, one finds that roughly only 50 % of the proton's momentum is carried by quarks and anti-quarks, whereas the rest is carried by gluons. Comparing Fig. 2.9 (left) to 2.9 (right) gives interesting insights into the scale dependence of the proton's substructure. Since quarks and gluons are believed to be point-like particles, one does not expect a dependence of the PDF on the scale Q^2, which in the context of DIS is directly related to the object sizes that can be resolved by the virtual photon[5]. The independence of the PDF on Q^2 is known as *Bjorken scaling*. However, as visible in Fig. 2.9 a small dependence on the scale can be observed, i.e. one finds an increase of the contributions at low x with increasing Q^2, as well as a decrease at large x. With increasing Q the scale becomes sensitive to gluon radiation q→qg on smaller length scales, thus leading to an increase of low-x quarks and gluons which could not be "seen" by the probe at larger length-scales [1]. This evolution of quark and gluon densities with scale Q^2 is well-described by pQCD and contained in the DGLAP equations via splitting functions that encode the probability of a given parton to split into qq, qg, gq or gg [30].

The vast amount of data entering the determination of PDFs, as well as in which region of the (x, Q^2)-phasespace they have constraining power, is illustrated in Fig. 2.10 [24], that shows the kinematic coverage of all measurements entering the NNPDF4.1 determination. The fitting considers over 4616 data points covering several orders of

---

[5] The wavelength λ of a photon is given by $\lambda \sim hc/Q$ and therefore the wavelength decreases with increasing Q, allowing to resolve smaller and smaller length scales.

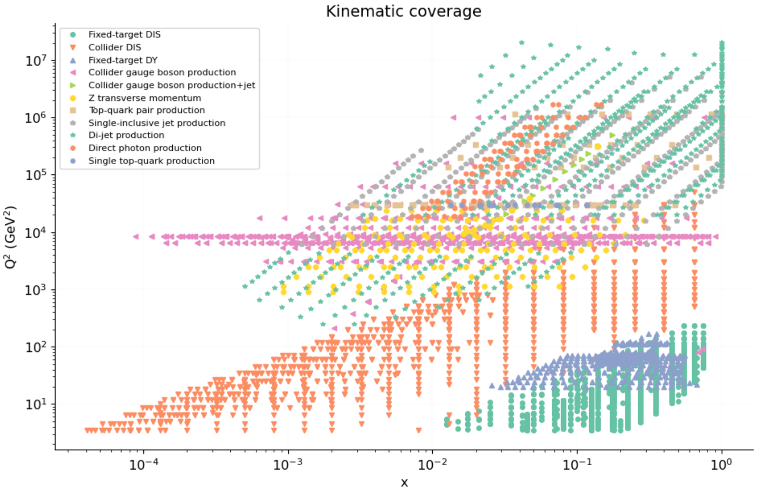

Figure 2.10: Kinematic coverage of measurements entering the NNPDF4.0 [24] determination in the (x, Q^2)-phasespace.

magnitude in x and Q^2, together leading to a unified picture of the initial state in hadronic collisions with an overall precision of about 3.5 %.

GLUON SATURATION AND CGC In the previous section, it was outlined how Bjorken-scaling is broken, i.e. how with increasing scale Q^2 the sensitivity to gluon splittings increases, which leads to an enhancement of low-x gluons. The PDF, rather than being static, *evolves* with the scale. The evolution of a PDF in (x,Q^2) phase-space can be described with QCD evolution equations, which incorporate parton splitting probabilities via dedicated functions, and allow interpolating from one region to the next. Figure 2.11 illustrates the evolution of QCD as a function of (x, Q), where sketches of a proton portray the parton density in reach regime. Both, for increasing Q and decreasing x one finds an increase of parton densities, as exemplified by Fig. 2.9. Different evolution equations become relevant in different regions of (x,Q^2) phase-space, as illustrated by arrows and the acronym of the corresponding evolution equation: At moderate to large x and Q^2 the parton densities are low enough and the evolution can be described using DGLAP [19]. For small x and moderate Q^2 one expects the BFKL [20] equations to describe the evolution. A key feature of the low-x regime is the drastic increase of the gluon density for $x \to 0$, since the *linear* equations like DGLAP and BKFL only contain splitting processes which lead to an increase in parton densities. It becomes clear that such an increase cannot continue indefinitely: At small enough x the density of gluons is so high that gluons recombine in a process of gluon fusion $(gg \to g)$. This requires *non-linear* equations to describe the evolution in this low-x regime, such as JIMWLK[31] or BK [32]. The non-linear effect of gluon fusion counteracts gluon splitting eventually leading to an equilibrium at which the gluon densities are saturated. The parametric form of gluon saturation scale Q_s is approximately [33]:

$$Q_s^2(x) \approx \frac{\alpha_s}{\pi R_h^2} xG(x, Q_s^2) \propto x^{-\lambda} \quad \text{with} \quad \lambda \approx 0.3, \tag{2.19}$$

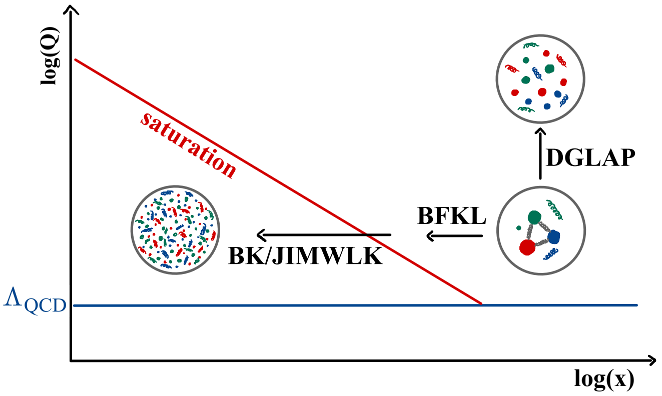

Figure 2.11: Illustration of the evolution of QCD as a function of x and Q, where the evolution equations allowing the description in each regime are indicated by arrows with the corresponding acronyms. See also Fig. 2.9 which shows the PDF for two different Q^2, which would correspond to the evolution described by DGLAP at moderate x values in this figure.

where α_s is the strong coupling constant, R_h the radius of the hadron, e.g. proton and $G(x, Q_s^2)$ the gluon density. For a given x the saturation scale $Q_{s,A}^2$ in a nucleus of mass number A is enhanced with respect to $Q_{s,N}^2$ of a single nucleon:

$$Q_{s,A}^2 \propto A^{1/3} Q_{s,N}^2 \tag{2.20}$$

In order to achieve small coupling in the saturation regime, the saturation has to be sufficiently larger than the QCD scale $\Lambda_{\mathrm{QCD}} \approx 200\,\mathrm{MeV}$, therefore making it beneficial to study saturation in nuclear environments, which will be discussed in Sec. 2.3.

A prominent model to describe the properties of saturated gluons is the Colour-Glass Condensate (CGC) [34], which is an effective field theory describing the weakly coupled state of gluons packed with a high density inside a hadron by approximating the low-x gluons with classical fields. The CGC is of special importance in the initial stages of nuclear collisions, where it produces a so-called glasma-field configurations from gluons liberated from the partons inside the colliding nuclei.

2.3 HEAVY-ION COLLISION

The study of collisions involving heavy ions, such as lead, offers unique ways for probing various fundamental aspects of QCD in extreme conditions. Ultra-relativistic heavy-ion collisions are complex and consist of different stages, each providing insights into different features of QCD as well as challenges for theorists and experimentalists trying to describe and measure them. These collisions involve very high energy densities, inaccessible with mere proton-proton collisions. For high enough energy densities, a new state of matter is formed – the so-called Quark-Gluon Plasma (QGP). In this soup-like state, quarks and gluons are found as quasi-free particle no longer confined inside of hadrons. This new state of matter is also of cosmological importance, since it is expected to have existed only a few microseconds after the Big Bang. Heavy-ion collisions therefore give us an experimental way to access these early stages of the universe by recreating the conditions of that time in the laboratory. The study of the other stages of the collision, such as the substructure of the incoming nuclei and its nuclear modifications, as well as the initial stage just before the formation of the QGP also offer exciting insights for our understanding of strongly interacting matter. It is important to realize that due to the peculiarity of QCD to display asymptotic freedom, we do not have the ability to tackle many of the observed phenomena with the well established tools of a perturbative treatment. Through the exploration of QCD dynamics in extreme conditions – provided by heavy-ion collision – one hopefully also improves our understanding of this complex theory in ordinary environments.

This section aims to provide an overview of heavy-ion collisions, which are at the heart of the A Large Ion Collider Experiment (ALICE) physics program. Section 2.3.1 gives an overview about the general phenomenology of a heavy-ion collision and its different stages, followed by a selection of experimental observables for the QGP in Sec. 2.3.2. Section 2.3.3 provides insights into the initial stages of the collision, with a special focus on nuclear modifications of the initial state.

2.3.1 *Phases of a heavy-ion collisions and QGP formation*

Colliders such as the LHC and Relativistic Heavy Ion Collider (RHIC) allow accelerating heavy ions such as Au and Pb to high energies ($\mathcal{O}$(TeV) at the LHC), which are then brought to collide inside the various experiments positioned at different points around the collider. Due to their high velocities, the incident nuclei, which are moving towards each other, get Lorentz-contracted in their direction of travel. The incoming nuclei therefore appear as discs in the centre-of-mass frame, where the diameter is about 14 fm and their thickness is reduced by approximately a factor of 100 and 2500 for RHIC and LHC, respectively [36]. Due to the contraction of the disc, the area density of partons inside the nucleus increases with increasing velocity. As will be discussed in Sec. 2.3.3, the momentum distribution of partons found in the nuclei goes beyond a mere superposition of free-proton PDFs that were introduced in Sec. 2.2.3, i.e. the fact that the protons and neutrons are very close to each other and also move inside the nucleus causes small modifications to the parton distributions that necessitate their description through dedicated nuclear PDFs (nPDFs).

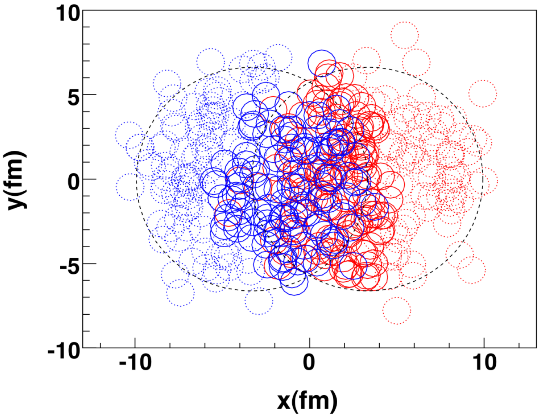

Figure 2.12: Illustration of a Pb–Pb collision with $b \approx 7$ fm in the picture of the Glauber model. Nucleons participating in the collision are shown as solid lines, whereas spectators are indicated by dashed lines [35].

Eventually, the two discs moving towards each other will overlap and collide. On the level of nucleons inside the nuclei, one finds that not all nucleons participate in the collision, i.e. not all nucleons will encounter a nucleon from the other colliding nucleus. This is due to the fact that the discs will not necessarily collide “head-on” but rather have some displacement which is described with the so-called impact parameter b. In essence, the larger the impact parameter the smaller the overlap between the colliding discs, and therefore the number participating nucleons N_{part}. This is illustrated in Fig. 2.12. The number of collisions N_{coll} between participating nucleons is usually much larger than N_{part}, due to the fact that a participating nucleon from one nucleus can interact with multiple nucleons from the other nucleus, where in a heavy-ion collision a nucleon at the centre of the nucleus will on average encounter about 12 nucleons from the other nucleus [36]. The impact parameter b, N_{part} as well as N_{coll} are not directly accessible experimentally, however, a well-established procedure known as Glauber-model calculation [35, 37] allows to determine these quantities on average for collision events which were classified according to event centrality. This is done by assuming a monotonic relation between the number of particles produced in a collision (or their energy) with the number of participants N_{part}, where these measured distribution can be fitted with predictions from the Glauber calculation. The event centrality is defined as the percentile of the hadronic cross-section for which more than a given energy or multiplicity threshold is produced, where a lower percentile corresponds to a more central/head-on collision [38].

Looking at the collision on the level of partons, one finds that the incoming discs are dominated by saturated low-x gluons, which can be described in this saturation regime as fields using the aforementioned CGC effective field theory. When these fields collide, colour is exchanged between the two colliding nuclei, i.e. longitudinal colour fields are created between the two fields of the incoming nuclei which stay coherent for a very brief amount of time ($\tau \lesssim 1\,\text{fm}/c$) after the collision forming the so-called GLASMA [39], which then gradually decays into gluons and $q\bar{q}$ pairs. The description of this very early stage of the collision is very involved and still a matter of current research, especially when and how these fields stop being coherent and form the QGP. Going back from the picture of fields to the picture of partons, one finds that most of the incoming partons interact with each other softly, i.e. the momentum transfer between the interacting partons is small and they are not significantly deflected. However, a small fraction interacts with large momentum transfer (hard), producing a probe with high transverse momentum (p_{T}) or mass, such as a jet[6], a Z boson or a photon, the latter of which is the probe of interest in this work and will be discussed in detail in Sec. 2.4.

At about $\tau \sim 1\,\text{fm}/c$ after the collision, the receding discs are about 2 fm apart and in the space between them one finds an expanding system of quarks and gluons which were produced in the aforementioned early stage of the collision. The energy density of this system is large, which was experimentally estimated to be $(12.3 \pm 1.0)\,\text{GeV}/\text{fm}^3$ for most-central Pb–Pb collisions at $\sqrt{s_{\text{NN}}} = 2.76\,\text{TeV}$ by the ALICE experiment [41], which is about 20 times the energy density of a hadron. At these large energy densities, the quarks and gluons are no longer bound inside hadrons, but rather form a collective medium, where the individual quarks are coupled to each other via the strong interaction and can travel distances larger than the radius of a nucleon ($\approx 0.84\,\text{fm}$ [42]). This new state of matter is called the Quark-Gluon Plasma (QGP), which was already postulated to exist as a consequence of asymptotic freedom by Collins and Perry [43] as well as Cabbibo and Parisi [44] in the mid-seventies. Remarkably, the plasma behaves likes a relativistic hydrodynamic fluid of strongly coupled quarks and gluons, which has to be described using hydrodynamic equations, while it was originally expected to be a weakly coupled plasma [36]. Comparing hydrodynamic models to experimental data of the anisotropy of particle production in heavy-ion collisions at the RHIC and

---

[6] A jet is a collimated spray of particles which are produced by the hadronization of an outgoing quark.

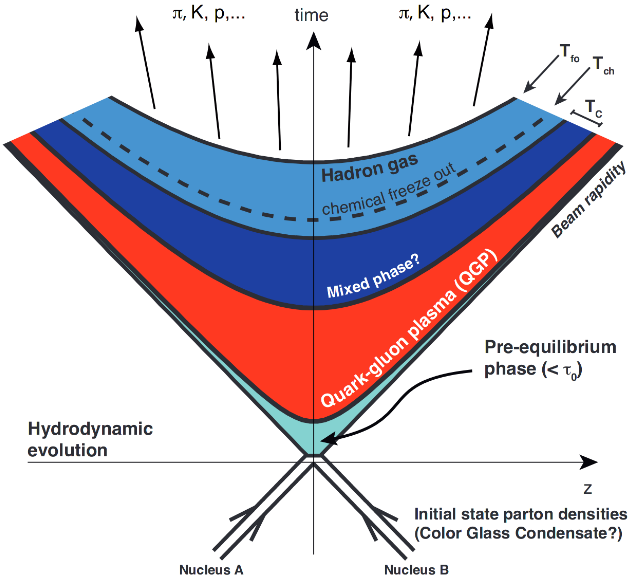

Figure 2.13: Evolution of a heavy-ion collision in space and time [40].

LHC [45], one finds that the specific viscosity[7] η/s, which is a material property that in essence quantifies the "liquidness" of a liquid, is on average close to theoretically predicted lower limit $\eta/s \geq 1/4\pi$, which is lower than that of any other known liquid. The initial conditions of the produced liquid are determined by the incoming nuclei, where their lumpiness leads to a non-uniform energy and temperature distribution. The QGP (which is far from equilibrium)then expands and cools, where its evolution is governed by hydrodynamics until the temperature falls below a critical threshold $T_c \approx 155$ MeV and the QGP undergoes a crossover phase transition and forms hadrons, which is known as the chemical freeze-out. The hadrons continue to interact with one-another, until the so-called thermal freeze-out occurs at $T \approx 95$ MeV and the hadrons freely move outwards and can be measured by the detectors [36].

The previously outlined process of QGP formation illustrated that QCD matter can exist in different phases, where a phase transition occurred with decreasing temperature from the QGP to ordinary hadronic matter – the same process that occurred micro seconds after the Big Bang in a rapidly expanding and cooling universe. Like for any other material, the phase diagram is of great interest, where one maps the state of the material to different regions in e.g. the phase-space spanned by pressure and temperature. A sketch of our current understanding of the phase diagram of QCD matter is given in Fig. 2.14, the exploration of which is a key motivation for studying heavy-ion collision. The white lines labelled with different centre-of-mass energies $\sqrt{s_{\mathrm{NN}}}$ indicate the path through this phase-space of an expanding and cooling QGP produced in a heavy-ion collision at the respective energy. The phase transition occurring at baryon doping $\mu_{\mathrm{B}} \approx 0$ is well understood within lattice QCD, where one finds a critical temperature for the crossover of QGP to hadronic matter of $T_c = (156.5 \pm 1.5)$ MeV [46]. The value was obtained for $\mu_{\mathrm{B}} = 0$, which is a good approximation for heavy-ion collisions at LHC energies, and a reasonable one for the energies reached at RHIC. The dependence of the probed baryon doping μ_{B} on the collision energy arises due to

---

[7] The ratio of shear viscosity η and entropy density s quantifies the effect that the shear viscosity has on the fluid. A large viscosity corresponds to a large resistance with respect to deformation/flow of the liquid

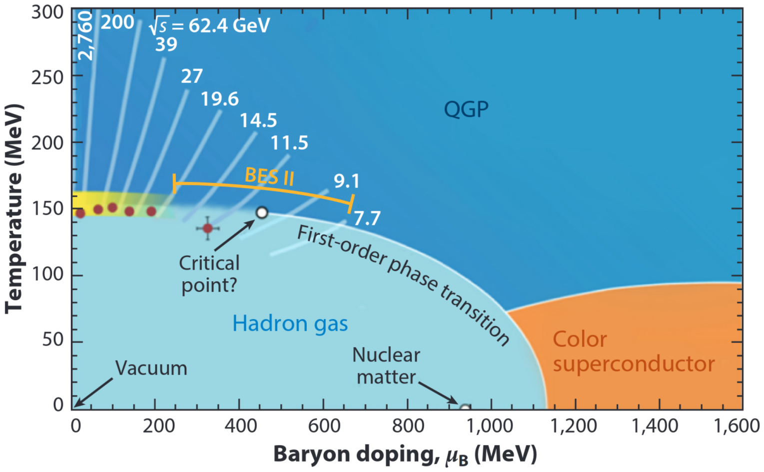

Figure 2.14: Features of the phase diagram of QCD matter as a function of temperature and baryon doping μ_B, the latter of which quantifies the excess of quarks over anti-quarks [36].

the fact that the number of particles produced in a collision increases with increasing centre-of-mass energy. Heavy-ion collisions at LHC energies produce thousands of particles, leading to $\mu_B \approx 0$ since the excess of quarks over anti-quarks in the initial state of colliding nuclei becomes negligible. For lower collision energies less particles are produced and therefore the abundance of quarks in the initial state becomes relevant. The study of a possible phase-transition of QCD matter at high μ_B, which is e.g. relevant at the large densities in neutron stars, will be possible in the future with the Compressed Baryonic Matter (CBM) experiment, which is currently being constructed at the future Facility for Antiproton and Ion Research (FAIR) in Darmstadt, Germany [47].

2.3.2 *Experimental probes for the QGP*

The QGP produced in heavy-ion collisions is very short-lived, undergoing the transition to hadronic QCD matter within about 10^{-22} s [48]. Consequently, no direct experimental observables exist to study the QGP in its lifetime. However, one has access to a vast amount of particles that get produced in heavy-ion collisions which can be either measured directly or reconstructed from their decay products. These particles get produced in various stages of the collision and contain information about the QGP, e.g. because they were produced by the QGP itself (e.g. thermal photons) or because they were produced in an earlier stage and then interact strongly with the QGP when traversing it (e.g. an outgoing quark from a hard scattering). Thanks to the ever improving detector design and technologies, one has access to a variety of properties of these produced particles with high precision including their energy, momentum, charge, position in $\eta - \phi$ space as well as the type of particle produced. In addition, the produced particles themselves also differ in their mass, flavour content, colour charge etc., which impacts their production mechanism (and time) as well as interactions with the QGP. All-together, this gives the experimentalist a great "toolbox"' to indirectly study the QGP, where depending on the observable, one gains access to a different QGP property. Measurements are often not limited to heavy-ion collision but also include a comparison to proton-proton collisions, where the formation of the QGP is

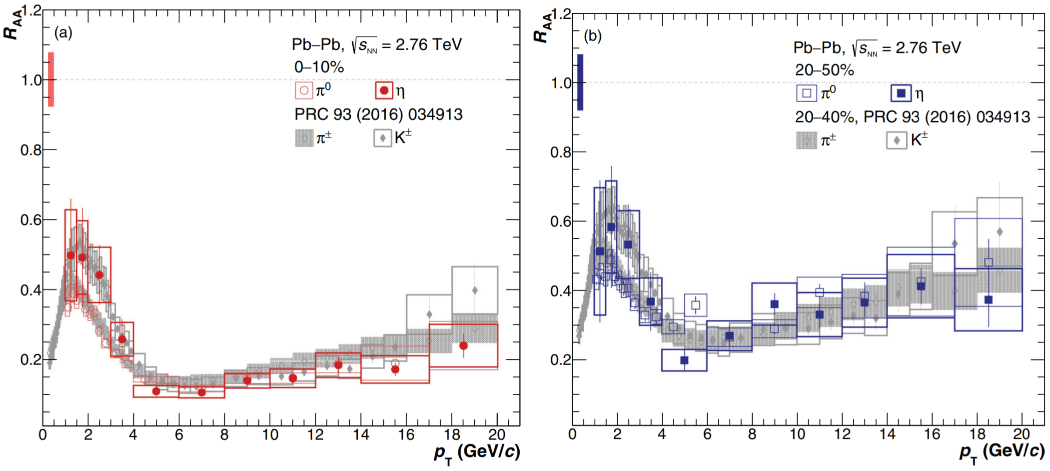

(a) 0-10 % centrality (b) 20-50 % centrality

Figure 2.15: Nuclear modification factor R_{AA} shown for a selection of identified particles (π^0, η, $\pi^\pm$ and $K^\pm$[49–51]) in two different centrality classes, measured by ALICE in Pb–Pb collisions at $\sqrt{s_{NN}} = 2.76$ TeV. Figure taken from Ref. [49].

not expected. These measurements serve as a baseline for the heavy-ion measurement, and information about the QGP is contained in the differences between both systems. Studies of asymmetric collision systems such as p–Pb serve as an additional reference point between pp and Pb–Pb collisions and furthermore give important insights into initial state effects (see. 2.3.3).

This section discusses a small selection of experimental observables, which are being used as an indirect probe for the QGP. Even though the exploration of the QGP and its properties is not the primary focus of this work, an understanding of the observables is important in order to give context to the importance of initial state effects, which have to be disentangled from QGP induced modifications of the final-state observables in order to come to meaningful conclusions about its presence and properties.

PARTON ENERGY LOSS Highly energetic quarks and gluons which are created in the initial hard scattering of the collision traverse the QGP. Since they are coloured objects, they should interact with the medium and suffer energy loss, similar to electrically charged particles traversing ordinary matter. Such an energy loss mechanism was first proposed by Bjorken in 1983 [52] and is commonly referred to as "jet quenching". The outgoing parton cannot be observed directly since it hadronizes into a collimated spray of particles (jet) and therefore the partonic energy loss has to be studied using these final-state particles. In order to quantify jet quenching one commonly studies p_T-differential yield of a given observable using the nuclear modification factor R_{AA} , given by:

$$R_{AA} = \frac{d^2N_{AA} \,/\, dy\, dp_T}{\langle N_{coll.}\rangle \cdot d^2N_{pp} \,/\, dy\, dp_T}, \tag{2.21}$$

where $N_{coll.}$ is the number of collisions between nucleons, as briefly introduced in Sec. 2.3.1 and obtained using Glauber model simulations and $d^2N_{AA} / dy\, dp_T$ and $d^2N_{pp} / dy\, dp_T$ are particle yields measured in a heavy-ion (AA) and proton-proton (pp) collisions, respectively. This ratio therefore quantifies differences in particle spectra in

AA collisions (where formation of the QGP is expected) with respect to proton-proton collisions (where the formation of the medium is not expected). The scaling of the proton-proton yields with $N_{\mathrm{coll.}}$ accounts for the fact that more individual collisions between nucleons occur in a AA collision compared to a collision of just two protons ($N_{\mathrm{coll.}} = 1$). A deviation of the R_{AA} from unity therefore indicates a modification of the yields in the heavy-ion collision that goes beyond the expectation of a mere superposition of individual collisions between nucleons. Such a deviation can then be attributed to the medium, where one expects a suppression in A–A collisions at sufficiently high collision energies due to jet quenching. However, modifications of the initial state itself (often referred to as cold nuclear matter/initial-state effects) can also modify the observed yields and therefore has to be carefully studied in other collision systems, such as p–A (see. Sec. 2.3.3).

Fig. 2.15 shows the R_{AA} for a selection of identified charged and neutral particles, measured by the ALICE experiment in Pb–Pb collision at $\sqrt{s_{\mathrm{NN}}} = 2.76\,\mathrm{TeV}$ [49–51]. The R_{AA} is shown for two centrality classes, where the 0-10 % class corresponds to head-on collisions with a mean number of collisions of about $N_{\mathrm{coll.}} \approx 1500$ and the 20-50 % class contains more peripheral collision events with $N_{\mathrm{coll.}} \approx 350$ [38]. One finds a clear suppression for all particles, which is decreasing with increasing momentum. This suppression is strongest for the most central collisions and furthermore one finds a dependence on collision energy, where a stronger suppression is observed compared to measurements at lower centre-of-mass energies (see e.g. PHENIX results at $\sqrt{s_{\mathrm{NN}}} = 200\,\mathrm{GeV}$ [53]). No such high-p_{T} suppression is observed for measurements of e.g. π^0 production in p–Pb collisions [54], as well for colourless probes in Pb–Pb such as γ [55], Z [56] and $W^{\pm}$ [57], which do not interact strongly with the medium. This indicates that the observed suppression at $p_{\mathrm{T}} \gtrsim 10\,\mathrm{GeV}/c$ cannot be attributed to effects in the initial state, but rather is originating from partonic energy loss due to the presence of the QGP.

DIRECT PHOTONS Photons are produced in all stages of a heavy-ion collision and are an ideal probe due to their lack of strong interaction, allowing them to carry information from the time of their production until their detection in the experimental apparatus, unaltered by final-state effects such as the aforementioned jet-quenching. The majority of photons in a collision are produced in electromagnetic decays of hadrons (mostly $\pi^0 \rightarrow \gamma\gamma$), however, a small fraction of the photons produced in a collision does not originate from particle decays, and these photons are referred to as *direct photons*. One distinguishes between multiple sources of direct photons [58], differing in their production mechanism and time: *Prompt photons* are produced in the initial stage of the collision in a hard scattering process of the partons from the incoming nuclei, such as Compton scattering or quark-antiquark annihilation. In addition, so-called *fragmentation photons* are produced by the outgoing quark during its hadronization to a jet. Studying prompt photons, which are associated with cold nuclear matter effects, is the main topic of this work and they will therefore be discussed separately in detail in Sec. 2.4. The second source of direct photons are *thermal photons*, which are produced by interactions between the constituents of the thermalized QGP or hadron gas and thus contain information about the plasma such as its temperature and collective flow [59]. Their contribution is expected at small momenta of $p_{\mathrm{T}} \lesssim 4\,\mathrm{GeV}/c$, whereas prompt photons are the dominant contribution to direct photons at $p_{\mathrm{T}} \gtrsim 5\,\mathrm{GeV}/c$ [60]. Direct photons at low-p_{T} are usually measured using a statistical approach, where expected contributions[8] from decay photons (γ_{decay}) are subtracted from the inclusive measurement of all photons produced in the collision ($\gamma_{\text{incl.}}$). An excess of photons that goes beyond the expected contribution from decay photons can then be attributed to be originating from direct photons, where the excess is quantified via:

$$R_\gamma = \frac{\gamma_{\text{incl.}}}{\gamma_{\text{decay}}} \tag{2.22}$$

and the number of direct photons ($\gamma_{\text{dir.}}$) is given by

$$\gamma_{\text{dir.}} = \gamma_{\text{incl.}} - \gamma_{\text{decay}} = 1 - \frac{1}{R_\gamma} \cdot \gamma_{\text{incl.}} \tag{2.23}$$

Fig. 2.16 shows a measurement of R_γ in Pb–Pb collisions at $\sqrt{s_{\mathrm{NN}}} = 2.76\,\mathrm{TeV}$ by ALICE in three different centrality classes [60]. An excess at high-p_{T}, which can be attributed to prompt photons, is visible in all three centrality classes, whereas a small-excess at $\lesssim 4\,\mathrm{GeV}/c$ at low-p_{T} can only be observed for mid-central and most central collisions. This excess is attributed to thermal photons, and its statistical significance was quantified to be about 2.6σ for most central collisions. An effective temperature $T_{\text{eff}} = (297 \pm 12^{\text{stat.}} \pm 41^{\text{sys.}})\,\mathrm{MeV}$ [60] was extracted from the inverse slope of the exponentially falling thermal photon spectrum, where T_{eff} is related to the average temperate of the medium during its evolution in space and time. The slope was extracted for $0.9\,\mathrm{GeV}/c < p_{\mathrm{T}} < 2.1\,\mathrm{GeV}/c$, where remaining contributions from prompt photons were subtracted according to NLO expectations. Similar measurements were performed by the PHENIX experiment for Au-Au collisions at $\sqrt{s_{\mathrm{NN}}} = 200\,\mathrm{GeV}$, where slightly lower effective temperatures of $T_{\text{eff}} = (221 \pm 19^{\text{stat.}} \pm 19^{\text{sys.}})\,\mathrm{MeV}$ [61] and $T_{\text{eff}} = (239 \pm 25^{\text{stat.}} \pm 7^{\text{sys.}})\,\mathrm{MeV}$ [62] were obtained.

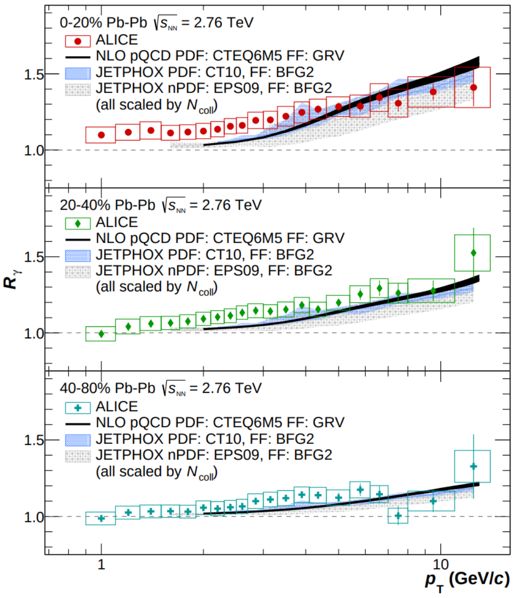

Figure 2.16: Measurement of direct photon excess in Pb–Pb collisions at $\sqrt{s_{\mathrm{NN}}} = 2.76\,\mathrm{TeV}$ in three different centrality classes [60].

2.3.3 *Nuclear Parton Distribution Functions and Initial State Effects*

When studying any hadronic collision process, a precise quantitative understanding of the partonic substructure of the incoming projectiles is crucial. Almost all entropy of a heavy-ion collision is produced in its initial stage, and therefore particle production is controlled by the conditions present in the initial state of the collision, i.e. before any hydrodynamic evolution of the hot QCD medium [36]. For soft particles ($p_{\mathrm{T}} \lesssim 1\,\mathrm{GeV}$), which are the majority of particles produced in a heavy-ion collision, the initial state of the collision determines event properties such as the particle multiplicity and collision

---

[8] The contribution from decay photons are estimated by using a cocktail approach, where one uses measured spectra of hadrons that produce decay photons (e.g. $\pi^0 \to \gamma\gamma$) and their decay is simulated using an MC generator in order to obtain the corresponding decay photon yields. See e.g. Fig. 1 in Ref. [60].

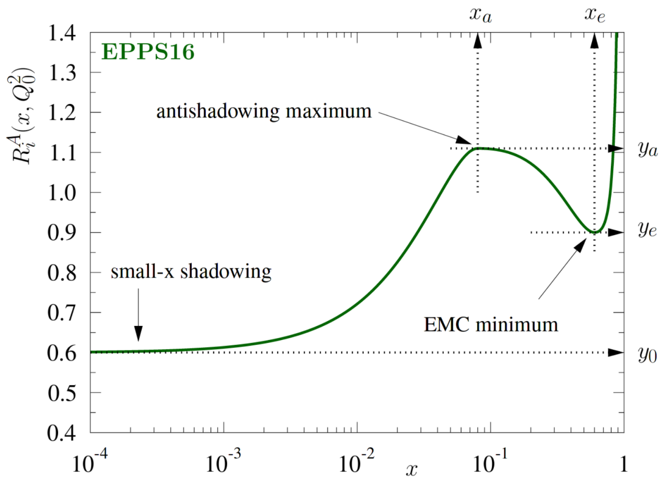

Figure 2.17: Illustration of the function used in EPPS16 [65] to describe the nuclear modification $R_i^A(x, Q_0^2)$ of a free-proton PDF, where Q_0^2 is the parametrization scale which was set to the charm pole mass $m_c = 1.3\,\text{GeV}$. The different effects leading to a suppression/enhancement in different x regimes are outlined in the text.

geometry [63]. The production cross-section of hard probes produced in a parton-parton scattering with large momentum transfer is also directly influenced by the PDFs of the incoming projectiles, as previously illustrated in Eq. 2.18. This fact is especially important when using a hard probe to study the QGP in heavy-ion collisions, since a modification in the initial state can lead to signatures that look very similar to those expected from a modification induced by the QGP (e.g. a suppression in the previously discussed R_{AA}).

The description of the initial-state of a proton-proton collision was already discussed in Sec. 2.2.3, where PDFs determined from fits to experimental data allow to describe the partonic structure of the proton, which can then be used in calculations of cross-sections. An intuitive extension of this approach to describe the initial state of a heavy-ion collision would therefore be to describe the nucleus as a superposition of free proton and neutron PDFs. However, such attempts fail to describe experimental data, and DIS experiments in the early 80s using iron and deuterium made clear that nuclear effects have to be considered when describing colliding nuclei [64]. In other words, the momentum distribution of partons inside a proton that is bound in a nucleus differs from the one observed for free protons in pp collisions. Today, a variety of collaborations provide dedicated nuclear PDFs (nPDFs) such as e.g. EPPS16 [65], nCTEQ15 [23] and nNNPDF3.0 [66] that incorporate modifications with respect to a free-proton baseline. The nPDF $f_i^{p/A}$ of a proton bound in a nucleus with mass number A is usually parameterized using the respective free-proton $f_i^p(x, Q^2)$ PDF modified with a scale-dependent modification factor $R_i^A(x, Q^2)$ that is absorbing the nuclear effects, i.e.

$$f_i^{p/A}(x, Q^2) = R_i^A(x, Q^2) \cdot f_i^p(x, Q^2), \tag{2.24}$$

where i is the respective parton species. Usually the nPDF is also provided for the full nucleus, which can be obtained by simple addition of the bound proton and bound neutron PDFs $f_i^{p/A}$ and $f_i^{n/A}$:

$$f_i^{\text{full}}(x, Q^2) = Z/Af_i^{p/A}(x, Q^2) + (A - Z)/Af_i^{n/A}(x, Q^2), \tag{2.25}$$

where Z is the atomic number of protons in the nucleus and the neutron PDF is directly related to the proton PDF via isospin symmetry[9]. The nuclear suppression $R_i^A(x, Q^2)$ is illustrated in Fig. 2.17, which shows the fitting function used for EPPS16 [65], where unity corresponds to no modification with respect to the free-proton case. Several effects play a role in different x regions:

SHADOWING AND ANTI-SHADOWING ($x \lessapprox 0.1$ and $x \approx 0.1 - 0.2$) A depletion at low-x is observed that can in principle be explained by multiple scattering of the hadronic component[10] of the exchanged virtual photon: Since the nucleus is a spatially extended system, interactions with the inner nucleons are "shielded" by the outer nucleons, where multiple interactions with these nucleons leads to an overall reduction of the cross-section with respect to a mere superposition of independent collisions. In other words, the outer nucleons absorb parts of the incoming projectile flux and thus cast their "shadow" on the inner nucleons. This process can be described as a quantum-mechanical interference of single and double scattering, where constructive and destructive interferences lead to shadowing and anti-shadowing, respectively. This explanation using multiple scattering is common for many models, however they differ in their phenomenological details. A different (potentially in some way equivalent) view of the shadowing phenomenon was proposed by Nikolalev and Zacharov [67], where shadowing is attributed to the fact that low-x partons due to the uncertainty relation can overlap with partons from other nucleons and fuse. For a review of these effects please refer to Ref. [64] and [68].

EMC EFFECT ($x \approx 0.2 - 0.8$) The discovery of the EMC effect [69] sparked great commotion in the scientific community and a variety of models exist to explain the observed enhancement at $x \approx 0.2 - 0.8$. The common "theme" of these models is a change in scale that leads to the enhancement. Explanations include enhanced pion presence, an increase in quark confinement size/nucleon size as well as an entirely different treatment of nucleons inside the nucleus without quarks. For a thorough review see Ref.[70].

FERMI MOTION ($x \gtrapprox 0.8$) This rise can be attributed to the fact that nucleons are not stationary inside the nucleus and themselves move with some average momentum. Therefore, when studying the momentum distributions of partons in nucleons in the context of a nuclear environment, the convolution with the momentum distribution of the nucleons themselves has to be considered [64].

Fig. 2.18 shows the modification of nPDFs in Pb at a scale $Q = 10\,\text{GeV}$ with respect to the free-proton baseline for 6 different parton species [66]. The lines indicate the

---

[9] I.e. one can obtain the neutron PDF by simply replacing the u contribution from the proton with the d contribution and vice versa.

[10] The virtual photon has a hadronic component due to the possible splitting to quark- anti-quark pairs.

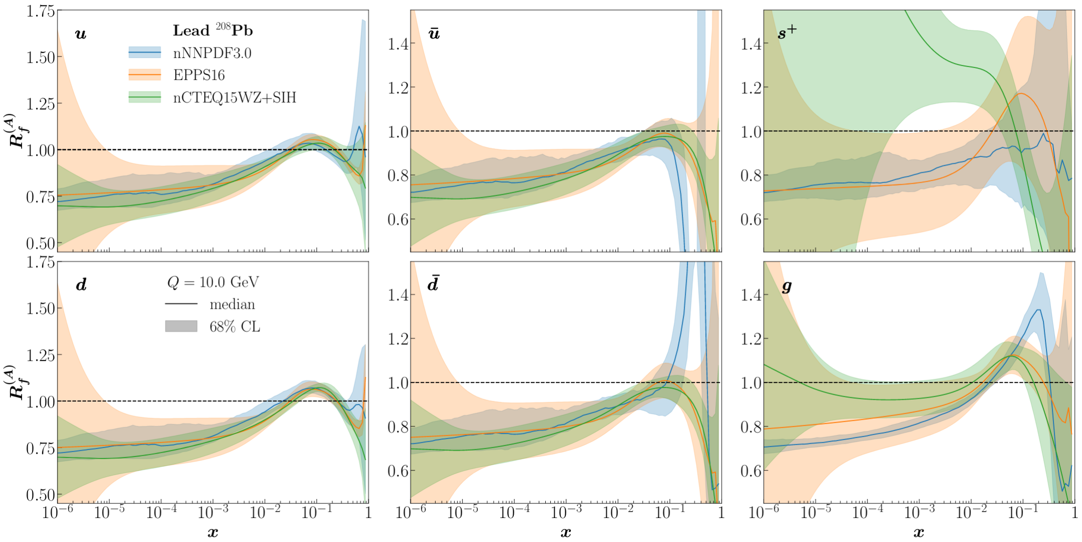

Figure 2.18: Nuclear modification of nuclear PDFs (nPDFs) for different parton species with respect to the free proton baseline. nNNPDF30 [66], EPPS16 [65] and nCTEQWZ+SIH [71] are shown, where the bands illustrate the uncertainties at a 68 % confidence level. Figure taken from Ref. [66].

central values for different nPDFs indicated in the legend, and the bands show the associated uncertainties at a 68 % confidence level. Overall, the shown nPDFs display the features of the previously outlined nuclear effects such as shadowing at low-x, however, the magnitude and onset differs for each parametrization. This is especially pronounced for the gluon nPDF shown in the bottom right panel, where one observes clear differences in the strength of shadowing and anti-shadowing at low-x. However, within the uncertainties, a more or less consistent picture of nPDFs nuclear modification arises for all shown nPDFs. While a lot of progress has been made in recent years to better constrain nPDFs, especially with inclusion of data from heavy-ion collisions at the LHC, the amount of data available for various nuclei is much smaller compared to their free-proton counterparts. This is illustrated when e.g. comparing the number of datapoints $n_{\mathrm{dat.}}$ used to constrain NNPDF40 compared to nNNPDF30, where $n_{\mathrm{dat}} = 4426$ [24] were used for the proton PDF and only $n_{\mathrm{dat}} = 2188$ [66] for the nPDF. The lack of constraints is especially visible for the gluon at low-x, where one finds steeply increasing uncertainties of $\gtrsim 30\,\%$ with decreasing x, as illustrated in Fig. 2.18. The free-proton PDF on the other hand is quite well constrained, where one finds uncertainties in the order of a few percent for the gluon PDF even at $x \sim 1 \times 10^{-4}$ [24]. Measurements of isolated photon production in p–Pb collisions, as presented in this thesis, can help to better constrain gluon nPDFs and thus improve our quantitative understanding of nuclear effects in the initial state, such as shadowing.

The concept of *gluon saturation* was already introduced in Sec. 2.2.3 where the growth of low-x gluons is expected to saturate below a specific scale Q_s. This is especially relevant for the initial state of heavy-ion collisions, where the saturation scale increases proportionally to the thickness $\sim A^{1/3}$ of the nucleus, due to the increased gluon densities in the Lorentz contracted nuclei. The CGC formalism then allows to perform calculation in this saturation regime, allowing to provide the initial conditions for the evolution of the collision system, which can have a significant impact on e.g. the shear

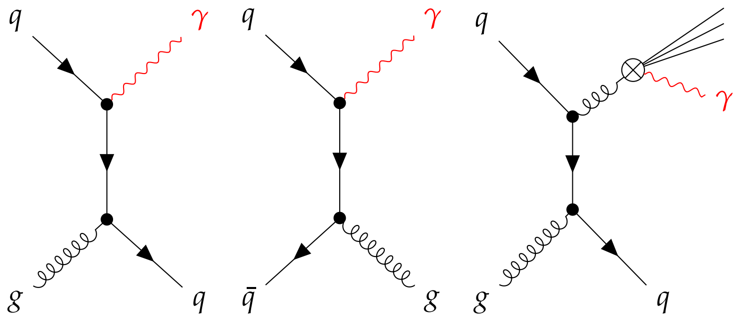

(a) Compton (b) annihilation (c) fragmentation

Figure 2.19: Feynman diagrams of prompt photon production processes.

viscosity of the QGP extracted from hydrodynamical calculations [63]. Given the importance of saturation effects for earliest stages of a heavy-ion collision, experimental searches for saturation phenomena are of great interest. Due to the aforementioned proportionality to the nucleus thickness, heavy-ion collisions are a better suited environment for these searches than mere proton-proton collisions. In particular, p–Pb collisions, which are studied in this work, provide a good handle on initial state effects due to the absence final state effects induced by the QGP, which play an important role in Pb–Pb collisions. Saturation effects are expected to be most pronounced in measurements at very forward rapidities, which on average probe lower x in the initial state, motivating the planned Forward Calorimeter (FoCal) [72] for ALICE. This new detector, as well as its expected performance for measuring isolated photon production will be discussed in detail in Sec. 12.

2.4 PROMPT PHOTONS

The previous section gave an overview of initial-state effects and their importance for our understanding of heavy-ion collisions, as well as the current landscape of PDFs and nPDFs which require constraints provided by experimental data. This section discusses the production of so-called prompt photons, which are produced directly in the initial hard scattering process and provide an excellent probe for the initial state, due to their lack of strong interaction, allowing them to reach the detector unaffected by final state effects. Furthermore, the majority of these photons is produced in quark-gluon Compton scattering ($qg \rightarrow \gamma q$), making prompt photon production sensitive to the gluon PDF, which is one of the least constrained PDF and not directly accessible via DIS measurements. In contrast to other hard probes of the initial state, such as inclusive hadron production or jet production, the (at LO) point-like coupling of the photon to the parton in principle gives particularly clean access to the initial state, unobscured by fragmentation of an outgoing quark to a hadron or procedures of jet reconstruction [73].

2.4.1 *Prompt photon production*

Prompt photons are produced in the primary hard scattering of partons from the colliding projectiles via two possible mechanisms: The photon can either participate

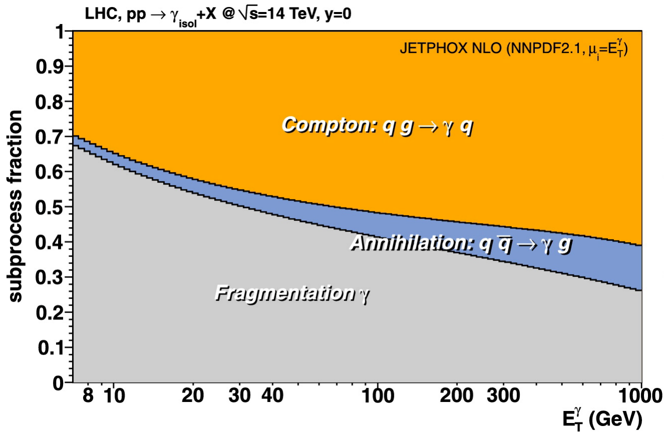

Figure 2.20: Relative contributions of subprocesses to the total prompt photon production cross-section at nominal LHC collision energy of $\sqrt{s} = 14\,\text{TeV}$ [75].

directly in the hard scattering as one of the outgoing particles, or it is produced indirectly from collinear fragmentation of an outgoing parton. The Feynman diagrams of the most probable processes of prompt photon production are given in Fig. 2.19. At LO, prompt photons are mainly produced via the Born-level processes of Compton scattering ($qg \rightarrow \gamma q$) and annihilation ($q\bar{q} \rightarrow \gamma g$), where NLO corrections are coming from subprocesses such as $qg \rightarrow \gamma gg$ and $q\bar{q} \rightarrow \gamma gg$. Photons produced in these processes are referred to as *direct prompt photons*, due to their (at LO) point-like connection to the incoming partons. However, calculations performed beyond LO also yield contributions of the *fragmentation type*, which result from a cascade of successive collinear splittings of an outgoing parton, that end up with a quark-photon splitting. The fragmentation of an outgoing quark or gluon to a photon can be absorbed in a non-perturbative parton-to-photon fragmentation function $D^{\gamma}_{q/g}(z, \mu_f)$, that is defined within a certain factorization scheme at given factorization scale μ_f [73].

The inclusive cross-section of prompt photon production $\sigma(p_\gamma)$ is given by the sum of the aforementioned two contributions and can be written as [73]:

$$\sigma(p_\gamma) = \sum_{a=q,\bar{q},g} \underbrace{\int_0^1 \frac{\mathrm{d}z}{z} \hat{\sigma}^a\left(\frac{p_\gamma}{z}; \mu_R, \mu, \mu_f\right) \cdot D^{\gamma}_a(z; \mu_f)}_{\text{fragmentation}} + \underbrace{\hat{\sigma}^{\gamma}\big(p_\gamma; \mu_r, \mu, \mu_f\big)}_{\text{direct}}, \tag{2.26}$$

where $\hat{\sigma}^a$ and $\hat{\sigma}^\gamma$ are the partonic cross-sections for the production of a parton a and a photon (γ), respectively, and $D^{\gamma}_{q/g}$ is the aforementioned parton-to-photon fragmentation function. To keep the notation simple, both $\hat{\sigma}^a$ and $\hat{\sigma}^\gamma$ already contain the convolution with the PDFs for the initial-state partons a coming from the colliding projectiles. The calculations depend on three different arbitrary scales: The renormalization scale μ_R, which enters the partonic cross-section via the determination of α_s, the factorization scale μ coming from the PDFs, as well as the fragmentation scale μ_f of the fragmentation function. The partonic cross-section contains the Born level processes ($qg \rightarrow \gamma q$ etc.), as well as higher-order corrections, and has so far been calculated up to NNLO [74].

The magnitude of the different contributions in Eq. 2.26 is illustrated in Fig. 2.20 [75], which shows the relative contribution of the three leading processes to the total prompt photon production cross-section as a function of the photons transverse energy E^{γ}_{T} for pp collisions at the nominal LHC collision energy $\sqrt{s} = 14\,\text{TeV}$. One finds that

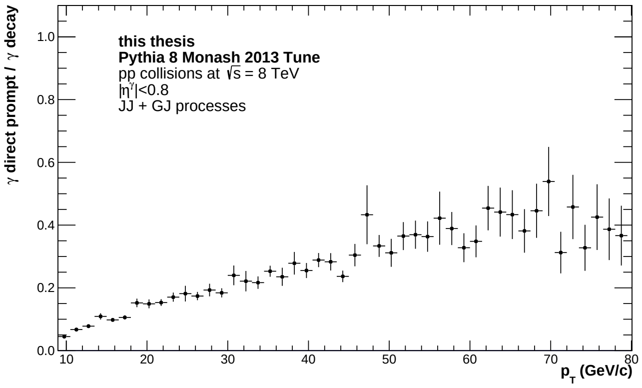

Figure 2.21: Signal to background ratio according to cross sections obtained with Pythia8 for pp collisions at $\sqrt{s} = 8\,\mathrm{TeV}$.

the majority of prompt photons with $E_{\mathrm{T}}^{\gamma} \lesssim 20\,\mathrm{GeV}$ are produced via fragmentation, whereas the contribution of direct prompt photon production via the qg Compton process starts to dominate for increasing photon energies. Prompt photon production via the $q\bar{q}$ annihilation process does not significantly contribute to the total cross-section in this collision system, where i.e. the annihilation contribution stays below $\approx 10\,\%$ over the whole shown energy range. Nonetheless, this contribution becomes sizeable e.g. in p$\bar{\mathrm{p}}$ collisions at the Tevatron [76], where the availability of anti-quarks in one of the projectiles enhances the annihilation contribution, especially at large E_{T}^{γ} (see. Fig. 1 (top) in Ref. [75]).

While it is interesting to get an idea of the fragmentation contributions as a function of photon energy, it is however important to point out that the distinction between direct- and fragmentation prompt photon production has no direct physical meaning beyond LO [73]: This is due to the fact that in order to calculate the fragmentation contribution, one in essence needs to absorb occurring singularities in the aforementioned non-perturbative fragmentation functions, which requires the introduction of the fragmentation scale μ_f. As visible in Eq. 2.26, this scale also appears in the direct part of the cross-section ($\hat{\sigma}^{\gamma}$), where it enters the higher order corrections of the Born level processes. Since μ_f is not a physical parameter and its choice is arbitrary, the distinction between fragmentation and direct production is similarly an arbitrary one, and only the sum of both contributions is a physical observable.

2.4.2 *Isolated prompt photon production*

The main challenge for measurements of prompt photon production is that most photons produced in a collision do not originate from the hard scattering process, but are rather produced by electromagnetic decays of hadrons (mainly π^0 and η). This is illustrated in Fig. 2.21, which shows the ratio of the prompt photons cross-section over the decay photons as a function of photon p_{T}. The cross-sections were obtained for pp collisions at $\sqrt{s} = 8\,\mathrm{TeV}$ using the Pythia 8.3 [77] Monte Carlo (MC) generator with the Monash 2013 tune [78], using the NNPDF2.3 QCD+QED LO proton PDF [79]. All final state photons that were produced in a particle decay are considered as decay photons, where the hadrons were produced using the `HardQCD` process group to produce jet-like events. The prompt photon cross-section is obtained using the `PromptPhoton`

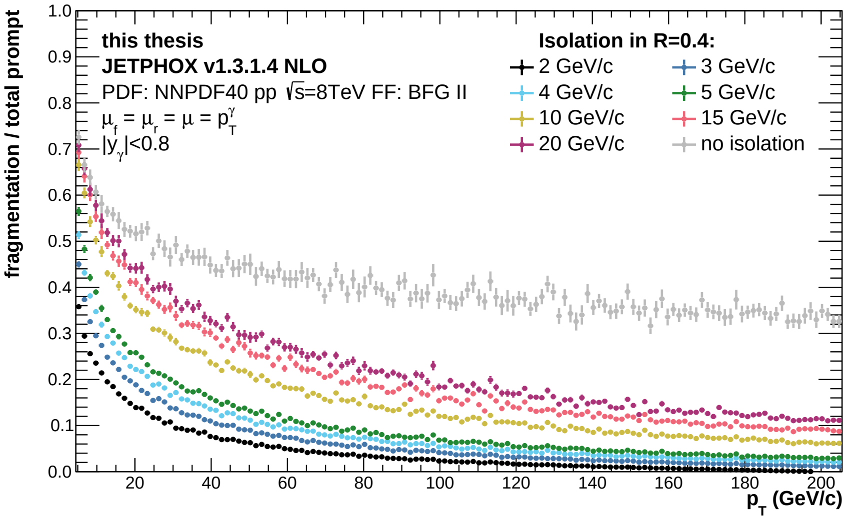

Figure 2.22: Fragmentation contribution for different isolation thresholds in a standard cone with radius $R = 0.4$ around the photon. The calculation is obtained using the JetPhox [73] program at NLO for pp collisions at $\sqrt{s} = 8$ TeV. The used PDF and fragmentation function, as well as the scales are given in the legend. The error bars represent the statistical uncertainties of the calculation.

process group, which contains the LO processes of direct prompt photon production. One finds very low signal-to-background ratios in the order of a few-percent at low-p_T, which then slowly increases towards higher photon momenta, illustrating the difficulty of a prompt measurement in a decay photon dominated environment. Even though Pythia only includes LO processes for prompt photon production, as well as parton shower algorithms, it has been shown [80] that it describes LHC isolated photon data reasonably well, and is therefore here considered sufficient for the purpose of showcasing the magnitude of the expected signal-to-background ratio.

Since prompt photons only contribute a small fraction to the photons produced in a hadronic collision, experiments commonly impose a so-called *isolation criterion*, which aims to suppress photons originating from hadronic decays by requiring that the energy depositions in the vicinity of the photon are below a certain threshold. A widely used choice for such an isolation requirement is to only consider photons where the sum of the transverse energy $\sum E_T$ of particles within a cone of radius R around the photons four-vector is below a given threshold $E_T^{\text{th.}}$, i.e.:

$$\sum E_T = \sum_i E_T^i \theta(R - R_i) < E_T^{\text{th.}} \quad \text{with} \quad R_i = \sqrt{(\eta_\gamma - \eta_i)^2 + (\phi_\gamma - \phi_i)^2}, \qquad (2.27)$$

where η_i (η_γ) and ϕ_i (ϕ_γ) are the pseudorapidity and azimuthal angle of the hadron (photon), respectively. The threshold $E_T^{\text{th.}}$ can be chosen to either be a fixed value, but also a fraction ϵ of the photon's transverse momentum. The isolation requirement is motivated by the fact that the hadrons associated with the decay photons are often produced in jets of particles originating from hadronization of the same parent parton, and therefore a decay photon will often be surrounded by hadronic and electromagnetic activity.

In addition to the experimental advantage of suppressing the decay photon background, isolation requirements also change the composition of the prompt photon cross-section, where the contribution from fragmentation photons is significantly suppressed because the fragmentation photons are produced collinearly to the parent parton. The suppression of the fragmentation contribution is illustrated in Fig. 2.22, which shows the fraction of fragmentation photons contributing to the isolated prompt photon cross-section for different fixed isolation thresholds. The ratios are obtained from calculations at NLO using the JetPhox [73] program[11], assuming a collision energy of $\sqrt{s} = 8\,\text{TeV}$ and requiring photon rapidities $|y| < 0.8$. The calculations use the latest NNPDF40 [24] proton PDFs and the BFG II [81] parton-to-photon fragmentation function. The scales μ_f, μ and μ_R are chosen to be the photon momentum p_T^γ, which is a choice commonly found in the literature (see. e.g. Ref. [80]). One finds an increasing suppression of the fragmentation contribution when applying increasingly tight isolation requirements, where an isolation of $E_\text{T}^\text{th.} = 2\,\text{GeV}$ in a cone of $R = 0.4$ reduces the contribution from $\approx 50\,\%$ to $\approx 10\,\%$ at $p_\text{T}^\gamma = 20\,\text{GeV}/c$. In the context of using isolated photons to probe the initial state, it is clear that such a suppression is desirable, as it increases the sensitivity to the initial-state while suppressing impact of the fragmentation function [82]. However, the fragmentation contribution is not suppressed entirely, where in particular those fragmentation photons carrying a large momentum fraction of their parent parton survive the isolation criterium [83].

In contrast to what might be suggested by Fig. 2.22, further suppression cannot be reached by decreasing R and $E_\text{T}^\text{th.}$ indefinitely, where $E_\text{T}^\text{th.} \to 0$ leads to divergences in the calculation of the isolated prompt photon cross-sections and small radii $R \sim 0.1$ similarly lead to unphysical results [73, 83, 84]. Different isolation criteria, such as the smooth cone isolation proposed by Frixione [85], manage to safely remove the entire fragmentation component of the isolated photon cross-section. However, due to the challenging implementation of such a criterium in an experimental setting, which is complicated by the finite resolution of the involved detectors, it will not be discussed here further and the reader is referred to e.g. Ref. [85], [86] and [84]. The experimental implementation and impact of the standard cone isolation introduced in Eq. 2.27, will be discussed in detail in Sec. 6.

2.4.3 *Sensitivity of isolated photons to the initial state*

Section 2.2.3 and 2.3.3 gave an overview about PDFs, as well as initial-state effects in nuclear collisions which can be encoded in nPDFs. In addition, saturation effects expected at very low-x and connected models such as the CGC model were discussed, which show that exploration of the initial-state over a wide range in x and Q is desirable, as well as relevant in ongoing research of heavy-ion physics. It is therefore important to briefly discuss the kinematic coverage of isolated photon measurements in x and Q, as well as their sensitivity to nuclear effects in the initial state.

The momentum fraction $x_{1,2}$ carried by a parton from the colliding projectiles 1 and 2 that is probed by a direct prompt photon produced with p_T^γ and η_γ, can be estimated from LO 2 → 2 scattering kinematics as

$$x_{1,2} = \frac{q_\text{T}}{\sqrt{s}}\left(e^{\pm\eta_a} + e^{\pm\eta_\gamma}\right) \overset{\eta_a \approx \eta_\gamma}{\approx} \frac{2p_\text{T}^\gamma}{\sqrt{s}} e^{\pm\eta_\gamma}, \tag{2.28}$$

---

[11] I am very grateful to Hendrik Poppenborg, who provided an easy-to-use interface for JetPhox called BashPhox (`https://github.com/hpoppenb/BashPhox`) that enabled me to use JetPhox easily and efficiently!

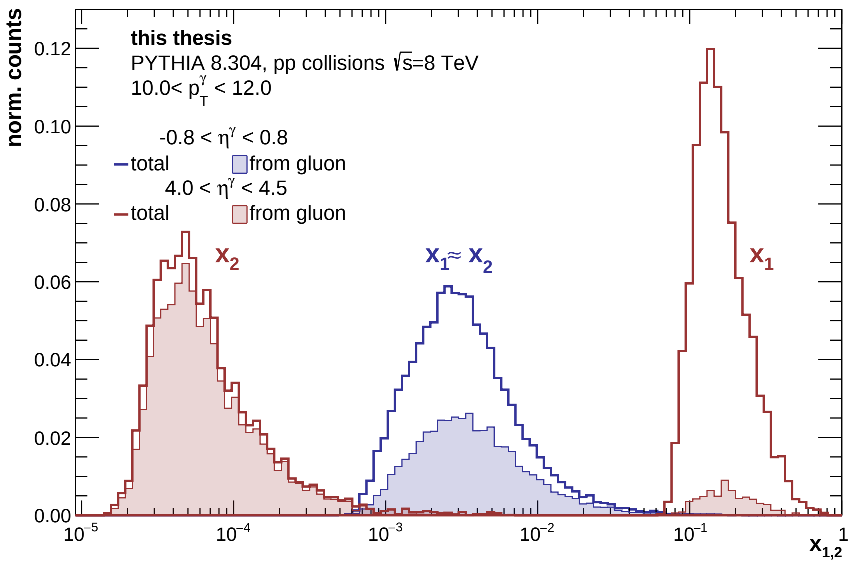

Figure 2.23: Momentum fraction $x_{1,2}$ of an incoming parton that is probed by a direct prompt photon produced in the LO hard scattering. The subscripts 1 and 2 identify the projectile that contains the parton entering the 2 → 2 scattering. The estimates are obtained using the Pythia event generator with the Monash 2013 tune, assuming pp collisions at $\sqrt{s} = 8\,\text{TeV}$. Photons are shown in one exemplary p_T-bin and for two different pseudorapidities η^γ.

where η_a is the pseudorapidity of the other parton produced in the scattering process and $\sqrt{s}$ is the centre-of-mass energy of the collision. The x-sensitivity of direct prompt photons is illustrated in Fig. 2.23, which was obtained by simulating direct prompt photon processes with Pythia 8.304 at LO assuming pp collisions at $\sqrt{s} = 8\,\text{TeV}$. Photons produced at mid-rapidity ($-0.8 < \eta^\gamma < 0.8$) and $10 < p_\text{T}^\gamma < 12\,\text{GeV}/c$ on average probe $x_{1,2} \sim 10^{-3}$. As indicated by the filled area, about 50 % of the probed partons are gluons. Photons produced at forward pseudorapidities ($4.0 < \eta^\gamma < 4.5$) probe significantly lower x down to $\lesssim 10^{-4}$. In contrast to a measurement at mid-rapidity, where x_1 and x_2 are roughly equivalent, measurements in one forward direction probe drastically different x, where one usually probes a low-x gluon in combination with a high-x quark from the other projectile. Measurements at forward rapidities are therefore an excellent way to probe the gluon density at low-x, which will be discussed in Sec. 12. In addition, the sensitivity to low-x partons can be further improved by performing measurements at low photon p_T, as well as large collision energies.

Since isolated photon measurements are sensitive to the partonic distributions in the initial state, measurements of their production in heavy-ion collisions allow studying nuclear modifications of the initial state, such as e.g. shadowing, which was introduced in Sec. 2.3.3. Small nuclear collision systems such as p–Pb are of particular interest, where in principle no formation of the QGP is expected and one can therefore measure modifications originating from the initial-state without the added complication of medium-induced modifications expected in Pb–Pb collisions. The nuclear modification factor R_AA, which was already introduced in the context of partonic energy loss in Eq. 2.21 to quantify a modification of the production cross-section of various hadrons in

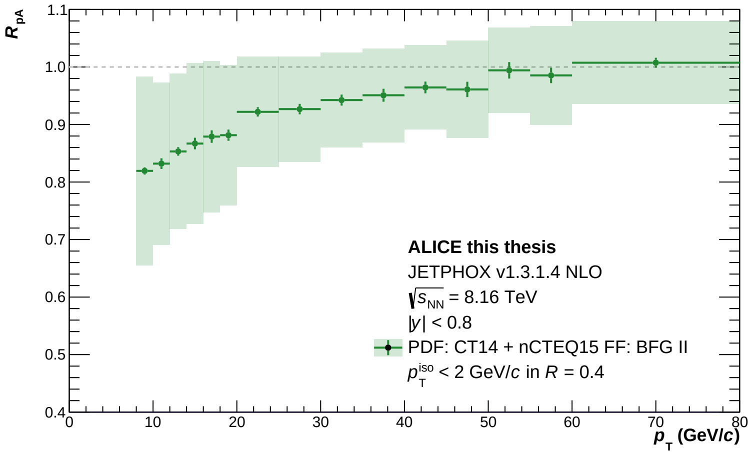

Figure 2.24: Calculation of the nuclear modification factor R_{pA} of isolated prompt photon production using JetPhox at $\sqrt{s_{\mathrm{NN}}} = 8.16\,\mathrm{TeV}$. The used PDFs are nCTEQ15 [23] (Pb) and CT14 [87] (proton). The isolation cut $\sum E_{\mathrm{T}}$, isolation radius R and photon rapidity y are given in the legend. The coloured band denotes the nPDF uncertainty at 90 % CL. The vertical lines denote the statistical uncertainty of the JetPhox calculation. All scales are chosen to coincide with the transverse momentum of the photon.

Pb–Pb collisions with respect to pp collisions, can be analogously defined for p–Pb collisions and is referred to as the R_{pA}:

$$R_{\mathrm{pA}} = \frac{\sigma_{\mathrm{pPb}}}{A \cdot \sigma_{\mathrm{pp}}} \quad \text{with} \quad A = 208, \tag{2.29}$$

where σ_{pp} and σ_{pPb} are the isolated prompt photon cross-section in pp and p–Pb collisions, respectively, and A is the mass number of lead. To illustrate the sensitivity of isolated photon measurements to possible nuclear modifications, the expected R_{pA} is calculated for the nCTEQ15 [23] nPDF using JetPhox at NLO, which is shown in Fig. 2.24. The proton PDF used for the pp baseline, as well as the proton projectile for the p–Pb collision is CT14 [87]. The collision energy $\sqrt{s_{\mathrm{NN}}} = 8.16\,\mathrm{TeV}$, as well as the photon rapidity $|y| < 0.8$ are chosen to coincide with those studied in the measurement presented in this work. One finds that the nuclear modifications encoded in the nPDF translates to a suppression of the isolated prompt photon cross-section of up to 20 % at low-p_{T} in p–Pb with respect to pp collisions. With increasing photon p_{T} this suppression weakens, and no suppression is expected for $p_{\mathrm{T}} \gtrsim 50\,\mathrm{GeV}/c$. The error band denotes the uncertainty coming from the nPDF, which was obtained

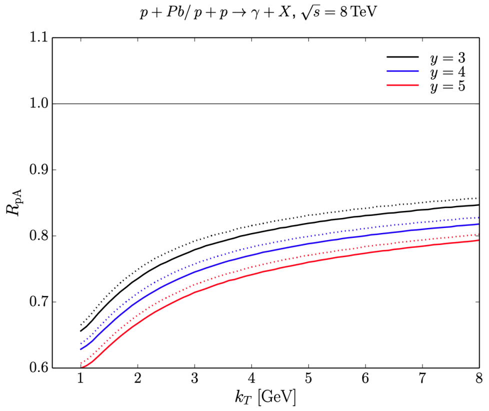

Figure 2.25: Isolated prompt photon R_{pA} in p–Pb collisions at $\sqrt{s_{\mathrm{NN}}} = 8\,\mathrm{TeV}$, calculated at LO in the CGC formalism [88]. Solid and dashed lines correspond to an isolation in a cone of $R = 0.4$ and $R = 0.1$, respectively.

by performing the calculation for all nPDF members and is in the order of 15 % at $p_{\mathrm{T}} = 12\,\mathrm{GeV}/c$.

Finally, the impact of potential non-linear QCD effects on a measurement of the isolated prompt photon R_{pA} in p–Pb collisions at $\sqrt{s_{\mathrm{NN}}} = 8\,\mathrm{TeV}$ at forward rapidities is illustrated in Fig. 2.25 [88]. The calculation is performed at LO in the CGC formalism and showcases significant suppressions for low photon transverse momenta.

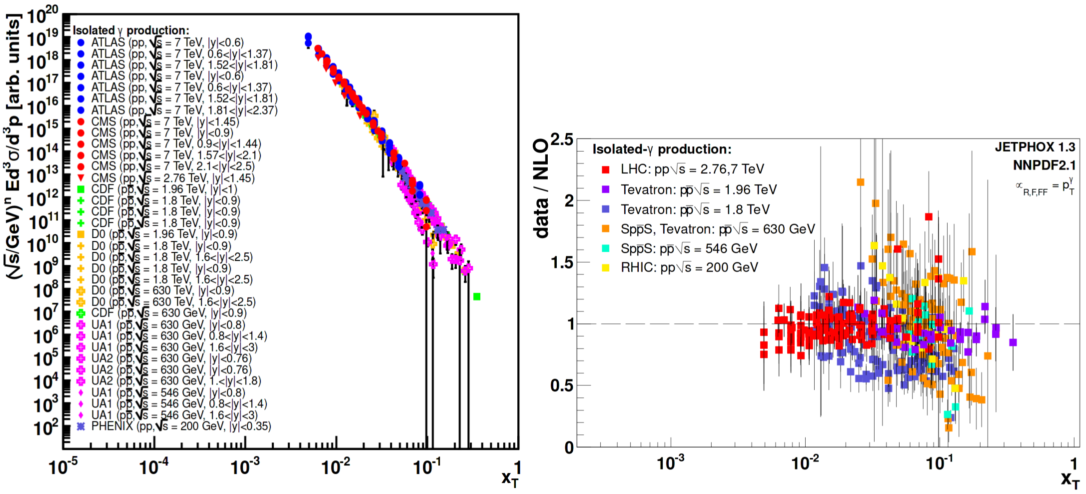

(a) (b)

Figure 2.26: **Left:** Overview of various isolated photon data as a function of $x_\mathrm{T} = 2E_\mathrm{T}^\gamma$. **Right:** Ratio of data over NLO predictions using the NNPDF2.1 proton PDF. The comparisons were compiled in Ref. [75] in 2012, and therefore only include the earliest measurements at LHC energies, i.e. by ATLAS[94, 95] and CMS [96–98]

2.4.4 *Existing measurements of isolated photon production*

Over the last decades, measurements of prompt photon production have been widely carried out at various fixed-target and collider experiments, spanning several orders of magnitude in centre-of-mass energies ranging from $\sqrt{s} \approx 20\,\mathrm{GeV}$ [89] up to 13 000 GeV [90–92]. An overview of measurements of the inclusive isolated prompt photon cross-section at $\sqrt{s} \geq 200\,\mathrm{GeV}$ is given in Tab. 2.1, including information about the covered photon momentum range as well as the used isolation criterium. A full review of all measurements is beyond the scope of this work, which is why measurements at lower collision energies, such as e.g. fixed target experiments using pion beams (see e.g. Ref. [89]), are not considered in this overview and the reader is referred to e.g. Ref. [93] for a review. In addition, these older measurements ($\sqrt{s} \lessapprox 65\,\mathrm{GeV}$) did not yet measure isolated photon production, but rather measured the inclusive prompt photon cross-section, which complicates comparisons to theory due to the stronger dependence on the fragmentation function, as well as the small scales involved at such low collision energies [75].

The available inclusive isolated prompt photon data has been compiled in 2012 by d'Enterria and Rojo in Ref. [75] and compared to NLO calculations. It includes the data of p-p̄ collisions collected at Tevatron and Sp$\bar{\mathrm{p}}$*S*, as well as the early LHC data available at the time of the review, i.e. the measurements in pp collisions at $\sqrt{s} = 2.76$ and 7 TeV performed by ATLAS [94, 95] and CMS [96–98]. The considered experimental data is shown as a function of $x_\mathrm{T} = 2E_\mathrm{T}^\gamma/\sqrt{s}$ in Fig. 2.26a.: One finds that all cross-sections follow power-law dependence $1/E_\mathrm{T}^n$, which translates to $2^n/(\sqrt{s}^n x_\mathrm{T}^n)$ for a spectrum in x_T. The shown x_T spectra therefore have been scaled with $\sqrt{s}^n$, where one finds that the data from different centre-of-mass energies collapses on a common curve for $n \approx 4.5$. This scaling behaviour with $\sqrt{s}^n$ indicates a universal production mechanism of prompt photons, where the extracted exponent is very close to the expected scaling behaviour of a 2→2 scattering [116]. The authors compared the measurements to pQCD calculations

Table 2.1: Overview of inclusive isolated photon cross-section measurements performed at $\sqrt{s} \geq 200\,\text{GeV}$.

system	$\sqrt{s}$ (TeV)	collaboration (collider)	p_{T} (GeV)	isolation	Ref.
p–$\bar{p}$	0.546	UA1 (Sp$\bar{p}$S)	16-51	$R = 0.7, \sum E_{\text{T}} < 2\,\text{GeV}/c$	[99]
p–$\bar{p}$	0.63	UA1 (Sp$\bar{p}$S)	16-100	$R = 0.7, \sum E_{\text{T}} < 2\,\text{GeV}/c$	[99]
		UA2 (Sp$\bar{p}$S)	14-92	$R = 0.265, \sum E_{\text{T}} < 0.25 p_{\text{T}}$	[100]
		UA2 (Sp$\bar{p}$S)	12-83	$R = 0.25, \sum E_{\text{T}} < 0.1\,\text{GeV}/c$	[101]
			12-51	$R = 0.53, \sum E_{\text{T}} < 2\,\text{GeV}/c$	[101]
p–$\bar{p}$	0.63	CDF (Tevatron)	8-38	$R = 0.4, \sum E_{\text{T}} < 4\,\text{GeV}/c$	[102]
		D0 (Tevatron)	7-50	$R = 0.4, \sum E_{\text{T}} < 2\,\text{GeV}/c$	[103]
p–$\bar{p}$	1.8	CDF (Tevatron)	11-132	$R = 0.4, \sum E_{\text{T}} < 4\,\text{GeV}/c$	[102]
		CDF (Tevatron)	10-65	$R = 0.4, \sum E_{\text{T}} < 1\,\text{GeV}/c$	[104]
		CDF (Tevatron)	8-132	$R = 0.7, \sum E_{\text{T}} < 2\,\text{GeV}/c$	[105]
		D0 (Tevatron)	10-140	$R = 0.4, \sum E_{\text{T}} < 2\,\text{GeV}/c$	[106]
		D0 (Tevatron)	9-126	$R = 0.4, \sum E_{\text{T}} < 2\,\text{GeV}/c$	[107]
p–$\bar{p}$	1.96	CDF (Tevatron)	30-400	$R = 0.4, \sum E_{\text{T}} < 0.1 p_{\text{T}}$	[108]
		D0 (Tevatron)	23-300	$R = 0.4, \sum E_{\text{T}} < 2\,\text{GeV}/c$	[109]
p–p	0.2	PHENIX (RHIC)	3-16	$R = 0.5, \sum E_{\text{T}} < 0.1 p_{\text{T}}$	[110]
p–p	2.76	CMS (LHC)	20-80	$R = 0.4, \sum E_{\text{T}} < 5\,\text{GeV}/c$	[98]
p–p	7	ATLAS (LHC)	15-100	$R = 0.4, \sum E_{\text{T}} < 3\,\text{GeV}/c$	[94]
		ATLAS (LHC)	45-400	$R = 0.4, \sum E_{\text{T}} < 4\,\text{GeV}/c$	[95]
		ATLAS (LHC)	100-1000	$R = 0.4, \sum E_{\text{T}} < 7\,\text{GeV}/c$	[111]
		CMS (LHC)	25-400	$R = 0.4, \sum E_{\text{T}} < 5\,\text{GeV}/c$	[96]
		CMS (LHC)	21-300	$R = 0.4, \sum E_{\text{T}} < 5\,\text{GeV}/c$	[97]
		ALICE (LHC)	10-60	$R = 0.4, \sum E_{\text{T}} < 2\,\text{GeV}/c$	[112]
p–p	8	ATLAS (LHC)	25-1500	$R = 0.4$ $\sum E_{\text{T}} < 4.8\,\text{GeV}/c + 4.2 \times 10^{-3} \cdot E_{\text{T}}$	[113]
		ALICE (LHC)	12-80	$R = 0.4, \sum E_{\text{T}}^{\text{ch.}} < 1.5\,\text{GeV}/c$	**this thesis**
p–p	13	ATLAS (LHC)	≥ 125	$R = 0.4$ $\sum E_{\text{T}} < 4.8\,\text{GeV}/c + 4.2 \times 10^{-3} \cdot E_{\text{T}}$	[90]
			125-2000	$R = 0.4$ $\sum E_{\text{T}} < 4.8\,\text{GeV}/c + 4.2 \times 10^{-3} \cdot E_{\text{T}}$	[91]
		CMS (LHC)	190-1000	$R = 0.4, \sum E_{\text{T}} < 5\,\text{GeV}/c$	[92]
p–Pb	8.16	ATLAS (LHC)	20-550	$R = 0.4$ $\sum E_{\text{T}} < 4.8\,\text{GeV}/c + 4.2 \times 10^{-3} \cdot E_{\text{T}}$	[114]
		ALICE (LHC)	12-80	$R = 0.4, \sum E_{\text{T}}^{\text{ch.}} < 1.5\,\text{GeV}/c$	**this thesis**
Pb–Pb	2.76	ATLAS (LHC)	22-280	$R = 0.3, \sum E_{\text{T}} < 6\,\text{GeV}/c$	[115]
		CMS (LHC)	20-80	$R = 0.4, \sum E_{\text{T}} < 5\,\text{GeV}/c$	[98]

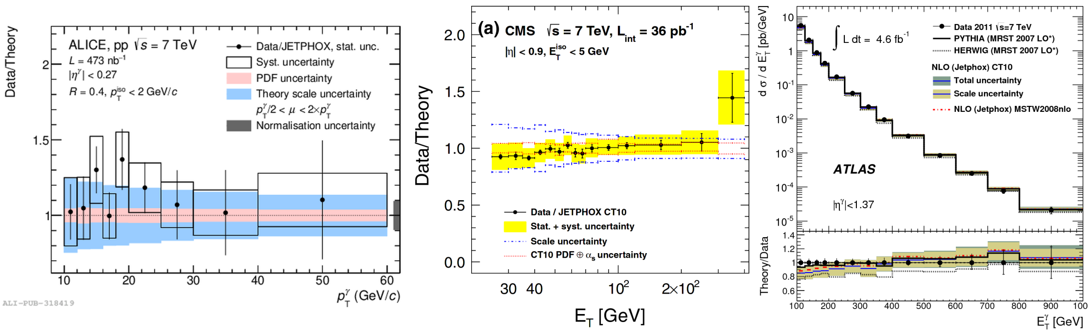

(a) ALICE (b) CMS (c) ATLAS

Figure 2.27: Selection of measurements in pp collisions at $\sqrt{s}$=7 TeV at mid-rapidity from ALICE [112], CMS [96] and ATLAS [111], compared to JetPhox calculations at NLO.

at NLO, using the NNPDF2.1 proton PDF [117] and find good agreement over the whole x_T range, as indicated by the agreement with unity in Fig. 2.26b. Altogether, this paints a picture of a good understanding of the underlying prompt photon production mechanisms, as well as the applicability of pQCD in calculations used to obtain isolated prompt photon cross-sections. The latter is especially important, considering that data reported by the E706 collaboration in fixed-target experiments at $\sqrt{s} \approx 30$ GeV [118–120] in the 1990s showed significant deviation from NLO pQCD calculations, casting doubt on the ability of such calculation to describe prompt photon production. This deviation from theoretical expectations led to speculations about the need for non-perturbative additions to the calculations and the abandonment of the usage of prompt photon data in global PDF fits [83]. However, such disagreement could not be observed for any other measurement and the E706 result remains an outlier to this day [75, 83].

MEASUREMENTS IN PP COLLISIONS AT THE LHC Since 2012, several more measurements were performed at the LHC: In pp collisions, the ALICE experiment reported isolated photon production at $\sqrt{s} = 7$ TeV [112], covering low photon momenta down to 10 GeV – unprecedented at LHC energies. ATLAS extended their measurement in pp collisions at $\sqrt{s} = 7$ TeV using additional data, allowing to reach prompt photon momenta of up to 1 TeV [111]. In addition, ATLAS [90, 91] and CMS [92] performed measurements at $\sqrt{s} = 13$ TeV, the highest currently available collision energy at the LHC. In pp collisions at $\sqrt{s} = 8$ TeV, which are also studied in this work, the ATLAS collaboration reported isolated prompt photon production down to $p_\mathrm{T} = 20$ GeV/c [113].

A selection of the results in pp collisions at $\sqrt{s} = 7$ TeV is shown in Fig. 2.27: The data was taken by ALICE [112], CMS [96] and ATLAS [111] and the considered photon pseudorapidity η is given in the legend. The used isolation criterium can be obtained from Tab. 2.1 and differs for each measurement. The data is compared to various theory calculations, where one finds overall good agreement with JetPhox NLO calculations within the experimental and theoretical uncertainties. The latter are quite large, where the uncertainty originating from the scale choice is in the order of up to ≈ 20 %. The ATLAS measurement, while still being overall consistent with the calculations, shows a slight tendency of an underestimation by the JetPhox NLO for the lowest considered photon E_T [111].

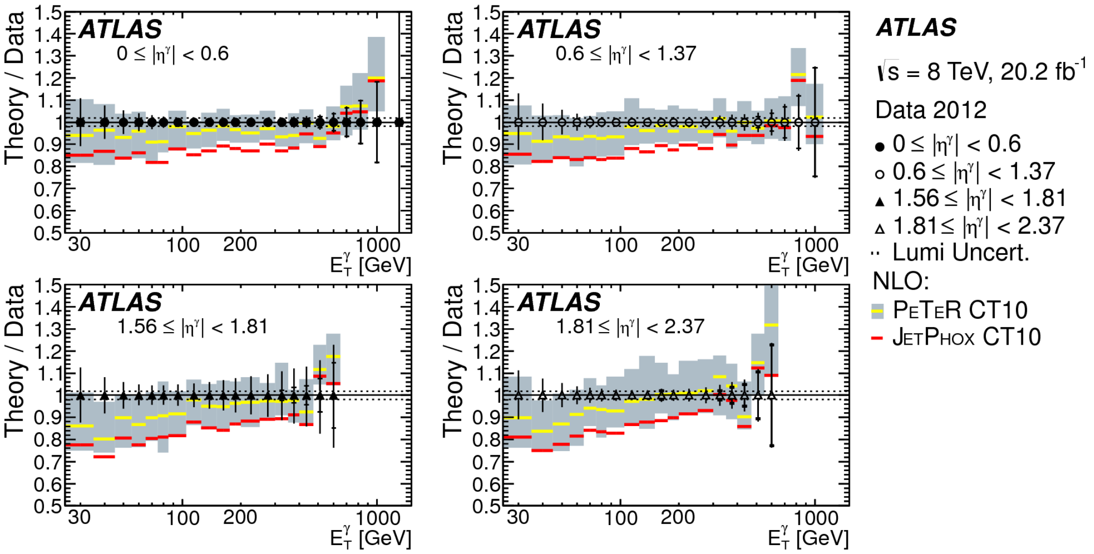

Figure 2.28: Measurement of isolated prompt photon production in pp collisions at $\sqrt{s} = 8$ TeV by ATLAS [113].

The isolated photon measurement in pp collisions at $\sqrt{s} = 8$ TeV by ATLAS [113] increased the recorded data by over factor 4 with respect to the measurement at $\sqrt{s} = 7$ TeV, enabling a significant reduction of experimental uncertainties. A comparison of the data to theoretical calculations is shown in Fig. 2.28 for four different η ranges: The decreased experimental uncertainties reveal an underestimation by the JetPhox NLO calculation for most of the covered phasespace, especially at low-E_T, where an underestimation of up to $\approx 20\,\%$ is observed. This difference decreases with increasing E_T, which is a similar trend to what had been observed by ATLAS at $\sqrt{s} = 7$ TeV [111]. The data is furthermore compared to theoretical calculations using the PeTeR [121, 122] program, which approximates corrections beyond NLO by including partial results at higher orders. The calculation has been carried out at what is known as next-to-next-to-next-to-leading-logarithmic (NNNLL) level, where the NLO results are normalized to JetPhox NLO in order to account for the isolation. As shown by the yellow curve in Fig. 2.28, the PeTeR predictions nicely describe the data, suggesting that corrections beyond NLO are required to better describe prompt photon production theoretically.

These findings are supported in measurements at $\sqrt{s} = 13$ TeV by ATLAS [90, 91] and CMS [92], where one similarly finds JetPhox NLO underestimating the data by up to 20 % while still being overall consistent with the data due to the scale uncertainties in a similar order of magnitude. This is illustrated in Fig. 2.29, which shows the comparison of the isolated prompt photon data reported by ATLAS in Ref. [91] to various calculations: The JetPhox calculation (blue) underestimates the data in all considered pseudorapidity range. The effect of including NNLO corrections when calculating the direct prompt photon contribution is illustrated by the black points, which show the prediction obtained at NNLO using the NNLOJet [123] program. One finds a significant improvement in the description of the data as well as a reduction of the scale uncertainty by a factor of 2-20 with respect to JetPhox [91]. The data is furthermore confronted with Sherpa [124] predictions, which is a MC event generator containing various virtual corrections and higher-order matrix elements. In contrast to pQCD NLO calculations like JetPhox, where the final states (hadron, photon, etc.) are encoded

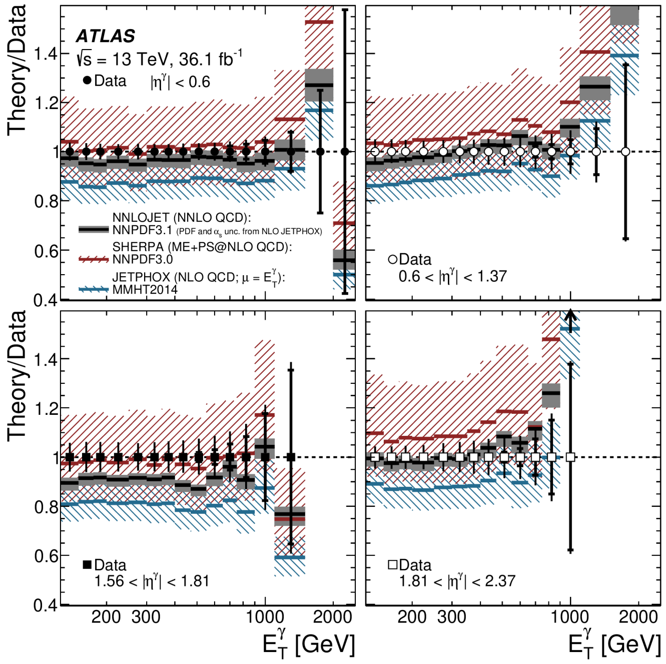

Figure 2.29: Ratio of various theoretical calculations over ATLAS data in pp collisions at $\sqrt{s}$ = 13 TeV[91].

in specific fragmentation functions, Sherpa makes use of a parton shower algorithm that models the fragmentation of an outgoing parton into the observed hadrons. The Sherpa prediction nicely describes the data, showcasing the benefit of using a parton shower to obtain the final-state observables. However, the detailed information from the parton shower increases the theoretical uncertainties due to the variety of introduced unphysical scales and parameters, as is illustrated by the large red band in Fig. 2.29. Similar findings are reported in Ref. [80], where POWHEG NLO calculations were matched to a parton shower from Pythia, which increases the predicted prompt photon cross-section with respect to JetPhox NLO[12].

In summary, the measurements performed in pp collisions at the LHC showcase the ability of theoretical calculations to well describe the isolated prompt photon data; in line with the observations at lower collision energies. The continuously increasing amount of data available at the LHC during its ongoing operation allowed to significantly decrease the experimental uncertainties, which are now smaller than the theoretical uncertainties NLO calculations. The increased experimental precision reveals a slight underestimation for calculations performed at NLO, where the agreement could be improved by including corrections beyond NLO, as well as using parton showers to describe the fragmentation to final-state observables.

MEASUREMENTS IN NUCLEAR COLLISIONS AT THE LHC As visible in Tab. 2.1, measurements of isolated prompt photon production in collisions involving heavy-ions are greatly outnumbered by those in pp and p$\bar{\text{p}}$.

The measurement in pp and Pb–Pb collisions at nucleon-nucleon centre-of-mass energies of $\sqrt{s_{\text{NN}}}$ = 2.76 TeV by CMS [98] was the first measurement of isolated prompt photon production in nuclear collisions and published in 2012. It covers a phasespace

---

[12] See e.g. Fig. 3 in [80] for a comparison to ATLAS data at in pp collisions $\sqrt{s}$ = 13 TeV

of $|\eta| < 1.44$ and transverse energies $20 \leq E_{\mathrm{T}} \leq 80\,\mathrm{GeV}$. Within the quite sizeable systematic uncertainties of 23 %-30 %, the measurement is in good agreement with JetPhox NLO predictions, both for pp and Pb–Pb. A possible nuclear modification of the parton densities in the initial state was studied using the nuclear modification factor R_{AA}, which is shown in Fig. 2.30 for 0 %-10 % most central collision class, together with various theoretical predictions. The ratio agrees with unity over the whole covered E_{T} range, showing no indication of nuclear modification within the uncertainties. Comparison to JetPhox calculations using various nPDFs that are indicated in the legend show good agreement with the data, where the central values also suggest that no significant modification ($\lesssim 10\,\%$) is expected in this high E_{T} range. A measurement by ATLAS [115] in the same Pb–Pb collision system covering $22 \leq E_{\mathrm{T}} \leq 280\,\mathrm{GeV}$ and various rapidity ranges similarly observes good agreement with theoretical calculation over the whole covered phasespace. However, the limited precision of the measurement in this dataset did not yet allow to quantitatively address nuclear effects and furthermore no R_{AA} is presented due to the lack of a pp baseline measured by ATLAS at this collision energy.

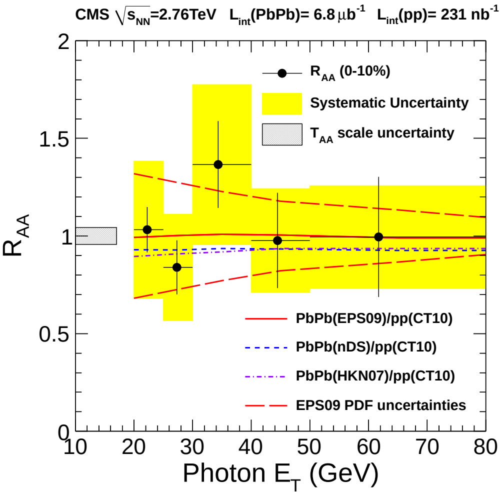

Figure 2.30: Nuclear modification factor R_{AA} of isolated prompt photon production in Pb–Pb collisions at $\sqrt{s_{\mathrm{NN}}} = 2.76\,\mathrm{TeV}$ measured by the CMS detector [98], shown together with JetPhox predictions using various nPDFs.

The most recent measurement of isolated prompt photon cross-section in nuclear collisions was performed in p–Pb collisions at $\sqrt{s_{\mathrm{NN}}} = 8.16\,\mathrm{TeV}$ by the ATLAS collaboration [114]: The measurement covers $20 \leq E_{\mathrm{T}} \leq 550\,\mathrm{GeV}$ in three different pseudorapidity intervals and is compared to NLO calculations using various nPDFs. Fig. 2.31a shows the isolated prompt photon cross cross-section, as well as the ratio to JetPhox NLO predictions. The pseudorapidity intervals denoted in each panel are giving in the nucleon-nucleon centre-of-mass frame, which is indicated by the use of $\eta^{\star}$ instead of η. This is to account for the Lorentz boost (see Sec. 2.2.1) of $\Delta y = \Delta\eta = \pm 0.465$ with respect to the laboratory frame, which occurs due to the asymmetry of the p–Pb collisions system, where the total energy carried by the Pb beam is greater than the proton beam energy, thus boosting the collision system in the lead-going direction. The data is confronted with JetPhox NLO calculations using the CT14 proton PDF for the proton beam, as well as the corresponding EPPS16 nPDF for the Pb beam. An underestimation by JetPhox NLO of up to $\approx 20\,\%$ at low E_{T} is observed, corroborating the conclusions from the previous paragraph for pp collisions.

Possible nuclear modifications of the parton densities were investigated using the nuclear modification factor R_{pA} shown in Fig. 2.31b, where the previously presented ATLAS measurement in pp collisions at $\sqrt{s} = 8\,\mathrm{TeV}$ [113] was used as a reference. At forward rapidities (left panel), the R_{pA} is consistent with unity over the full covered

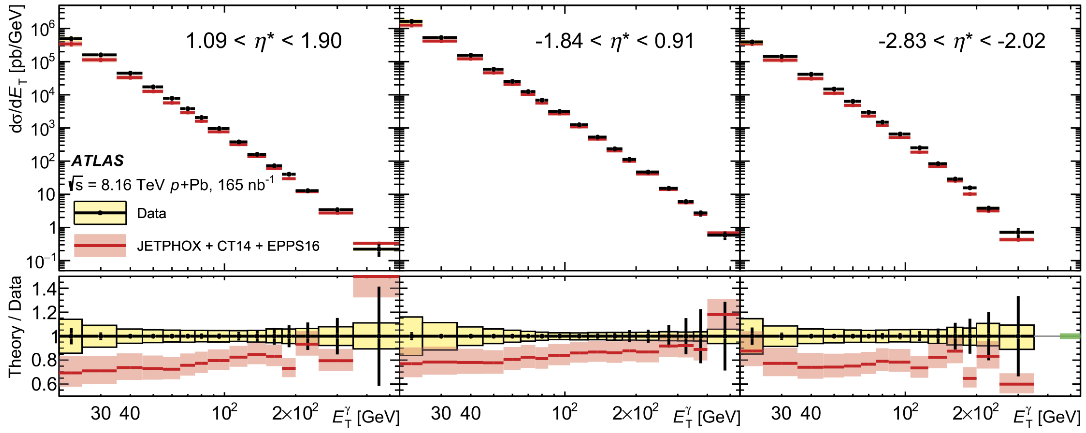

(a) Isolated prompt photon cross-section

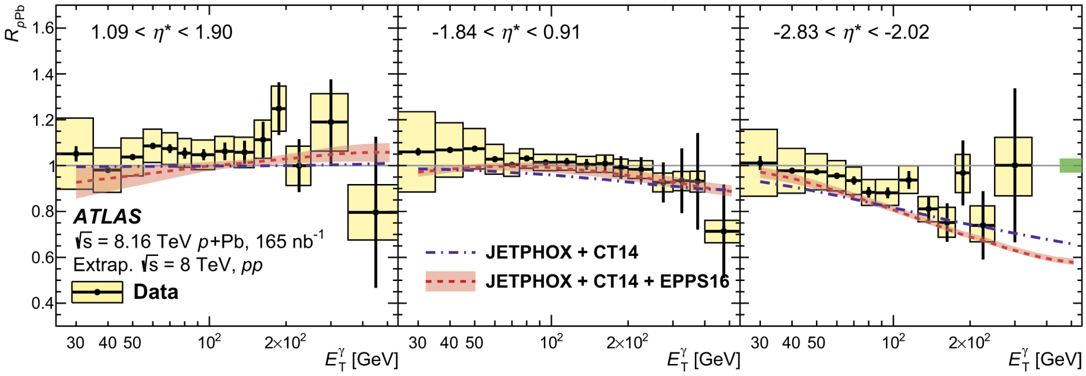

(b) Nuclear modification factor R_{pA}

Figure 2.31: **Top:** Isolated prompt photon cross-section in p–Pb collisions at $\sqrt{s} = 8.16\,\mathrm{TeV}$ as a function of photon transverse energy E_{T}, shown in three different centre-of-mass rapidity $\eta^\star$ intervals measured by the ATLAS experiment [114]. The data is confronted with JetPhox NLO calculations using the CT14 and EPPS16 PDFs for the proton and lead beam respectively. **Bottom:** Nuclear modification factor R_{pA} in at the same centre-of-mass energy as given above, confronted with JetPhox calculations. The pp reference was measured at $\sqrt{s} = 8\,\mathrm{TeV}$ [113] and extrapolated to 8.16 TeV. All shown calculations include isospin effects.

momentum range. The JetPhox prediction using the EPPS16 nuclear nPDF predicts a slightly reduced value for low-E_{T}, as well as a minor enhancement for $E_{\mathrm{T}} \gtrapprox 100\,\mathrm{GeV}$, which can be attributed to shadowing and anti-shadowing of the gluon PDF. The calculations are also performed using the CT14 proton (neutron) PDF, which does not incorporate nuclear effects such as shadowing, showcasing that $R_{\mathrm{pA}} \approx 1$ is expected in the absence of nuclear effects. The data is compatible with both predictions within the uncertainties, showcasing that the experimental precision is not yet sufficient to resolve possible nuclear effects, which are expected to be at most in the order of 10 % in the covered E_{T} range. At mid-rapidity (middle panel) and backward-rapidity (right panel), one finds an increasing suppression of isolated prompt photons at high E_{T} with respect to the pp baseline, which is especially pronounced for $-2.83 < \eta^\star < -2.02$. Such a suppression is compatible with both JetPhox predictions, indicating that it does not originate from a nuclear modification of the parton densities inside the nucleus, but rather originates from the proton-neutron asymmetry inside the Pb

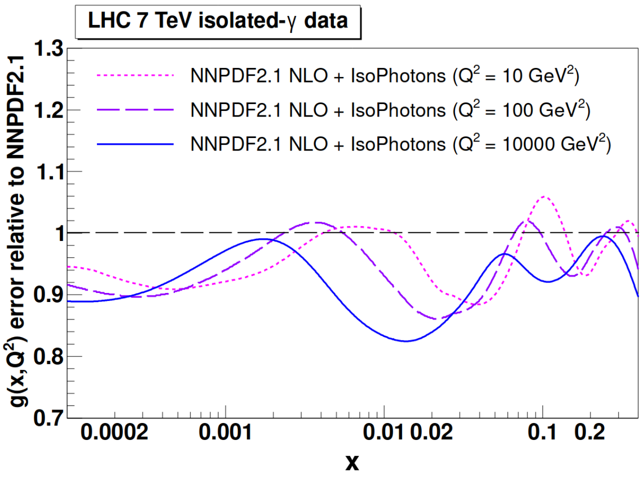

Figure 2.32: Relative reduction of the gluon PDF uncertainties with respect to the NNPDF2.1 proton PDF when including isolated prompt photon data in pp collisions at $\sqrt{s} = 7\,\text{TeV}$[94–97] via reweighting. The studies were performed using JetPhox at NLO. Figure taken from Ref. [75].

nucleus. This asymmetry becomes relevant especially at backward-rapidities and high photon energies, which probe an x-regime dominated by the up- and down -quark composition inside the proton/neutron.

In summary, the studies of the R_{pA} in p–Pb collisions at $\sqrt{s} = 8.16\,\text{TeV}$ by ATLAS are in good agreement with theoretical calculations within the uncertainties, but the precision does not yet allow drawing conclusions about the presence of nuclear effects such as gluon shadowing. Comparisons of the data to model calculations incorporating initial-state energy-loss of the incoming partons [125], which are not shown here and discussed in detail in Ref. [114], similarly are compatible with the assumption of no such energy loss before the hard scattering.

IMPACT ON PDF FITS As previously mentioned, the significant data-theory discrepancy observed by the E706 collaboration in fixed-target experiments at $\sqrt{s} \approx 30\,\text{GeV}$ [118–120] in the 1990s questioned the ability of NLO calculations to adequately described prompt photon production. This discrepancy, together with the fact that precise jet production data became available at the Tevatron, lead to the abandonment of the use of isolated prompt photon data in global PDF fits [75]. After the last usage of prompt photon data in the MRST99 [126][13] PDF, it took more than 20 years until isolated prompt photon data was used again in 2021 in the global fits of the NNPDF40 [24] PDF and the nNNPDF30[66] nPDF. This resurgence is largely owed to multiple studies [75, 83, 128] of the available experimental data that were carried out in the last decade. These studies not only demonstrated an overall good agreement of theoretical predictions with the isolated prompt photon data, but also showed the potential of such measurements to better constrain the gluon PDFs. In addition, the recent availability of NNLO calculations[74] allowed to significantly reduce the large scale uncertainties, thus further improving the constraining power of isolated prompt photon measurements.

---

[13] MRST99 is a corrected version of MRST98 [127]. Therefore, most details about the data used in MRST99 can be found in Ref. [127] instead.

The impact of the in 2012 available data on the NNPDF2.1 PDF was studied in Ref. [75]: The potential impact is evaluated using a Bayesian reweighting technique, where predictions using the JetPhox program at NLO for all available members of the NNPDF2.1 PDF are confronted with the available experimental data and reweighted according to the agreement with experimental data[14]. The authors find a relative reduction of the gluon PDF uncertainties of up to 20 % when including the early LHC data at $\sqrt{s} = 7\,\text{TeV}$ [94–97] via reweighting in NNPDF2.1, which is illustrated in Fig. 2.32.

Similar studies were carried out in Ref. [128] in 2018, evaluating the impact of the ATLAS measurements at $\sqrt{s} = 8$[113] on the NNPDF3.1 proton PDF [129]. The ATLAS data at $\sqrt{s} = 13\,\text{TeV}$ [90, 91] was not yet included in the evaluation, since the high-precision measurement presented in Fig. 2.29 [91] has not been published at that point. The authors confront the data with NNLO predictions and find good agreement with the ATLAS data, as well as no tension with existing datasets constraining the gluon density, such as inclusive jet production. The inclusion of the ATLAS data leads to a moderate reduction of the gluon PDF uncertainties, as well as a softening of gluons with $x \gtrsim 0.1$.

To date, the NNPDF collaboration has been the first and only group to include isolated prompt photon data in global PDF fits since MRST99[126]: Their newest proton NNPDF40[24] includes inclusive isolated prompt photon data from ATLAS at $\sqrt{s} = 8\,\text{TeV}$ [113] and 13 TeV[90], reporting a "mild impact on the gluon PDF"[24]. However, as for the study in Ref. [128], the global fit did not yet include the re-analysis of the ATLAS data at $\sqrt{s} = 13\,\text{TeV}$ [91], where the integrated luminosity $\mathcal{L}_{\text{int}}$ is increase by a factor of 10 with respect to the included measurement [90]. The newest nPDF nNNPDF30[66] includes the measurement by ATLAS in p–Pb collisions at $\sqrt{s_{\text{NN}}} = 8.16\,\text{TeV}$. Even though the NNPDF collaboration does not explicitly report any significant improvement of the gluon nPDF uncertainties resulting from the inclusion of the ATLAS data, the uncertainties could be significantly reduced when including data of prompt D^0 meson production in p–Pb collisions at $\sqrt{s} = 5\,\text{TeV}$ by LHCb [130] at forward rapidities, increasing the statistical significance of the reported gluon shadowing at low-x. This highlights the potential of measurements at forward rapidities, which is central to the physics program of the FoCal, discussed in detail in Sec. 12.

2.4.5 *Other measurements involving prompt photons*

The previous section outlined existing measurements of the isolated photon production cross-section as well as the nuclear modification factor in various collision systems. However, other types of interesting measurements involving isolated photons exist, which, even though they are not the focus of this work, are briefly discussed in the following. Measurements of the correlation of isolated prompt photons with a hadronic observable, such as a jet or a single hadron, can be used to study the medium-induced partonic energy loss mechanism, which was already introduced in Sec. 2.3.2: Since the

---

[14] The agreement for each member is quantified using:

$$\chi_k^2 = \frac{1}{N_{\text{dat.}}} = \sum_{i=1}^{N_{\text{dat.}}} \frac{(\sigma_{i,k}^{\text{th}} - \sigma_i^{\text{exp}})^2}{\Delta_{\text{tot}}^2} \tag{2.30}$$

, where N_{dat} are the number of datapoints of a particular measurement, σ_i^{exp} the measured cross-section with total uncertainty Δ_{tot} and $\sigma_{i,k}^{\text{th}}$ the theoretical prediction for data point i using the PDF member k [75].

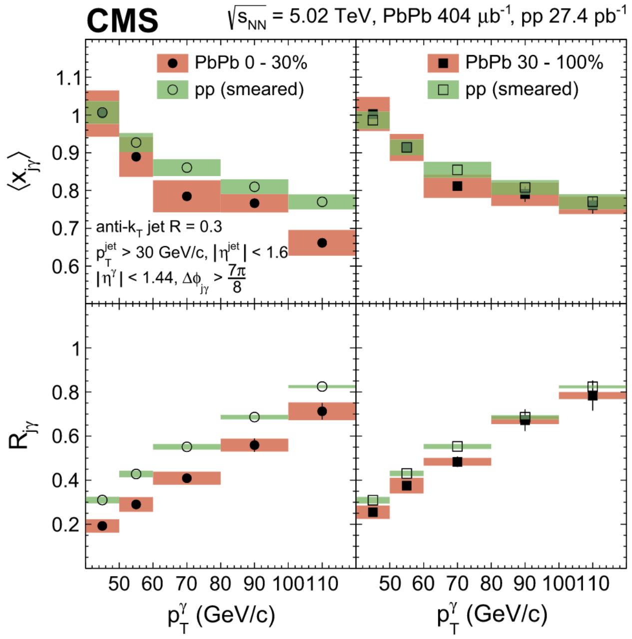

Figure 2.33: **Top:** Mean asymmetry ratio $< x_{j\gamma} >=< p_{\mathrm{T}}^{\mathrm{jet}}/p_{\mathrm{T}}^{\gamma} >$ quantifying the photon+jet p_{T} imbalance for most-central (left) and semi-central (right) Pb–Pb collisions compared to a smeared pp baseline. **Bottom:** Number of associated jets per photon R_{ij} shown for pp and Pb–Pb collisions in the same centrality bins as above. The jet definition is given in the legend [131].

photon does not carry colour charge, it does not interact strongly with the medium and therefore reaches the detector unaffected by the QGP. In contrast, a jet is produced via the hadronization of a parton and therefore sensitive to medium-induced partonic energy loss. On average, a photon and parton produced in the same hard-scattering process will be emitted back-to-back in azimuth angle and the photon p_{T} reflects the initial energy of the parton before any medium-induced energy loss and fragmentation into a jet. Measurements of isolated photons and jets produced in the same collision event thus allow to probe partonic energy loss, e.g. by studying the photon-jet azimuth angle difference and p_{T} ratio of jet and photon, where the latter serves as a gauge for the initial parton energy and the latter reflects the energy of the parton after the medium-induced modification. An example of such a measurement is presented in Fig. 2.33, which shows the isolated-photon+jet measurement reported by CMS in pp and Pb–Pb collisions at $\sqrt{s_{\mathrm{NN}}} = 5.02\,\mathrm{TeV}$[131]: The correlation in azimuthal angle φ between photons and jets, and the photon+jet p_{T} imbalance $x_{\mathrm{j}\gamma} = p_{\mathrm{T}}^{\mathrm{jet}}/p_{\mathrm{T}}^{\gamma}$ is studied for back-to-back photon+jet events with $\Delta\varphi > \frac{7\pi}{8}$, where a systematically smaller ratio is observed for Pb–Pb compared to pp, indicating the presence of partonic energy loss due to the presence of the QGP. This suppression is strongest for the most central collisions, as expected for partonic energy loss. A similar picture emerges when studying the number of associated jets per photon $R_{\mathrm{j}\gamma}$ as a function of photon p_{T}, which is found to be lower in Pb–Pb collision than those of the pp reference, indicating an increased energy loss in the nuclear environment. Similar measurements have been performed in smaller collision systems such as p–Pb, where no such suppression could be observed [132].

Also of interest is the measurement of prompt photon pairs, which can serve as a precision test of higher-order pQCD effects. In addition, prompt diphoton production

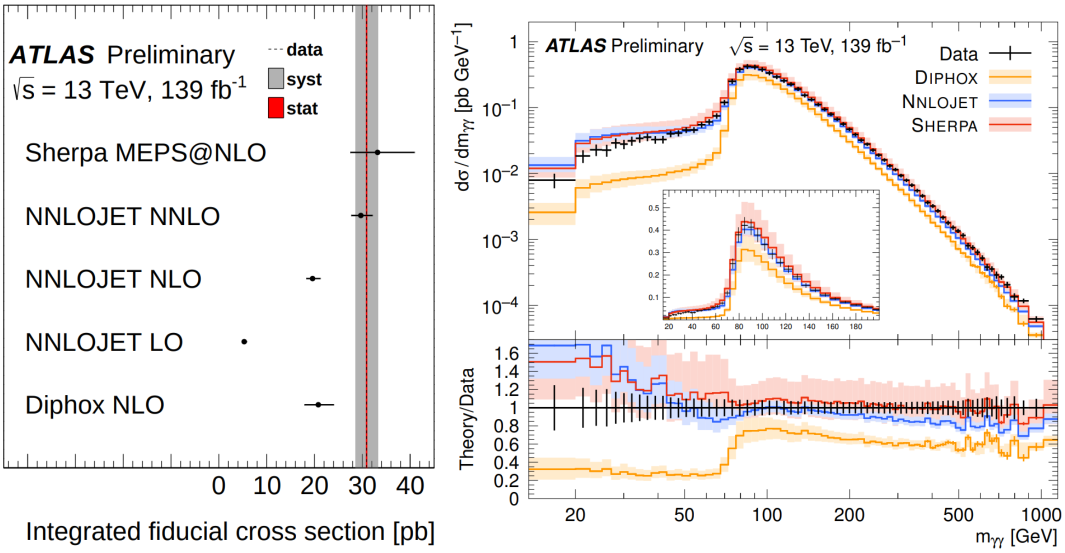

(a) integrated fiducial cross-section (b) cross-section as a function of diphoton mass $m_{\gamma\gamma}$

Figure 2.34: Prompt photon pair production measured by ATLAS in pp collisions at $\sqrt{s} = 13\,\text{TeV}$ [90]. **Left:** Integrated fiducial cross-section of prompt photon pair production compared to various pQCD calculations up to NNLO, where the Sherpa prediction includes parton showers. **Right:** Same cross-section shown differentially as a function of the diphoton mass $m_{\gamma\gamma}$

is an irreducible background for other measurements, such as the reconstruction of a Higgs boson decaying via H → $\gamma\gamma$, as well as photonic signatures of physics beyond the standard model [133, 134]. Fig. 2.34 which shows a measurement of prompt photon pair production in pp collision at $\sqrt{s} = 13\,\text{TeV}$ by ATLAS [134]. The integrated cross-section shown in Fig. 2.34a illustrates the need for corrections of the cross-section beyond NLO, as already observed for the single isolated prompt photon measurements discussed in the previous sections. The prompt photon pair cross-section as a function of diphoton mass $m_{\gamma\gamma}$ is shown in Fig. 2.34b, which is especially relevant for estimations of the background for diphoton decays in different invariant mass regions.

3

EXPERIMENTAL SETUP

CERN was founded in 1954[1] and is considered one of the world-leading laboratories to study fundamental particle physics. It is located at the Franco-Swiss border near Geneva and comprises several particle accelerators and facilities. Today, over 17500 scientists from more than 70 countries collaborate together in order to advance humanity's knowledge, either directly at Conseil Européen pour la Recherche Nucléaire (CERN) or at institutes around the world. The financial burden of these scientific endeavours is shared by to-date 23 member states, which make world-class research possible by combining their financial resources that allow to build and operate the large machines necessary to study matter on the most fundamental level. Important discoveries made at CERN include the discovery of the W and Z bosons in 1983 [135, 136], as well as the discovery of the Higgs boson in 2012 [137, 138], the latter of which was the final missing piece of the Standard Model.

This chapter gives an overview of the experimental setup used in this work, describing the LHC and the connected accelerator chain, as well as the ALICE detector. The latter consists of several sub-detectors, which are outlined individually, with a special focus on those relevant to this work. Finally, this chapter concludes with a general discussion of ALICE data taking and collision event reconstruction, including a brief introduction to the O^2 framework, which will replace the current structures for Run 3 (2022) of LHC operation.

3.1 THE LARGE HADRON COLLIDER (LHC)

The Large Hadron Collider (LHC) [139] is both the largest and highest energetic particle accelerator in the world. It is located at CERN close to Geneva between 40 m and 170 m below the surface[2] in the old tunnel of the Large Electron-Positron collider (LEP). The LHC is a circular superconducting accelerator, consisting of two rings that contain counter-rotating beams of particles which are accelerated using radiofrequency (RF) cavities and can be collided at four interaction points, which are distributed along the 26.7 km circumference of the accelerator. An ultra-high vacuum of 10×10^{-10} mbar created in the beampipes ensures minimal interactions of the circulating beams with residual gases. The particles are kept on their quasi-circular[3] path using 1232 superconducting dipole magnets, which can operate at fields above 8 T, thanks to cooling below 2 K using liquid helium. In contrast to particle-anti-particle colliders, such as the LEP or Tevatron, the LHC is designed to collide particles of same charge, requiring a magnetic dipole field of opposite field direction for the two beams. Since the available space is constrained by the LEP tunnel, a "two-in-one" magnet design has been adapted to achieve the opposite dipoles, where the coils of superconducting wires producing

---

[1] General information about CERN, such as founding date and number of employees were taken from the official website https://home.web.cern.ch/.

[2] The varying depth originates from the proximity to the Jura mountains. The plane of the accelerator is inclined by 1.4 % to partially counteract the terrain topology.

[3] The LHC consists of eight bent and eight straight sections, making it a decagon rather than an actual circle.

the magnetic fields for each colliding beam are embedded in a single dipole cold mass. Beam focussing and other optics functions are performed by 392 main quadrupole magnets. The high magnetic fields provided by the dipoles allow the LHC to reach beam energies of up to 7 TeV per proton, corresponding to a centre-of-mass energy of $\sqrt{s} = 14\,\mathrm{TeV}$. In addition to the achievable centre-of-mass energy, a key metric of an accelerator is the luminosity $\mathcal{L}$ that it can deliver at the interaction points: The number of collision events per second $\mathrm{d}N_{\mathrm{event}}/\mathrm{d}t$ for a given event with cross-section σ_{event} is given by

$$\frac{\mathrm{d}N_{\mathrm{event}}}{\mathrm{d}t} = \mathcal{L}\sigma_{\mathrm{event}} \tag{3.1}$$

and therefore a high luminosity is crucial to study rare processes such as the production of a Higgs boson or physics beyond the standard model. The luminosity is mainly determined by the number of particles in each colliding beam, their revolution frequency, as well as how well the beam can be focussed at the interaction point. In addition, the two beams have to be collided at a crossing angle at the interaction point, which reduces the luminosity but allows to steer the delivered luminosity at each of the four interaction points individually and also suppresses unwanted collisions outside the collision point. A beam at the LHC consists of up to 2808 so-called bunches, each containing up to 1.7×10^{11} protons, with a nominal bunch spacing of 25 ns. The revolution frequency of the beams is 400.79 MHz, which is limited by the operation frequency of the RF cavities that accelerate the beams. In 2017, the LHC delivered peak luminosities of more than $2 \times 10^{34}\,\mathrm{cm}^{-2}\mathrm{s}^{-1}$ in proton-proton operation, exceeding its design value by a factor of two [140].

As implied by its name, the LHC is designed for the collision of hadrons (in contrast to its predecessor LEP), where most its operation time each year is allocated to proton-proton (pp) collisions. However, the LHC can also be used as an ion collider, allowing for collision of lead ions (Pb–Pb), as well as asymmetric collisions or protons and lead (p–Pb or Pb–p). The same magnetic dipole field of 8.33 T used for pp collisions allows reaching beam energies of up to 2.76 TeV per nucleon in Pb–Pb collisions, corresponding to a total centre-of-mass energy of 1.15 PeV. While the LHC regularly provided lead collisions as part of its heavy-ion program for about one month each year, also other ion species can in principle be accelerated at the LHC. This was demonstrated in 2017, where Xenon ions were successfully accelerated and collided with a centre-of-mass energy of $\sqrt{s_{NN}} = 5.44\,\mathrm{TeV}$ per nucleon pair [141].

3.1.1 *Injection scheme*

Since the dipole magnets at the LHC can only operate within a certain range of magnetic field strength, the particle beams need to be pre-accelerated to 450 GeV beam energy (0.54 T dipole field) before injection into the LHC. This is achieved by CERN's existing accelerator complex, where a variety of older accelerators are repurposed and connected to each other to achieve suffiecient pre-acceletation in several stages. An overview of the accelerators present at CERN as of 2022 is given in Fig. 3.1. Before any acceleration, a source of protons, as well as heavy-ions is needed. The protons originate from a bottle of hydrogen gas which is injected into the duplasmatron ion source [143], where the hydrogen atoms are subsequently stripped from their electrons in an electric field. The process of providing heavier ions is more involved than providing protons, due to the

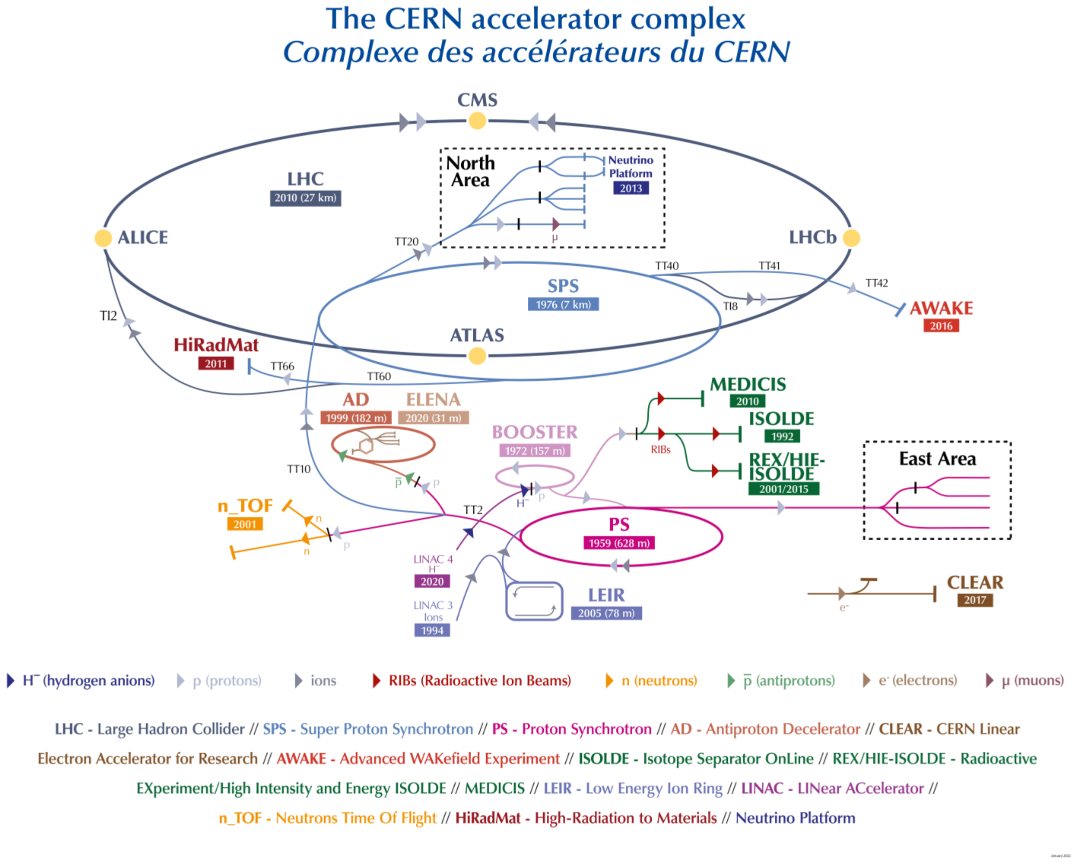

Figure 3.1: Overview of accelerators and connected experiemtns at CERN, as of 2022 [142].

high amount of electrons (82 for Pb) that need to be stripped. The Pb originates from a solid strip, which is evaporated in an oven and injected into the Electron Cyclotron Resonance Ion Source (ECRIS) [144], which acts as a cyclotron, combining microwaves and a magnetic field to achieve successive ionizing collisions with electrons of increasing energy that strip the electrons from the Pb atom. The same procedure can be employed to achieve other heavy-ions, however the field strength has to be adjusted accordingly.

The acceleration process begins differently for protons and heavy-ions: The protons are first accelerated in the Linac 2 [145, 146], which is a 80 m long linear accelerator reaching a beam energy of 50 MeV. From there, they are injected into the Proton Synchrotron Booster (PSB) [147], which is a four-ring synchrotron that accelerates the protons up to 1.4 GeV. The heavy-ions from the ECRIS are initially accelerated in the Linac 3 [148] up to 4.2 MeV per nucleon. The Linac 3 replaced Linac 1 in 1994, which had been only able to accelerate ions up to about the mass of calcium. The thus accelerated ions are injected into the Low Energy Ion Ring (LEIR) [149], which accumulates, cools and accelerates the beam to 72.2 MeV per nucleon.

From this point onwards the acceleration chain is the same for protons and heavy-ions, which get injected into the Proton Synchrotron (PS) [150] from PSB and LEIR, respectively. The PS is a synchrotron with a circumference of 628 m, which started operation in 1959 as at the time the strongest accelerator in the world, putting CERN on the world map of research institutions for particle physics [151]. Since its construction it has undergone several upgrades for LEP and later LHC, and today accelerates protons

(Pb-ions) up to 25 GeV (5.9 GeV per nucleon). From there, the protons and ions get injected into Super Proton Synchrotron (SPS) [152], where they are further accelerated to 450 GeV and 176.4 GeV per nucleon, respectively. The SPS has a circumference of 6.9 km and began operation in 1976. It is well known for enabling the discovery of the $W^{\pm}$ and Z bosons [135, 136] in 1983, years before the operation of the LEP. This was achieved by operating the SPS as a proton-anti-proton collider as early as 1981. Today, the SPS does not only serve as a pre-accelerator for the LHC, but also provides particle beams for various fixed target experiments [153] that e.g. study the spin of the nucleus (COMPASS [154]) or search for dark matter (NA64 [155]). After acceleration in the SPS, the beam is sufficiently energetic to be injected into the LHC, where the two beams of opposite direction can finally be collided with unprecedented beam energies of up to 7 TeV per proton beam.

3.1.2 *Experiments and physics at the LHC*

There are four main interaction points at the LHC, where the accelerated particles are collided and studied in four dedicated experiments, each emphasizing a different physics topic:

A Toroidal LHC Apparatus (ATLAS) [156] and Compact Muon Solenoid (CMS) [157] are general purpose detectors which are designed for the unprecedented high luminosities provided by the LHC for pp collisions. As already illustrated in Eq. 3.1, maximizing the measured luminosity is crucial in order to gather a sufficient amount events containing rare standard model processes, such as the production of the Higgs boson, as well as other rare signatures of physics beyond the standard model, such as supersymmetry and new gauge bosons. The search for the Higgs boson, which was finally discovered by ATLAS [137] and CMS [138] in 2012, played an important role during the design of the sub-systems for both detectors. The various decay channels of the Higgs boson containing photons, leptons and jets in the final state are reflected in the core design principles of both detectors: Very good electromagnetic and hadronic calorimetry with almost full-coverage in azimuthal angle (for e.g. $\mathrm{H} \rightarrow \gamma\gamma$ and missing mass for neutrino measurements), good charged-particle momentum resolution and muon identification (for e.g. $\mathrm{H} \rightarrow ZZ^{*} \rightarrow l^{+}l^{-}l^{'+}l^{'-}$), as well as good capabilities to reconstruct secondary vertices occuring very close to the collision vertex (for e.g. $\mathrm{H} \rightarrow \tau^{+}\tau^{-}$). Both, ATLAS and CMS are especially suited for the measurement of highly energetic particles, which is also reflected in the choice of magnetic fields, where e.g. the 4 T superconducting solenoid of CMS provides sufficient bending power to unambigously determine the charge of the muon for momenta up to ≈ 1 TeV [157]. The discovery of the Higgs boson furthermore illustrates the synergy of ATLAS and CMS, where the observation of Higgs decays by both experiments, positioned on opposite sides of the LHC, serves as an important cross check for the discovery and improves its statistical significance. For more details on the sub-detectors and their characterustics, please refer to Ref. [156] and [157].

The LHCb experiment [158] is located at interaction point 8 of the LHC and focusses on rare decays of heavy flavor hadrons containting charm or beauty quarks. Studies of such decays are especially interesting in the search for physics beyond the Standard Model, which could manifest itself indirectly as CP violation that goes beyond the expectations according to the Cabibbo-Kobayashi-Maskawa (CKM) mechanism. This

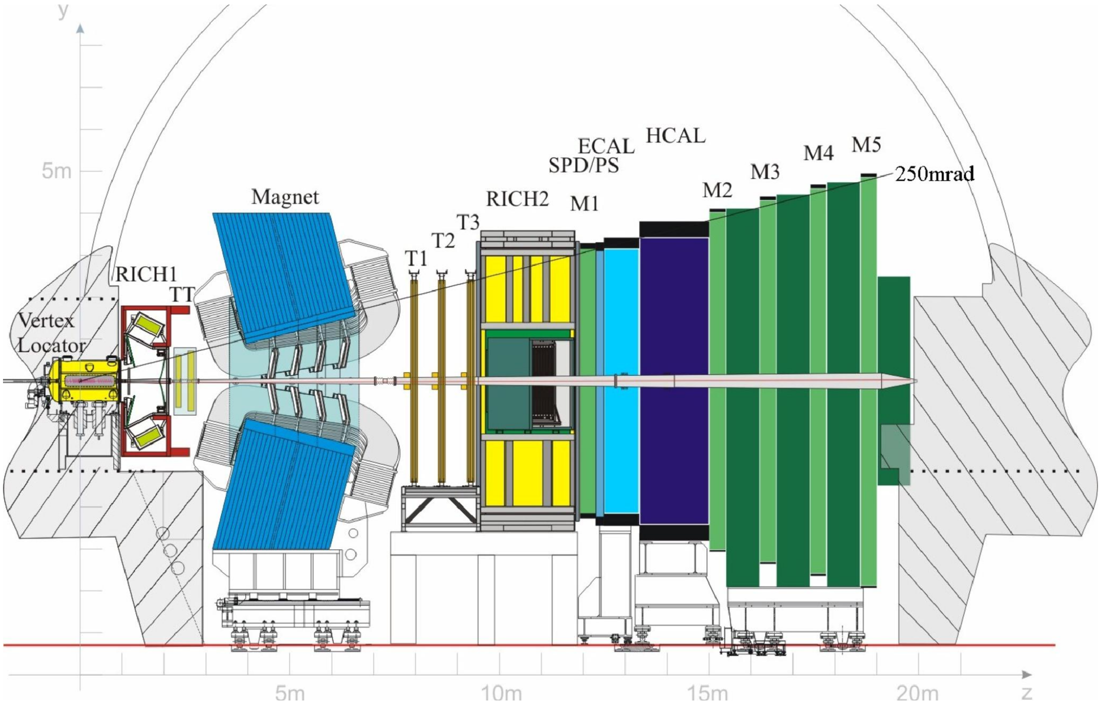

Figure 3.2: Schematic overview of the Large Hadron Collider beauty (LHCb) detector [158].

is directly connected to the question why our universe consists of more matter than anti-matter, which can not be explained by the strength of CP violation described by the standard model. Fig. 3.2 gives a schematic overview of the LHCb detector: The layout of the detector is quite different compared to e.g. ATLAS and CMS: Instead of surrounding the collision vertex with multiple layers of different subdetectors, often spanning the full azimuthal angle, the LHCb experiment consists of a single-arm which is located only on one side of the collision vertex and surrounding the beampipe. This choice is motivated by the fact that highly energetic b and $\bar{\mathrm{b}}$ hadrons are dominantely produced in the same cone, either in forward or backward direction. This layout allows the LHCb detector to cover forward pseudorapidities of $2 < \eta < 5$ for both charged- and neutral particles, where a silicon based tracking system enables a momentum resolution of 0.4 % to 0.5 % and the ECAL and HCAL provide electromagnetic- and hadronic calorimetry, respectively. Considering the focus of this work on studying the initial-state of heavy ion collisions and cold nuclear matter effects, the measurement of prompt D^0 meson production in p–Pb collisions at $\sqrt{s_{\mathrm{NN}}} = 5.02\,\mathrm{TeV}$ by LHCb [130] is particularly noteworthy: D^0 meson production is particularly sensitive to gluons in the initial state, due to its dominant production via gluon fusion ($gg \rightarrow \mathrm{c}\bar{\mathrm{c}}$). The measurement reports the prompt D^0 production cross section, as well as the nuclear modification factor R_{pA} at forward- backward rapidities of $1.5 < y^* < 4.0$ and $-5.0 < y^* < -2.5$, respectively, which allowed to improve the gluon nPDF uncertainties of nNNPDF3.0 by up to a factor five [66]. As previously stated, this highlights the importance of forward measurements at the LHC to gain further insights into hirtherto unconstrained regions of the phasespace of the initial state.

ALICE is the only dedicated heavy-ion detector at the LHC. It is used in this work to study isolated prompt photon production in pp and p–Pb collisions, and is therefore separetly discussed in the following section.

In addition to the four main experiments ATLAS, CMS, LHCb and ALICE, there are several smaller experiments, which are able to perform measurements at very large rapidities and are often positioned several hundred meters away from the main interaction points along the beam line: The TOTal Elastic and diffractive cross section Measurement (TOTEM) experiment [159] consists of four tracking telescopes, as well as several Roman Pot stations, which are placed within ± 220 m from the interaction point used by CMS. This enables the study of charged particles at large pseudorapidities of $3.1 \leq |\eta| \leq 6.5$. Its main physics objectives are the measurement of the total pp cross-section and the study of elastic and diffractive scatterings at the LHC. The Monopole and Exotics Detector At the LHC (MoEDAL) detector [160, 161] is located around the interaction point used by the LHCb experiment and consists of a large array of nuclear track detectros, as well as trapping detectors which can measure and capture exotic particles for further study. Its main physics goals are the search for magnetic monopoles, as well as the detection of massive, charged and slow-moving particles that may be produced in physics processes beyond the standard model [161]. The Large Hadron Collider forward (LHCf) experiment [162] consists of two imaging calorimeters, which are at located ± 140 m from the ATLAS interaction point and enable the measurement of neutral particles with $\eta > 8.4$. The experiment is motivated by cosmic ray experiments, which rely on MC simulations to describe the interaction of cosmic rays with earth's atmosphere, causing a cascade of particles. Measurements of highly energetic neutral pions and neutrons produced at very forward rapidities at the LHC, allow LHCf to provide better constrains of these phenomenological models and therefore improve the calibration and interpretation of large-scale cosmic ray experiments.

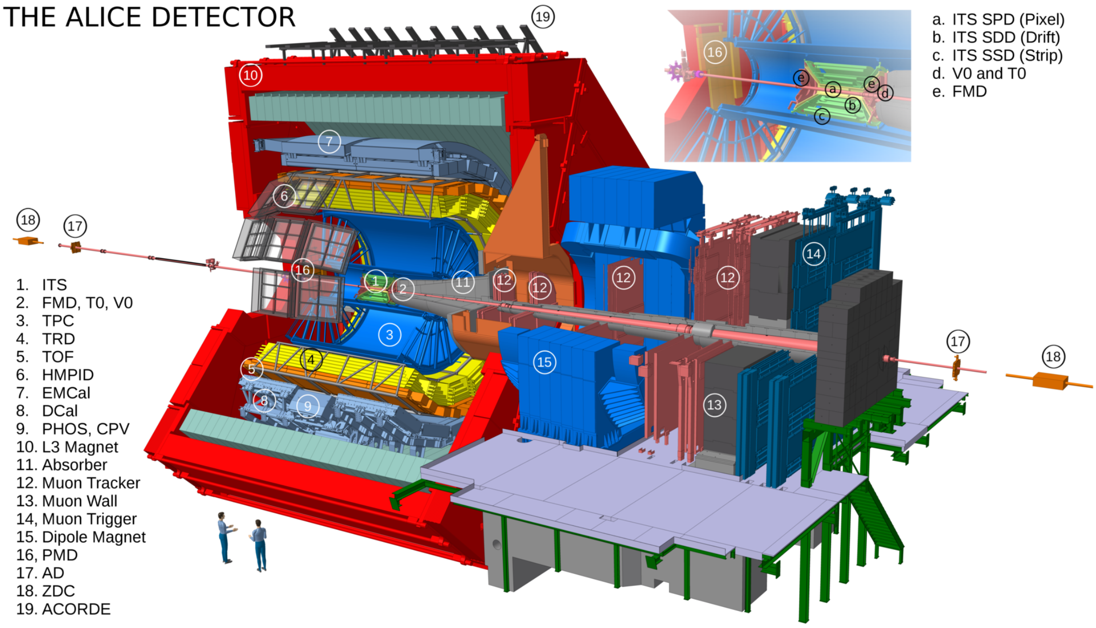

Figure 3.3: Schematic overview of the ALICE detector in Run 2 [163].

3.2 A LARGE ION COLLIDER EXPERIMENT (ALICE)

A Large Ion Collider Experiment (ALICE) [164] is the dedicated heavy-ion experiment at the LHC and focusses on the study of QCD in extreme conditions of high temperatures and energy densities. The study of the QGP, which is created in heavy-ion collisions and requires a variety of different measuremets to explore its properties (see Sec. 2.3.2) is one of the key motivations for the ALICE experiment. However, since the experiments proposal in 1993, its physics program has been continously extended to also include a variety of other QCD-related observables – both in the soft and hard sector. Examples of this are the study of high-Q processes such as prompt photon production, which is discussed in this work, as well as heavy-flavour, quarkonia and high-p_{T} hadron production, where the experiment can provide important insights.

The ALICE detector is located at interaction point 2 of the LHC, about 52 m below ground under the commune of St. Genis-Pouilly in France. It has a size of $16 \times 16 \times 26\,\mathrm{m}^3$ and weights about 10 000 t. Its physics program necessitates robust particle identification, as well as wide covered transverse momentum range for hadrons, electrons, photons and muons, even in the high-multiplicity environment of Pb–Pb collisions, where up to 10 000 particles are produced at mid-rapidity. These capabilities are provided by 19 subsystems, which are shown in the schematic overview of the ALICE detector given in Fig. 3.3. In addition, the coverage and purpose of each detector is given in Tab. 3.1.

One can group the systems into two distinct parts: The majority of subdetectors are located inside the L3 solenoid magnet (shown in red), which provides a nominal magnetic field of 0.5 T that bends the tracks of charged particles, allowing to determine their momentum. These detectors are referred to as the central barrel. The forward muon spectrometer is located outside the L3 magnet and furthermore placed behind an absorber in order to shield the muon arm from the high multiplicities of unwanted

Table 3.1: Overview of coverage and purpose of the ALICE subdetectors. Detectors used in the presented analysis are highlighted in **bold** [165].

Detector	Acceptance		Radial distance IP (cm)	Purpose
	η	φ		
SPD (ITS)	$\|\eta\| < 2(1.4)$	full	3.9 (7.6)	tracking, vertex
SDD (ITS)	$\|\eta\| < 0.9$	full	15.0 (23.9)	tracking, PID
SSD (ITS)	$\|\eta\| < 1$	full	38.0 (43.0)	tracking, PID
TPC	$\|\eta\| < 0.9$	full	$85 < r < 247$	tracking, PID
TRD	$\|\eta\| < 0.8$	full†	$290 < r < 368$	tracking, $e^\pm$ id.
TOF	$\|\eta\| < 0.9$	full†	$370 < r < 399$	PID
PHOS	$\|\eta\| < 0.12$	$220° < \varphi < 320°$	$460 < r < 478$	photons
EMCal	$\|\eta\| < 0.7$	$80° < \varphi < 187°$	$430 < r < 455$	photons, jets, $e^\pm$ id.
DCal	$0.22 < \|\eta\| < 0.7$	$260° < \varphi < 327°$	$430 < r < 455$	photons, jets, $e^\pm$ id.
HMPID	$\|\eta\| < 0.6$	$1.2°\varphi < 55.8°$	490	PID
V0A	$2.8 < \eta < 5.1$	full	340	trigger, centrality
V0C	$-3.7 < \eta < -1.7$	full	900	
T0A	$4.5 < \eta < 5$	full	360	trigger,vertex,time
T0C	$-3.3 < \eta < -2.9$	full	70	
PMD	$1.8 < \eta < 2.6$	full	580	multiplicity
FMD1,FMD2	$1.7 < \eta < 5.0$	full	75, 83, 320	multiplicity
FMD3	$-3.4 < \eta < -1.7$	full	-62, -75	
ZDC	$\|\eta\| > 8.8$	full	± 113 m	neutrons
	$6.5 < \|\eta\| < 7.5$	$\|\varphi\| < 10°$	± 113 m	protons
	$4.8 < \|\eta\| < 5.7$	$\|2\varphi\| < 32°$	7.3 m	photons
MCH	$-4.5 < \eta < -2.5$	full	$-1420 < r < -536$	$\mu^\pm$ tracking
MTR	$-4.5 < \eta < -2.5$	full	$-1710 < r < -1610$	$\mu^\pm$ trigger

particles, such as electrons and hadrons, exploiting the in comparison low interaction rate of muons with the traversed material.

This section introduces the individual sub-systems and discusses their physics performance, with a special focus on the systems used in this analysis. Furthermore, important upgrades of the sub-detectors performed for Run 3 of LHC operation (which is just starting at the time of writing this thesis) will be discussed.

3.2.1 *Inner Tracking System (ITS)*

The Inner Tracking System (ITS) [166] is the closest detector to the beampipe and consists of six cylindrical layers of silicon-based detectors that are located between 4 and 43 cm in radial distance from the nominal interaction point, as illustrated in the detector layout shown in Fig. 3.4. The ITS is used to measure and identify charged particles, which leave signals when traversing the 6 ITS layers. These signals are combined to

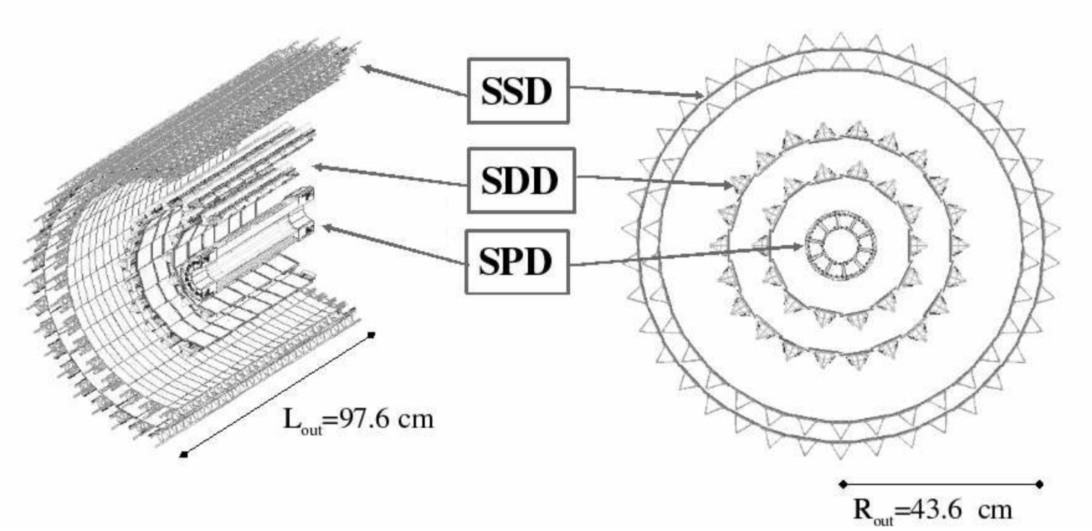

Figure 3.4: Layout of the ITS [164].

reconstruct the trajectory of a given particle, which is known as "tracking". Due to its closeness to the interaction point, the tracking information provided by the ITS allows to reconstruct the position where a collision occurred (primary vertex), as well as the determination of the impact parameter of secondary tracks originating from decays of strange, charm and beauty particles that live long enough to travel a few cm away from the interaction point before decaying (secondary vertices).

The two innermost layers of the ITS are Silicon Pixel Detectors (SPDs), which consist of almost 9 million two-dimensional pixels located at radii of 3.9 and 7.6 cm and cover $|\eta| < 2.0$ and $|\eta| < 1.4$, respectively, over the full azimuthal angle. The highly-granular silicon pixel design was chosen to cope with the very high particle densities (up to 50 particles per cm^2) found this close to the interaction point. The main purpose of the SPD layers are the precise determination of the primary collision vertex, as well as the determination of the aforementioned secondary vertices of weak decays, where a spatial resolution of 300 µm in beam direction and 200 µm in the $\varphi - R$ plane is achieved. The next two intermediate layers are Silicon Drift Detectors (SDDs), which are located at radii of 15 and 23.9 cm, covering $|\eta| < 0.9$ over the full azimuthal angle. It consists of 260 drift modules, each composed of a 300 µm silicon-based drift sensor, where the position of the signal is determined using 256 anodes, as well as the drift

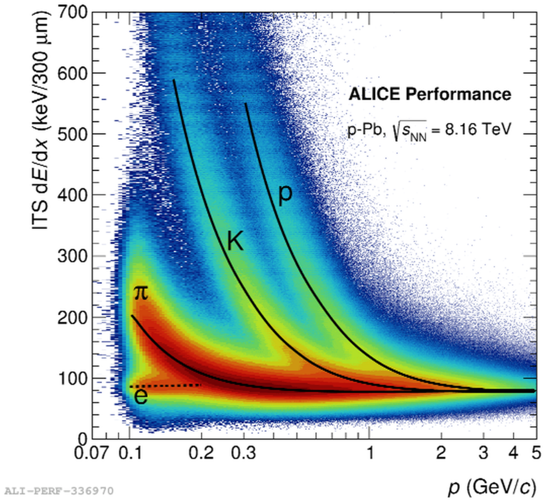

Figure 3.5: Specific energy loss $\mathrm{d}E/\mathrm{d}x$ of charged particles measured in the ITS as a function of track momentum in p–Pb collisions at $\sqrt{s_{\rm NN}}$ = 8.16 TeV [167]. Solid black lines indicate the expected energy loss for different particle species according to the Bethe-Bloch formula (See Eq. 3.2).

time. In addition, the integration of the signal provides two out of four $\mathrm{d}E/\mathrm{d}x$ samples for the measurement of the specific energy loss, which is used for particle identification. The outermost two layers form the Silicon Strip Detector (SSD), which are located at radii of 38 and 43 cm and cover $|\eta| < 1.0$ over the full azimuthal angle. The layers complement the $\mathrm{d}E/\mathrm{d}x$ information provided by the SDD with two additional samples and furthermore provide important track points needed to match ITS tracks to the Time Projection Chamber (TPC), which is ALICE's main tracking detector discussed in the following section. Figure 3.5 shows the $\mathrm{d}E/\mathrm{d}x$ information provided by SDD and SSD as a function of track momentum[4], showcasing the PID capabilities of the ITS for low-momentum particles with $p < 1.5\,\mathrm{GeV}/c$. In addition, the additional space points provided by the ITS close to the primary vertex allow track reconstruction of low-momentum particles with $p < 200\,\mathrm{MeV}/c$ that are significantly bent in the magnetic field and do not reach the TPC. Tracking of high-p_T particles also profits from the ITS when used together with the TPC, where the additional space-points improve the overall momentum resolution, as discussed in the following section.

During the second long LHC shutdown (LS2), the ITS has been upgraded in preparation for the significantly increased interaction rate in Run 3 (starting 2022) [168]. The upgrade focussed on increasing the readout-rate capabilities of the ITS, as well as improving its tracking capabilities to strengthen the ALICE's heavy-flavour physics program. The completely revised geometry, segmentation and readout, as well as a reduction of the beampipe diameter by about 40 % will allow for an expected increase in read-out rate from previously 1 kHz up to 100 kHz in Pb–Pb collisions, as well as an improvement of impact parameter resolution by a factor 3 and 5, in the $r\varphi$ and z coordinates, respectively [168, 169].

3.2.2 *Time Projection Chamber (TPC)*

The Time Projection Chamber (TPC) [170] is the main tracking detector of ALICE and is located in the central barrel enclosed by the 0.5 T L3 magnet. It is designed to provide measurements of charged particles with good two-track separation, as well as particle identification and vertex reconstruction. A schematic overview of the TPC is given in Fig. 3.6. The detector is made up of a $90\,\mathrm{m}^3$ gas-filled cylindrical field cage, with a total of $32.5\,\mathrm{m}^2$ of readout chambers at the end caps. The active volume covers $|\eta| < 0.9$ over the full azimuthal angle from 84.8 cm up to 246.6 cm in radial distance from the interaction point[5]. Charged particles traversing the gas volume of the TPC leave a track of ionization electrons along their path and the freed electrons are accelerated towards readout chambers via a uniform 100 kV electric field, that is applied between the end caps and the electrodes located at the centre of the detector. After a maximum drift time of $\sim 90\,\mu\mathrm{s}$, the freed electrons reach the readout chamber, which consists of Multi-Wire Proportional Chambers (MWPCs) with pad readout that allows to determine a 2D projection of the charged particle's trajectory in the detector. By measuring the drift time of the freed electrons, one can calculate the third spatial coordinate, and thus a 3D measurement of the charged particle's trajectory is obtained. The magnetic field of the L3 magnet, which is oriented in parallel to the electric drift field, bends the trajectory of the charged particles and therefore allows to calculate its momentum and charge sign

---

[4] The track momentum was obtained using the combined track reconstruction in ITS and TPC.

[5] For tracks reconstructed with reduced track length, an increased acceptance of $|\eta| < 1.5$ can be achieved.

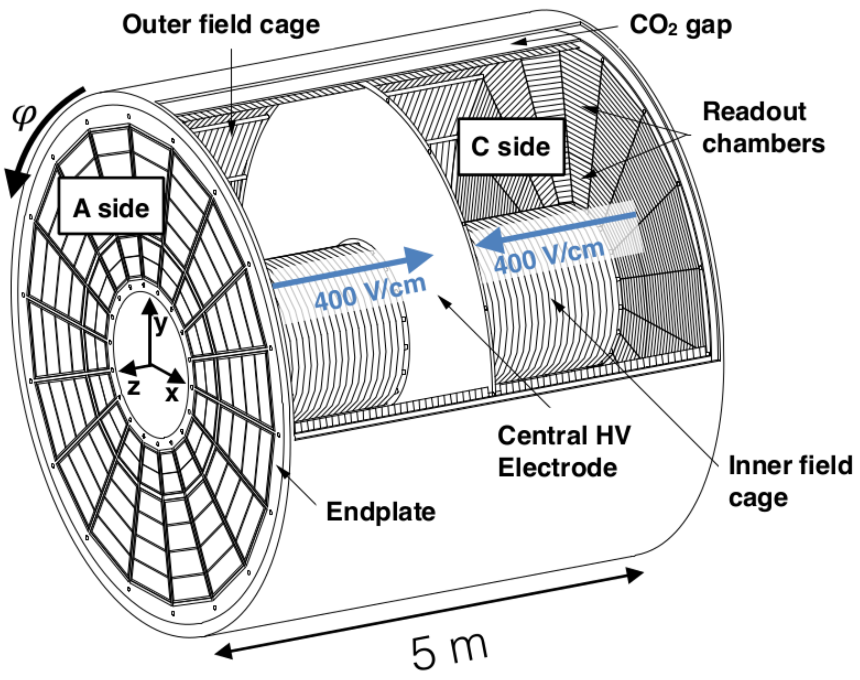

Figure 3.6: Schematic overview of the TPC [171].

from the curvature in the magnetic field, given an assumption of the particles rest mass. Since the measurement of the trajectory happens at discrete space points, given by the spacing of the wires in radial direction and precision of the drift time measurement, the trajectory has to be reconstructed by connecting the individual signals to a continuous line, which is known as track reconstruction and discussed in Sec 3.3.1. One of the main challenges of the TPC are its large volume, where electrons drift for several meters before being detected in the readout chamber. This makes the detector sensitive to small distortions in the electric field, e.g. caused by the presence of remaining ions that "pile up" in the active detector volume. Furthermore, a high drift velocity is required to reduce the drift time and therefore the "busy time" of the detector. The drift speed and the magnitude of the space charge effect are sensitive to the used gas-mixture, which as been optimized and adjusted before and during ALICE operation: Initially, the ALICE TPC used a gas mixture of 90 % Ne and 10 % CO_2, which was adapted to use Nitrogen (2016) and later Argon (2018) instead of Neon, in order to further reduce the space-charge build-up [170, 172].

The tracking performance of the TPC is illustrated in Fig. 3.7a, which shows the p_T resolution of standalone TPC tracks. In addition, the p_T resolution of track using the combined tracking information of ITS and TPC is shown, as well as the impact of further constrains provided by the reconstructed primary vertex. One finds a sub-percent precision for TPC standalone tracks with $p_T > 1\,\mathrm{GeV}/c$, which is further improved by including information from the ITS and the reconstructed primary vertex [165]. In addition to its tracking capabilities, the TPC enables particle identification by measuring the energy loss $\mathrm{d}E/\mathrm{d}x$ of charged particles within the detector volume as a function of their momentum p, which is shown in Fig. 3.7b for operation at a lower than nominal magnetic field strength of $B = 0.2\,\mathrm{T}$ [174]. The expected mean energy loss per path

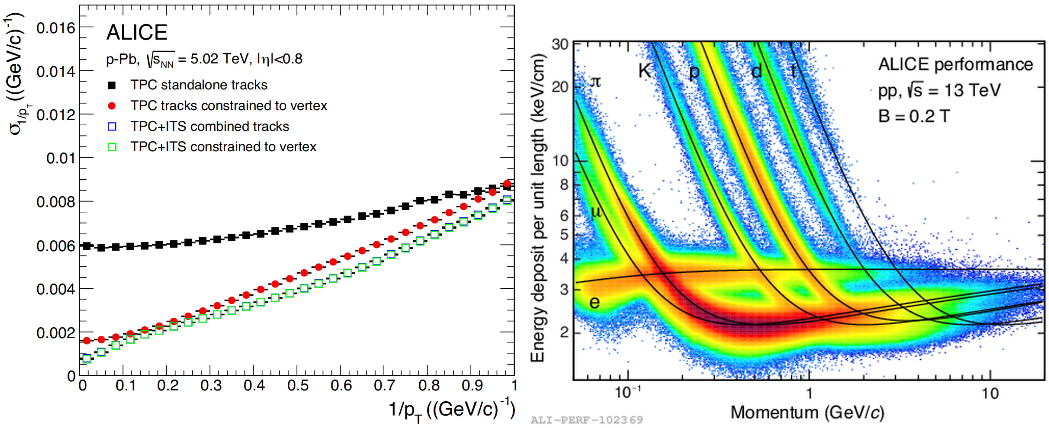

(a) transverse momentum resolution (b) particle identification

Figure 3.7: **Left:** The p_T resolution of standalone TPC tracks, as well as tracks using information from ITS and TPC. In addition, tracks that were constrained by the reconstructed primary vertex are shown [165]. **Right:** Specific energy loss $\mathrm{d}E/\mathrm{d}x$ as a function of particle momentum p, measured using a lower than nominal magnetic field strength of $B = 0.2\,\mathrm{T}$ [173]. The solid lines show the expected mean energy loss of different particle species according to the Bethe-Bloch equation (Eq. 3.2) [174].

length of different moderately relativistic heavy charged particles traversing a medium is well described by Bethe-Bloch equation [11]:

$$\left\langle -\frac{\mathrm{d}E}{\mathrm{d}x} \right\rangle = Kz^2 \frac{Z}{A} \frac{1}{\beta^2} \left[\frac{1}{2} \ln \frac{2m_e c^2 \beta^2 \gamma^2 W_{\max}}{I^2} - \beta^2 - \frac{\delta(\beta\gamma)}{2} \right] \quad \text{for} \quad 0.1 \lessapprox \beta\gamma \lessapprox 1000 \tag{3.2}$$

Here Z and A are the atomic number and atomic mass of the absorber, and z and $\beta = v/c$ are the charge number and speed of the incident particle, where the latter is expressed as a fraction of the speed of light c. The other variables are material dependent quantities, and the reader is referred to Ref. [22] (in particular Tab. 34.1) for further elaborations. The expected mean energy loss of different particle species is illustrated in Fig. 3.7b by solid black lines. As can be seen, there is a clear separation visible between different particle species for $p \lesssim 1\,\mathrm{GeV}/c$, which can be used to identify charged particles on a track-by-track basis. At higher momenta, where the separation is less pronounced one has to resort to statistical methods, e.g. via multi-Gaussian fits of the $\mathrm{d}E/\mathrm{d}x$ distribution [165].

The readout rate of the TPC during Run1 and Run2 of LHC operation was mainly limited to a few kHz in Pb–Pb collisions due to the triggered operation of a gating grid, which is transparent to electrons after an interaction trigger but then is closed to block ions from entering the active detector area after the electrons passed through. For Run3, novel readout-chamber were installed, which have intrinsic ion-blocking capabilities that allow for TPC operation with continuous readout, enabling readout rates of up to 50 kHz in Pb–Pb collisions [175]. The concept of continuous readout is further discussed in Sec. 3.3.2.

3.2.3 *Transition Radiation Detector (TRD)*

The ALICE Transition Radiation Detector (TRD) [177, 178] covers a pseudorapidity range of $|\eta| < 0.84$ over the full azimuth and is located in the central barrel from $290 < r < 368\,\text{cm}$ in radial distance from the interaction point. The detector provides electron identification and triggering, as well as general tracking capabilities that extend the tracking of ITS and TPC by roughly 70 cm in radial direction. In addition, the TRD serves as a reference to correct for distortions in the TPC due to the presence of space charges (see Sec. 3.2.2).

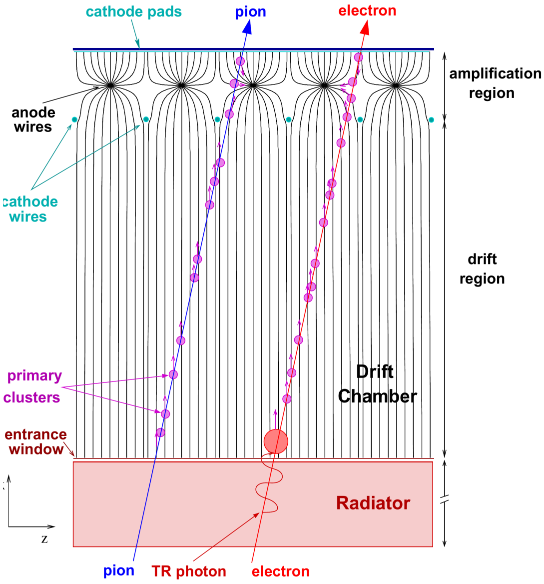

Figure 3.8: Schematic cross-section of a TRD module in *rz*-direction [176].

The TRD consists of 540 individual modules which are arranged in 18 so-called supermodules (SMs)[6], each containing 5 stacks of modules with 6 layers. The design of an individual detector module is illustrated in Fig. 3.8, which shows a schematic cross-section of a TRD module in the *rz*-plane: A module consists of a sandwich radiator of 48 mm thickness, followed by a 30 mm drift region and a 7 mm MWPC with pad readout. Charged particles traversing the TRD module will produce electrons from ionization of the counting gas mixture (Xe/CO_2), which subsequently drift towards the anode wires, where they are detected in the readout pads following gas amplification. This allows for the tracking of charged particles, as well as their identification using the specific energy loss $\text{d}E/\text{d}x$ in the TRD gas, as previously introduced for the TPC and ITS. In addition to ionization and the resulting energy loss in the medium, the TRD exploits an additional phenomenon known as Transition Radiation (TR), which was first predicted by Glinzburg and Frank in 1946 [179]. TR occurs when a charged particle traverses an interface between to materials of differing dielectric constants, which is emitted in form of a photon at a small angle ($\theta \approx 1/\gamma$) with respect to the incident particle [176]. The production of TR depends on the Lorentz factor $\gamma = 1/\sqrt{1-\beta^2}$, where an onset-like behaviour is observed for $\gamma \sim 1000$ and the characteristics of the TR spectrum can be modified by employing multiple boundaries of precise thickness and separation, which are realized in the ALICE TRD radiator using a fibre foam sandwich material. This γ dependence can be exploited for particle identification, where e.g. lighter particles such as the electron travel at more relativistic velocities than the heavier charged pions at the same momentum. Charged particles with $\gamma \gtrapprox 1000$ will produce about 1.45 photons in the energy range of 1 to 30 keV in the TRD radiator, which subsequently convert within the first centimetres of the large-Z drift gas. The produced conversion electrons will drift towards the anodes in addition to those produced via ionization, leading to a larger signal for highly-relativistic charged particles. This is illustrated in Fig. 3.9a, which shows the average amplitude of the

---

[6] During Run1 of LHC operation, only 13 out of 18 SMs were installed, before the full acceptance of 18 SMs was reached for the beginning of Run2.

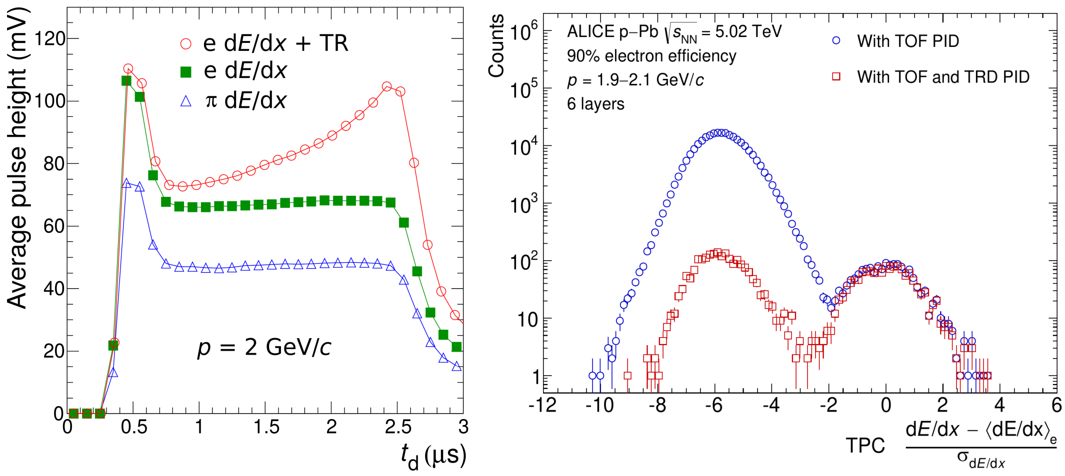

(a) Signal in TRD (b) electron identification

Figure 3.9: **Left:** Average amplitude of the cathode pad signal as a function of drift time for different particle species [176]. **Right:** Standard deviations between measured and expected energy loss of an electron in the TPC, where in addition TOF and TRD electron identification was applied [178].

cathode pad signal as a function of drift time for electrons and pions with $p = 2\,\mathrm{GeV}/c$: A clear signal separation is observed for electrons and pions, attributed to the specific ionizing energy loss of the two particle species. However, for large drift times an increasing separation is observed, which is attributed to the early conversion of TR photons produced by the incident electron traversing the radiator.

The electron identification capabilities of the TRD are illustrated in Fig. 3.9b [178], which shows the standard deviations between measured and expected energy loss of an electron in the TPC. The results were obtained in p–Pb collisions at $\sqrt{s_{\mathrm{NN}}} = 5.02\,\mathrm{TeV}$ for tracks with a momentum of $1.9 < p < 2.1\,\mathrm{GeV}/c$. Applying the TRD electron identification with 90 % electron efficiency (red) suppressed hadrons by about a factor of 130 with respect to a mere selection using the TOF detector (blue), showcasing the capabilities of the TRD to increase the electron purity of the track sample at low-momenta.

In addition to its particle identification, the space points provided by the TRD can be used to reconstruct the tracks of charged particles, either using only the information of the TRD or in combination with the track points from ITS and TPC. For standalone tracking a transverse momentum resolution of about $2.5 - 3\,\%$ is achieved. Inclusion of the TRD in addition to ITS and TPC improves the momentum resolution by about 40 % at high-p_{T} [178]. The tracking capabilities of the TRD furthermore allow correcting distortions of TPC track points, which can get shifted due to the accumulation of charged ions in the TPC gas chamber [180]. This is achieved by using ITS-TPC-TRD-TOF tracks as a reference to obtain corrections for the distorted TPC points, which can get shifted by several centimetres. Finally, the TRD provides Level 1 event triggers (see also Sec. 3.2.5), which can be used to enhance the number of recorded events containing electrons, jets, cosmic-ray muons and light nuclei. A trigger decision is provided using the so-called Global Tracking Unit (GTU) within 6.1 μs after the collisions. For example, studies in p–Pb collisions at $\sqrt{s_{\mathrm{NN}}} = 5.02\,\mathrm{TeV}$ [178] demonstrate an enhancement of electron candidates of about 700 with respect to minimum-bias collisions when using a trigger threshold of 3 GeV/c.

3.2.4 *Time of Flight Detector (TOF)*

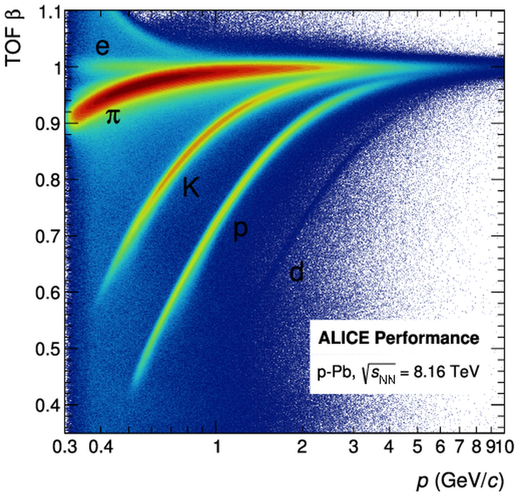

ALI-PERF-337022

Figure 3.10: Relative velocity β of TOF-matched tracks as a function of track momentum p [181].

The Time-Of-Flight (TOF) detector [182] consist of a large array of Multigap Resistive Plate Chambers (MRPCs) located at 370–399 cm in radial distance from the interaction point, covering $|\eta| < 0.9$ over the full azimuthal angle with over 150 000 readout channels. The detector enables the identification of pions and kaons with momenta up to 2.5 GeV/c, as well as protons up to 4 GeV/c. This is achieved by a precise measurement of the arrival time of particles in the TOF detector, which can be measured with a timing resolution of $\delta t \approx 80$ ps for pions at $p_{\rm T} \approx 1$ GeV/c [165]. The thus obtained arrival time is used together with the collisions time (provided by the T0 detector with $\delta t \lessapprox 25$ ps) to calculate the relative velocity $\beta = v/c$, which is shown in Fig. 3.10 for p–Pb collisions at $\sqrt{s_{\rm NN}} = 8.16$ TeV. A clear separation is visible for different particle species, which is especially pronounced for heavy-particles at low momenta. The total resolution of the TOF β signal for a given momentum interval depends on the track multiplicity. One finds an improving resolution with increasing track multiplicity, approaching the intrinsic resolution of about 80 ps for multiplicities $n_{\rm trk.} \gtrapprox 25$ [165].

3.2.5 *Electromagnetic Calorimeters (EMCal and DCal)*

The ElectroMagnetic Calorimeter (EMCal) [183, 184] is a sampling calorimeter consisting of alternating layers of natural lead and scintillation material with wavelength shifting fibres, which enables the measurement of electromagnetic (EM) observables such as electrons from heavy-flavor decays, the EM component of jets and photons, the latter of which can in turn be used to reconstruct mesons. The EMCal furthermore provides dedicated hardware trigger for jets and photons, which will be discussed at the end of this section. The detector is located about 4.5 m in radial direction from the interaction point, and covers $|\eta| < 0.7$ over

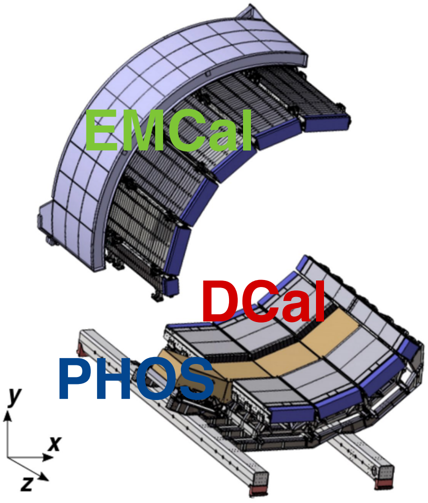

Figure 3.11: Schematic overview of the EMCal and DCal geometry together with the PHOS detector. Figure adapted from Ref. [183].

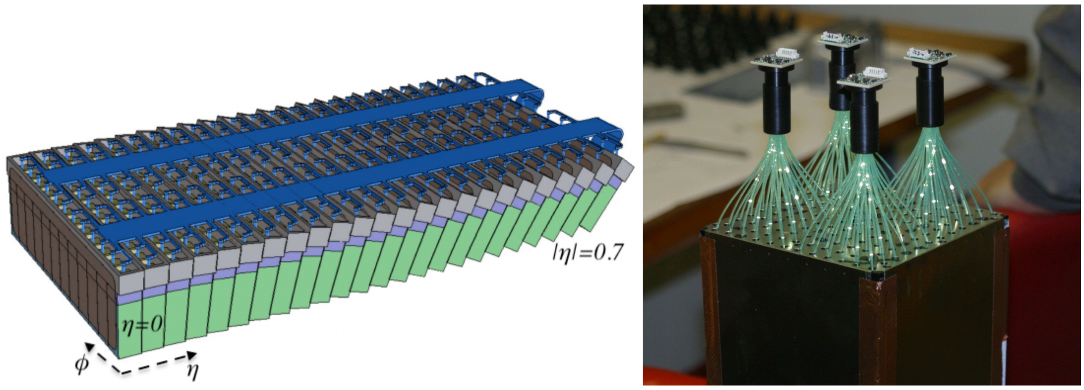

(a) EMCal super module

(b) EMCal module

Figure 3.12: **Left:** Schematic view of a full-size EMCal SM, where the modules are arranged with an angle of about 1.5° to achieve a projective surface in η [184]. **Right:** Photo of a EMCal module, showing fibre bundles coming from the four towers that connect the scintillator layers to the APDs [183].

$\Delta\varphi = 107°$ in azimuth. A schematic view of the EMCal is shown in Fig. 3.11, which for reference also shows the PHOS located on the opposite side of the EMCal in azimuth. In 2014, the EMCal acceptance was extended on the opposite side in azimuth with the so-called Di-Jet Calorimeter (DCal) [185], which surrounds the PHOS as illustrated in Fig. 3.11, covering $0.22 < |\eta| < 0.7$ for $260° < \varphi < 320°$ and $|\eta| < 0.7$ for $320° < \varphi < 327°$. Its name highlights its purpose to enable dijet and hadron-jet correlation measurements, however, despite differing name it is identical to the EMCal in detector design, readout as well as triggering, and is therefore commonly treated as an extension of the EMCal rather than an independent detector.

The EMCal is made up of 12 SMs, two of which are 1/3 the size of the other full-sized SMs. The DCal extends the coverage with 6 2/3-sized SMs and 2 1/3-size SM. Each full-size SM consists of 192 so-called modules, which are the basic constituents of the calorimeter. Fig. 3.12a gives a schematic view of a full-size SM, showcasing the arrangement of the individual modules. An arrangement with increasing angle for increasing η ensure a projective geometry in $\eta - \varphi$ space. Each module contains 2×2 towers, which can be readout individually and each cover $\Delta\eta \times \Delta\varphi \simeq 0.0143 \times 0.0143$. The tower is divided into alternating layers of Pb and scintillation material amounting to about 20 radiation lengths, where the Pb layers serve as passive absorbers that cause an incident particle to deposit most of its energy in form of EM showers. The scintillation layers are the active medium of the detector, where the shower produces scintillation photons which get transported by wavelength shifting fibres to the Avalanche Photo-Diodes (APDs) located at the end of the tower, as illustrated in Fig. 3.12b. Following a readout chain which is discussed in detail in Ref. [183], one finally obtains a digital signal of the deposited energy with a dynamic range from $\sim 16\,\mathrm{MeV}$ to $250\,\mathrm{GeV}$ with 14 bit precision. Several calibrations for the tower energy, the energy nonlinearity of the detector response, signal timing, signal leakage and SM temperatures need to be applied before these signals can be used in physics analyses. In addition, signals from adjacent towers are combined using clusterization algorithms to reconstruct most of the energy of a EM probe, which can deposit energy in multiple towers. The various calibrations and clusterization algorithm will be discussed in Sec. 5.

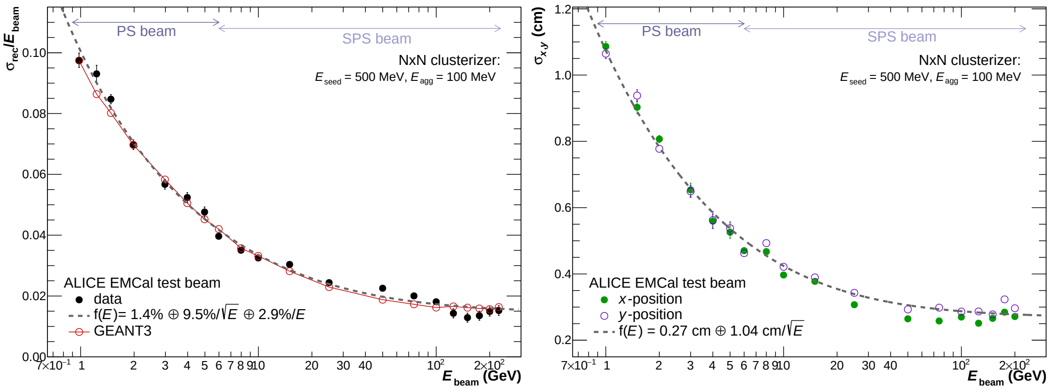

(a) energy resolution (b) position resolution

Figure 3.13: Energy and momentum resolution of the EMCal as a function of beam energy obtained from tests of a mini-module of 8 × 8 towers at the PS and SPS [184].

The response of the EMCal to incident particles has been studied in 2010 using a mini-module of 8 × 8 towers, which has been placed in particle beams of electrons, muons and hadrons from the PS and SPS. The two accelerators provide beams of well-defined energy ranging from 0.5 to 250 GeV and the position of incidence of the beam particle was determined using three MWPC which were placed in front of the mini-module. The energy resolution of the EMCal is shown in Fig. 3.13a, and is found to be better than 4 % at high energies and up to 14 % for very-low energies [184]. The detector response is well-described by MC simulations with GEANT3 [186], as indicated by the red solid line. Since the signal of the test beam was usually spread over about 8–10 towers, the signal of multiple towers can be combined to obtain the hit position from a logarithmic weighting of the tower energies. As illustrated in Fig. 3.13b, a position resolution of under 1 cm is achieved, which is smaller than the tower size of about 6 cm.

In addition to their capabilities to measure the energy and position of EM probes, the EMCal and DCal provide hardware based event triggers that are used to enhance photon and jet signals [183]. The triggers systems are based on specific hardware board – the Trigger Region Units (TRUs) – which can provide trigger decisions at Level-0 (L0) and Level-1 (L1) in ALICE, allowing a processing time of 1.2 µs and 6.5 µs, respectively. The signals from 2 × 2 towers is summed in the Front End Electronics (FEE) boards, which is referred to as a FastOR signal. At L0 level, the EMCal trigger evaluates the energy sum in a sliding 2 × 2 FastOR (4 × 4 towers) window within one TRU, which itself covers 1/3 of the area of a full-size SM. The energy sum is compared to a trigger threshold by each TRU, which subsequently provide their output to the Summary Trigger Unit (STU) that finally forms a L0 trigger decision based on the logical OR of the individual TRU output [184]. If the L0 trigger is accepted by the ALICE Central Trigger Processor (CTP) [187], the energy sum in a sliding 4 × 4 is formed again in the STU, this time across TRU boundaries. This allows to provide an improved high-energy shower L1 trigger decision over the full acceptance of the detector, which is commonly referred to as the gamma trigger. Two energy thresholds can be defined, which are referred to as the high and low threshold of the trigger. In order to enhance jet signals, the EMCal also provides a L1 trigger decision based on energy sums over larger areas of 16 × 16 or 32 × 32 towers, which are referred to as EJ2 and EJ1 depending on the used trigger threshold. While the jet triggers are not used in this work, the L0 trigger and the two L1 gamma triggers are used in this analysis to enhance the photon sample, especially for large photon energies. The trigger configuration and thresholds for the used data taking periods are discussed in Sec. 4.1.

3.2.6 *Photon Spectrometer (PHOS)*

The Photon Spectrometer (PHOS) [188] is an electromagnetic calorimeter with high-resolution and granularity, located on the opposite side of the EMCal, as indicated in Fig. 3.11. Its main physics objective are the measurement of low-p_T direct photons (see. Sec 2.3.2), as well as the study of the QGP with high-p_T neutral pions and γ-jet correlations. The detector is located at $r = 460\,\mathrm{cm}$ radial direction and consists of three full modules and one half module, covering $|\eta| < 0.125$ in pseudorapidity and 70° in azimuth. The high granularity and energy resolution is achieved using a total of 12 544 lead-tungstate ($\mathrm{PbWO_4}$ crystals) with a size of $22 \times 22\,\mathrm{mm}^2$ each, which are coupled to APDs followed by low-noise preamplifiers. In order to increase the scintillation light yield of the crystals as well as reduce electronic noise of the APD, the PHOS modules are kept at a temperature of $-25\,°\mathrm{C}$, which is stabilized with a precision of $0.1\,°\mathrm{C}$ [189]. In contrast to the EMCal, which consists of alternating layers of passive and active detector material (sampling calorimeter), the PHOS is a homogeneous calorimeter where the EM shower is created and measured in the lead-tungstate crystals of the PHOS. This technology generally allows to achieve a better energy resolution than sampling calorimeters [11], however comes with an increase cost, which is reflected in the smaller acceptance of the PHOS with respect to the EMCal.

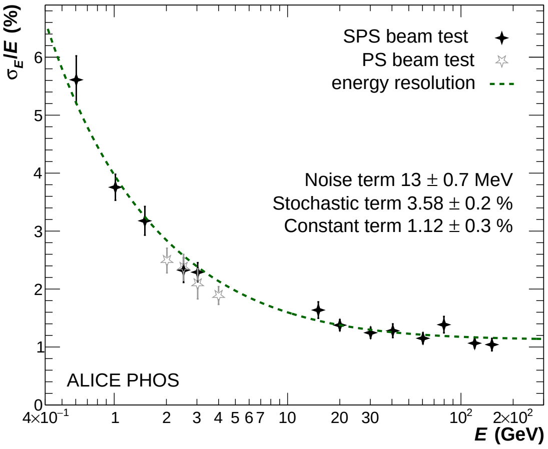

Figure 3.14: Energy resolution of the PHOS as a function of PS and SPS electron beam energy. Original figure taken from Ref. [189], adaptation from Ref. [190].

The energy resolution of the PHOS was evaluated using electron beams provided by the PS and SPS and is shown as a function of beam energy in Fig. 3.14 [189]. The test beam setup used a PHOS prototype comprised of 256 crystals, where the deposited energy of the electron is obtained by summing the signals from individual crystals in a 3×3 window. Furthermore, the mass resolution of π^0 and η mesons was studied and found to be 8.39 MeV and 17.6 MeV, respectively. The small dimensions of the crystals are in the order of the Molière radius of the scintillator (2 cm), allowing to achieve a good position resolution, which was determined to be [188]:

$$\sigma_{xy}[mm] = \sqrt{(3.26\,\sqrt{\mathrm{E[GeV]}})^2 + 0.44^2} \tag{3.3}$$

In additional to its modules used for calorimetry, the PHOS is equipped with a Charged-Particle Veto (CPV) detector, which is placed on top of currently one PHOS module [188, 191]. The detector consists of a gas-filled MWPC with cathode-pad readout, which allows to determine the position of charged particle tracks with a precision in the order of 3 mm [188]. This enables the rejection of showers from charged-particles in the PHOS module by geometrically matching the track position in the CPV to the position of EM deposits in the crystals. The installation of the CPV only 5 mm on top of the PHOS module ensures a good charged track extrapolation, which can be further improved by incorporating TPC information to more precisely determine the direction of the track.

Like the EMCal, the PHOS can provide an event trigger at L0, which is based on the energy sum in a sliding 4 × 4 crystal window within one TRU that covers 28 × 16 crystals [192]. In addition, triggers at L1 allow selecting events with energy deposits in the PHOS above three different energy thresholds to further enhance the statistics for photons at high-p_{T}.

3.2.7 *High Momentum Particle Identification Detector (HMPID)*

The High-Momentum Particle Identification Detector (HMPID) [193] is made up of 7 identical Ring Imaging Cherenkov (RICH) counters, which cover $|\eta| < 0.6$ in pseudorapidity and 57.6° in azimuth. The detector extends the hadron identification provided by the other tracking detectors in the central barrel to higher p_{T}, by exploiting the fact that charged particles traversing the radiator of the HMPID produce Cherenkov radiation. The Cherenkov angle θ_c at which this radiation is emitted depends on the velocity βc of the incident particle and can therefore be used to identify the particle species at a given momentum. The HMPID provides a separation of 3σ for Kaons from other charged particles, in particular from pions at $p_{\mathrm{T}} < 3\,\mathrm{GeV}/c$, as well as protons for $p_{\mathrm{T}} < 5\,\mathrm{GeV}/c$ [165].

3.2.8 *Zero Degree Calorimeter (ZDC)*

The Zero Degree Calorimeters (ZDCs) [194] consists of two hadronic sampling calorimeter, which are located at ± 116 m from the interaction point, as well as of two electromagnetic calorimeters which are positioned on both sides of the beampipe 7 m away from the interaction point. The detector is designed to determine the centrality of heavy-ion collisions, by measuring the energy of protons and neutrons that did not interact in the collisions, commonly referred to as spectators. The spectator neutrons carry their energy in forward direction at an angle of 0° with respect to the beampipe, and can therefore be detected in a ZDC sub-detector placed between the two beampipes. The charged protons get deflected in the magnetic elements of the LHC and can thus be distinguished from neutrons by placing a ZDC sub-detector on one side outside the beampipe. Since not all participants can get detected, e.g. when the spectators are bound into fragments, the electromagnetic calorimeters allow measuring particle production in forward direction (mainly photons from π^0 decays). The deposited energy in forward direction is related to the collision centrality and therefore further helps to distinguish central and peripheral collisions.

3.2.9 *Photon Multiplicity Detector (PMD)*

The Photon Multiplicity Detector (PMD) [195] is positioned at forward pseudorapidities of $2.3 \leq \eta \leq 3.7$ and designed to determine the multiplicity as well as the $\eta - \varphi$

distribution of photons in this region. These measurements serve as estimators for the reaction plane of the collision, which e.g. is used to when calculating the elliptic flow of final-state particles, see e.g. Ref. [196]. The large particle densities in the forward regions exclude traditional calorimetric techniques for a feasible detector design. The detector is rather based on a shower inducing converter, which is sandwiched between two highly granular gas proportional counters, where the chamber placed in front of the radiator is used as a CPV and the chamber behind the radiator is used to measure the charged particles produced in the shower.

3.2.10 *Forward Multiplicity Detector (FMD)*

The Forward Multiplicity Detector (FMD) [197] provides information on the multiplicity of charged particles in the pseudorapidity range of $-3.4 < \eta < -1.7$ and $1.7 < \eta < 5.0$ and further allows for the determination of the reaction plane. It consists of five rings of SSDs, which are located around 60 cm-320 cm from the interaction point. Its coverage not only extends the accessible pseudorapidity region for multiplicity determinations, but also its overlap with the coverage of the inner pixel layers of the ITS serve as an important cross-check.

3.2.11 *V0 detector*

The V0 detector [197] consist of two arrays of scintillation counters, which cover the pseudorapidity ranges $2.8 < \eta < 5.1$ (V0A) and $-3.7 < \eta < -1.7$ (V0C). Each array is segmented into 32 individual counters which are distributed in four rings and have a time resolution of better than 1 ns [164]. The V0A is located 329 cm away from the nominal vertex on the opposite side of the muon spectrometer and the V0C array is position in front of the hadronic absorber of the muon arm about 86 cm from the vertex. The detector serves several purposes in the experiment: Firstly, the total charge signal of the arrays is used as a minimum bias (MB) event trigger, which can be operated requiring the coincidence of a signal above a given threshold in V0A *and* V0C (V0AND or INT7), as well as a mode requiring a signal either in the SPD or in at least one of the V0 arrays (V0OR or INT1). The V0AND trigger is used as a MB trigger in this analysis for both datasets (see Sec. 4.1), and its efficiency to select inelastic pp collisions was evaluated using MC simulations and found to be around 80 % [198]. The obtained MB sample contains a non-negligible background coming from interaction of the beam with residual gas within the beampipe. This background can be further suppressed using event selection criteria based on the V0 time information, exploiting the fact that the arrival time of particles in the two arrays for beam-gas interactions differs from the arrival time of particles produced in genuine collision events (see Sec. 4.1). Based on the energy deposited in the scintillation arrays, the V0 detector furthermore provides estimates for the charged particle multiplicity and consequently centrality of a collision, where the relation between the deposited energy and multiplicity can be obtained from detailed detector simulations. Since the detector is also granular in azimuthal direction, the deposited energy as a function of azimuthal angle can be used as an experimental estimator of the reaction plane [199].

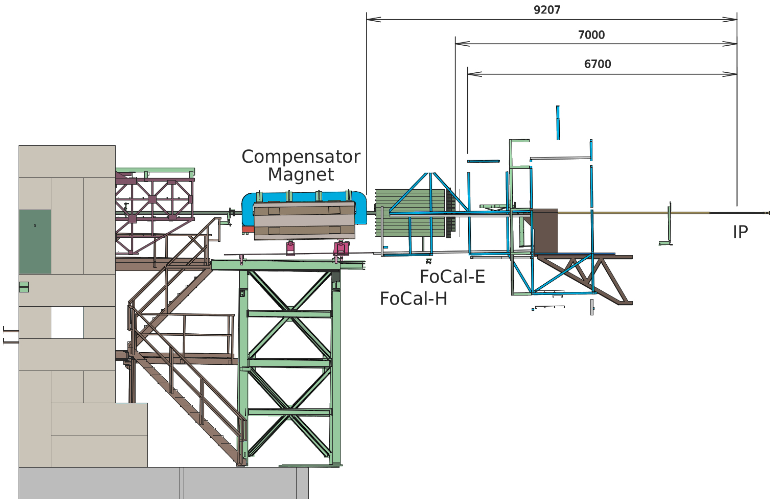

Figure 3.15: Schematic overview of the A-side of the ALICE experiment, indicating the planned position of the FoCal about 7 m away from the interaction point (IP) in front of the compensator magnet [72].

3.2.12 *T0 detector*

The T0 detector [197] consists of two arrays of Cherenkov counter, which cover a pseudorapidity range of $-3.28 \leq \eta \leq -2.97$ (T0C) and $4.61 \leq \eta \leq 4.92$ (T0A). The detector provides timing information with a precision of about 50 ps, which allows to determine the real time a collision occurred. This information provides the start time for the TOF measurement, and furthermore allows to determine the vertex position with a precision of about ± 1.5 cm. Furthermore, the T0 detector provides a wakeup signal for the TRD prior to the L0 trigger, as well as a MB event trigger which selects inelastic pp collisions with an efficiency of about 50 % [164].

3.2.13 *Forward Calorimeter (FoCal)*

The Forward Calorimeter (FoCal) is an electromagnetic- and hadronic calorimeter which was proposed in a Letter Of Intent [72] as an upgrade of the ALICE detector for data-taking in Run 4 of LHC operation (est. 2027-2029). It will be positioned at forward pseudorapidities covering $3.4 < \eta < 5.5$ over the full azimuthal angle, thus providing unique possibilities for QCD studies in the small-x regime (see Sec. 12). Its physics program is closely related to the measurement presented in this work, and performance studies for future measurements of isolated prompt photons with the FoCal will be discussed in detail in Sec. 12.

The FoCal is planned to be positioned about 7 m from the interaction point on the A-side of the experiment outside the ALICE magnet, as illustrated in Fig. 3.15. This ensures sufficient distance from the interaction point, which is required in order to compensate for the large particle densities expected for large rapidities due to the kinematic boost of the particles produced. The FoCal consists of two parts, an electromagnetic Si+W sampling calorimeter (FoCal-E), which is followed by a hadronic calorimeter (FoCal-H), a sampling hadronic calorimeter based on a spaghetti-type design where scintillation fibres are inserted into tubes of the absorber material (copper). The FoCal-E is optimized

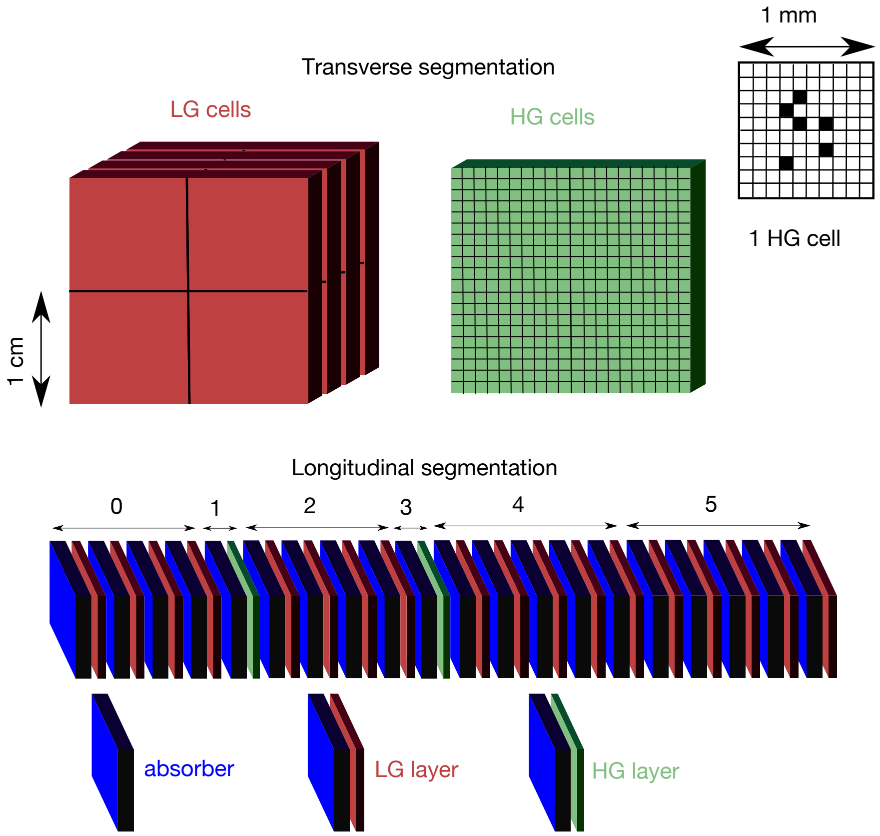

Figure 3.16: Schematic view of the longitudinal structure of the FoCal-E. The top of the figure illustrates the design of the silicon pads (LG cells) and silicon pixels (HG cells) [72].

for small shower sizes and good shower separation, motivating the use of tungsten as an absorber material which has a small Molière radius and radiation length of $R_M = 9\,\mathrm{mm}$ and $X_0 = 3.5\,\mathrm{mm}$, respectively. The large energies at forward pseudorapidities require a sufficient depth of the calorimeter to achieve a sufficiently linear response. The FoCal-E has a total depth of around $20X_0$, which corresponds to about 15–20 cm depending on the distance between the individual layers of the calorimeter. A hybrid design of silicon pads and pixels is chosen for the active material of the FoCal-E, which is illustrated in the schematic view of its longitudinal structure in Fig. 3.16. The calorimeter is designed with 18 pad layers, each having a transverse cell size of $\approx 1\,\mathrm{cm}^2 \approx R_M^2$. In addition, two additional highly-granular silicon pixel layers with a transverse size of $30\,\mu\mathrm{m}^2$ are positioned at the 5th and 10th layer, to achieve sufficient separation power for photons from π^0 decays[7]. The silicon pads and pixels can be read out individually, allowing longitudinal tracking of the EM showers evolution in addition to the measurement of its transverse profile. The current envisioned design of the FoCal-H is a sampling calorimeter where scintillation fibres are inserted into copper tubes, which serve as an absorber material, an approach known as a spaghetti-type calorimeter first prototyped by the SPACAL collaboration [200]. The final FoCal-H is envisioned to have a depth of about 1.1 m and the similar transverse dimensions as the FoCal-E of about $r = 0.45\,\mathrm{m}$.

---

[7] To put the separation power required into perspective. For a symmetric $\pi^0 \to \gamma\gamma$ decay with $\eta_{\pi^0} = 4$ and $p_{\mathrm{T}}^{\pi^0} \approx 15\,\mathrm{GeV}/c$ the separation of the two photons at a detector 7 m away from the interaction point is only 5 mm [72].

A first prototype tower of the FoCal-H has been tested at the SPS in the fall of 2021, as well as a larger prototype consisting of 9 towers at the PS in the summer of 2022[8].

Overall, the FoCal offers excellent performance for photon and π^0 measurements in the forward region in pp and p–Pb collisions, where the combination of an electromagnetic- and hadronic calorimeter enables photon isolation. The performance of the detector has been studied in detail using full detector simulation and reconstruction, where more details are discussed in Sec. 12.

3.3 ALICE ANALYSIS FRAMEWORK AND EVENT RECONSTRUCTION

This section outlines the analysis framework used in this work, which consists of a variety of software used for event reconstruction, simulation and physics analysis. Due to the complexity of the framework involved, special focus is put on aspects relevant to this work, e.g. the algorithm used to reconstruct the tracks of charged particles, which are used for photon isolation in this analysis. Sec. 3.3.2 gives an outlook for readout and event reconstruction during the ongoing Run3 of ALICE operation. While the described tools for Run3 are not used in this analysis, an overview is given due to the personal involvement in developing an analysis structure for analyses involving the EMCal within this new framework, enabling further developments for future analyses of isolated prompt photons in Run3.

3.3.1 *Run1 and Run2 – AliRoot and AliPhysics*

The ALICE collaboration maintains a central software framework based on ROOT [201], an object-oriented data analysis framework developed at CERN and written in C++. The framework is divided into AliRoot[202] and AliPhysics [203], where the former handles tasks closely related to the ALICE detector (event reconstruction, data processing, MC event generators and detector simulations) and the latter contains the code for various physics analyses that process the reconstructed collision events and compute physics observables. A record of all changes made to ALICE software is kept using the distributed version control system git [204] and regularly tagged in order to ensure reproducibility of event reconstructions and physics results. The computing power required for the various tasks performed within the ALICE software framework is provided by the Worldwide LHC Computing Grid (WLCG) [205, 206], which consists of 170 computing centres amounting to a total of over 1 million computer cores.

EVENT RECONSTRUCTION The raw signals from each individual detector are transported to the Data Acquisition (DAQ) and High Level Trigger (HLT) after receiving the ALICE Level-2 (L2) trigger signal after about 100 µs, which can either accept all L1 triggered events or apply additional event rejections. The raw data is combined to collision events in DAQ system and HLT [207], where the latter furthermore applies an online compression to reduce the data size of the TPC by about a factor of five [165]. Typical readout rates in pp and p–Pb collisions are in the order of $\mathcal{O}(10)$kHz and $\mathcal{O}(100)$kHz for MB collisions and rare triggers, respectively. For Pb–Pb collisions the

---

[8] No public reference is available for these tests yet and information about the tested modules is taken from internal communication with Constantin Loizides and personal presence during the test beam.

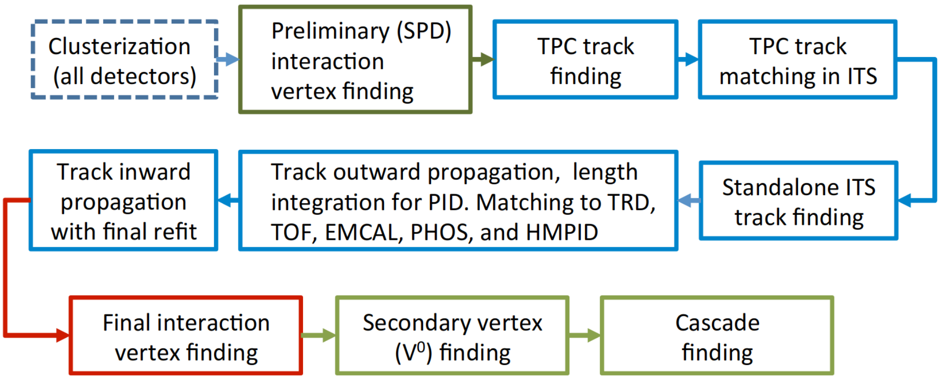

Figure 3.17: Schematic overview of vertex- and track finding in the central barrel [165].

rate is slightly lower with about 3 – 5 kHz [165]. The stored raw event data – consisting of the digitized signals of sensitive detector elements at a certain time – is not yet usable for physics analysis. It needs to be calibrated and higher-level objects such as charged particle trajectories (tracks) need to be reconstructed, which is happening "offline", i.e. after the raw data was written to storage.

The procedure used to reconstruct tracks in the central barrel is illustrated schematically in Fig. 3.17 and described in detail in Ref. [165]. The procedure begins by clusterization of all detector output, where cluster refers to a set of adjacent digits presumably generated by the same particle. A first preliminary estimate of the primary interaction vertex is obtained by using the clusters in the two innermost layers of the ITS, where the primary vertex is taken to be the point where the largest number of trajectories extrapolated from cluster pairs intersect. Next, the actual track reconstruction begins, which includes information from both ITS and TPC and consists of several track finding stages. The first stage starts from the outer wall of the TPC using the first two TPC clusters and the primary vertex as seeds for the tracking algorithm, which propagates the seeds inwards using a Kalman filter [208] approach that updates and refines the track parameters at each inward step until the inner TPC wall is reached. The thus obtained tracks from each seed can ideally contain a maximum of 159 clusters, which is given by the number of tangential pad rows in the TPC. A dedicated algorithm ensures that no pair of tracks shares more than between 25 % and 50 % of the same clusters in order to avoid multiple reconstructions of the same physical track. In addition, tracks containing less than 20 clusters and/or are missing more than 50 % of the clusters expected for a given trajectory are rejected to ensure an overall good quality of the track sample. A first mass hypothesis[9] is assigned for each rack using the specific energy loss $\mathrm{d}E/\mathrm{d}x$ in the TPC gas, which allows taking into account ionization energy losses during the tracking steps. The thus reconstructed TPC tracks are then used as the seeds for track finding in the ITS, where the propagation continues inwards using each added cluster as a new seed. This results in a variety of possible track candidates in the ITS for each TPC track, where each candidate is assigned a χ^2 value taking into account penalties for missing clusters that can occur due to dead areas in the ITS. The track candidates with the lowest χ^2 value are extrapolated to the point of closest approach to the preliminary primary vertex, which is then used as a starting point for the second stage of track propagation

---

[9] A minimum mass of $m_{\pi^\pm} \approx 139.6\,\mathrm{MeV}/c^2$ is assigned due to the ambiguity of the electron identification in the TPC.

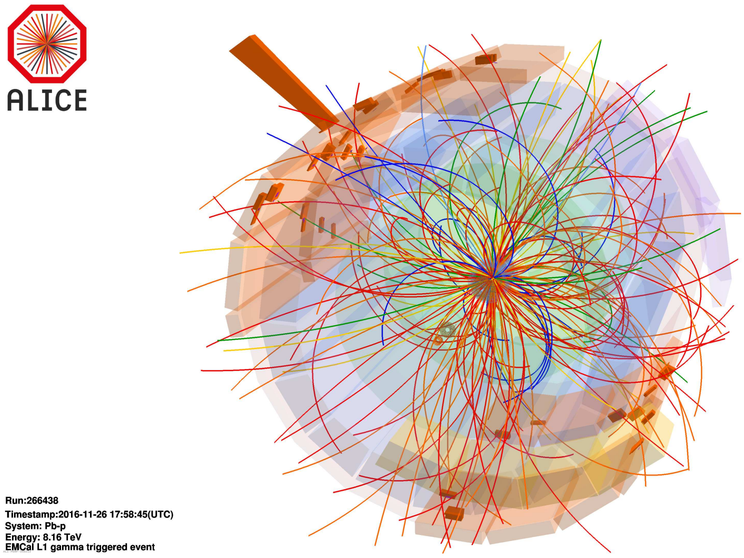

Figure 3.18: Event display of fully reconstructed exemplary p–Pb collision event at $\sqrt{s_{\mathrm{NN}}} = 8.16\,\mathrm{TeV}$ which was recorded using the L1 EMCal gamma trigger [209]. Reconstructed charged tracks are indicated as solid lines and energy deposits in the EMCal are represented by orange towers.

in outward direction. The outward propagation includes time-of-flight information from the TOF detector, which allows to verify the mass hypothesis provided by the energy loss in the TPC during the previous tracking step. Once the outer wall of the TPC is reached, a matching to hit points in the TRD and TOF is attempted before an extrapolation of the tracks to the surface of the EMCal and PHOS calorimeters, where the tracks are matched to clusters. The central barrel tracking concludes with a final track propagation step in inward direction, where the tracks found in each detector are refitted using the previously found clusters and important track parameters such as position, direction and inverse curvature are calculated. These final tracks are furthermore used to improve the preliminary determination of the primary collision vertex. The achievable transverse momentum resolution of was previously given in Fig. 3.7a for TPC as well as ITS-TPC tracks. The TPC track finding efficiency for primary particles in pp and p–Pb collisions is about 80 %. The efficiency for matching TPC to ITS tracks is above 90 % at $p_{\mathrm{T}} \approx 10\,\mathrm{GeV}/c$ [165].

After the primary collision vertex has been found, a dedicated algorithm begins the search for so-called secondary vertices which arise from the decay of long-lived particles that travel several centimetres away from the primary collision vertex before decaying, resulting in charged tracks that do not originate from the primary vertex. The algorithm selects tracks with a minimum distance of closest approach to the primary vertex of 0.5 mm (1 mm) in pp (Pb–Pb) collisions and searches for characteristic decay topologies of unlike-sign pairs of charged tracks originating from a common vertex (V^0 candidates). This allows to reconstruct e.g. decays of $K^s_0 \rightarrow \pi^+\pi^-(c\tau \approx 2.68\,\mathrm{cm})$ and $\Lambda^0 \rightarrow p\pi^-(c\tau \approx 7.89\,\mathrm{cm})$ [11], as well as the reconstruction of photons via their decay to e^+e^- pairs. Secondary tracks are not used in this analysis and the reader is referred to Ref. [165] for more details. Finally, Fig. 3.18 shows a fully reconstructed p–Pb collision event, which was recorded in 2016 at a centre-of-mass energy of $\sqrt{s_{\mathrm{NN}}} = 8.16\,\mathrm{TeV}$ using the EMCal L1 trigger [209].

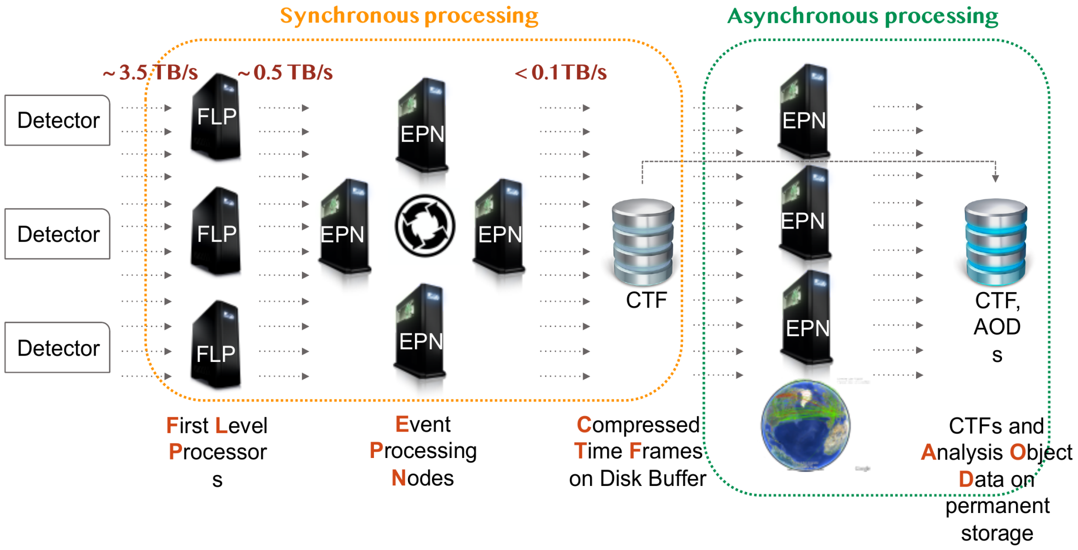

Figure 3.19: Different stages of the data reconstruction workflow in Online-Offline Computing System (O^2), which is used for ALICE data taking in Run 3 and Run 4 [217].

MC EVENT GENERATORS & DETECTOR SIMULATION The AliRoot framework provides a unified interface to several MC generators such as Pythia [77], DPMJET [210], EPOS [211] and Hijing [212], which allow generating pp, p–A and A–A collision events. Furthermore, the framework contains a full implementation of the ALICE detector geometry, including active detector material like silicon layers, drift gasses as well as support structures of the various sub-detectors. This geometry can be used with particle transport tools like GEANT3 [186], GEANT4 [213] and FLUKA [214], which track the particles propagation through the detector material and simulate various material interactions relevant in the corresponding energy regimes. The response of each sub-detector to interactions with its sensitive detector material is handled by detector specific code in the AliRoot framework, which generates so-called digits, that correspond to the raw signal of the respective detector including detector readout effects. MC datasets are commonly "anchored" to the conditions during data taking, taking e.g. into account the detector setup, calibration and used gases. More information about the AliRoot simulation framework can be found in Ref. [215]. The MC generators used in this work are outline in Sec. 4.3.

3.3.2 *Run3 and beyond – The O2 framework*

The running conditions of the LHC during Run 3, which has just started in the summer of 2022, will deliver pp, p–Pb and Pb–Pb collisions at unprecedented anticipated interaction rates of 200 kHz for pp and p–Pb collisions, as well as up to 50 kHz for Pb–Pb collisions [216]. For Pb–Pb collisions, this corresponds to a data throughput from the detector greater than 1 TB/s, which is about two orders of magnitude more than in Run 1. This drastic increase in available data enables ALICE to perform precise measurements of a variety of probes, especially those characterized by a very small signal-to-background ratio, such as heavy flavour hadrons, low-momentum quarkonia, as well as low-mass di-leptons. The increased interaction rates requires a completely revised computing system for data processing and event reconstruction, as well as new continuous read-out for the tracking detectors to avoid trigger dead time. This new system is called O^2 [216], which is designed to reduce the data volume stored to disk by reconstructing the detector synchronously with data taking in several steps, including an early calibration of the data determined by accumulated calibration parameters. Fig. 3.19 illustrates the different stages of the O^2 reconstruction workflow, which can be divided into a synchronous and asynchronous stage, where the former happens in parallel to the data taking and the latter several weeks after the data was recorded [217]. The raw data from the individual triggered- and continuous detectors arrives with about 3.5 TB/s at the First Layer Processing (FLP) nodes, which apply a suppression of detector noise (zero suppression) and divides the continuous detector data into packages called sub-time frames, which contain about 20 ms of data. These zero-compressed packages reduce the data stream to about 0.6 TB/s, which is sent to the so-called Event Processing Nodes (EPNs) for synchronous event reconstruction and calibration, as well as further compression (e.g. on-the-fly clusterization and tracking). The reconstructed data from each detector, which contains already first calibrations obtained accumulatively during the ongoing data-taking is stored in Compressed Time Frames (CTFs) at a rate of below 100 GB/s. This marks the beginning of the asynchronous stage, where refined calibrations and additional reconstruction steps are applied after about 2 to 4 weeks after the creation of the CTFs. The output of this final reconstruction step is stored in Analysis Data Objects (AODs), which are made available for physics analyses that are carried out using the new O2Physics [218] analysis framework. The computing power required for the synchronous stage is provided by 200 FLPs and 250 EPNs, whereas the asynchronous stage is shared between the EPNs and the WLCG [217].

Part II

MEASUREMENT OF ISOLATED PROMPT PHOTON PRODUCTION IN PP AND P-PB COLLISIONS AT $\sqrt{s_{\mathrm{NN}}} = 8$ AND 8.16 TEV WITH ALICE

4

DATA SETS

ALICE started data taking in 2009 with the first physics data from pp collisions at $\sqrt{s} = 0.9\,\mathrm{TeV}$. Since then the experiment has collected data in various collision systems and energies during Run 1 (2009–2013) and Run 2 (2015–2018) of LHC operation, which are summarized in Tab. 4.1. The year 2022 marked the beginning of Run 3, which began with pp collisions at unprecedented collision energies of $\sqrt{s} = 13.6\,\mathrm{TeV}$. This chapter gives a description of the data used in this thesis, with a special focus on the event- and trigger selection. In addition, the MC simulations are discussed which are needed for the efficiency and purity determination of the measurement.

Table 4.1: Overview of ALICE data taking campaign until 2022. The data used in this work is written in bold text.

	year	system	$\sqrt{s_{\mathrm{NN}}}$ (TeV)
LHC Run 1	2010	pp	0.9
		pp	7
	2011	pp	2.76
		pp	7
		Pb–Pb	2.76
	2012	**pp**	**8**
		p–Pb	5.02
Long Shutdown 1			
LHC Run 2	2015	pp	13
		pp	5.02
		Pb–Pb	5.02
	2016	pp	13
		p–Pb	5.02
		p–Pb	**8.16**
	2017	pp	13
		Xe–Xe	5.44
	2018	pp	13
		Pb–Pb	5.02
Long Shutdown 2			
	2022	pp	13.6

In this work, pp collision data at $\sqrt{s} = 8\,\mathrm{TeV}$ and p–Pb collision data at $\sqrt{s_{\mathrm{NN}}} = 8.16\,\mathrm{TeV}$ is analysed, which was recorded in 2012 and 2016, respectively. To uniquely identify datasets, ALICE follows a naming convention beginning with the year the data was recorded (e.g. 2012) and a letter indicating a so-called period. A period corresponds to roughly one month of data taking, during which ideally no significant changes of beam configuration, detector setup and triggers are introduced. Each period is further divided into so-called runs, which can last from a few minutes up to multiple hours. Each run marks a timeframe of uninterrupted data taking, where neither the LHC nor the ALICE detector systems encountered any problems. Following this naming convention, the periods analysed in this work are LHC12[a–i] for the pp collision data and LHC16[r,s] for the p–Pb collision data. For the latter, the change from period LHC16r to LHC16s marks a change of beam configuration, where in particular the direction of the colliding proton and lead beam was inverted (p–Pb to Pb–p). A full list of all runs analysed for each period is given in Sec. B. Suitable runs are chosen following extensive quality assurance work from various groups[1], ensuring that the main sub-detector

---

[1] In particular, a lot of QA for the studied datasets has been performed as part of the PhD projects from Nicolas Schmidt [190] and Daniel Mühlheim [219].

systems relevant for this work (ITS,TPC and EMCal/DCal) are working under nominal conditions.

4.1 EVENT SELECTION

Collision events suitable for physics analysis have to fulfil a variety of selection criteria which reject background events originating e.g. from beam-gas interactions and pileup. The term "pileup" refers to the fact that multiple collisions can end up in a single read-out time window of the sub-detectors, either originating from collisions within the same LHC bunch (in-bunch pileup) or collisions from a subsequent bunch (out-of-bunch pileup).

The selection begins with the so-called Physics Selection (PS), which is provided in the AliPhysics framework [203] and rejects calibration events as well as background events by applying a selection according to the timing information in V0A and V0C arrays. In addition, the correlation between clusters and tracklets in the SPD detector allows for further rejection of background and pileup events, where background events are often characterized by a low-number of tracklets and a large number of SPD clusters. This is illustrated in Fig. 4.1, which shows the number of SPD clusters in dependence of the number of SPD tracklets, where the red dotted line illustrates the applied cut of $N_{\text{cluster}} > 4 \times N_{\text{tracklet}} + 65$. Further removal of in-bunch pileup, which amounts to about 3.5 % of events, is achieved by rejecting collision events with multiple reconstructed primary vertices, where at least 3 contributing tracklets for each vertex and a separation of 8 mm are required in the SPD. Due to the SPD's large readout window of about 300 ns, this vertex requirement also helps to reduce out-of-bunch pileup. Further out-of-bunch pileup rejection is achieved with the so-called past-future protection, which uses V0 information from the surrounding 10 bunch crossings with respect to a triggered event to check for activity outside the SPD integration window.

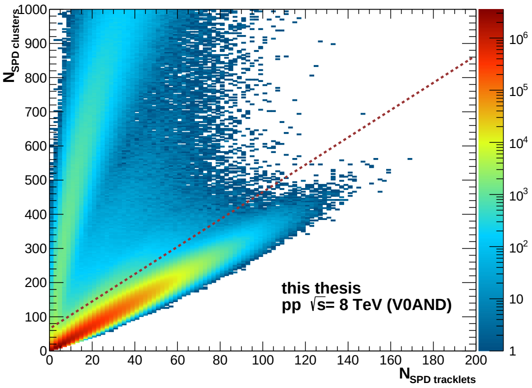

Figure 4.1: Number of SPD clusters as a function of SPD tracklets. The visible correlation can be used to suppress background events e.g. from beam-gas interactions. Events located above the red dashed line are rejected.

All events selected in this analysis have to fulfil at least a so-called minimum-bias trigger condition, which is provided by the V0 detector and requires a coincidence of a signal in both scintillation counters (V0A and V0C). The minimum bias trigger is commonly referred to as V0AND or INT7 and its efficiency to select inelastic pp collision events was evaluated using MC simulations and found to be around 80 % [198]. Furthermore, events selected for analysis are required to have a reconstructed primary collision vertex within $|z_{\text{vtx}}| < 10$ cm from the nominal interaction point, where in addition the reconstructed vertex is required to have at least one global track or SPD tracklet pointing to it. Observables presented in this work are mostly normalized with the number of inspected events $N_{\text{norm,evt}}$, which is given by

$$N_{\text{norm,evt}} = N_{\text{Y},|z_{\text{vtx}}|<10\,\text{cm}} + \frac{N_{\text{Y},|z_{\text{vtx}}|<10\,\text{cm}}}{N_{\text{Y},|z_{\text{vtx}}|<10\,\text{cm}} + N_{\text{Y},|z_{\text{vtx}}|>10\,\text{cm}}} N_{\text{Y,no vtx}}, \tag{4.1}$$

where the suffix Y denotes the studied trigger class (e.g. INT7) and $N_{\text{Y},|z_{\text{vtx}}|<10\,\text{cm}}$ ($N_{\text{Y},|z_{\text{vtx}}|>10\,\text{cm}}$) is the number of events with a reconstructed primary vertex within (outside) of $\pm 10\,\text{cm}$. The second term takes into account the events where no primary vertex could be reconstructed ($N_{\text{Y,no vtx}}$), which is scaled to include the fact that not all of those events would have had a vertex within $\pm 10\,\text{cm}$ of the nominal interaction point.

Rather than simply stating the number of collision events inspected by a certain trigger, it is more meaningful to give the integrated luminosity of a trigger sample, which is also required to convert measured invariant yields to an invariant cross-section. The integrated luminosity $\mathcal{L}_{\text{int}}$ is calculated via

$$\mathcal{L}_{\text{int}} = \int \mathcal{L} \mathrm{d}t = \frac{N_{\text{norm,evt}}}{\sigma_{\text{MB}}} \cdot \kappa_{\text{trigger}} \tag{4.2}$$

where $N_{\text{norm,evt}}$ is the number of events inspected by a given trigger, including the correction for missing primary vertices as given in Eq. 4.1. The cross section visible to the minimum bias trigger (σ_{MB}) is determined in so-called Van der Meer scans [220], which are performed by displacing the LHC beams and sweeping them transversely across each other. The cross section inspected by the INT7 trigger was found to be $\sigma_{\text{MB}}^{\text{pp}} = (55.8 \pm 1.2)\,\text{mb}$ [221] for pp collisions at $\sqrt{s} = 8\,\text{TeV}$ and $\sigma_{\text{MB}}^{\text{pPb}} = (2.09 \pm 0.04)\,\text{b}$ ($\sigma_{\text{MB}}^{\text{Pbp}} = (2.10 \pm 0.04)\,\text{b}$) [222] for p–Pb (Pb–p) collisions at $\sqrt{s_{\text{NN}}} = 8.16\,\text{TeV}$. Higher level triggers such as the EMCal gamma triggers (see also Sec. 3.2.5) require in addition the inclusion of a so-called trigger rejection factor κ_{trigger}, which quantifies the higher inspected luminosity with respect to the minimum bias trigger. The procedure to obtain these rejection factors is outlined in the following section. Finally, Tab. 4.2 summarizes the data samples analysed in this work, including the names of the used triggers, trigger thresholds, the trigger rejection factors, as well as the integrated luminosities and absolute number of collision events.

4.2 EMCAL TRIGGERED DATA

As previously discussed in Sec. 3.2.5, the EMCal provides several hardware triggers to enhance the statistics of high-p_{T} observables, such as photons and jets. In addition to the MB trigger, this analysis uses EMCal L0 and L1 triggered data, which is crucial in order to provide sufficient statistics for the measurement of photons up to $p_{\text{T}} = 80\,\text{GeV}/c$, as presented in this work. For the pp sample, the EMC7 (L0) and EGA (L1) triggers are used, which trigger on energy deposits in the EMCal above thresholds of 2 GeV and 10 GeV, respectively. In the p–Pb analysis the two L1 gamma triggers are used, which are referred to as EG2 and EG1 selecting events above a threshold of 5.5 GeV and 8.0 GeV, respectively. In order to avoid double counting, events fulfilling multiple trigger conditions are only associated with the trigger class of the trigger with the lowest threshold, thus making the individual trigger classes exclusive.

Table 4.2: Overview of the analysed data samples using different triggers in pp and p–Pb collisions, including the thresholds and rejection factors of each trigger, the integrated luminosities $\mathcal{L}_{\text{int}}$ as well as the number of inspected events $N_{\text{norm,evt}}$. All quantities are corrected for the masking of bad TRUs and the reduced trigger efficiency, as discussed in Sec. 4.4

System	Trigger	Threshold (GeV)	Trigger rejection factor (κ_{trigger})	$N_{\text{norm,evt}}$	$\mathcal{L}_{\text{int}}$ (nb^{-1})
pp	INT7	-	1	106.8×10^6	1.91
	EMC7	2.0	77.63 ± 0.05	30.3×10^6	42.14 ± 0.02
	EGA	10	$16\,493 \pm 461$	1.8×10^6	530 ± 14
p–Pb	INT7	-	1	36.9×10^6	0.018
	EG2	5.5	340 ± 7	0.48×10^6	0.078 ± 0.002
	EG2	8.0	1229 ± 27	2.39×10^6	1.41 ± 0.03

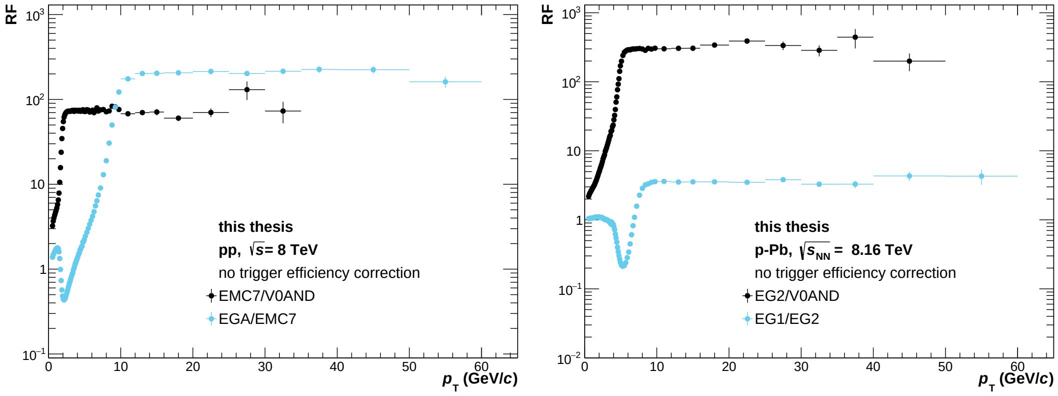

(a) pp

(b) p–Pb

Figure 4.2: Trigger rejection factor as a function of cluster p_{T} obtained using the ratios of EMCal cluster spectra measured in the different trigger samples with respect to the MB baseline in pp collisions (left) and p–Pb collisions (right).

The usage of these hardware triggers greatly enhances the inspected integrated luminosity and number of reconstructed EMCal clusters. This enhancement of the trigger with respect to the MB baseline (which has a known cross section) has to be quantified and is expressed in the so-called trigger rejection factor κ_{trigger}, which can then be used to correctly calculate $\mathcal{L}_{\text{int}}$ of the respective trigger according to Eq. 4.2. The rejection factor is determined by studying event-normalized EMCal cluster spectra (see. Sec. 5[2]) in each trigger class and calculating the ratio to the MB baseline. This ratio should become constant at high-p_{T} and correspond to the trigger rejection factor under the assumption that the cluster reconstruction efficiency itself is not modified by the respective trigger. These cluster spectra ratios are shown in Fig. 4.2 for the pp and p–Pb datasets, showing a clear rise corresponding to the turn-on of the EMCal triggers followed by a constant plateau where the trigger has become fully efficient. The turn-on

---

[2] Only minimal selections are applied for the trigger rejection factor determination, i.e. $\sigma^2 > 0.1$, $F_+ < 0.97$ and cluster time selections.

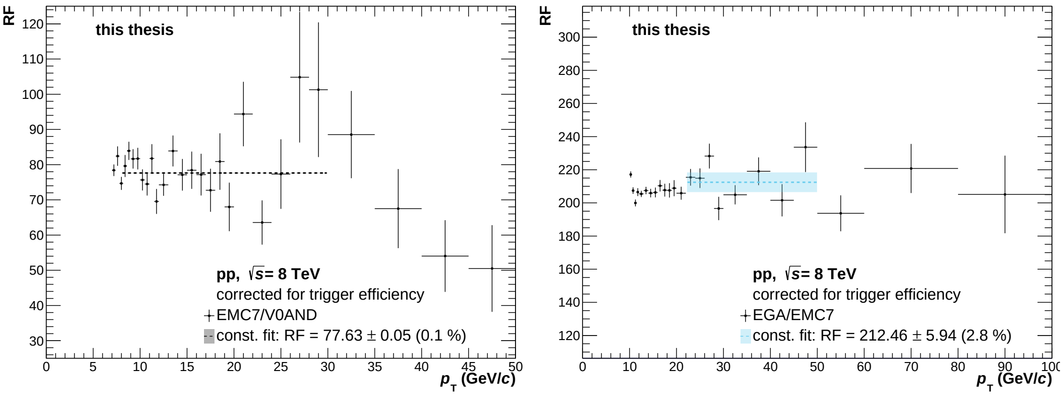

(a) pp EMC7/MB (b) pp EGA/EMC7

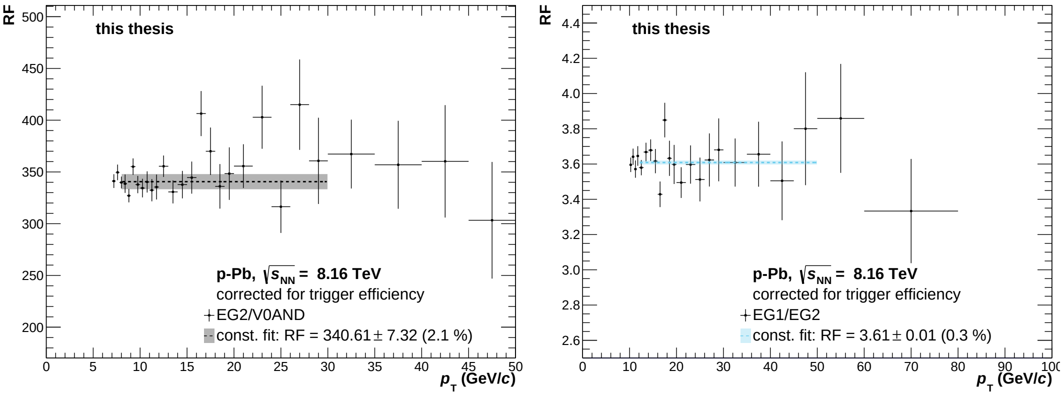

(c) p–Pb EG2/MB (d) p–Pb EG1/EG2

Figure 4.3: Trigger rejection factor as a function of cluster p_T obtained using the ratios of EMCal cluster spectra measured in the different trigger samples with respect to the MB baseline in pp collisions (top) and p–Pb collisions (bottom). The clusters spectra used to obtain the ratios are corrected for the respective trigger efficiencies, as discussed in Sec. 4.3.1.

region is in-line with the trigger threshold given in Tab. 4.2 where however a smearing is observed that originates from the conversion of analogue trigger signals to energy values which can vary for each trigger channel depending on their calibration. Due to the limited statistics of the MB baseline at high-p_T, the ratios are calculated in steps always with respect to the next lowest trigger rather than calculating the ratio of each EMCal trigger to the MB baseline directly.

As stated earlier, the determination of the trigger rejection factor relies on the respective triggers being fully efficient in the high-p_T plateau region. However, detailed studies of the trigger efficiency using MC simulations showed that the EMCal gamma triggers do not become fully efficient at high-p_T and that kinematic biases may lead to residual slopes in the plateau region. These studies and findings are discussed in detail in Sec. 4.3.1. In order to account for these biases and inefficiencies, the cluster spectra are first corrected using the trigger efficiencies obtained from simulations of the trigger response in MC. The ratios of the thus corrected cluster spectra are shown in Fig. 4.3 for pp and p–Pb collision data, respectively. All ratios are compatible with a constant fit above the respective trigger threshold, where the fit is indicated by a dashed line in the respective panel. The fitted constant is then used to extract the trigger rejection

Table 4.3: Overview of the MC productions used in this analysis. For each of them a JIRA ticket is given, which can be used to access additional information at `https://alice.its.cern.ch/jira/browse/ALIROOT-XXXX`.

system	name	configuration	Ticket
pp	**LHC16c2(_plus)**	Pythia **Jet-Jet MC** anchored to `LHC12`	6181
	LHC17g5a1	Pythia **Gamma-Jet MC** anchored to `LHC12` with γ in EMCal acc.	7267
	LHC17g5b	Pythia **Jet-Jet MC** anchored to `LHC12` with $p_{\mathrm{T},\gamma} > 3.5\,\mathrm{GeV}/c$ in EMCal acc.	7267
	LHC17g5c	Pythia **Jet-Jet MC** anchored to `LHC12` with $p_{\mathrm{T},\gamma} > 7\,\mathrm{GeV}/c$ in EMCal acc.	7267
p-Pb	**LHC18b9**	Pythia **Jet-Jet MC** + EPOS anchored to `LHC16rs` data	7690
	LHC21d2b_[1,2]	Pythia **Jet-Jet MC** + DPMJET anchored to `LHC16rs` data with $p_{\mathrm{T},\gamma} > 3.5\,\mathrm{GeV}/c$ in EMCal/DCal acc.	8668
	LHC21d2c_[1,2]	Pythia **Jet-Jet MC** + DPMJET anchored to `LHC16rs` data with $p_{\mathrm{T},\gamma} > 7\,\mathrm{GeV}/c$ in EMCal/DCal acc.	8668
	LHC21d2a_[1,2]	Pythia **Gamma-Jet MC** + DPMJET anchored to `LHC16rs` with γ in EMCal/DCal acc.	8668

factor, which is given in the respective legend. The uncertainty of the rejection factor is estimated by several variations of the p_{T}-interval used for the fit and indicated by a shaded band.

The final trigger rejection factors and their uncertainties are listed in Tab. 4.2, highlighting the EMCal triggers ability to enhance the cluster sample by up to three orders of magnitude.

4.3 MONTE CARLO SIMULATIONS

Multiple MC event generators are used in various steps of this analysis to obtain corrections such as the acceptance, efficiency and the purity of the measurement. For all these use cases, it is essential that the different generators not only accurately describe the physics processes of interest (e.g. $\mathrm{gq} \rightarrow \gamma\mathrm{q}$) and overall event properties such as multiplicities, but also that the material interactions of the produced particles and the response of the ALICE sub-detectors are accurately modelled using additional programs. This section gives an overview of the MC generators used to simulate pp and p–Pb collisions, as well as the program needed to further propagate the produced particles through the ALICE detector. Tab. 4.3 gives a full list of MC productions used in this work, giving also their reference names following ALICE naming convention as well as links to detailed internal documentation for each production. The ability of these programs to adequately describe the data taking conditions is demonstrated throughout this work for various observables that are essential to this analysis.

PYTHIA The general purpose MC event generator PYTHIA 8[77] is widely used in high-energy particle physics and aims to accurately describe the properties of a high-energy collision. It provides event-by-event collision data which is obtained by a combination of perturbative calculations and phenomenological models which can be tuned by $\mathcal{O}(100)$ parameters to match experimental data. The hard scattering of two partons from incoming hadrons is described by calculating the matrix elements of $2 \rightarrow 2$ and $2 \rightarrow 3$ scatterings using LO perturbation theory, where additional fixed-order radiative correction can be incorporated via additional matrix elements. Scatterings between additional partons, which are known as Multi Parton Interactions (MPIs), are also modelled in a dedicated framework. The hard scattering is followed by Initial-State Radiation (ISR) and Final-State Radiation (FSR) which incorporate the emission of additional particles by the incoming- and outgoing partons of the scattering, respectively. The non-perturbative process of hadronisation is incorporated in Pythia through various models, where the default is based on the Lund string fragmentation model [223, 224] that iteratively models the probability that the "strings" spanned by self-interacting gluons between q-$\bar{\text{q}}$ pairs break into hadronic states.

In this work, two types of Pythia MCs are used to describe pp collisions, which are commonly referred to as Jet-Jet (JJ) and Gamma-Jet (GJ) MCs and distinguish between the choice of scattering processes considered in the Pythia simulation. The JJ MC production represent an inclusive sample of hard QCD scatterings, including $2 \rightarrow 2(3)$ scatterings involving light quarks and gluons as well as heavy flavour production. These productions also include various soft QCD processes and a phase-space cut is applied to avoid singularities of perturbative QCD for low momentum transfers [77]. To increase the number of high-Q scatterings, which become increasingly rare with increasing p_{T}, the simulation is performed in several bins given by the momentum transfer of the scattering process ($p_{\mathrm{T}}^{\mathrm{hard}}$). The obtained cross sections in each $p_{\mathrm{T}}^{\mathrm{hard}}$-bin are then weighted according to:

$$\omega_{\mathrm{JJ}} = \frac{\sigma_{\mathrm{evt}}}{N_{\mathrm{trials}}/N_{\mathrm{gen.}}}, \tag{4.3}$$

where N_{trials} is the number of trials needed by Pythia to satisfy the $p_{\mathrm{T}}^{\mathrm{hard}}$ condition, σ_{evt} is the overall cross section of the simulated processes and $N_{\mathrm{gen.}}$ is the number of generated events. In addition, two special JJ productions are used for each dataset to enhance the presence of electromagnetic probes in the EMCal acceptance. This is achieved by requiring for each event at least one photon above a given p_{T}-threshold within the acceptance of the EMCal detector. These productions will be referred to as JJlow and JJhigh in the following, depending on the chosen p_{T}-threshold.

The additional GJ MCs are used in this work to estimate the efficiency and purity of the measurement and only consider $2 \rightarrow 2$ LO scattering processes that contain one or two photons in the final state. In addition to these prompt photons produced directly in the hard scattering, additional photons are produced in parton showers and hadronic decays. As for the JJ MCs, the generation is performed in several $p_{\mathrm{T}}^{\mathrm{hard}}$-bins and weighted accordingly.

DPMJET By default, the Pythia productions outlined in the previous section describe hard-scattering processes in pp collisions. The analysed p–Pb collision data requires additional simulations to describe the bulk of soft particles produced in nuclear collisions. The DPMJet-III [210] event generator is based on the phenomenological Dual Parton model and allows describing soft multiparticle production in hadron-hadron,

hadron-nucleus and nucleus-nucleus collisions, as well as various photon scatterings involving hadrons and nuclei. Nuclear cross sections are calculated within the Gribov-Glauber formalism following the algorithms of DIAGEN[225]. The output from DPMJET is combined on an event-by-event basis with the simulated hard JJ and GJ processes from PYTHIA in a procedure known as embedding. This allows to obtain a production which contains all the hard processes of interest while at the same time adequately describing the bulk of soft particles expected in nuclear collisions.

EPOS LHC The EPOS LHC [211] MC event generator allows to simulate both heavy-ion collisions and cosmic ray showers in air. It has been tuned using early LHC data of pp, p–Pb and Pb–Pb collisions, and gives a good description of soft particle production with transverse momenta from $p_{\mathrm{T}} = 0$ up to a few GeV/c. The scattering of two protons (and nuclei) are described by multiple scatterings of partons within Gribov-Regge theory [226], and the hadronization of the outgoing partons is described using a string based collective hadronization model that takes into account the local densities observed in the early stages of the collision.

GEANT In order to track and describe the propagation of the particles produced by an event generator through the active- and passive material of ALICE, the GEANT3 [186] program is used for each production. The framework allows the implementation of so-called volumes with various material properties, which have been centrally implemented for the ALICE detector in the ALIROOT framework. The material interaction of the produced particles are simulated in steps along their trajectory using MC methods, where effects such as various energy loss mechanisms, pair creation and scatterings are taken into account according to the corresponding theoretical models.

4.3.1 *Trigger Simulation*

As mentioned in Sec. 4.2, the EMCal-γ triggers do not become fully efficient, even above the trigger threshold. In other words, not every particle with an energy above the trigger threshold will cause the trigger to fire, e.g. due to the presence of FastOR channels (2×2 towers summed in FEE) that are not working correctly (high noise or no signal) and reduce the trigger acceptance. Such effects need to be accounted for in the used MCs productions in order to accurately describe the signal efficiency (see Sec. 7), as well as to determine the rejection factor free of potential underlying kinematic biases (see below). The trigger response is simulated in MC using the so-called trigger maker [184], which mimics the L0 and L1 EMCal triggers by inspecting the trigger patches from the FEE, following the trigger logic outlined in Sec. 3.2.5. The trigger thresholds, patch sizes and sliding windows are adapted for each production to match the conditions of the triggers during data taking in order to achieve an optimal description of the trigger in MC. The simulation includes an implementation of random detector noise, which was assumed to have a width of 50 MeV for each FastOR channel [184]. Furthermore, FastOR channels that were found to not work properly in data (either because of large detector noise or no signal at all) are masked and not included in the simulated trigger

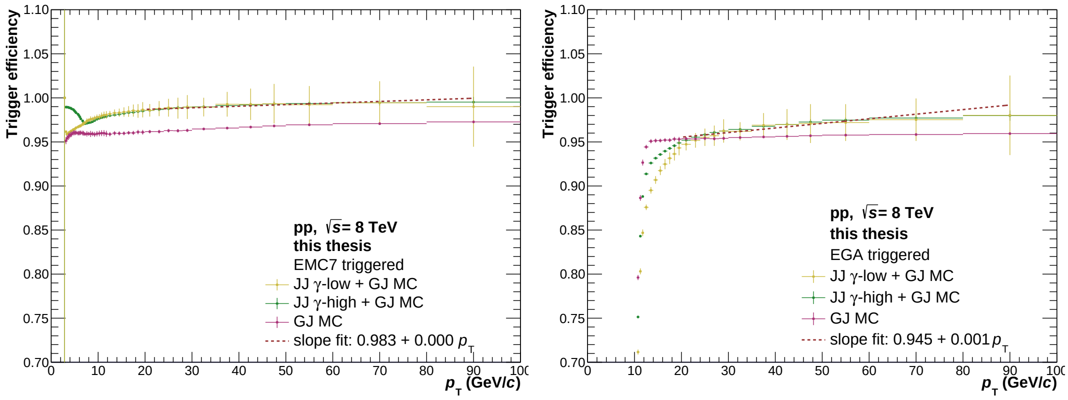

(a) EMC7 trigger (b) EGA trigger

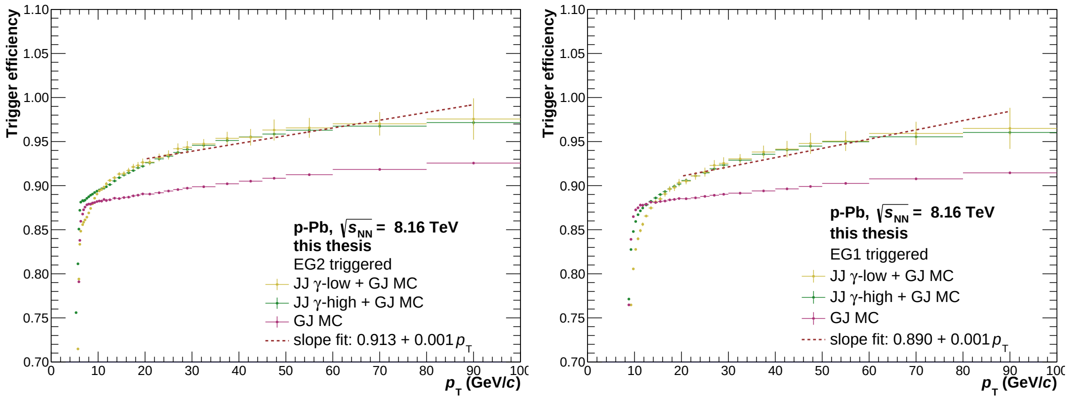

(c) EG2 trigger (d) EG1 trigger

Figure 4.4: Trigger efficiencies as a function of EMCal cluster p_T for different MC samples and triggers. The samples specified as "JJ γ-low(high)+GJ" are obtained as the sum of the respective JJ and GJ, where weights according to the absolute cross sections obtained from PYTHIA are applied.

decision[3]. In cases where a large fraction of FastORs of a given TRU were found to be bad, all FastORs belonging to that TRU were masked instead (1/3 of full-sized SM).

Fig. 4.4 shows the efficiencies of the respective EMCal triggers used in this work. The efficiencies are obtained as the ratio of the cluster spectra obtained using a simulation of the specified trigger with respect to a common baseline where no trigger simulation is used. Multiple MC samples have been used, which are represented by different colours and denoted in the legend. The steep trigger turn-on at low-p_T is clearly visible for all triggers close to the expected trigger thresholds, except for the EMC7 L0 trigger, where the efficiency could not be evaluated down to $p_T \sim 2\,\text{GeV}$ due to the smallest p_T^{hard}-bin starting at $5\,\text{GeV}/c$, as well as other technical limitations. Above the respective trigger thresholds, it can be clearly observed that:

1. The trigger efficiency does not reach unity, even for the highest covered transverse momenta.

---

[3] I would like to use this opportunity to in particular thank Gustavo Conesa Balbastre and Markus Fasel, who spend a lot of time providing and improving the maskings used in this work, as well as for Markus' patience explaining all the details of the trigger maker.

2. The efficiency is not constant, but rather displays a slope. Furthermore, the steepness of the slope depends on the used MC sample.

3. The trigger efficiency is smaller in p–Pb collisions at $\sqrt{s_{\mathrm{NN}}} = 8.16\,\mathrm{TeV}$ than in the pp data at $\sqrt{s} = 8\,\mathrm{TeV}$.

The first point can be explained considering the fact that masked FastORs effectively result in a loss of trigger acceptance. In cases were all FastORs of a given TRU are masked, this corresponds to an acceptance loss of 1/3 of a full-sized SM per TRU, which is not visible to the L0 and L1 triggers. The differences between the efficiencies observed for the pp and p–Pb collision data is expected, as the number of masked FastORs was found to have increased between 2012 (pp) and 2016 (p–Pb) due to degradation of the EMCal hardware. Considering these trigger acceptance losses, one would expect a constant efficiency above the trigger thresholds. However, a clear slope is visible above the trigger threshold, indicating the presence of kinematic biases. These biases can be explained considering the activity in the vicinity of the respective cluster: For example, for a cluster which is part of a jet, i.e. a collimated spray of particles depositing their energy within a given radius (e.g. $R = 0.4$) in the calorimeter, a loss of trigger acceptance may cause some, but not all the energy of the given jet to be "invisible" to the trigger. More explicitly, even if a cluster falls within an area of masked FastORs, the trigger condition may still be fulfilled by energy depositions of particles in the cluster's vicinity. This becomes increasingly probable with increasing cluster energy, resulting in the observed slope. These conclusions are supported when looking at the efficiencies obtained using only the GJ MC, where one overall finds smaller slopes than observed for the samples that include the JJ MCs: As discussed later in Sec. 6, the clusters found in the prompt photon dominated GJ MC sample tend to be isolated, i.e. the clusters do not have many particles in their vicinity. This reduces the aforementioned kinematic bias but also results in an overall smaller trigger efficiency for prompt photons.

The trigger efficiency was found to be only about 88 % for the signal dominated GJ p–Pb collision samples just above the respective trigger thresholds. This showcases that corrections for trigger inefficiencies and potential biases are important to obtain an unbiased prompt photon cross section. Furthermore, Fig. 4.4 showcases that the trigger efficiency depends on the event activity in the vicinity of the trigger particle, where in particular isolated objects like prompt photons (GJ) tend to be less affected than clusters produced by particles that are part of a jet. Therefore, two corrections related to the trigger efficiency are employed in this analysis:

1. The event normalized cluster spectra in data are corrected using the trigger efficiency obtained from the weighted sum of GJ and JJ MCs *before* calculating the trigger rejection factors, as outlined in Sec. 4.2. In particular, the GJ+JJ γ-low are used for $p_{\mathrm{T}} < 25\,\mathrm{GeV}/c$, whereas GJ+JJ γ-high are used above this threshold, in order to reduce any potential bias arising from the photon p_{T} requirements indicated in Tab. 4.3 for the respective productions.

2. The trigger efficiency is also implicitly contained in the signal efficiency determination discussed in Sec. 7, which is performed using the GJ MC.

The purpose of the first correction is two-fold: It not only corrects for the overall trigger acceptance loss due to misbehaving FastOR channels, but furthermore removes residual slopes that can bias the constant fit in the plateau region. The obtained rejection factors can therefore be interpreted as the rejection power of fully efficient EMCal triggers. This has the additional advantage that the normalized cluster spectra ratios become a more robust proxy for the rejection power of the EMCal triggers, suppressing potential biases arising from the used cluster selection criteria. The dependence of the trigger efficiency on the studied observable is instead now contained within the signal efficiency, which is determined using the GJ MC and discussed in Sec. 7.

5

PHOTON RECONSTRUCTION

The reconstruction of photons produced in a collision is at the core of this measurement and is achieved using the EMCal (DCal) detector, which was introduced in Sec. 3.2.5, including important metrics such as its acceptance, as well as its energy and position resolution. While the PHOS detector offers a higher granularity compared to the EMCal, the EMCal is chosen in this analysis due to its large acceptance, which is about 6 times larger than that of the PHOS and thus allows to significantly increase the statistics of the cluster sample. In p–Pb collisions, the addition of the DCal allows to extend the geometrical coverage even further.

This section gives an overview how energy deposits in the calorimeter are combined to clusters, how the energy deposits (and clusters) are calibrated and what selections are applied to select photon candidates from the obtained cluster sample. Finally, important additions to the MC production are discussed, which ensure an accurate description of the cluster shape – a quantity essential for the purity determination in this measurement. Throughout this section, the term "cell" is used instead of "tower", which is commonly used to denote the analysis-level object rather than the physical tower of the detector.

5.1 EMCAL CLUSTERIZATION

A particle hitting the EMCal produces an electromagnetic shower, which can spread its energy over multiple adjacent cells. In order to reconstruct as much of the energy of the original particle as possible, it is therefore essential to not only consider the energy of individual cells but rather to combine the energy deposits of multiple cells into clusters using dedicated algorithms. While ideally a cluster is produced by a single particle, depending on the granularity of the detector, multiple particles can contribute to a single cluster. A common example of multiple particles contributing to the same cluster are photons from highly energetic $\pi^0 \rightarrow \gamma\gamma$ and $\eta \rightarrow \gamma\gamma$ decays, where with increasing meson energy the opening angle between the photons decreases until the photons can no longer be distinguished as two individual clusters but rather appear as one single *merged cluster*.

Several clusterization algorithms are implemented for the EMCal within the AliRoot framework, each differing in its photon reconstruction efficiency and capability to separate individual clusters from photon pairs produced in meson decays [184]. The two most frequently used algorithms in physics analyses are illustrated schematically in Fig. 5.1. The so-called V1 clusterizer begins with the cell of the highest energy deposition in a given region, requiring that its energy is above the seed threshold E_{seed}. Cells in the vicinity of the seed cell that share a common side with cells already in the cluster are aggregated to the cluster, as long as the energy of each cell is above the aggregation threshold E_{agg}. The V2 clusterizer modifies the procedure outlined above by requiring in addition that the energy of each cell aggregated to the cluster is smaller than energy of the previously aggregated cell. The effect of this requirement is illustrated schematically in Fig. 5.1: The energy deposition of adjacent cells in one dimension is shown in yellow, where two peaks are visible which could originate from two overlapping energy deposits

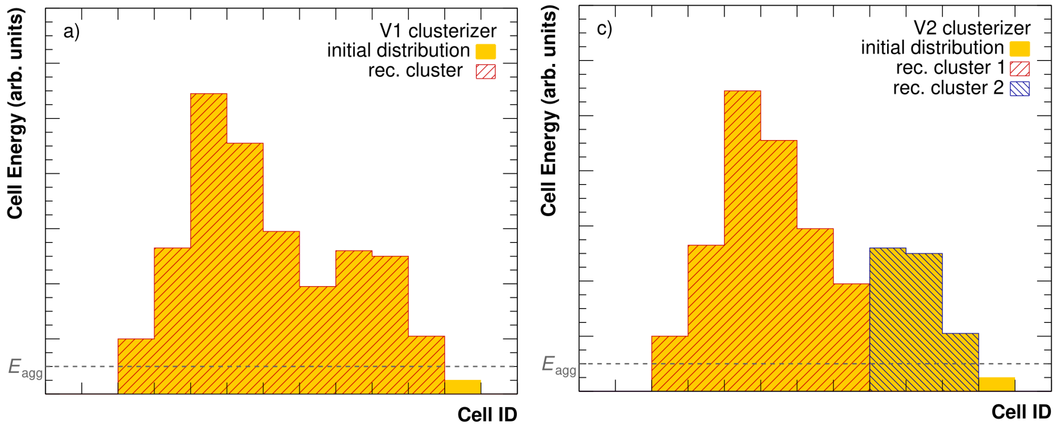

(a) V1 clusterizer (b) V2 clusterizer

Figure 5.1: Schematic overview of the two most used clusterisation algorithms, which are illustrated in one dimension of simplicity. The energy deposition in individual EMCal cells is illustrated in yellow, while the red and blue shaded areas illustrate which cells are considered by the algorithm to belong to the same cluster [184].

produced by two particles (e.g. two photons). While the V1 clusterizer favours to aggregate all cells to a single big cluster (red shaded area), the additional requirement imposed by the V2 algorithm causes the aggregation of cells into two clusters, where the splitting is caused by the local maximum on the right side of the distribution. The ability of each algorithm to split shower overlaps into its individual contributions has been quantified in Ref. [184] using simulations of $\pi^0 \to \gamma\gamma$ decays, where one finds that the V1 algorithm begins to aggregate the contributions of both photons into a single cluster around π^0 transverse momenta of $\approx 6\,\mathrm{GeV}/c$, whereas the same is observed for the V2 algorithm at higher p_T of $\approx 10\,\mathrm{GeV}/c$.

In this work the V1 algorithm is used with $E_\mathrm{seed} = 500\,\mathrm{MeV}$ and $E_\mathrm{agg} = 100\,\mathrm{MeV}$, where the thresholds are chosen to reduce the sensitivity of the algorithm to detector noise. The choice of the V1 algorithm instead of the V2 algorithm is motivated by the purity determination of the measurement, which is discussed in Sec. 8 and heavily relies on the discrimination of signal and background using the shape of a cluster. In essence, by also considering large clusters with multiple local maxima for physics analysis, the cluster shape contains more information about whether the cluster originated from a single particle (e.g. from prompt photon signal) or shower overlaps (e.g. from $\pi^0 \to \gamma\gamma$ decay background).

The total cluster energy E_clus is calculated as the sum of the individual cell energies c via

$$E_\mathrm{clus} = \sum_i E_i^\mathrm{cell}, \tag{5.1}$$

where the index i denotes a cell belonging to the given cluster. The position of a cluster (x, y, z) is calculated as the weighted average of the contributing cell positions (x_i, y_i, z_i) as:

$$\langle x \rangle = \sum_i \frac{w_i x_i}{w_\mathrm{tot}}, \quad \langle y \rangle = \sum_i \frac{w_i y_i}{w_\mathrm{tot}}, \quad \langle z \rangle = \sum_i \frac{w_i z_i}{w_\mathrm{tot}} \quad \text{with} \quad w_\mathrm{tot} = \sum_i w_i, \tag{5.2}$$

where the weights w_i are calculated from the cell energies via

$$w_i = \max(0, w_{\max} + \ln(E_i^{\text{cell}}/E_{\text{clus}})) \quad \text{with} \quad w_{\max} = 4.5. \tag{5.3}$$

5.2 EMCAL CALIBRATIONS AND CORRECTIONS

Before the EMCal data can be used for physics analysis, several calibrations and corrections need to be applied on the cell- and cluster level that e.g. account for a nonlinear response of the electronics to energy signals or calibrate the timing information provided by individual cells. An overview of these calibrations is given in the following sections, where the used procedures are described in further detail in Ref. [184]. The discussed cell-level corrections are applied before the clusterization procedure outlined in the previous section, whereas corrections on cluster level are naturally applied after the clusterization is completed.

5.2.1 *Bad channel maps*

Some cells of the calorimeter may malfunction during data taking and give an improper response to energy depositions, either producing a noisy signal or no signal at all, resulting in a discontinuous energy spectrum. These cells are referred to as *bad channels* and have to be masked and excluded from clusterization and subsequent analysis. Bad channels can e.g. be the result of a broken FEE card, which can be switched off and replaced at the next available opportunity for physical access to the EMCal detector.

In order to identify bad channels, the distribution of hits per cell and the mean energy distribution are considered, using the assumption that these distributions should be similar for all cells within statistical uncertainties. However, due to material interactions of particles traversing the detector, the average number of hits in a cell positioned behind the support structure of the TRD can be significantly lower than for other cells, which has to be accounted for. This is achieved by applying scaling factors for the hit distribution, which are obtained as the ratio of the average number of hits of all cells belonging to the same column/row in η and ϕ with respect to the average calculated for all EMCal cells. After the scaling procedure, the energy- and scaled hit distribution of each cell is compared to the Gaussian fit of the respective distributions from all cells, and cells with distributions deviating by more than $\pm 5\sigma$ from the expected mean are masked as bad channels. In addition, the timing information of each cell is considered to identify noisy cells firing at random times and mask them accordingly. The masking procedure is repeated iteratively, improving the parametrization of the average number of hits expected for each channel by excluding the bad channels found in the previous step.

Fig. 5.2 shows map of the cells masked as "good" (green) and "bad" (red) as a function of cell indices in η-ϕ space for exemplary run ranges in the pp and p–Pb datasets. Bad channel maps are commonly identified in blocks of runs rather than for each run individually to ensure a sufficient sample size, where the block size is chosen taking into account changes in the bad channel map over time. In the pp collision data recorded in 2012, about 3 % of all cells were masked as bad, amounting to about 380 bad cells of the 11 520 total EMCal cells. In the p–Pb collision data, which was recorded in 2016 and includes the DCal, the fraction of bad channels increased to about 6 %. This

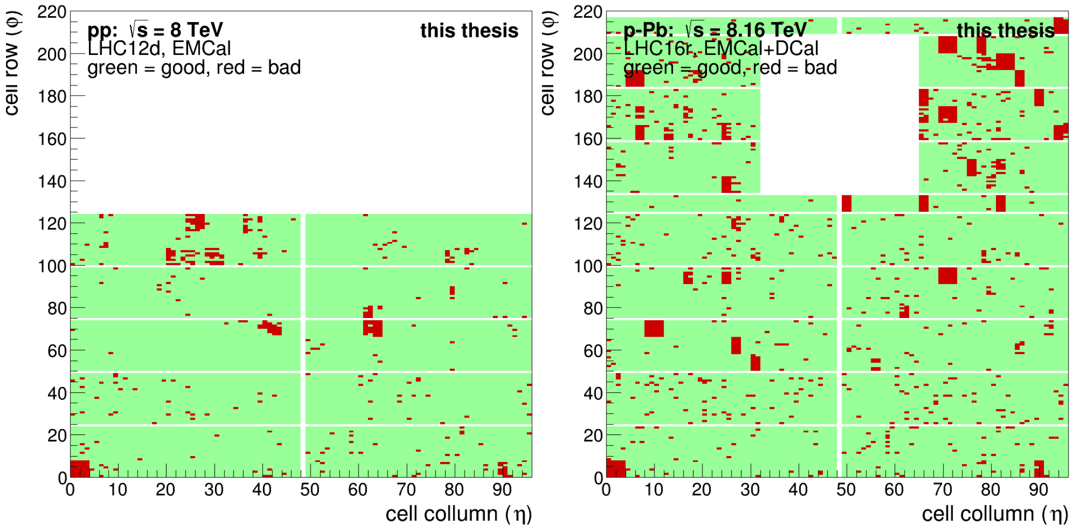

(a) pp

(b) p–Pb

Figure 5.2: Overview of EMCal channels marked as bad (red) in pp and p–Pb collisions at $\sqrt{s_{\mathrm{NN}}}$ = 8 TeV and 8.16 TeV. The bad channel determination procedure is outlined in the text and the shown bad channels are taken from an exemplary run range during the data taking periods given in the respective legends. The pp collision data (left) was taken during LHC Run 1 and consequently no DCal is yet present.

increase can be mainly attributed to the inclusion of the DCal, which has an overall larger fraction of bad channels than the EMCal, as well as a degradation of the hardware over time. The number of bad channels is taken into account in the efficiency correction of the measurement, where in particular the same bad channel masking is applied to cells from the MC production.

5.2.2 *Time calibration*

The average timing resolution of a cell with an energy above 2 GeV is below 3 ns, which is smaller than the LHC bunch spacing of 25 ns [184]. The EMCal signals are sampled at 10 MHz about every 100 ns. This is different from the LHC clock speed, resulting in 4 possible shifts of the registered cell times with respect to the triggered bunch crossing time of 0 ns. In addition, the signal propagation through the EMCal cables leads to a constant offset of about 600 ns, resulting in a total shift of the triggered bunch registered by a cell between about 600 ns and 700 ns. The time offset for each cell is determined in a calibration procedure on a run-by-run basis and the stored timing information is shifted accordingly. The mean of the calibrated cell times was found to deviate no more than about 0.8 ns from the triggered bunch crossing time, illustrating accuracy of the calibration procedure[184].

5.2.3 *Temperature calibration*

As discussed in Sec. 3.2.5, the EMCal scintillation light signal is measured using APDs positioned at the end of each tower. The gain of these APDs depends linearly on the ambient temperature and therefore has to be calibrated accordingly to ensure a uniform response. This is achieved using temperature sensors which are positioned close to the APDs in various locations, as well as a dedicated Light-Emitting Diode (LED) system, which allows to provide a light pulse of known intensity lasting several nanoseconds [184]. The intensity of the LED pulse is determined using a dedicated readout hardware and the obtained signal is referred to as the LED monitoring signal. The APD response for various temperatures is then obtained using dedicated calibration events, which contain the generated LED pulses rather than collision data. The calibration factors are obtained by comparing the measured signal in each cell to the LED monitoring signal as a function of ambient temperature, where all cells are calibrated to their response at a given reference temperature. The average temperature is about 20 °C and 24.5 °C for DCal and EMCal modules, respectively, where temperature variations of up to 1.2 °C for the former and 4 °C for the latter are observed. The obtained correction factors are given in Ref. [184] and were found to not exceed 5 % for most cells.

5.2.4 *Energy calibration and nonlinearity*

Precise knowledge of the energy response of a calorimeter to incoming particles is crucial, and therefore the relationship between reconstructed energy and true energy of an incoming particle is commonly studied in controlled environments that provide beams of particles with known energies. For the EMCal, these studies were performed in dedicated test beam setups [227] at the Proton Synchrotron (PS) and Super Proton Synchrotron (SPS). The setup consists of 8×8 EMCal cells, which were placed in electron and hadron beams with energies ranging from 750 MeV up to 230 GeV. In addition, a set of three MWPC was placed in front of EMCal prototype to provide a position reference of incoming particles in x and y. The energy response of the EMCal prototype to electron beams is shown in Fig. 5.3, where the ratio of reconstructed and beam energy ($E_{\text{rec.}}/E_{\text{beam}}$) is given as a function of the reconstructed energy. The ranges indicated at the top of the figure illustrate which energy ranges could be accessed by the test setup at the PS and SPS, respectively. While the energy response of the detector is roughly linear for low energies ($E_{\text{rec.}} \lesssim 10$ GeV), a non-linear response is observed for larger energies. Such a non-linear response is common for most calorimeters, and for the EMCal arises due to the signal shapers on the FEE cards, effects due to the shower hit position not being in the centre of a cell, as well as energy losses due to material interactions in front of the EMCal. The nonlinear response arising due to the signal shaper in the FEE card was studied using a pulse generator in the laboratory, which could be used to parametrize the FEE response for various pulse amplitudes using a 6th order polynomial. In particular, it was found that the buffer size of the shaper results in some part of the signal to be lost, which can

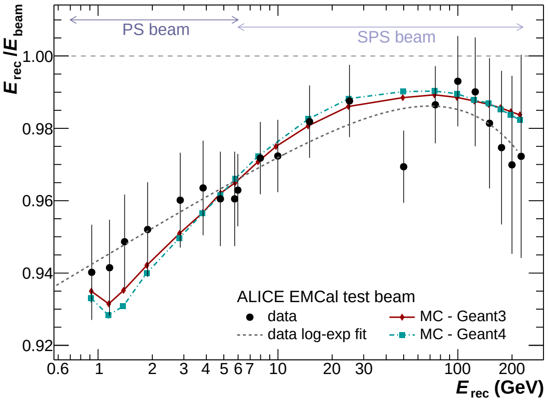

Figure 5.3: Energy response of the EMCal calorimeter to electrons obtained using a test beam setup [227] at the PS and SPS. Figure taken from Ref. [184].

amount to up 30 GeV being missed for incident particles with energies of about 160 GeV. The obtained parametrization is applied as a correction to the cell energies and amounts to a correction of up to 6 % [184], and is already included in Fig. 5.3. The remaining nonlinearity is parametrized using a fit of the ratio shown in the figure, which is applied to the reconstructed energy on cluster level, amount to a correction of 1 % to 6 %. This nonlinearity is well described by MC simulations using an implementation of the test beam setup in GEANT3 and GEANT4, as illustrated by the magenta and red curves in the figure.

After the nonlinearity of the energy response is determined, the absolute energy scale of each cell needs to be studied and corrected, with the goal of achieving a uniform energy response of each cell to a signal of well-defined energy. This calibration is performed for each cell using $\pi^0 \rightarrow \gamma\gamma$ decays in LHC collision data: The invariant mass of π^0 candidates $m_{\gamma\gamma}$ is obtained for all cluster pairs in a given event via

$$m_{\gamma\gamma} = \sqrt{2E_{\gamma,1}E_{\gamma,2}(1 - \cos\theta_{12})}, \tag{5.4}$$

where $E_{\gamma,1,2}$ are the energies of the respective clusters and θ is the opening angle between the two photons. In addition, at least one cluster is required to contain the cell which should be calibrated at its centroid in order to establish a connection between the reconstructed mass and respective cell energy. The thus obtained invariant mass distribution for each cell exhibits a peak originating from $\pi^0 \rightarrow \gamma\gamma$ decays, which is then fitted with a Gaussian to obtain the reconstructed π^0 mass $\mu^{\pi^0}_{\text{rec}}$ given by the mean of the Gaussian. The calibration factor c_i of cell i is calculated via

$$c_i = \left(\frac{M^{\text{PDG}}_{\pi^0}}{\mu^{\pi^0}_{\text{rec}}}\right)^n, \tag{5.5}$$

where $M^{\text{PDG}}_{\pi^0}$ is the nominal π^0 mass and the exponent $n = 1.5$ was found to show a faster convergence of the iterative calibration procedure [184]. In addition, constant correction factors are applied depending on the cell position to account for the expected modification of π^0 mass position due to material interactions. The calibration of the absolute energy scale for each cell is on average about 6 % to 8 %. Remaining mis-calibration, i.e. deviations from the expected π^0 mass, are found to be less than 1 % [184].

The good agreement between data and MC on a percent level for the energy response of the EMCal was illustrated in Fig. 5.3 for the test beam setup. However, during actual data taking at LHC Point 2, there is more material present in front of the EMCal, where in particular a lot of photon conversions occur within the TRD and TOF, which are placed directly in front of the EMCal. While this material is taken into account in the determination of the absolute energy scale in data, it may lead to disagreements between data and MC depending on the accuracy of the material implementation in GEANT. This necessitates an additional correction, which is commonly referred to as the *MC cluster energy fine-tuning*. Like the determination of the absolute energy scale, the procedure is based on the $\pi^0 \rightarrow \gamma\gamma$ decay as a reference, which is reconstructed in data and MC using Eq. 5.4. However, rather than calculating the invariant mass for cluster pairs in the EMCal, one photon is reconstructed using the so-called Photon Conversion Method (PCM) which allows reconstructing photons which converted in the ITS and TPC via the produced electron/positron tracks. This hybrid PCM-EMC

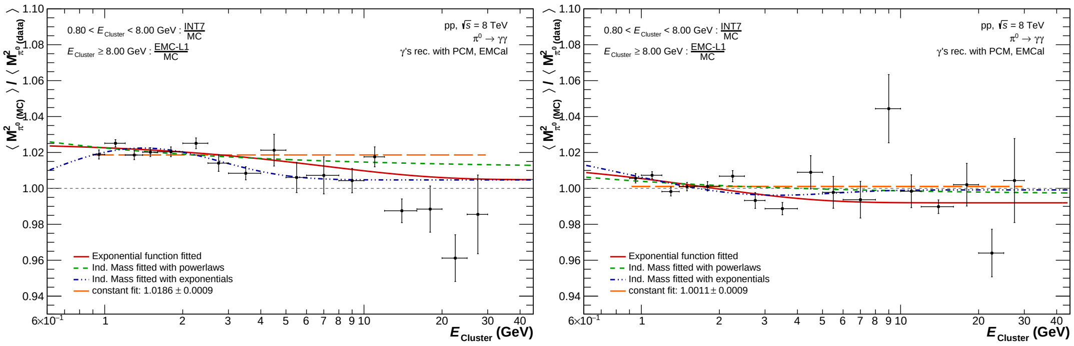

(a) before correction (b) after correction

Figure 5.4: Ratio of π^0 squared invariant mass positions in data with respect to MC for pp collisions at $\sqrt{s} = 8\,\text{TeV}$ before (left) and after (right) the MC cluster energy fine-tuning is applied. The π^0 candidates are reconstructed using a PCM-EMC hybrid approach, as outlined in the text. The differences between data and MC visible on the left are fitted using an exponential function, which is then used to correct the cluster energy E_{clus} in MC. Figure courtesy of Joshua König.

approach profits from the good momentum resolution of the tracking detectors and avoids cluster merging, which was outlined in Sec. 5.1 and starts to shift the invariant mass position for $p_{\text{T}}^{\pi^0} \gtrsim 6\,\text{GeV}/c$ when photon pairs begin to be reconstructed as a single cluster. The invariant mass distribution exhibits a peak around the nominal π^0 mass, which is fitted using a Gaussian in slices of cluster energy, where in addition exponential tails on each side accounting for electron bremsstrahlung and shower overlaps. The mean of the Gaussian is then used to obtain the measured π^0 mass $M_{\pi^0(\text{data,MC})}$ in data and MC, respectively. Fig. 5.4a shows the ratio of the squared invariant π^0 masses $M^2_{\pi^0(\text{MC,data})}$ reconstructed in MC and data, respectively, before application of the MC fine-tuning correction. A difference of up to about 2 % is observed, which is parametrized as a function of cluster energy using an exponential function. Due to the proportionality of the squared invariant mass to the cluster energy (see Eq. 5.4), the obtained parametrization can then be used as a correction for the cluster energy in MC. Fig. 5.4b shows the same ratio of data and MC after the correction is applied, where an excellent agreement between data and MC on a per-mille level is observed. This agreement is essential for an accurate determination of the efficiency of the measurement and the effect of any residual mis-calibration is included in the evaluation of the systematic uncertainties discussed in Sec. 9.

5.3 CLUSTER SELECTION AND PHOTON IDENTIFICATION

After all steps outlined in the previous sections, one obtains a sample of calibrated EMCal and DCal clusters. In order to select clusters for this analysis, several selection criteria are applied which ensure the overall quality of the cluster sample and furthermore aim to identify clusters originating from (prompt) photons. An overview of these selection criteria is given in Tab. 5.1. Each selection is discussed in detail in the following sections, where Sec. 5.3.1 discusses selections ensuring the overall quality of the sample, and Sec. 5.3.2 and Sec. 5.3.3 discuss the cluster shape and track matching procedure, respectively, which are used to identify photon cluster candidates.

Clusterization	
detector	EMCal (pp) and EMCal+DCal (p–Pb)
algorithm	V1
minimum seed energy E_{seed}	500 MeV
minimum cell energy E_{agg}	100 MeV
cell time t_{cell}	$-500\,\text{ns} \leq t_{\text{cell}} \leq 500\,\text{ns}$
Acceptance	
pseudorapidity	$\eta < 0.67$
azimuth angle	$1.4 < \varphi < 3.28$ (EMCal)
	$4.57 < \varphi < 5.70$ for $0.23 < \lvert\eta\rvert < 0.67$ (DCal)
	$5.58 < \varphi < 5.70$ for $\lvert\eta\rvert < 0.67$ (DCal)
Cluster quality and photon identification	
minimum cluster energy	$E_{\text{cluster}} > 0.7$ GeV
cluster time	-30 ns $\leq t_{\text{cluster}} \leq 35$ ns
minimum number of $N^{\text{cells}}_{\text{cluster}}$	≥ 2
number of local maxima (NLM)	NLM≤ 2
min. distance to bad channel	≥ 2
shape parameter σ^2_{long}	$0.1 \leq \sigma^2_{\text{long}} \leq 0.3$
Cluster–prim. track matching	$\lvert\Delta\eta\rvert \leq 0.05$
	$\lvert\Delta\phi\rvert \leq 0.05$
	with additional $E_{\text{clus}}/p_{\text{track}} > 1.75$ veto
exotics removal	$F_{+} < 0.97$

Table 5.1: Overview of EMCal/DCal cluster selection and photon identification used in this analysis. The purpose of each selection is elaborated in the text.

5.3.1 *General cluster selection*

After clusterization of cells using the V1 algorithm with $E_{\text{seed}} > 500\,\text{MeV}$ and $E_{\text{agg}} > 100\,\text{MeV}$ (see Sec. 5.1), each cluster is required to have an energy E_{clus} exceeding 700 MeV. This selection removes contaminations from the energy loss E_{MIP} of Minimum Ionizing Particles (MIPs), which was determined to be about 236 MeV using a 6 GeV muon beam in the test beam setup [184]. It furthermore reduces the sensitivity to the chosen seed and aggregation thresholds of the clusterizer. In addition, each cluster is

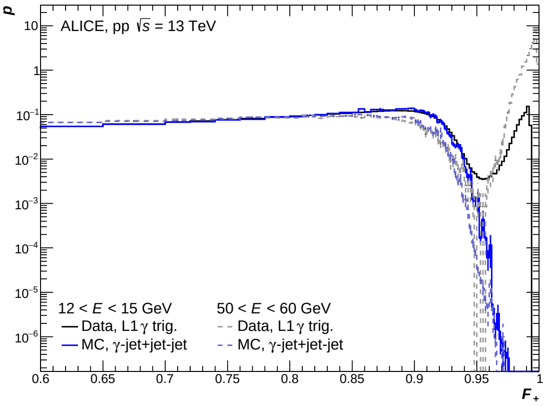

Figure 5.5: Exoticity F_{+} for data and MC shown in two exemplary cluster energy ranges [184].

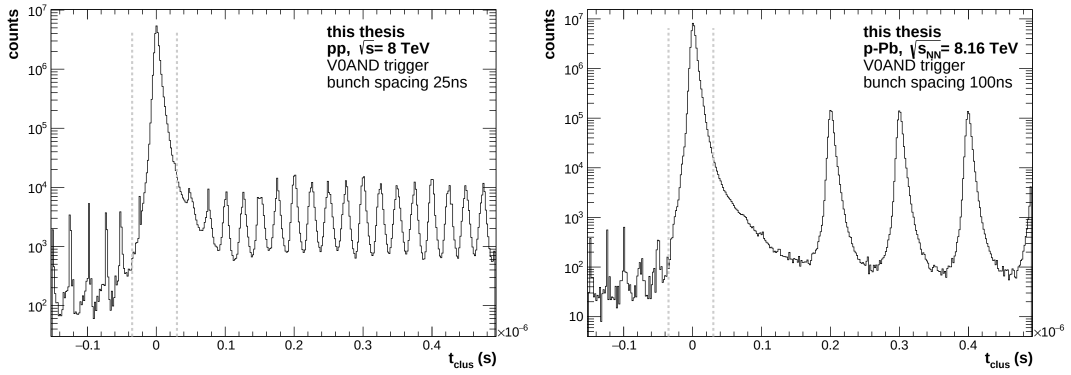

(a) pp

(b) p–Pb

Figure 5.6: Time signal t_{clus} of the leading cell in each cluster, shown for the pp (left) and p–Pb sample. The imposed selection of $-35\,\text{ns} < t_{\text{clus}} < 30\,\text{ns}$ is indicated by grey solid lines and removes out-of-bunch contributions from subsequent bunch crossings. The bunch spacing used for LHC operation is given in the respective legend.

required to consist of at least 2 cells, which removes contributions of neutrons hitting the APDs, which tend to produce an energy deposits in a single cell. Such contributions are referred to as *exotics*, and are further suppressed by removing clusters where the leading cell contains more than 97 % of the total cluster energy. The exoticity $F_+ = 1 - E_+/E_{\text{cell}}^{\text{max}}$ is shown in Fig. 5.5 for data and MC, motivating the used cut of $F_+ < 0.97$: While the distribution in MC shows a clear decrease above $F_+ \gtrsim 0.9$, a clear peak is observed in data for $F_+ \gtrsim 0.95$, which is attributed to exotic clusters. This peak is absent in MC, where signals from neutrons hitting the APDs are not simulated.

While no strict timing requirements are imposed for the individual cells entering the clusterisation ($|t_{\text{cell}}| < 500\,\text{ns}$), a requirement on the cluster time, which is given by the time signal in the leading cell of a cluster, ensures the reduction of out-of-bunch pileup. This is illustrated in Fig. 5.6, which shows the cluster time t_{clus} in pp and p–Pb collisions at $\sqrt{s_{\text{NN}}} = 8\,\text{TeV}$ and 8.16 TeV, respectively. Following the main peak centred around $t_{\text{clus}} \approx 0\,\text{ns}$, one observes multiple small contributions from subsequent bunch crossings. The time difference of each bunch crossing is given by the bunch spacing used for LHC operation, which was 25 ns and 100 ns in the pp and p–Pb sample, respectively. The imposed selection of $-35\,\text{ns} < t_{\text{clus}} < 30\,\text{ns}$ is indicated in grey dashed lines, selecting the main bunch crossing and removing out-of-bunch pileup.

5.3.2 *The shower shape*

The energy distribution within a given cluster contains important information about a clusters origin, which is important to identify prompt photon clusters and furthermore to determine the purity of the isolated photon sample, as discussed in Sec. 8. The shape of the energy distribution in a cluster, often referred to as the *shower shape*, can be described by an ellipse, which is calculated using the energy distribution along the η and φ direction. In particular, the distributions are represented by a covariance matrix

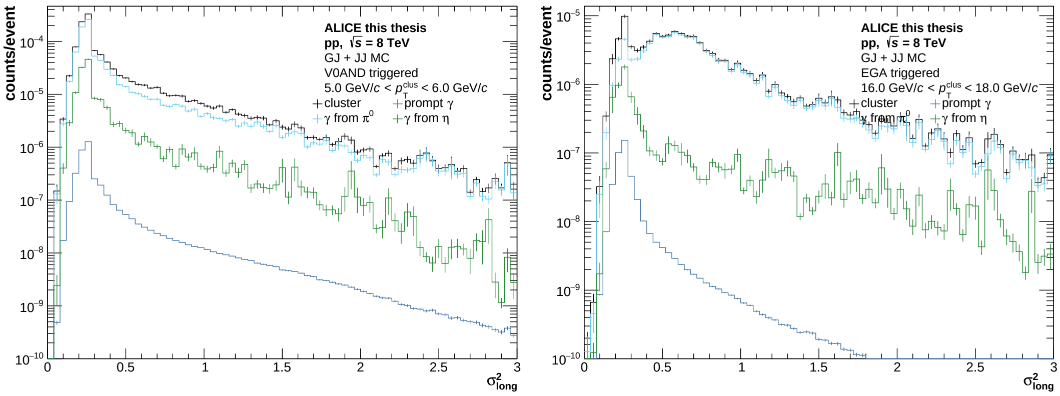

(a) low cluster p_{T} (b) high cluster p_{T}

Figure 5.7: Long axis σ^2_{long} of the cluster shape ellipse shown for two exemplary cluster p_{T} ranges for MC productions of pp collisions at $\sqrt{s} = 8\,\text{TeV}$. The cluster shape is shown for contributions from different photon sources, showcasing the discrimination power of the cluster shape.

with terms $\sigma^2_{\varphi\varphi}$, $\sigma^2_{\eta\eta}$ and $\sigma^2_{\varphi\eta}$, which are calculated using the relative η and φ directions with respect to the leading cell via:

$$\sigma^2_{\alpha\beta} = \sum_i \frac{w_i \alpha_i \beta_i}{w_{\text{tot}}} - \sum_i \frac{w_i \alpha_i}{w_{\text{tot}}} \sum_i \frac{w_i \beta_i}{w_{\text{tot}}} \tag{5.6}$$

where α_i and β_i are the cell indices in η or φ direction and the weights w_i and w_{tot} are given in Eq. 5.3. The long and short axis of the ellipse can then be calculated from the covariance matrix via:

$$\sigma^2_{\text{long}} = 0.5 \cdot \left(\sigma^2_{\varphi\varphi} + \sigma^2_{\eta\eta}\right) + \sqrt{0.25 \cdot \left(\sigma^2_{\varphi\varphi} - \sigma^2_{\eta\eta}\right)^2 + \sigma^2_{\eta\varphi}} \tag{5.7}$$

$$\sigma^2_{\text{short}} = 0.5 \cdot \left(\sigma^2_{\varphi\varphi} + \sigma^2_{\eta\eta}\right) - \sqrt{0.25 \cdot \left(\sigma^2_{\varphi\varphi} - \sigma^2_{\eta\eta}\right)^2 + \sigma^2_{\eta\varphi}}. \tag{5.8}$$

The discriminatory power of the cluster shape is illustrated in Fig. 5.7, which shows the σ^2_{long} distribution in MC for the pp collision sample in two exemplary cluster p_{T} intervals. The MC sample is obtained by adding the GJ and JJ MC with weights according to the cross sections given by Pythia, which allows to illustrate the origin of clusters for signal and background processes. A clear photon peak is visible around $\sigma^2_{\text{long}} \approx 0.25$, which is dominantly produced by photons from $\pi^0 \rightarrow \gamma\gamma$ decays. Similarly, sub-dominant contributions of photons from $\eta \rightarrow \gamma\gamma$ decays as well as prompt photons tend to produce narrow showers with $\sigma^2_{\text{long}} \approx 0.25$. Important differences arise for large photon p_{T} above about $10\,\text{GeV}/c$, which is illustrated in Fig. 5.7b: A second peak around $\sigma^2_{\text{long}} \approx 0.7$ is observed, which originates from $\pi^0 \rightarrow \gamma\gamma$ decays with small opening angles, resulting in a reconstruction of both photons in a single elongated merged cluster. The same effect becomes increasingly relevant for the η meson at photon p_{T} above $20\,\text{GeV}/c$, where in particular about 90 % of clusters from $\eta \rightarrow \gamma\gamma$ decays are found to be merged for a meson p_{T} of about $40\,\text{GeV}/c$ [184]. Most importantly, cluster merging is not relevant for prompt photons, which tend to produce narrow clusters independent of the cluster p_{T}. This allows to suppress photons from π^0 and η decays by imposing a shower shape selection

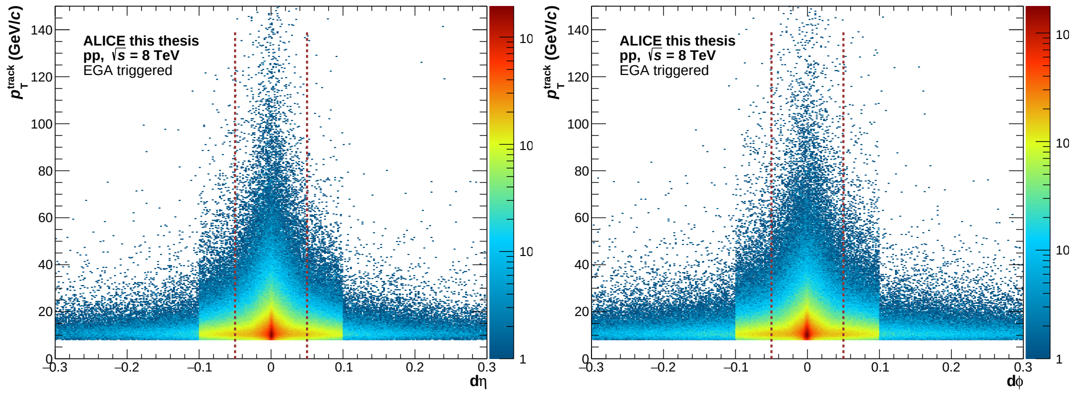

(a) $\Delta\eta_{\text{track-cluster}}$ (b) $\Delta\phi_{\text{track-cluster}}$

Figure 5.8: Distance $\Delta\eta$ (left) and $\Delta\phi$ (right) between charged tracks and EMCal clusters in pseudorapidity and azimuth, respectively. The distance is calculated after propagation of the tracks measured in ITS and TPC to the EMCal surface, taking into account the expected energy loss of charged particles when traversing the TRD and TOF as well as the curvature of tracks due to the magnetic field. The red dashed lines indicate the $\Delta\eta$ and $\Delta\phi$ requirement imposed for this analysis to reject clusters originating from charged particles.

of $\sigma^2_{\text{long}} \leq 0.3$. Furthermore, a low threshold of $\sigma^2_{\text{long}} \geq 0.1$ is chosen to suppress residual contributions of exotics in the sample. In order to ensure that the calculated cluster shape is not affected by bad channels (see. Sec. 5.2.1), the centroid of each cluster is required to be at least two cells away from a bad channel. Finally, each cluster is required to consist of at most two local maxima, which helps to suppress shower overlaps from multiple particles. The ability of the MC to describe the shower shape in data has been studied in detail and is discussed in Sec. 5.4.

5.3.3 *Cluster-track matching*

While the EMCal is designed to measure electromagnetic showers from electrons and photons, also other charged particles can deposit part of their energy in the EMCal via ionization or nuclear interactions. In order to reject clusters originating from charged particles, the information from the tracking detectors can be used in a procedure commonly known as *cluster-track matching*: In this procedure, charged tracks reconstructed in ITS and TPC are extrapolated to the EMCal surface, where in particular a radial distance of 450 cm from the beam axis is used, which corresponds to the average depth of the energy deposition. The extrapolation is first performed in steps of 20 cm, taking into account the expected energy loss due interaction with detector material, mainly in the TOF and TRD. In addition, the extrapolation takes into account the curvature of the charged track due to the magnetic field. For every cluster-track pair the distance $\Delta\phi$ and $\Delta\eta$ is calculated, where an additional improved extrapolation with a step size of 5 cm is performed for tracks with an angular distance smaller than 0.2 rad [184]. The thus obtained $\Delta\eta$ and $\Delta\phi$ distributions are illustrated in Fig. 5.8 for pp collisions at $\sqrt{s} = 8$ TeV. The distributions are shown as a function of the transverse momentum of the track ($p_{\mathrm{T}}^{\mathrm{track}}$), where one finds a wider distribution in ϕ due to the orientation of the magnetic field. In this analysis, a requirement of $\Delta\eta < 0.05$ and $\Delta\phi < 0.05$ is imposed for all cluster-track pairs, rejecting clusters where a track is found within the given distance thresholds. The requirement is illustrated as red dashed lines in the figure, and is rather strict with respect to the selections used in other analyses involving photons, such as e.g. the measurement of neutral mesons [54]. This stricter selection is motivated by the charged isolation requirement introduced in Sec. 6, where it was found that insufficient rejection of clusters with associated tracks lead to structures in the charged isolation energy, which are correlated to the photon energy and mainly originating from early photon conversions.

In order to avoid accidental fake cluster-track matches, the ratio $E_{\mathrm{clus}}/p_{\mathrm{track}}$ of the cluster energy with respect to the track momentum is considered. In particular, the requirement $E_{\mathrm{clus}}/p_{\mathrm{track}} < 1.75$ is imposed, allowing to reject cluster-track matches where the track carried significantly lower momentum with respect to the cluster energy. This requirement becomes especially relevant for large cluster energies above 10 GeV, and the exact threshold was determined using studies of the photon reconstruction efficiency and purity, as discussed in Ref. [184]. The $E_{\mathrm{clus}}/p_{\mathrm{track}}$ distribution is shown in an exemplary cluster p_{T} bin for pp data and MC in Fig. 5.9. The distribution shows a clear peak around one from charged particles depositing almost their full energy in a cluster (mainly electrons), as well as a significant tail for large $E_{\mathrm{clus}}/p_{\mathrm{track}}$ values. This is well described by the MC, which was obtained using the weighted sum of the GJ and JJ MC. The $E_{\mathrm{clus}}/p_{\mathrm{track}}$ veto of 1.75 is indicated as a red dashed line.

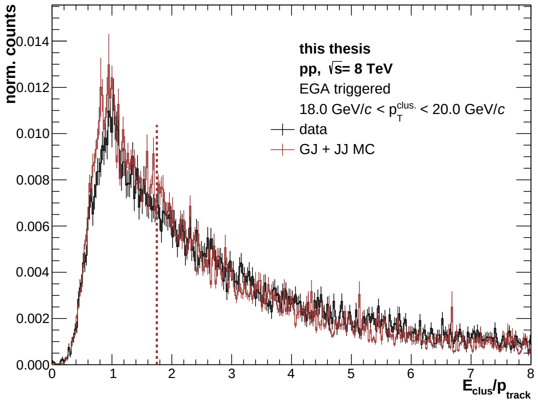

Figure 5.9: Ratio of cluster energy E_{clus} and track momentum p_{track} for matched cluster-track pairs, shown for pp collision data and the corresponding MC in an exemplary cluster p_{T} bin. Each distribution is normalized to its integral in order to allow for a comparison of the shape. The imposed veto of $E_{\mathrm{clus}}/p_{\mathrm{track}} < 1.75$ is indicated by a red dashed line and is used to suppress fake cluster-track matches.

5.4 CROSS-TALK EMULATION

The shower shape, as discussed in Sec. 5.3.2, is a crucial observable in this measurement, where it is not only used to help identify photon clusters but furthermore essential in the determination of the purity of the measurement (see. Sec. 8). It is therefore important that the shower shape is well described by the used MC productions, which enter the efficiency and purity determination of the measurement. Tests in the laboratory revealed an effect known as *cross talk*, i.e. a signal in one channel can induce a signal in a different channel belonging to the same so-called T-card [184]. The T-card is an adaptor which connects the preamplifiers of 2 × 8 adjacent towers via a ribbon cable to the FEE cards. The laboratory studies demonstrated that the cross-talk between channels is of random nature and mainly arises due to the used ribbon cables. This causes modifications in the energy and time distribution of adjacent and consequently also modifies the shape of the reconstructed cluster. Since these cross-talk effects are not considered in the MC

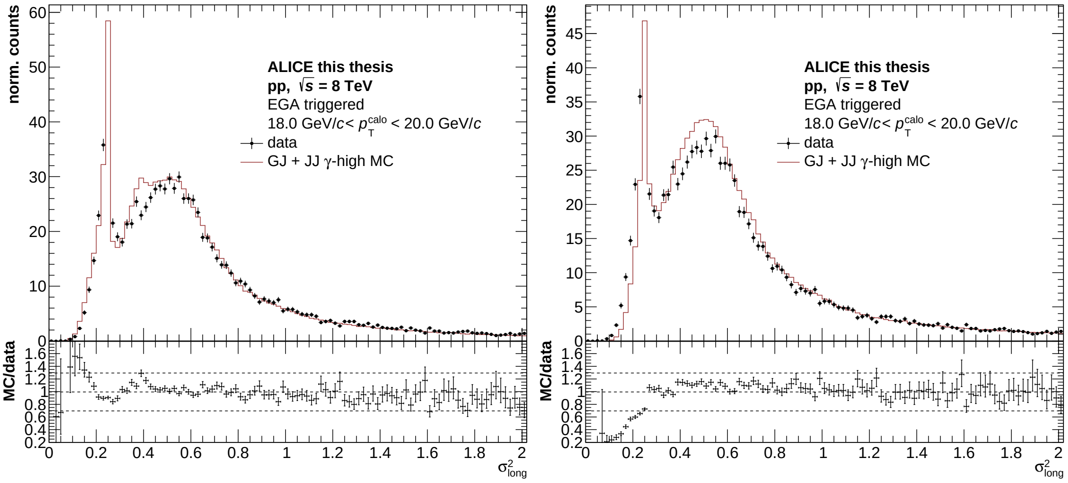

(a) no cross-talk emulation

(b) with cross-talk emulation

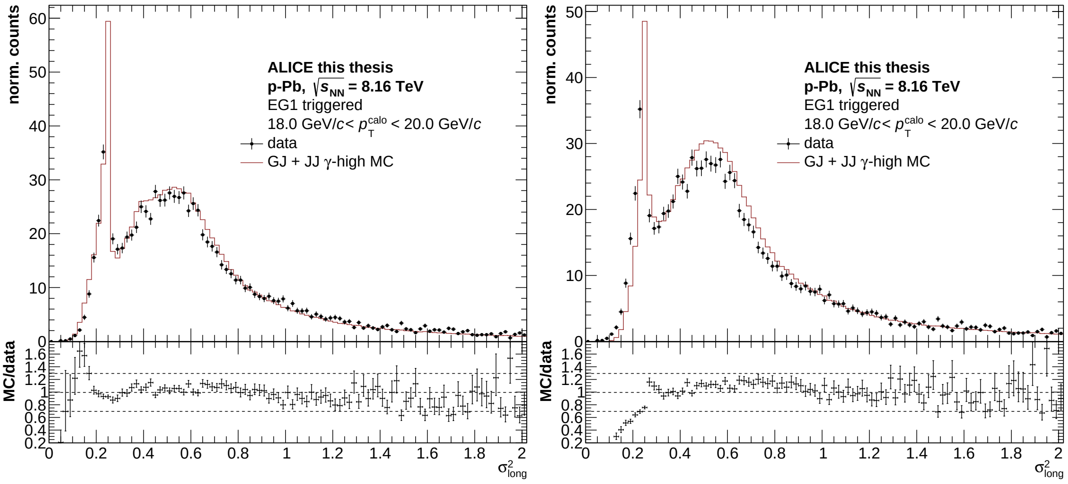

(c) no cross-talk emulation

(d) with cross-talk emulation

Figure 5.10: Long axis σ^2_{long} of the shower shape ellipse shown for data and MC in pp collisions (top) and p–Pb collisions (bottom) before (left) and after (right) the cross talk emulation is applied.

productions, this may lead to a disagreement of the cluster shape in data and MC, where in particular broader σ^2_{long} distributions are observed in data with respect to MC. This lead to the development of a simulation of cross-talk effects which can be applied to the MC productions, using the assumptions that cross talk may affect all cells, even if they are two rows apart as long as they belong to the same T-card, as well as the assumption that the cross-talk magnitude may depend on the cell energy and the EMCal SM. The developed model is documented in Ref. [184] and induces for a given cell Gaussian random energy signals in nearby cells belonging to the same T-card. The model parameters have been tuned using detailed comparisons of the cluster shape in data and MC using mainly data in pp collisions at $\sqrt{s} = 13$ TeV, and since recent additions also include an η dependence, which accounts for the differing cable length depending on the cells position. Fig. 5.10 shows the comparison of the shower shape parameter σ^2_{long} in data and MC before and after the cross-talk emulation was applied, where the MC sample contains Pythia GJ and JJ processes. Even before any cross-talk emulation, one finds an overall reasonable description of the shower shape in both collision systems studied in this work. However, the MCs tend to slightly underestimate wide showers ($\sigma^2_{\text{long}} \gtrsim 1$) and overestimate narrow showers ($\sigma^2_{\text{long}} \lesssim 0.2$). After applying the cross talk emulation in MC, the description of the shower shape improves for $\sigma^2_{\text{long}} \gtrsim 0.3$, however, very narrow clusters with $\sigma^2_{\text{long}} \lesssim 0.2$ are now underestimated by the used MC. This indicates that additional tuning of the cross-talk emulation parameters in these datasets could further improve the MC description in the future. The impact of the observed residual deviations between data and MC on the fully corrected isolated prompt photon production cross section is estimated by performing the full analysis with and without cross-talk emulation, as discussed in Sec. 9, resulting in changes between about 3 % and 5 % on the level of the fully corrected cross sections.

6

ISOLATION

The concept of isolation was introduced in Sec. 2.4.2, where it was shown that an isolation requirement in a cone around a photon suppresses contributions from decay photons as well as fragmentation photons. An isolation requirement for photon clusters fulfilling the selections outlined in the previous section is therefore applied in order to obtain a sample of prompt photon candidates. In this analysis, the activity in the vicinity of the photon is quantified using the sum of the transverse momentum of charged tracks in a cone of radius $R = 0.4$ around the photon. In particular, the isolation quantity $p_{\mathrm{T}}^{\mathrm{iso}}$ is calculated as

$$p_{\mathrm{T}}^{\mathrm{iso}} = \sum_{R_i<R} p_{\mathrm{T},i}^{\mathrm{track}} \quad \text{with} \quad R_i = \sqrt{\left(\varphi_i - \varphi_\gamma\right)^2 + (\eta_i - \eta_\gamma)^2}, \tag{6.1}$$

where $p_{\mathrm{T},i}^{\mathrm{track}}$ is the transverse momentum of track i and R_i its radial distance to the photon candidate γ in the $\eta - \varphi$ plane.

The following sections outline the charged track selection, followed by a discussion of additional corrections that need to be applied to the isolation quantity to account for any Underlying Event (UE) event activity arising due to MPIs. Finally, the obtained charged isolation distributions and the imposed isolation requirements are discussed in the Sec. 6.4.

6.1 CHARGED TRACK SELECTION

In order to calculate the charged isolation quantity $p_{\mathrm{T}}^{\mathrm{iso}}$, tracks are reconstructed following the procedure outlined in Sec. 3.3.1, taking into account information from the ITS and TPC. While considering only tracks which have hit information from both tracking detectors would provide the track sample with the best track p_{T} resolution, this approach leads to a non-uniform distribution of tracks in the $\eta - \varphi$ plane due to missing parts of the SPD detector, which were switched off during some data taking periods. Instead, this analysis relies on a sample of so-called *hybrid tracks*, which is made up of two track classes: The first class are *good global tracks*, which contain at least one hit in the SPD detector, and in addition, the track finding procedure is required to include a successful re-fit of the hits taking into account all ITS information. The second

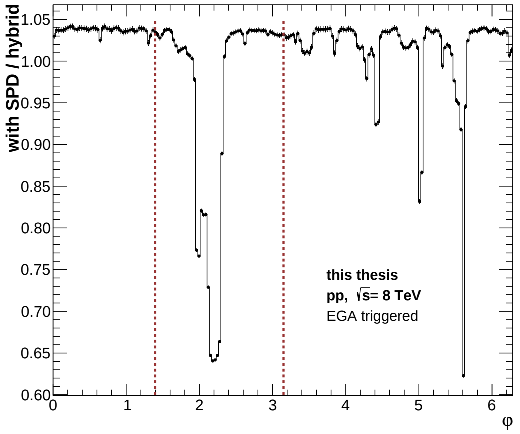

Figure 6.1: Ratio of track azimuthal angle φ for a track sample where at least one hit in the SPD detector is required with respect to the hybrid track sample used in this analysis. The azimuthal angle coverage of the EMCal is illustrated by red dashed lines

Table 6.1: Overview of the track selection. Tracks fulfilling the requirements are used to calculate the charged isolation quantity in the vicinity of a photon according to Eq. 6.1

Name	selection
track sample	hybrid tracks in ITS and TPC: hit in SPD & ITS refit OR no hit in SPD & prim. vtx. constrain OR no successful ITS refit & prim vtx. contrain
min. clusters in TPC	$N^{\mathrm{TPC}}_{\mathrm{clus.}} > 70$
tracking fit quality	$\chi^2/\mathrm{cls.} < 5$
acceptance	$\|\eta < 0.9\|$ and full azimuthal angle
transverse momentum	$p_{\mathrm{T}} > 100\,\mathrm{MeV}/c$
DCA to prim. vertex	$d_{xy} < 2.4\,\mathrm{cm}$ $d_z < 3.2\,\mathrm{cm}$
fraction shared TPC cls.	$\kappa_{\mathrm{shared}} < 40\,\%$

class are complementary tracks that either do not contain any hit in the SPD or do not have a successful ITS refit. For these cases, the track momentum resolution is improved by including the reconstructed primary collision vertex to constrain the fit of the track. The impact of the SPD hit requirement on the track sample is illustrated in Fig. 6.1, which shows the ratio of track azimuthal angle φ for a track sample where at least one hit in the SPD detector is required with respect to the hybrid track sample used in this analysis. A requirement of at least one hit in the SPD would lead to significant depletion of tracks due missing SPD sectors, especially in the acceptance of the EMCal (red dashed lines), motivating the use of the aforementioned hybrid track sample instead.

Several track selections are applied in additionally applied to ensure a good track quality, which are summarized in Tab. 6.1. All selected tracks are required to lie within a pseudorapidity range of $|\eta| < 0.9$, which is given by the geometrical coverage of the ITS and TPC. Furthermore, the reconstructed track is required to contain at least 70 out of 159 possible clusters in the TPC, which ensures a sufficient number of clusters to perform a fit with a satisfactory p_{T} resolution and suppresses "fake" tracks that do not originate from particles produced in the collision. A good track fit quality is furthermore ensured using the χ^2 value of the track fit, which is calculated between the track helix and the associated TPC clusters and required to not exceed 5 per TPC cluster. In order to reject cases where multiple tracks are reconstructed for the same charged particle, track candidates which share more than 40 % of their TPC clusters with another track in the same event are rejected. A lower threshold on the track transverse momentum of $p_{\mathrm{T}} > 100\,\mathrm{MeV}/c$ to rejects tracks which bend too much in the magnetic field and can no longer be reconstructed with an adequate momentum resolution. Finally, all tracks are constrained to originate from the primary collision vertex by applying a loose selection based on their Distances of Closest Approach (DCA) to the vertex. In particular, the DCA is required to be smaller than 2.4 cm in the xy plane and 3.2 cm in the z coordinate.

All tracks fulfilling the aforementioned selection criteria are considered in the calculation of the isolation quantity according to Eq. 6.1. Since this quantity serves as a proxy for the overall activity of particles in the vicinity of the photon, no requirements

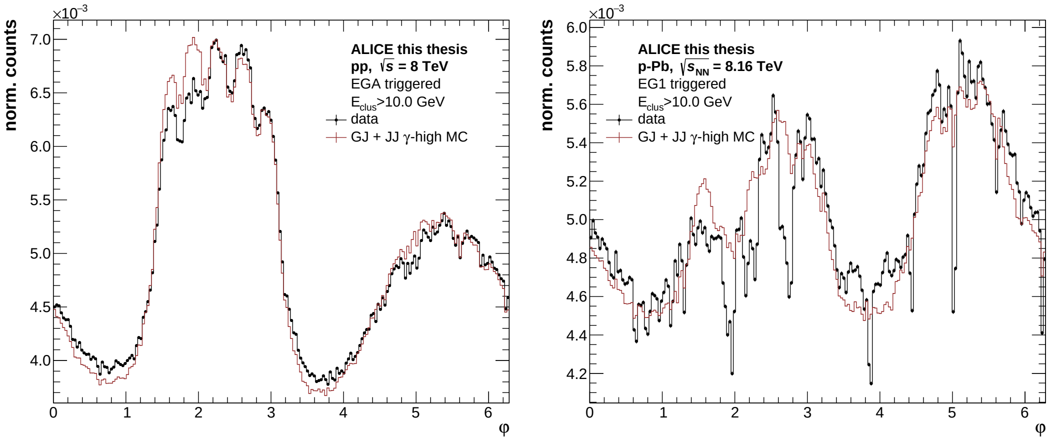

(a) pp collisions

(b) p–Pb collisions

Figure 6.2: Comparison of track azimuthal angle φ reconstructed in data and the MC sample in pp (left) and p–Pb collisions (right).

for particle identification are imposed for the track sample. Fig. 6.2a and 6.2b show a comparison of the track azimuthal angle φ distribution in data and MC for the highest energy EMCal photon trigger in pp and p–Pb collisions, respectively. In addition to the trigger condition, each event is required to have at least one reconstructed EMCal cluster with an energy above 10 GeV, which allows to compare the track properties for events that contain a photon well above the respective trigger thresholds. The shape of the φ-distribution arises due to the EG1 trigger and the imposed cluster requirement, which dominantly selects events with activity in the EMCal $(1.4 < \varphi < 3.28)$ and DCal $(4.56 < \varphi < 5.70)$. Even though no DCal is present in the pp data, a secondary peak of tracks in the DCal acceptance is observed due to dijet events produced back-to-back in azimuth, where one of the jets caused the EG1 in the EMCal to fire. A more complicated structure is observed in p–Pb data, where the DCal detector is present and considered in the trigger condition, leading to an enhanced peak in the DCal acceptance. Several depletions are observed (see e.g. $\varphi \approx 2$), which can be attributed to the fact that about 19 % of the p–Pb data is missing parts of the TPC acceptance that were switched off during data taking. Overall, the azimuthal distributions are reasonably well described by the MC, which include a mimicking of the EMCal triggers and furthermore take into account the missing TPC acceptance for the p–Pb data. Remaining disagreements between data and MC observed in very localized φ regions in the p–Pb data is attributed to the SDD detector, which was not included in the readout of all runs during data taking, leading to the observed depletions in data. This is not considered in the used MC productions, however, these slight discrepancies in small areas are not expected to have a significant effect on the analysis, where the tracks enter the determination of the isolation in a cone of radius $R = 0.4$. Good agreement between data and MC is also observed for the transverse momentum distributions shown in Fig. 6.3a and 6.3b for pp and p–Pb, respectively, showcasing the ability of the MC to accurately describe the measurement of charged tracks using the tracking detectors of ALICE.

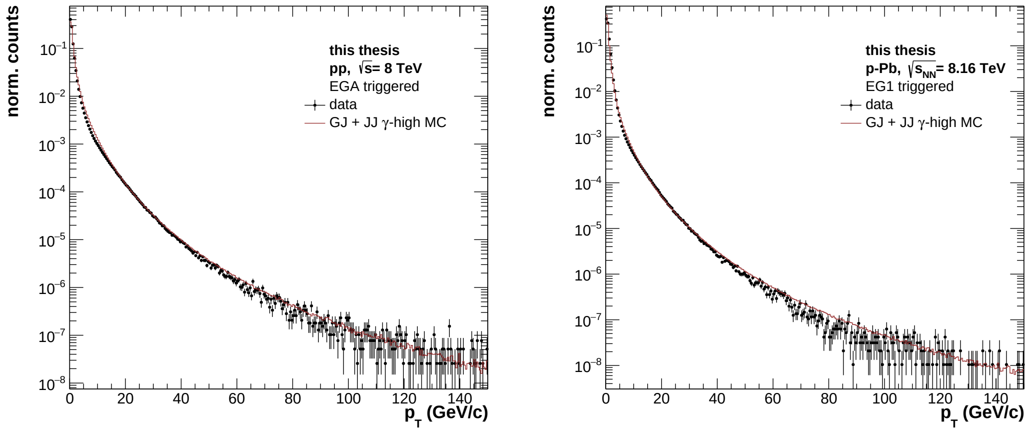

(a) pp collisions

(b) p–Pb collisions

Figure 6.3: Comparison of track transverse momentum (p_T) reconstructed in data and the MC sample in pp (left) and p–Pb collisions (right).

6.2 UNDERLYING EVENT DESCRIPTION

In order to accurately determine the activity in the vicinity of a given photon, the Underlying Event (UE) needs to be considers. While prompt photons are produced in the hard scattering of the collision, many other particles may be produced in small momentum transfer processes that can not be fully treated perturbatively. These particles are commonly referred to as the UE of the collision, and their production can e.g. be described within the framework of Multi Parton Interactions (MPIs) [228] that consider the possibility of multiple independent interactions of parton pairs. In contrast to the hard scattering, which can e.g. produce a prompt photon or a collimated spray of particles (jet), the particles attributed to the UE on average tend to be produced roughly uniformly in $\eta - \varphi$ space. This means that even a prompt photon may not appear to be isolated due to the UE activity which can fall within the isolation cone. The UE contamination therefore needs to be estimated and subtracted from the isolation quantity $p_\mathrm{T}^\mathrm{iso}$ in order to obtain an unbiased estimate of the activity in the vicinity of the high-p_T photon. This UE estimate is performed in this analysis using two independent approaches, which are discussed in the following.

6.2.1 *Perpendicular cone method*

The main approach used in this analysis to estimate the UE is the *perpendicular cone method*. In this method, the sum of transverse momentum of tracks in two cones with radius $R = 0.4$ is considered, where the cone axes are rotated by $\Delta\varphi = \pm 90^\circ$ in azimuth with respect to the momentum vector of the photon candidate. The transverse momentum density $\rho_\mathrm{UE}^\mathrm{perp}$ is calculated via:

$$\rho_{\mathrm{UE}}^{\mathrm{perp}} = \frac{\sum_{R_i^{1,2}<R} p_{\mathrm{T},i}^{\mathrm{track}}}{2\cdot(\pi R^2)} \quad \text{with} \quad R_i^{1,2} = \sqrt{\left(\varphi_i - (\varphi_\gamma \pm \pi/2)\right)^2 + (\eta_i - \eta_\gamma)^2}, \tag{6.2}$$

where $2\pi R^2$ is the area of both estimation cones and $R_i^{1,2}$ is the radial distance of track i with respect to the axis of each cone. The method is motivated by the event topology, where one finds that the region perpendicular to the plane of the hard $2 \rightarrow 2$ scattering is sensitive to the UE event activity, as it will most likely contain fewer particles originating from the hard scattering itself [229]. Following these considerations, the perpendicular cones are used to probe this "transverse region", where the high-p_{T} photon serves as a proxy for the plane of the hard scattering.

6.2.2 *Estimation using jet finding algorithm*

In this method, the transverse momentum density is estimated using a dedicated jet finding algorithm, which is commonly used to identify collimated sprays of particles (jets) in an event by combining observed particles in $\eta - \phi$ space into a single four momentum vector using clustering techniques with various distance metrics. In particular, the k_{T} jet finding algorithm [230] is used to cluster charged tracks in a given collision event with resolution parameter $R = 0.4$, which is illustrated for a Pythia pp collision in Fig. 6.4. This particular algorithm is chosen due to its sensitivity to the background of an event, which arises because the algorithm begins the clusterization with the softest particles. Moreover, the irregular shapes of the found jets allow for a more uniform sampling of the transverse momentum of particles in the covered phasespace [40]. An estimate of the UE density is then obtained as the median of all reconstructed jet transverse momenta $p_{\mathrm{T},i}^{\mathrm{jet}}$ per jet area A_i^{jet}, i.e.:

$$\rho_{\mathrm{UE}}^{\mathrm{JF}} = \mathrm{median}\left\{\frac{p_{\mathrm{T},i}^{\mathrm{jet}}}{A_i^{\mathrm{jet}}}\right\}, \tag{6.3}$$

where the k_{T}-jet transverse momentum is required to be above 150 MeV/c. In order to reduce sensitivity of this estimate to jets originating from the hard scattering rather than the soft UE, the two highest momentum jets are excluded from the estimation. The use of the median ensures the stability of the estimate against statistical outliers.

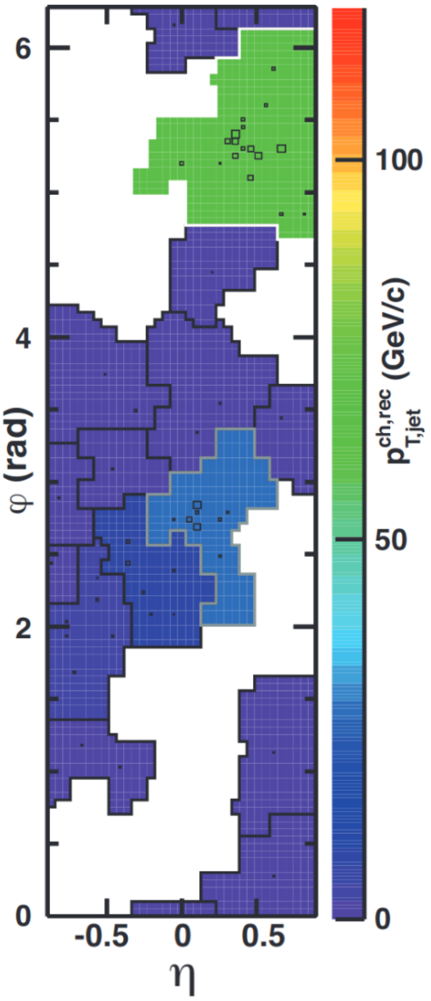

Figure 6.4: Reconstructed charged jets using the k_{T} algorithm shown for a pp collision at $\sqrt{s}$ = 2.76 TeV simulated with Pythia. Figure adapted from Ref. [40].

6.2.3 *Comparison of UE estimates*

The event-by-event estimates for the UE in a cone of $R = 0.4$ in pp and p–Pb collisions at $\sqrt{s_{\mathrm{NN}}}$ = 8 TeV and 8.16 TeV are shown in Fig. 6.5a. Both UE estimation techniques give

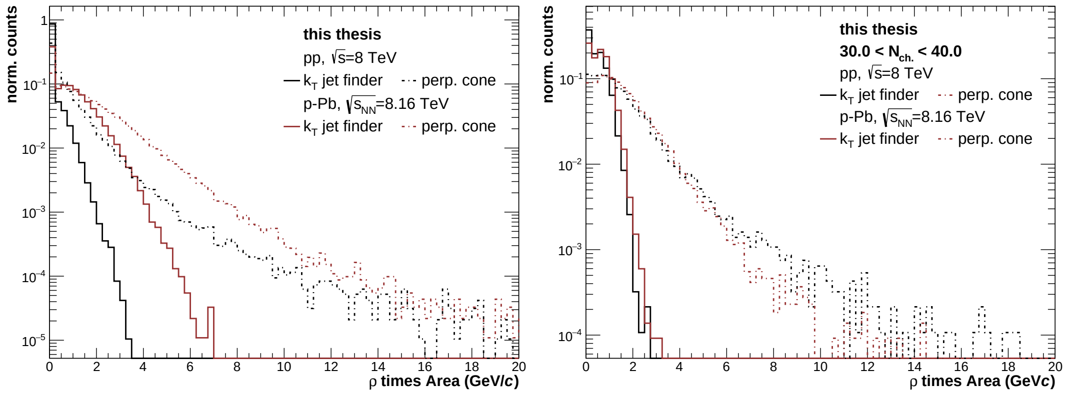

(a) all events

(b) $30 < N_{\mathrm{ch.}} < 40$

Figure 6.5: Estimates of the UE density ρ in pp and p–Pb collisions for two different estimation approaches. The densities are multiplied with the isolation cone area $\pi \cdot 0.4^2$ to illustrate the contribution of the UE to the charged isolation. The left figure shows the UE estimates for events fulfilling the highest available EMCal trigger in the respective collision system, whereas a selection according to the number of charged tracks N_{ch} in a given event is imposed in addition for the figure on the right.

similar results, where in particular one finds an average UE density of $\rho_{\mathrm{UE}} \lesssim 1\,\mathrm{GeV}/c$ and $\approx 1.5 GeV/c$ in pp and p–Pb collisions, respectively. Overall, these densities are of a similar order of magnitude as reported for other measurements (see. e.g. Ref. [231] and [232]). The slightly larger UE event density observed in p–Pb collisions can be attributed to the larger event multiplicity, where in particular on average about 18 and 38 charged tracks were reconstructed per pp and p–Pb collision event containing at least one isolated photon cluster, respectively. This is illustrated in Fig. 6.5b, which shows the UE estimates in pp and p–Pb collisions only for events which contained between 30 and 40 charged tracks, where one finds very similar UE densities for both collision systems. One key difference between both estimation techniques is observed in the tails of the distributions shown in Fig. 6.5, where one finds a larger tail for the perpendicular cone method compared to the approach using the k_{T} jet finder. This can be attributed to a larger sensitivity of the perpendicular cone method to event-by-event fluctuations, which are suppressed in the jet finding approach due to the use of the median and rejection of the two leading jets.

In this work, it was decided to employ the perpendicular cone approach as the default method for UE estimation, due to its simplicity and straight forward implementation. The jet finding approach is used to estimate the systematic uncertainty arising due to the UE estimation, which is discussed in Sec. 9.

6.3 CORRECTION DUE TO LIMITED TPC ACCEPTANCE

While the ITS and TPC cover the full 2π in azimuthal angle, their acceptance is limited to pseudorapidities of $|\eta| < 0.9$. This means that for EMCal clusters with $|\eta| > 0.5$, the isolation cone with radius $R = 0.4$ does not fully fit within the acceptance of the tracking detectors. This necessitates a correction of the isolation energy to account for the area $A_{\text{cone}}^{\text{excess}}$ of the isolation cone that does not fit within the acceptance of the tracking detectors. The correction κ can be obtained analytically via:

$$\kappa = 1 - \frac{A_{\text{cone}}^{\text{excess}}}{A_{\text{cone}}^{\text{full}}} \quad \text{with} \quad A_{\text{cone}}^{\text{full}} = \pi R^2, \tag{6.4}$$

where $A_{\text{cone}}^{\text{full}}$ is the nominal area of the full isolation cone. The excess area that does not fit into the rectangular TPC acceptance can be calculated as the area of a circular segment with angle β and radius R via

$$A_{\text{cone}}^{\text{excess}} = \frac{1}{2} R^2 (\beta - \sin\beta) \quad \text{with} \quad \beta = 2 \cdot \arccos\left(\frac{\eta_{\text{max,TPC}} - \eta_{\text{clus}}}{R}\right), \tag{6.5}$$

where $\eta_{\text{max,TPC}} = 0.9$ is the maximum pseudorapidity covered by the tracking detectors and η_{clus} is the pseudorapidity of the EMCal cluster which marks the centre of the isolation cone. The angle β is obtained using the radius R and the distance of the centre of the isolation cone to the edge of the TPC acceptance. Fig. 6.6 shows the applied correction factors as a function of absolute cluster pseudorapidity $|\eta|$ for three different isolation cone radii. The coverage of the EMCal/DCal of $|\eta| < 0.67$ is indicated as a grey dotted line. For the isolation cone radius of $R = 0.4$ used in this analysis one finds that a correction becomes necessary for clusters with $|\eta| > 0.5$ and is in the order of at most 15 %.

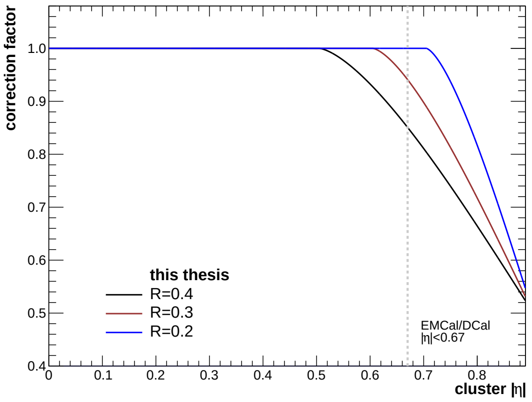

Figure 6.6: Correction factors used to account for the limited ITS and TPC acceptance (Eq. 6.4) shown as a function of cluster pseudorapidity η. The correction is shown for various isolation cone radii R, however, only cones with $R = 0.4$ are used in this work.

6.4 CHARGED ISOLATION

Taking into account the previously discussed corrections, the isolation quantity $p_{\mathrm{T}}^{\text{iso}}$ introduced in Eq. 6.1 becomes:

$$p_{\mathrm{T}}^{\text{iso}} = \frac{1}{\kappa} \sum_{R_i < R} p_{\mathrm{T},i}^{\text{track}} - \rho_{\text{UE}} \pi R^2 \quad \text{with} \quad R_i = \sqrt{(\varphi_i - \varphi_\gamma)^2 + (\eta_i - \eta_\gamma)^2}, \tag{6.6}$$

where κ denotes the correction for the limited acceptance of the tracking detectors and ρ_{UE} is the UE density. Fig. 6.7a and 6.7b show the distribution of the fully corrected isolation quantity $p_{\mathrm{T}}^{\text{iso}}$ for all photon cluster candidates in pp and p–Pb collisions, respectively, using an isolation cone radius of $R = 0.4$. Negative values are observed due to the UE estimation, which might lead to an over subtraction due to localized fluctuations. The distributions obtained from data (black) are compared to two types of MC production, where one finds that clusters in the signal dominated GJ MC (red) are significantly more isolated than clusters from the background dominated JJ MC (blue). This discriminatory power of the isolation quantity is further illustrated in Fig. 6.7c and

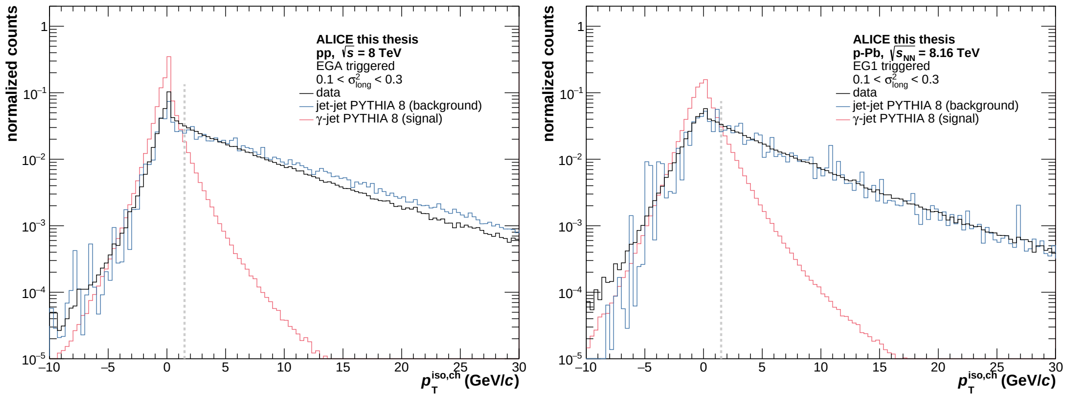

(a) pp (b) p–Pb

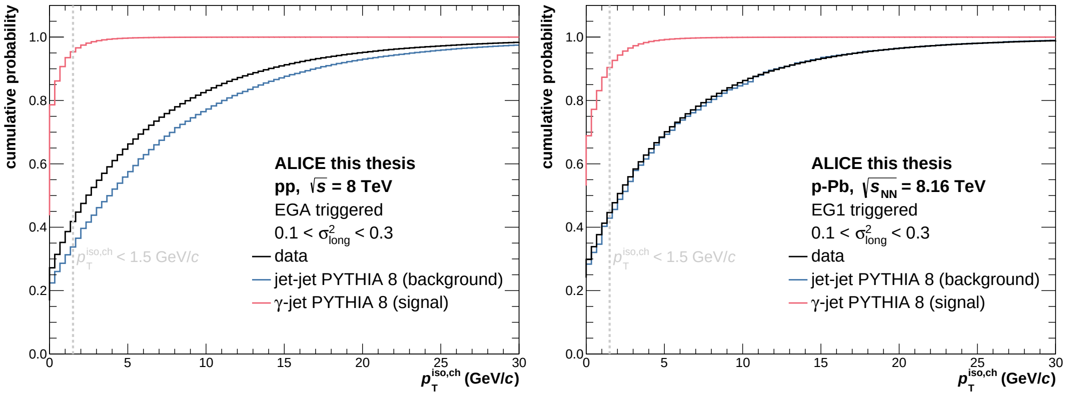

(c) pp (d) p–Pb

Figure 6.7: **Top:** Charged isolation quantity $p_{\mathrm{T}}^{\mathrm{iso}}$ (see Eq. 6.6) for all photon candidates in pp and p–Pb collisions. An isolation cone with radius $R = 0.4$ is used, and the isolation requirement of $p_{\mathrm{T}}^{\mathrm{iso}} < 1.5\,\mathrm{GeV}/c$ imposed in this analysis is illustrated by a grey dashed line. The isolation is shown for data (black), as well as the prompt photon signal dominated GJ MC and background dominated JJ MC. **Bottom:** Cumulative distributions $\int_{-20}^{p_{\mathrm{T}}^{\mathrm{iso}}} p_{\mathrm{T}}^{\mathrm{iso}}\,\mathrm{d}p_{\mathrm{T}}^{\mathrm{iso}}$ shown for data and the two MC productions, illustrating the discriminatory power of the isolation quantity.

Fig. 6.7d, which show the cumulative distributions $\int_{-20}^{p_{\mathrm{T}}^{\mathrm{iso}}} p_{\mathrm{T}}^{\mathrm{iso}}\,\mathrm{d}p_{\mathrm{T}}^{\mathrm{iso}}$ of the isolation quantity in both collision systems: While only about 30 % of clusters from the background dominated JJ MC fulfil an isolation requirement of $p_{\mathrm{T}}^{\mathrm{iso}} < 1.5\,\mathrm{GeV}/c$ (grey dashed line), over 90 % of all clusters from the signal dominated GJ MC are found to have an isolation quantity below this threshold. This motivates the usage of an isolation quantity in this work, where the isolation threshold of $1.5\,\mathrm{GeV}/c$ and radius $R = 0.4$ were chosen for an optimal reconstruction efficiency and purity, as well as to be consistent with the isolation requirements of other measurements.

Fig. 6.8 shows the fraction of photon clusters candidates which fulfil the isolation requirement of $p_{\mathrm{T}}^{\mathrm{iso}} < 1.5\,\mathrm{GeV}/c$ in pp and p–Pb collisions using the respective highest EMCal trigger. One finds that about 40 % of the clusters with transverse momenta of $15\,\mathrm{GeV}/c$ are isolated, which drops to about 35 % with increasing p_{T}. If the UE in measured and accounted for properly in the calculation, one does not expect a significant difference of the ratio between both collision systems, as seen in the figure. One finds agreement between pp and p–Pb within the uncertainties, indicating that the UE

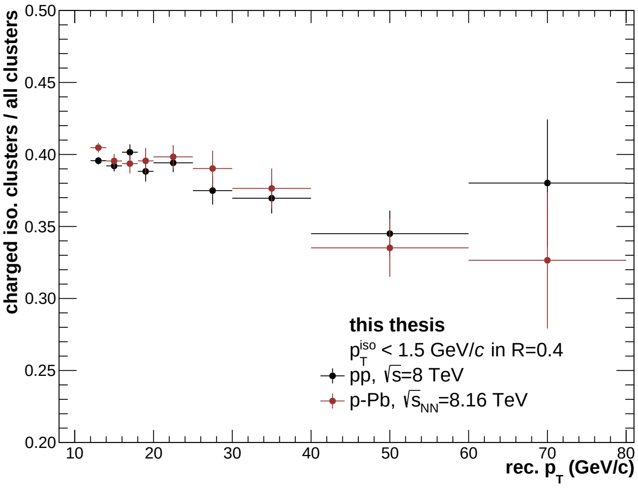

Figure 6.8: Fraction of photon clusters fulfilling the isolation requirement of $p_{\mathrm{T}}^{\mathrm{iso}} < 1.5\,\mathrm{GeV}/c$ in pp and p–Pb collisions.

estimation accurately corrects for differences due to the larger soft background in p–Pb.

6.5 MC GENERATOR LEVEL ISOLATION

As discussed in Sec. 2.4.2, the isolation requirement not only suppresses the contribution from decay photons, but furthermore changes the composition of the prompt photon cross-section, where in particular the contribution from fragmentation photons is reduced by the isolation criterium. Theoretical calculations therefore commonly report the *isolated* prompt photon cross section, where the contribution from fragmentation photons is significantly suppressed. The isolation criterium is therefore part of the *signal definition*, and directly affects the composition of the reported cross section. This means that a charged isolation on MC generator level[1] has to be applied as part of the signal definition used to calculate the efficiency (Sec. 7), in order to ensure comparability of the measurement with theoretical calculations. The MC generator level isolation quantity $p_{\mathrm{T}}^{\mathrm{iso\ gen}}$ is obtained using Eq. 6.6, considering all charged primary particles with $p_{\mathrm{T}} > 100\,\mathrm{MeV}/c$ in the isolation cone. The UE is estimated using the perpendicular cone method for primary charged particles fulfilling the same transverse momentum requirement. The UE needs to be considered, as e.g. NLO calculations of the hard scattering process producing a prompt photon do not consider MPIs and therefore no UE enters the isolation cone. No correction for the limited acceptance of the tracking detectors needs to be considered, as their acceptance does not enter the signal definition. Fig. 6.9 shows the MC generator level charged isolation for pp and p–Pb collisions for photon candidates with transverse momenta of $16\,\mathrm{GeV}/c < p_{\mathrm{T}}^{\mathrm{calo}} \leq 18\,\mathrm{GeV}/c$. An isolation cone of $R = 0.4$ is used and the UE estimated using the perpendicular cone method is subtracted. The distribution is shown for the GJ and JJ MC productions samples, where the aforementioned clear difference between signal and background is observed. The isolation on generator level is compared to that obtained using reconstructed tracks and found to be very similar, indicating a high reconstruction efficiency for charged

---

[1] The term "generator level" refers to particles produced by the event generator (e.g. Pythia), rather than clusters and tracks they produce in the detector.

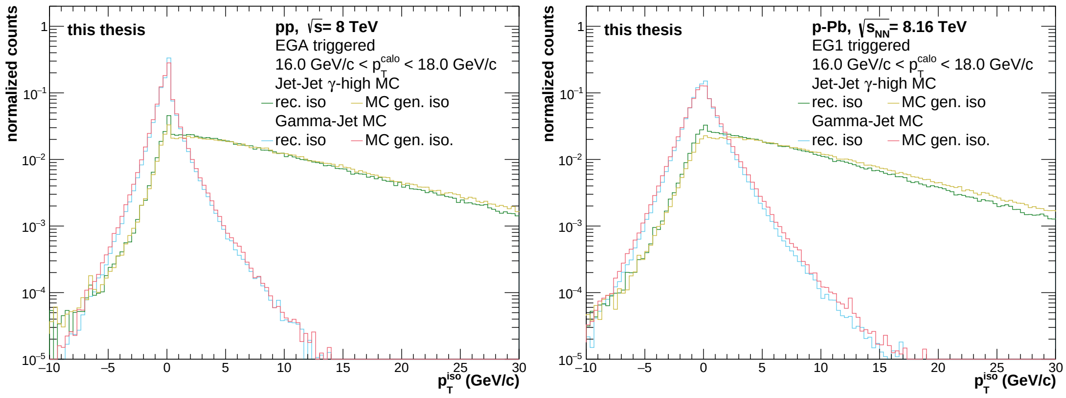

(a) pp (b) p–Pb

Figure 6.9: MC generator level charged isolation for pp and p–Pb collisions for different MC production of pp and p–Pb collisions compared to the isolation using reconstructed quantities. An isolation cone of $R = 0.4$ is used and the UE estimated using the perpendicular cone method is subtracted.

tracks. In this analysis, the MC generator level isolation enters the efficiency calculation via the signal definition, as well as the purity estimation. In particular, a generator level charged isolation of $1.5\,\text{GeV}/c$ in a cone with $R = 0.4$ is required for photons which are labelled as direct prompt or fragmentation photons by Pythia.

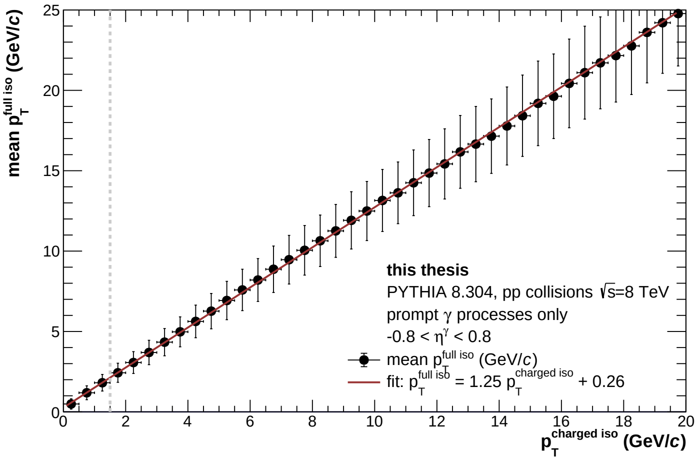

Figure 6.10: Mean full isolation (charged & neutral particles) as a function of charged isolation in a cone of $R = 0.4$. The figure is obtained using the Pythia event generator, where only prompt photon processes were simulated. The charged isolation requirement used in this analysis is indicated by a grey dotted line and the relation between charged and full isolation is described by a fit using a first order polynomial.

While this analysis only considers charged particles in the isolation cone, theoretical calculations often impose an isolation which accounts for all particles within the cone, i.e. an additional component from neutral particles. Therefore, a Pythia study was performed to establish a relationship between the charged and full isolation, where the latter refers to the inclusion of both charged and neutral particles. Fig. 6.10 shows mean full isolation $p_\mathrm{T}^\text{full iso}$ as a function of the charged-only isolation $p_\mathrm{T}^\text{charged iso}$ in a cone of $R = 0.4$ for pp collisions at $\sqrt{s} = 8\,\text{TeV}$ simulated with Pythia. The shown uncertainties indicate the standard deviation of the $p_{\mathrm{T}}^{\text{full iso}}$ distribution, not taking into account the underlying correlation with the $p_{\mathrm{T}}^{\text{charged iso}}$ quantity. One observes a linear relationship between both quantities, which can be described using a first order polynomial fit of:

$$p_{\mathrm{T}}^{\text{full iso}} = (1.25 \pm 0.04) \cdot p_{\mathrm{T}}^{\text{charged iso}} + (0.26 \pm 0.25) \qquad \text{in GeV}/c \tag{6.7}$$

The charged isolation requirement of $p_{\mathrm{T}}^{\text{charged iso}} < 1.5\,\mathrm{GeV}/c$ imposed in this analysis is indicated by a grey dotted, which corresponds to a full isolation of about 2 GeV/c. The measurement presented in this work is therefore comparable to theoretical calculations requiring an isolation of 2 GeV/c as well as other measurements, such as e.g. the measurement of isolated prompt photon production in pp collisions at $\sqrt{s} = 7\,\mathrm{TeV}$ by ALICE [112], which required a charged+neutral isolation of 2 GeV/c.

7

EFFICIENCY

Not all isolated prompt photons produced in a collision can be reconstructed, as signal is lost due to inefficiencies of the involved detectors, as well as the various selections outlined in the previous sections. One has to correct for this loss of signal with the so-called *reconstruction efficiency*, which expresses what fraction of the “true” signal that could be reconstructed in the analysis. The efficiency can be obtained using the information from MC event generators like PYTHIA coupled with the full response of the involved detectors (see Sec. 4.3), where the relation between true generator level particles and reconstructed signal candidates is precisely known. The validity of such an approach depends on the ability of the MC to describe both the physics observable of interest, as well as the response of the involved detectors. The former can be difficult to establish without circular arguments and the latter has been demonstrated in the previous sections. In addition to the reconstruction efficiency, the *purity* of the measurement accounts for the fact that not all reconstructed signal candidates do in fact originate from a true isolated prompt photon. To transform a reconstructed observable to a production cross section, the thus obtained corrections are applied together with a normalization by the integrated luminosity. The aforementioned dependence on the MC event generator and its ability to describe the observable of interest is minimized by using a data-driven approach for the purity estimation, which is discussed in detail in Sec. 8.

7.1 DEFINITIONS AND TERMINOLOGY

The physics observable of interest is a prompt photon, which is defined as a photon produced either directly in the hard scattering (e.g. Compton scattering or annihilation) or via fragmentation. As outlined in Sec. 2.4.2, suppression of the fragmentation contribution is desirable to decrease the dependence of the observable on the theoretical description of the photon fragmentation process. The contribution from fragmentation photons are suppressed using an isolation requirement, which changes the composition and phasespace of the prompt photon cross section and one therefore refers to the physics observable of interest as *isolated* prompt photons. A true signal photon is therefore defined as:

Definition 7.1.1 (True signal photon)**.** A particle which is a photon that either was produced directly from the hard scattering or a fragmentation process, according to the information provided by the MC event generator. In addition, the photon is required to fulfil a charged isolation on generator level of $p_{\mathrm{T}}^{\mathrm{iso\ gen}} < 1.5\,\mathrm{GeV}/c$ in a cone of $R = 0.4$.

On the level of reconstructed quantities, a cluster found in the MC production is mapped to the particles on generator level following a central procedure provided by the ALICE software, where in particular all particles contributing energy to a given cluster can be obtained using the information provided by GEANT. This enables the determination of whether a cluster was directly or indirecly produced by a photon, where in particular one can define a true photon cluster as

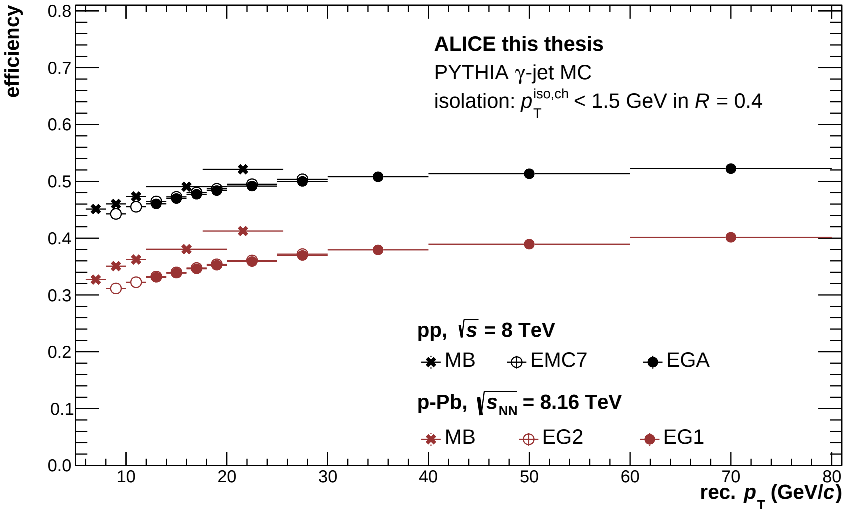

Figure 7.1: Isolated prompt photon reconstruction efficiency in pp and p–Pb collisions as a function of the transverse momentum of the cluster. The efficiency is obtained according to Def. 7.1.3 using the GJ MC productions of the respective collision systems. The efficiency is shown for different trigger samples, which are denoted in the legend and differ in their respective trigger efficiency (see Sec. 4.3.1).

Definition 7.1.2 (True photon cluster)**.** A calorimeter cluster where the leading contribution to the clusters energy was found to be either a photon or an electron/positron originating from a photon conversion.

A cluster fulfilling all the selection criteria outlined in the previous sections, i.e. photon selection criteria and charged isolation, is referred to as a *signal candidate* or *prompt photon candidate* in the following. If the cluster and the particle which produced it fulfil Def. 7.1.1 and Def. 7.1.2, the cluster is referred to as a *true signal cluster*.

Using this terminology, one can define the reconstruction efficiency, which gives the fraction of signal that could be reconstructed in the analysis, without considering "false positives" of clusters that fulfil the selection criteria but do not originate from a signal photon. It is defined as

Definition 7.1.3 (Reconstruction efficiency)**.**

$$\epsilon_{\mathrm{rec.}}(p_{\mathrm{T,\,rec.}}) = \frac{\mathrm{d}N^{\mathrm{signal}}_{\mathrm{clus.}}(p_{\mathrm{T,\,rec.}}) \Big/ \mathrm{d}p_{\mathrm{T,\,rec.}}}{\mathrm{d}N^{\mathrm{signal}}_{\mathrm{gen.}}(p_{\mathrm{T,\,true}}) \Big/ \mathrm{d}p_{\mathrm{T,\,true}}}, \tag{7.1}$$

where $N^{\mathrm{signal}}_{\mathrm{clus.}}$ is the number of true signal clusters and $N^{\mathrm{signal}}_{\mathrm{gen.}}$ the number of true signal photons within the acceptance of the calorimeter.

The efficiency is given as a function of cluster transverse momentum $p_{\mathrm{T,\,rec.}}$, however, the number true signal photons is obtained as a function of true transverse momentum $p_{\mathrm{T,\,true}}$. Therefore, the efficiency correction implicitly contains a correction for the detector resolution effects, i.e. the fact that $p_{\mathrm{T,\,rec.}} \neq p_{\mathrm{T,\,true}}$.

7.2 ISOLATED PHOTON EFFICIENCY

Fig. 7.1 shows the validated reconstruction efficiency for pp and p–Pb collisions, which is obtained using the respective GJ MC productions. Differences between the efficiency in MB with respect to the EMCal triggers arise due to the trigger efficiency, which is introduced in the simulation via an emulation of the trigger decision, as outlined in Sec. 4.3.1. The reconstruction efficiency increases with transverse momentum, where one finds the highest efficiency of about 50 % for photons in pp collisions with $p_{\mathrm{T}} \gtrapprox 40\,\mathrm{GeV}/c$. However, a significant difference of the reconstruction efficiencies in pp and p–Pb collisions is observed, where the efficiency in p–Pb collisions is found to be between 20 % and 30 % lower than in pp collisions.

In order to investigate these differences, the reconstruction efficiency is first expanded into individual components according to the various selection steps of the analysis. The expanded efficiency can be written as:

$$
\begin{aligned}
\epsilon_{\text{rec.}} &= \frac{N^{\text{signal}}_{\text{clus.}} \quad \text{that fulfil } \mathbb{S}_{\text{cluster sel.}} \wedge \mathbb{S}_{\text{track matching}} \wedge \mathbb{S}_{\text{cluster shape}} \wedge \mathbb{S}_{\text{isolation}}}{N^{\text{signal}}_{\text{gen.}}} && (7.2)\\
&= \frac{N^{\text{signal}}_{\text{clus.}} \quad \text{that fulfil } \mathbb{S}_{\text{cluster sel.}}}{N^{\text{signal}}_{\text{gen.}} \quad \text{except } p_{\mathrm{T}}^{\text{iso gen}} < 1.5\,\mathrm{GeV}/c \text{ requirement}} && (7.3)\\
&\times \frac{N^{\text{signal}}_{\text{clus.}} \quad \text{that fulfil } \mathbb{S}_{\text{cluster sel.}} \wedge \mathbb{S}_{\text{track matching}}}{N^{\text{signal}}_{\text{clus.}} \quad \text{that fulfil } \mathbb{S}_{\text{cluster sel.}}} && (7.4)\\
&\times \frac{N^{\text{signal}}_{\text{clus.}} \quad \text{that fulfil } \mathbb{S}_{\text{cluster sel.}} \wedge \mathbb{S}_{\text{track matching}} \wedge \mathbb{S}_{\text{cluster shape}}}{N^{\text{signal}}_{\text{clus.}} \quad \text{that fulfil } \mathbb{S}_{\text{cluster sel.}} \wedge \mathbb{S}_{\text{track matching}}} && (7.5)\\
&\times \frac{N^{\text{signal}}_{\text{clus.}} \quad \text{that fulfil } \mathbb{S}_{\text{cluster sel.}} \wedge \mathbb{S}_{\text{track matching}} \wedge \mathbb{S}_{\text{cluster shape}} \wedge \mathbb{S}_{\text{isolation}}}{N^{\text{signal}}_{\text{clus.}} \quad \text{that fulfil } \mathbb{S}_{\text{cluster sel.}} \wedge \mathbb{S}_{\text{track matching}} \wedge \mathbb{S}_{\text{cluster shape}}} && (7.6)\\
&\Big/ \frac{N^{\text{signal}}_{\text{gen.}}}{N^{\text{signal}}_{\text{gen.}} \quad \text{except } p_{\mathrm{T}}^{\text{iso gen}} < 1.5\,\mathrm{GeV}/c \text{ requirement}}, && (7.7)
\end{aligned}
$$

where the $\mathbb{S}_{\text{cluster sel.}}$ is a short-form notation denoting all selection criteria applied on a cluster level (see. Tab. 5.1), except the selection according to the shape parameter and the cluster-track matching, which are given separately as $\mathbb{S}_{\text{cluster shape}}$ and $\mathbb{S}_{\text{track matching}}$, respectively. The charged isolation requirement given in Eq. 6.6 is denoted as $\mathbb{S}_{\text{isolation}}$. The respective denominator $\mathrm{d}p_{\mathrm{T}}$ given in Eq. 7.1 is omitted for readability. The individual contributions are referred to as *reconstruction efficiency* (Eq. 7.3), *track matching efficiency* (Eq. 7.4), *cluster shape efficiency* (Eq. 7.5) and *isolation efficiency* (Eq. 7.6). The fraction κ of true signal photon, which fulfil a generator level charged isolation of $p_{\mathrm{T}}^{\text{iso gen}} < 1.5\,\mathrm{GeV}/c$ in a cone of $R = 0.4$ is given in Eq. 7.7. The *trigger efficiency*, which has been introduced in Sec. 4.3.1, is included in the reconstruction efficiency and shown in Fig. A.1. The individual contributions are shown together with the total validated reconstruction efficiency in Fig. 7.2 for both collision systems. A very high isolation efficiency is found in both systems, which exceeds $\gtrapprox 95\,\%$ for the covered p_{T} range. Differences between both systems are observed for all remaining contributions, which does not allow to identify a singular step in the analysis responsible for the loss of efficiency in the p–

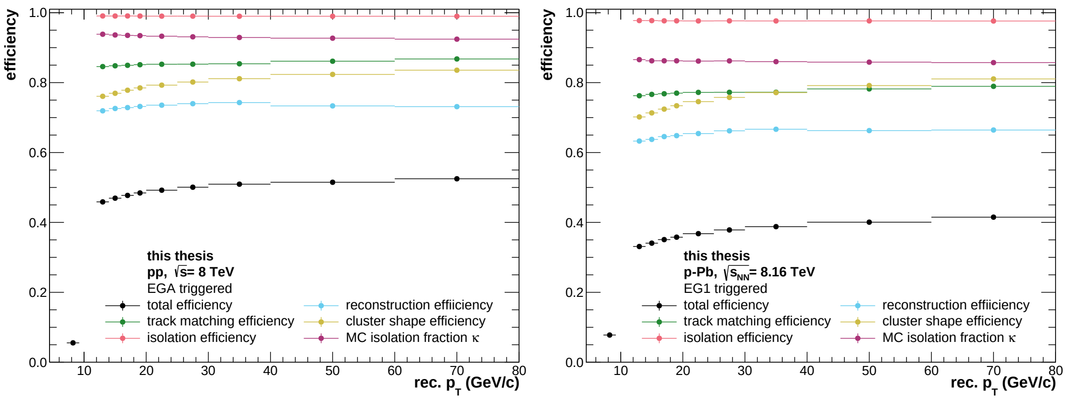

(a) pp collisions at $\sqrt{s} = 8\,\text{TeV}$ (b) p–Pb collisions at $\sqrt{s_{\text{NN}}} = 8.16\,\text{TeV}$

Figure 7.2: Individual contributions to the reconstruction efficiency shown for pp (left) and p–Pb collisions. The efficiencies are obtained using the MC productions of the respective collision system.

Pb data. This necessitated further investigations, which are outlined in the following section.

7.3 EFFICIENCY DIFFERENCE IN PP AND P–PB COLLISIONS

The observed difference of efficiencies found for pp and p–Pb collisions has been further investigated, which allowed to identify four main reasons for the observed lower efficiency in the p–Pb sample:

1. The pp collision data was recorded during Run 1 of ALICE data taking in 2012. At this time, 4 out of 10 full-sized EMCal SMs did not yet have TRD modules installed in front of them. This results in a lower material budget in front of the EMCal and an overall increased photon reconstruction efficiency. By the time the p–Pb collision data was recorded in 2016, all TRD modules were installed, therefore affecting photon measurements in all EMCal modules.

2. As discussed in Sec. 5.2.1, the fraction of bad EMCal cells increased from about 3.3 % in the pp data to about 6.6 % in the p–Pb data, resulting in a corresponding efficiency loss[1].

3. The event multiplicity in p–Pb collisions is on average about two times larger than in pp collisions. Several selection criteria are sensitive to the multiplicity, such as e.g. the shower shape selection, the $N_{\text{cell}} > 1$ requirement and the track matching procedure. This sensitivity may cause a given selection to be less efficient at selecting the prompt photon signal. For example, the increased track density in p–Pb collisions increases the probability that multiple particles contribute to the same cluster. This leads to an overall slight elongation of the found cluster shapes in p–Pb collisions with respect to pp collisions, which in turn leads to a larger number of clusters being rejected by the requirement of $0.1 \leq \sigma^2_{\text{long}} \leq 0.3$.

---

[1] While bad channels technically cause a loss of the geometrical acceptance of the detector, they are here included in the term efficiency, as they can potentially be entangled with the efficiency of the clusterization procedure.

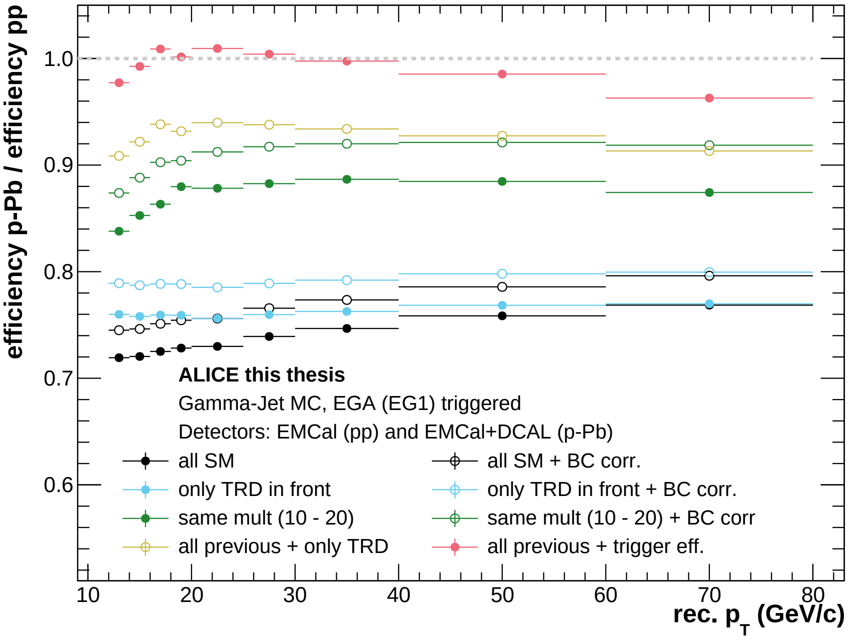

Figure 7.3: Ratio of the isolated prompt photon reconstructed efficiency in p–Pb collisions with respect to pp collisions obtained from the respective GJ MC samples. Taking into account all effects explained in the text (red markers) almost fully removes the initially observed differences of up to 30 % (black markers).

4. The trigger efficiency depends on the number of malfunctioning EMCal TRUs as well as other kinematic biases, as discussed in Sec. 4.3.1. Overall, the efficiencies of both EMCal photon triggers were found to be about 7 % lower in the p–Pb collision data with respect to the triggers in pp collisions (see Fig. A.1).

In order to quantify these effects and to check if they can fully account for the differences observed between both collision systems, the efficiency was corrected for each effect to allow for a "fair" comparison of the efficiency between pp and p–Pb collisions. Fig. 7.3 shows the ratio of the efficiencies obtained in p–Pb collisions with respect to pp collisions, where the black points illustrate an initial difference between about 20 % and 30 %. Correcting both efficiencies for the fraction of of bad channels observed in each system, a slight improvement in the order of a few percent is observed, which is indicated by the open black markers. The missing TRD modules in front of 4 EMCal SMs in the pp data were found to have a similar impact, where one finds a residual difference of about 20 % when excluding the aforementioned 4 SMs from the pp data (blue points). The resulting loss of acceptance is taken into account accordingly. In order to decrease the sensitivity of the selections to the event multiplicity, the efficiencies are studied considering only events with a charged track multiplicity N_{tracks} of $10 < N_{\text{tracks}} < 20$. Together with the corrections for the other effects, this leads to a residual difference below 10 % for the efficiencies obtained in the respective collision systems. Finally, taking into account the lower trigger efficiency observed in p–Pb collisions, one obtains good agreement of the isolated prompt photon efficiency in both collision systems, which is illustrated by red markers. This showcases that the magnitude of the discussed effects is sufficient to explain the differences observed between both collision systems.

In summary, the studies elucidate the cause of the lower prompt photon reconstruction efficiency in the p–Pb sample, which can be attributed to the differing material budget in front of the EMCal detector, the degradation of EMCal channels over time, the higher multiplicity in p–Pb collisions with respect to pp collisions and a differing trigger efficiency attributed to malfunctioning TRUs during p–Pb data taking. It is important to emphasize that the corrections applied in Fig. 7.3 were only used to understand these differences and are not required in the analysis, as the number of bad channels, the detector material, as well as the event multiplicity are all accounted for by the MCs.

8

PURITY

The isolated photon purity P is defined as the fraction of all prompt photon candidates ($N^{\text{rec.}}_{\text{clus.}}$) which were produced by the isolated prompt photon signal. In particular, the purity is defined as:

$$P(p_{\text{T, rec.}}) = \frac{N^{\text{signal}}_{\text{clus.}}(p_{\text{T, rec.}})}{N^{\text{rec.}}_{\text{clus.}}(p_{\text{T, rec.}})}, \tag{8.1}$$

where $N^{\text{signal}}_{\text{clus.}}$ denotes the number of true signal clusters and $p_{\text{T, rec.}}$ is the transverse momentum of the reconstructed cluster. The purity therefore gives an estimate of the remaining number of photonic background clusters in the sample of signal candidates after the application of all selections discussed in the previous sections.

Due to the low signal-to-backround ratio of the isolated prompt photon observable, a good understanding of the isolated photon purity is crucial. In contrast to the validated reconstruction efficiency, which was estimated using only the information from the GJ MC, this approach can not be used to estimate the purity, as it would introduce a dependence on the ability of the MC to accurately describe the prompt photon signal-to-background ratio. This dependence is not present for the determination of the *validated* reconstruction efficiency, as it is only considering true signal clusters and signal photons in numerator and denominator, respectively. In other words, determining the purity purely from MC information would introduce a dependence on the isolated prompt photon cross section – the very quantity one aims to determine in this work. Instead, two different data-driven[1] approaches are used to determine the purity: A *template fitting approach* and the so-called *ABCD method*, which are each covered in their own sections in the following. Both methods use the cluster shape parameter σ^2_{long} and the isolation quantity $p_{\text{T}}^{\text{iso}}$ to determine the purity, which both contain information about the origin of a photon, as discussed in Sec. 5.3.2 and Sec. 6.4, respectively. The template fitting approach has been previously employed in other prompt photon measurements, such as e.g. the measurement of isolated photon-hadron correlations in pp and p–Pb collisions at $\sqrt{s_{\text{NN}}} = 5.02\,\text{TeV}$ with ALICE [132]. Similarly, the ABCD method has been used in several publications, such as e.g. the measurement of isolated prompt photon production in pp collisions at $\sqrt{s} = 7\,\text{TeV}$ by ATLAS [94, 95] and ALICE [112]. While both methods were found to give compatible purity estimates for both collision systems, the ABCD method is used as the default method to determine the purity of the measurement presented in this work. The purities obtained using the template fit approach are used as a semi-independent[2] cross-check and are presented alongside the purities obtained using the ABCD method in Sec. 8.3.

---

[1] Even though both approaches contain input from MC that leads to sizeable corrections, the approach will be referred to as "data-driven" in the following, since they do not rely on absolute cross sections from MC.

[2] They are not fully independent purity estimation approaches, because they both in essence extract the signal purity using the same information contained in the shower shape and isolation energy.

8.1 TEMPLATE FIT METHOD

In this approach, the σ^2_long distributions of all clusters fulfilling the photon selection and charged isolation are fitted using a two-component template fit, where the components described the shape of signal and background clusters, respectively. In particular, the self-normalized signal ($\mathbb{S}$) and background ($\mathbb{B}$) templates are linearly combined via:

$$N_\mathrm{data}\left(\sigma^2_\mathrm{long}\right) = N_\mathrm{sig} \cdot \mathbb{S}\left(\sigma^2_\mathrm{long}\right) + \left(1 - N_\mathrm{sig}\right) \cdot \mathbb{B}\left(\sigma^2_\mathrm{long}\right), \tag{8.2}$$

where N_data is the number of prompt photon cluster candidates observed in data and N_sig is the number of signal clusters in the sample. The latter is the only free parameter of the fit and can then be used to obtain the purity of the measurement.

The signal template is obtained from the GJ MC using the clusters shape parameter σ^2_long distribution of all true signal clusters, i.e. clusters produced by prompt or fragmentation photons fulfilling an isolation on reconstruction and generator level of $p_\mathrm{T}^\mathrm{iso} < 1.5\,\mathrm{GeV}/c$ and all other previously discussed selection criteria. Since the self-normalised signal template is used, no dependence of the purity on the prompt photon cross section predicted by the MC is introduced. The background template is taken from data, where one exploits the fact that none-isolated clusters are dominated by contributions from background photons (mainly $\pi^0 \rightarrow \gamma\gamma$ decays). In particular, the template is obtained using the σ^2_long distribution of anti-isolated clusters in data with $4\,\mathrm{GeV}/c \leq p_\mathrm{T}^\mathrm{iso} \leq 10\,\mathrm{GeV}/c$, that furthermore fulfil the general cluster selection criteria given in Tab. 5.1.

The linear combination of both templates according to Eq. 8.2 is fitted to the σ^2_long distribution of prompt photon candidates in the region $0.01 \leq \sigma^2_\mathrm{long} \leq 1.9$ using a binned standard likelihood fit. The fit is performed using the `TFractionFitter` class [233], which can be accessed using the `ROOT` [201] framework. The statistical uncertainties of the templates are taken into account in the standard likelihood fit of the data, following an approach outlined in Ref. [234]. Fig. 8.1 and 8.2 show the σ^2_long distribution of isolated prompt photon candidates for the highest available EMCal/DCal trigger sample in pp and p–Pb collisions, respectively. The distributions are shown in different cluster p_T intervals and two-component template fit is denoted by a blue line. One finds good agreement between fit and data, as indicated by the χ^2/ndf in the respective legend and the ratio of data with respect to the fit in the bottom panels. Modest disagreements can be observed for σ^2_long, which is attributed to cross-talk related discrepancies between data and MC in this region, as outlined in Sec. 5.4. The signal template is shown as a red line and the purity P of the sample is determined via integration in the photon signal region $0.1 \leq \sigma^2_\mathrm{long} \leq 0.3$:

$$P = \frac{\int_{0.1}^{0.3} N_\mathrm{sig} \cdot \mathbb{S}\left(\sigma^2_\mathrm{long}\right) \mathrm{d}\sigma^2_\mathrm{long}}{\int_{0.1}^{0.3} N_\mathrm{data}\left(\sigma^2_\mathrm{long}\right) \mathrm{d}\sigma^2_\mathrm{long}}, \tag{8.3}$$

and the obtained purity in each p_T interval are given in the respective legend. Similar figures for the EG2 and EMC7 triggered samples can be found in Sec. A.2. The obtained purity as a function of cluster p_T is presented together with the prediction from the ABCD method in Sec. 8.3 after a full discussion of both methods and corrections in the following sections. A correction of the background template discussed in Sec. 8.1.1 is already applied for Fig. 8.1 and 8.2, respectively.

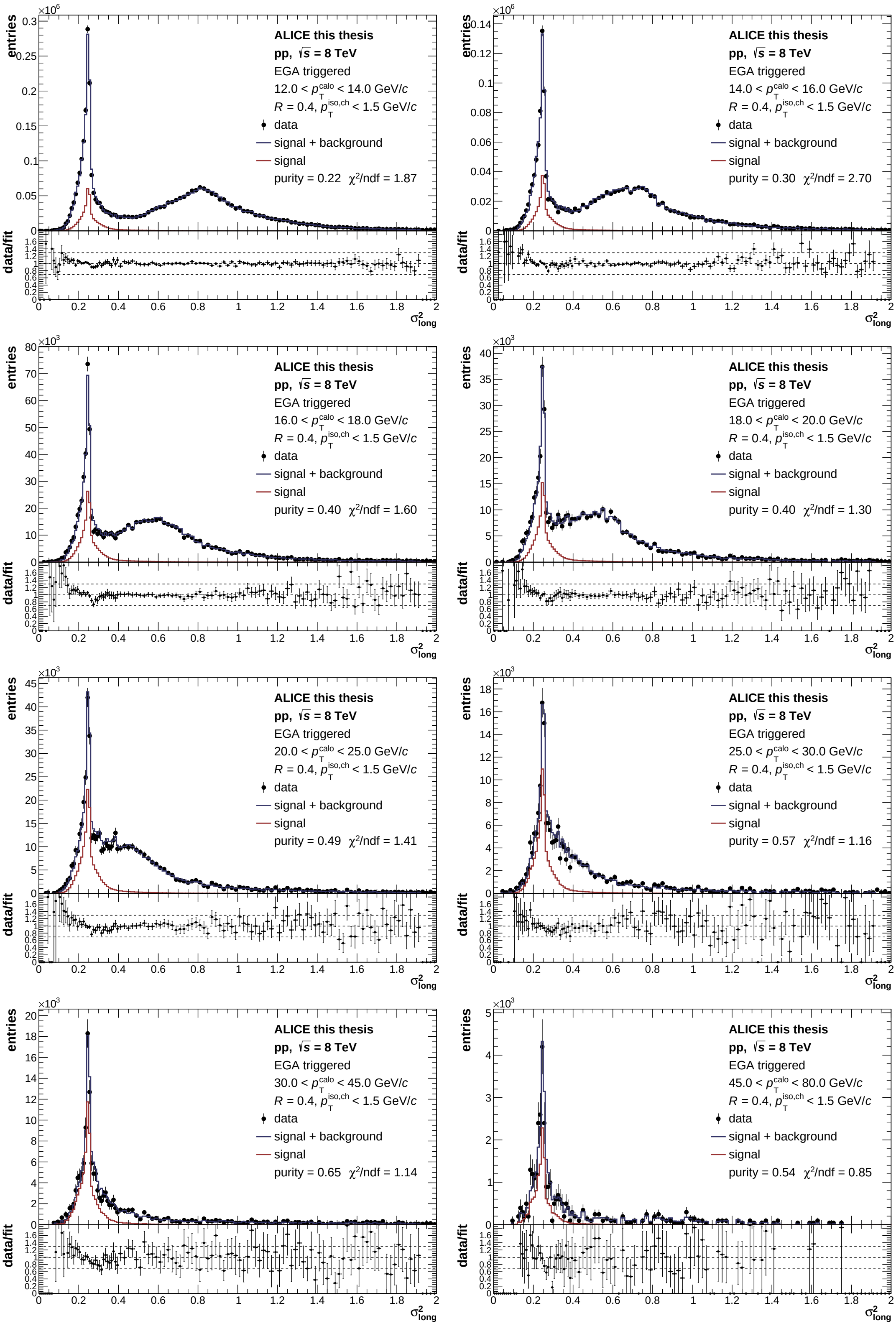

Figure 8.1: Two-component template fit (Eq. 8.2) of the long axis σ^2_{long} of the shower shape ellipse in pp collisions at $\sqrt{s} = 8\,\mathrm{TeV}$ for different cluster p_{T} intervals. The signal and background templates are obtained from GJ MC and data, respectively, as outlined in the text. The purity is obtained in the photon signal region $0.1 \leq \sigma^2_{\mathrm{long}} \leq 0.3$ according to Eq. 8.3.

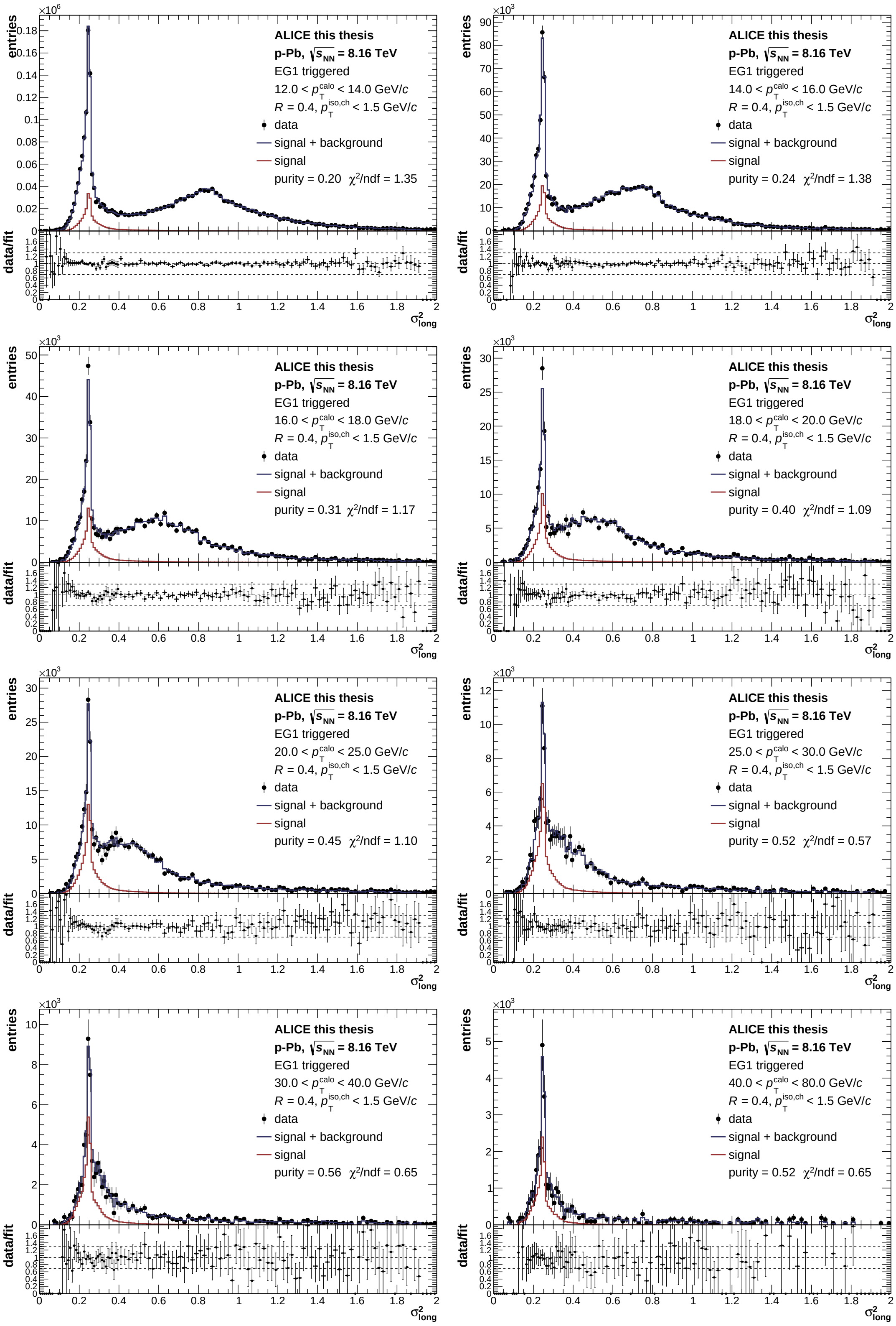

Figure 8.2: Two-component template fit (Eq. 8.2) of the long axis σ^2_{long} of the shower shape ellipse in p–Pb collisions at $\sqrt{s_{\text{NN}}}$ = 8.16 TeV for different cluster p_{T} intervals. The signal and background templates are obtained from GJ MC and data, respectively, as outlined in the text. The purity is obtained in the photon signal region $0.1 \leq \sigma^2_{\text{long}} \leq 0.3$ according to Eq. 8.3.

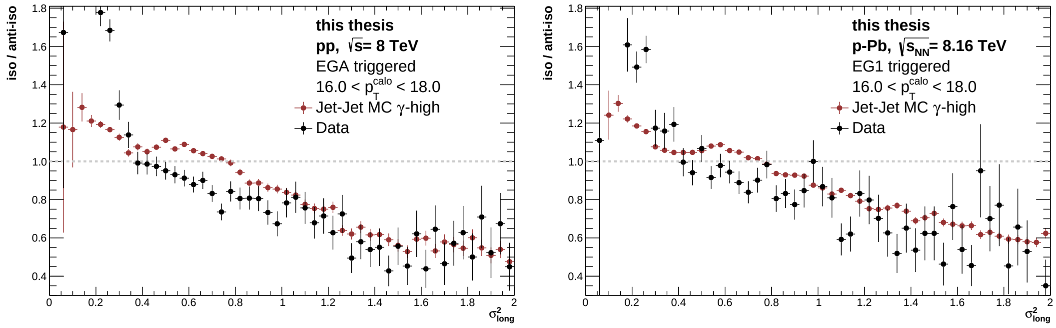

(a) pp collisions (b) p–Pb collisions

Figure 8.3: Ratio of shower shape parameter σ^2_{long} for isolated clusters ($p_{\text{T}}^{\text{iso}} < 1.5\,\text{GeV}$) with respect to anti-isolated clusters ($4\,\text{GeV}/c \leq p_{\text{T}}^{\text{iso}} \leq 10\,\text{GeV}/c$). The ratios are shown for data (black) and the background dominated JJ MC (red), where the latter is used as a bin-by-bin correction of the background template according to Eq. 8.4.

8.1.1 *Correction of background template*

Ideally, the background template $\mathbb{B}$ describes the shower shape of clusters from background sources which nonetheless fulfil a charged isolation of $p_{\text{T}}^{\text{iso}} < 1.5\,\text{GeV}$. However, definite information about whether a cluster originated from a background source is not available in data, especially for *isolated* clusters where a significant contribution from the prompt photon signal is expected. In order to obtain the shower shape distribution of background clusters in a data-driven way, the background template was instead determined in a region of phasespace which is known to be dominated by background clusters, where in particular the anti-isolation requirement suppresses contributions from signal photons. This anti-isolated region serves as a proxy to describe the shape of background clusters in the isolated region. This approach is only valid under the assumption that the shower shape of anti-isolated background clusters is identical to the shape of isolated background clusters. In other words, anti-isolated clusters are only a valid proxy if there is no correlation between the isolation quantity and the shower shape parameter σ^2_{long}. However, this assumption is not strictly true, as illustrated in Fig. 8.3: The figure shows the ratio of the self-normalized shower shape for isolated clusters with respect to anti-isolated clusters for data and the JJ MC in pp and p–Pb collisions for an exemplary p_{T} bin. If the there is no difference between shower shapes in isolated and anti-isolated environment, a ratio of unity is expected, which is illustrated by the grey dashed lines. Instead, a clear depletion of elongated clusters is observed for $\sigma^2_{\text{long}} \gtrsim 0.4$, showcasing that the shower shape is correlated with the isolation quantity. This can be understood considering shower overlaps: The isolation quantity is a measure of the activity in the vicinity of the photon, where in particular anti-isolated clusters have more surrounding activity than isolated clusters. This increases the probability to have multiple particles contributing to the same cluster, causing its elongation in anti-isolated environments.

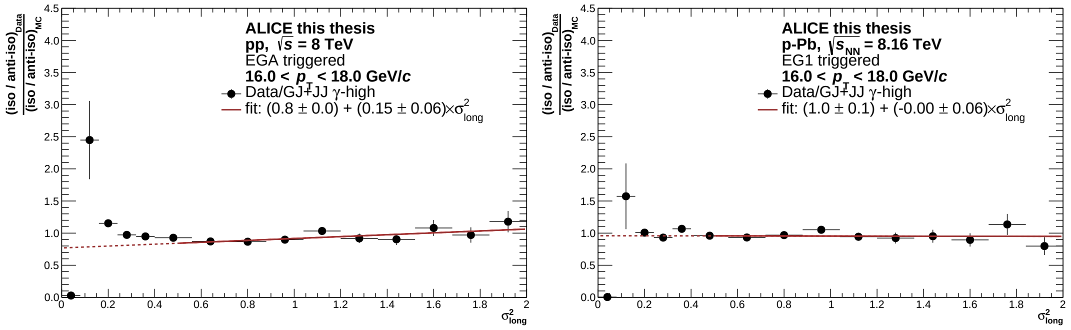

(a) pp collisions (b) p–Pb collisions

Figure 8.4: Double ratio calculated according to Eq. 8.5 in an exemplary p_{T}-interval for pp (left) and p–Pb (right) collisions. A first-order polynomial fit is indicated by a red line, where the solid part of the line indicates the fit region. A slope of ≈ 0 indicates agreement between data and MC in their description of the isolation dependence of the shower shape parameter.

To account for the correlation between shower shape and isolation quantity, a correction

$$\lambda\left(\sigma^2_{\mathrm{long}}\right) = \frac{N^{\mathrm{JJ\,MC}}_{\mathrm{iso}}\left(\sigma^2_{\mathrm{long}}\right)}{N^{\mathrm{JJ\,MC}}_{\mathrm{anti\text{-}iso}}\left(\sigma^2_{\mathrm{long}}\right)} \tag{8.4}$$

is obtained using the background dominated JJ MC productions in the respective system, where $N^{\mathrm{JJ\,MC}}_{\mathrm{iso}}$ and $N^{\mathrm{JJ\,MC}}_{\mathrm{anti\text{-}iso}}$ denote the number of charged isolated and anti-isolated clusters, respectively. In order to maximize the available statistics, the decay photon triggered JJ MCs are used (see. Tab. 4.3). In particular, for clusters with $p_{\mathrm{T}} < 16\,\mathrm{GeV}/c$ the decay photon triggered JJ MCs with $p_{\mathrm{T},\gamma} > 3.5\,\mathrm{GeV}/c$ are used, whereas the MCs with the higher trigger of $p_{\mathrm{T},\gamma} > 7\,\mathrm{GeV}/c$ are used for clusters with $p_{\mathrm{T}} \geq 16\,\mathrm{GeV}/c$. The obtained correction corresponds to the red points in Fig. 8.3 and is applied bin-by-bin to the background template in each p_{T} interval.

Using the MC to correct for the relative difference of the cluster shape in isolated and anti-isolated environments relies on the fact that this difference is correctly captured by the MC. This is checked by calculating the double ratio:

$$R_{\mathrm{shape}}\left(\sigma^2_{\mathrm{long}}\right) = \frac{\left(N_{\mathrm{iso}}/N_{\mathrm{anti\text{-}iso}}\right)_{\mathrm{Data}}}{\left(N_{\mathrm{iso}}/N_{\mathrm{anti\text{-}iso}}\right)_{\mathrm{MC}}} \tag{8.5}$$

which quantifies the agreement of Eq. 8.4 between data and MC[3]. The thus obtained double ratio is shown in Fig. 8.4 for pp and p–Pb collisions for an exemplary p_{T}-interval for events fulfilling the EGA/EG1 trigger. The double ratios for all used triggers and p_{T}-intervals are presented in Sec. A.2. The key feature quantifying the agreement of data and MC in their description of the shower shape for clusters of differing isolation is the slope of the double ratio. This is due to the fact that the correction calculated in Eq. 8.4 does not aim to correct for the absolute scale of the fraction $N_{\mathrm{iso}}/N_{\mathrm{anti\text{-}iso}}$, but

---

[3] While for the background template weights only the JJ MC is used, the double ratio is obtained using the weighted sum of GJ and JJ, reducing the disagreement of data and MC in the signal region $\sigma^2_{\mathrm{long}} < 0.3$. This region is however excluded in the fit, and the no significant difference could be observed when using GJ+JJ or only JJ MC.

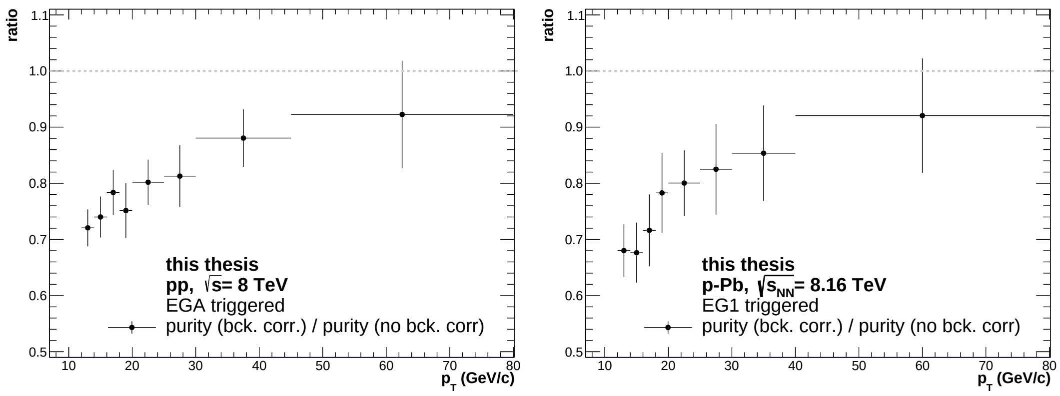

(a) pp collisions (b) p–Pb collisions

Figure 8.5: Ratio of the purity obtained from the template fitting approach including a correction of the background template according to Eq. 8.4 with respect to the purity obtained without this correction. The results are shown for EGA/EG1 triggered pp (left) and p–Pb (right) collision events, and the correction is found to modify the purity by up to about 30 %.

rather for its σ^2_{long} dependence. An agreement in the description of this dependence in data and MC then manifests itself in a vanishing slope of the double ratio. The slope is quantified using a first-order polynomial, which is fitted to the double ratio in the region $0.5 \le \sigma^2_{\text{long}} \le 1.7$, as indicated by the red line. The region $\sigma^2_{\text{long}} < 0.5$ is excluded from the fit, as it contains none-negligible signal contributions, which should not be considered to evaluate the accuracy of the MC in the background region. The slope of the thus fitted distribution is given in the respective legend with its statistical uncertainties. The slope is small and consistent with zero within its uncertainties for most studied p_T-intervals, showcasing the ability of the MC to describe the isolation dependence of the shower shape parameter. However, small residual slopes can be observed for some p_T intervals (see e.g. Fig. 8.4a), which are discussed in more detail for the ABCD method in Sec. 8.2.1.

Finally, Fig. 8.5 shows the effect of the background template correction given in Eq. 8.4 on the purity obtained from the template fit method for EGA/EG1 triggered pp and p–Pb collisions. A modification of up to 30 % is observed for $p_T < 20\,\text{GeV}/c$, which decreases with increasing p_T, where one finds a correction of about 10 % for the highest covered momenta. In addition, the correction was found to improve the χ^2/ndf of the template fit, indicating an overall improved description of the data. This showcases that taking into account correlations of the shower shape and isolation energy is crucial in order to accurately determine the purity at low p_T.

8.2 THE ABCD METHOD

The second method used to estimate the signal purity is a two-dimensional sideband method, which in the following will be referred to as *the ABCD method*. The method considers the two-dimensional distribution of isolation quantity $p_{\mathrm{T}}^{\mathrm{iso}}$ and shower shape σ_{long}^2 in data, which is divided into four regions $\mathbb{A}$, $\mathbb{B}$, $\mathbb{C}$ and $\mathbb{D}$ according to the selections given in Tab. 8.1. The purity in the signal region $\mathbb{A}$ is then obtained using the three background dominated control regions $\mathbb{B}$, $\mathbb{C}$ and $\mathbb{D}$. The two-dimensional distribution of isolation and shower shape is shown for EGA/EG1 triggered pp and p–Pb collision events in Fig. 8.6, where the aforementioned regions are indicated accordingly.

In the following, the cluster yield in each region is denoted by the variable N, where the subscript "n" and "w" indicated if the cluster fulfils the narrow ($0.1 \leq \sigma_{\mathrm{long}}^2 \leq 0.3$) or wide ($0.4 \leq \sigma_{\mathrm{long}}^2 \leq 2.0$) shower shape selection, respectively. Similarly, the subscript "iso" and "$\overline{\mathrm{iso}}$" indicate whether the cluster is found to be charged isolated ($p_{\mathrm{T}}^{\mathrm{iso}} \leq 1.5\,\mathrm{GeV}/c$) or anti-isolated ($p_{\mathrm{T}}^{\mathrm{iso}} \geq 4\,\mathrm{GeV}/c$), respectively, where the isolation quantity is determined with $R = 0.4$ as discussed in Sec. 6. Denoting the yield of true signal- and background clusters with the variables S and B, one can give the purity P in the signal region as

$$P = \frac{S_n^{\mathrm{iso}}}{N_n^{\mathrm{iso}}} = 1 - \frac{B_n^{\mathrm{iso}}}{N_n^{\mathrm{iso}}}. \tag{8.6}$$

Since the true background contribution B_n^{iso} in the signal region is not known in a data-driven approach, it has to be estimated using the yields in the background dominated control regions. This is achieved by considering *relative differences* of the background contribution in different regions. Assuming the cluster shape and the isolation quantity are uncorrelated, the change of background yield B when going from isolated to anti-isolated environments should be independent of the cluster shape. In other words, the ratio of the background cluster yield in region $\mathbb{A}$ with respect to region $\mathbb{C}$ should be the same as the ratio of background yield in $\mathbb{B}$ with respect to $\mathbb{D}$. Given this assumption, one can write explicitly:

$$\frac{B_n^{\mathrm{iso}}/B_n^{\overline{\mathrm{iso}}}}{B_w^{\mathrm{iso}}/B_w^{\overline{\mathrm{iso}}}} = 1 \Rightarrow B_n^{\mathrm{iso}} = \frac{B_w^{\mathrm{iso}}}{B_w^{\overline{\mathrm{iso}}}} \cdot B_n^{\overline{\mathrm{iso}}}, \tag{8.7}$$

Table 8.1: Selections used for the different regions of the ABCD method. The purity in the signal region $\mathbb{A}$ is estimated using the background dominated control regions $\mathbb{B}$, $\mathbb{C}$ and $\mathbb{D}$ as described in the text.

Region	Isolation ($p_{\mathrm{T}}^{\mathrm{iso}}$)	Shower shape	Description
$\mathbb{A}$	$\leq 1.5\,\mathrm{GeV}/c$	$0.1 \leq \sigma_{\mathrm{long}}^2 \leq 0.3$	narrow isolated ($N_{\mathrm{n}}^{\mathrm{iso}}$)
$\mathbb{B}$	$\leq 1.5\,\mathrm{GeV}/c$	$0.4 \leq \sigma_{\mathrm{long}}^2 \leq 2.0$	wide isolated ($N_{\mathrm{w}}^{\mathrm{iso}}$)
$\mathbb{C}$	$\geq 4.0\,\mathrm{GeV}/c$	$0.1 \leq \sigma_{\mathrm{long}}^2 \leq 0.3$	narrow anti-isolated ($N_{\mathrm{n}}^{\overline{\mathrm{iso}}}$)
$\mathbb{D}$	$\geq 4.0\,\mathrm{GeV}/c$	$0.4 \leq \sigma_{\mathrm{long}}^2 \leq 2.0$	wide anti-isolated ($N_{\mathrm{w}}^{\overline{\mathrm{iso}}}$)

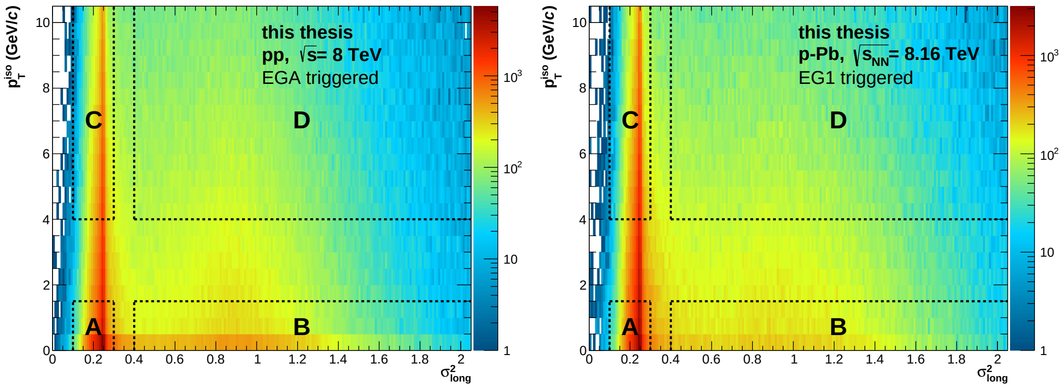

(a) pp collisions (b) p–Pb collisions

Figure 8.6: Two-dimensional distribution of isolation quantity p_T^{iso} and shower shape σ^2_{long} for EGA/EG1 triggered pp (left) and p–Pb (right) collision data. The signal region $\mathbb{A}$ and the three background dominated control regions $\mathbb{B}$, $\mathbb{C}$ and $\mathbb{D}$ used to determine the purity with the ABCD method are denoted by black dashed lines.

By substitution of B_n^{iso} in Eq. 8.6 with Eq. 8.7 on obtains:

$$P = 1 - \frac{B_n^{\overline{\text{iso}}}/N_n^{\text{iso}}}{B_w^{\overline{\text{iso}}}/B_w^{\text{iso}}} \tag{8.8}$$

Assuming that the signal contribution in the background control regions is negligible, i.e. $B_n^{\overline{\text{iso}}} \approx N_n^{\overline{\text{iso}}}$, $B_w^{\overline{\text{iso}}} \approx N_w^{\overline{\text{iso}}}$ and $B_w^{\text{iso}} \approx N_w^{\text{iso}}$, one obtains:

$$P_{\text{ABCD}}^{\text{raw}} = 1 - \frac{\overbrace{N_n^{\overline{\text{iso}}}}^{\mathbb{C}} \; / \; \overbrace{N_n^{\text{iso}}}^{\mathbb{A}}}{\underbrace{N_w^{\overline{\text{iso}}}}_{\mathbb{D}} \; / \; \underbrace{N_w^{\text{iso}}}_{\mathbb{B}}}. \tag{8.9}$$

In summary, the purely data-driven purity estimate given in Eq. 8.9 is exactly true if the following assumptions are exactly true:

ASSUMPTION 1: The signal contribution is negligible in the background control region ($B_n^{\overline{\text{iso}}} \approx N_n^{\overline{\text{iso}}}$, $B_w^{\overline{\text{iso}}} \approx N_w^{\overline{\text{iso}}}$ and $B_w^{\text{iso}} \approx N_w^{\text{iso}}$).

ASSUMPTION 2A: The isolation energy and the shower shape are uncorrelated and the the probability that a cluster is isolated does therefore not depend on its shape. In particular, $\left(B_n^{\text{iso}}/B_n^{\overline{\text{iso}}}\right)\Big/\left(B_w^{\text{iso}}/B_w^{\overline{\text{iso}}}\right) = 1$ used in Eq. 8.7 must be true.

The first assumption is found to be sufficiently correct, and has been further tested by varying the anti-isolation and wide shower shape selection, resulting in a small impact on the fully corrected cross section, as discussed in Sec. 9. However, the assumption of no correlation between the shower shape and isolation quantity is not correct! This has been previously discussed for the template fitting approach and is reflected in the suppression of isolated wide clusters shown in Fig. 8.5. The second assumption (Eq. 8.7) is therefore not exactly true, and an additional correction of the obtained purity is

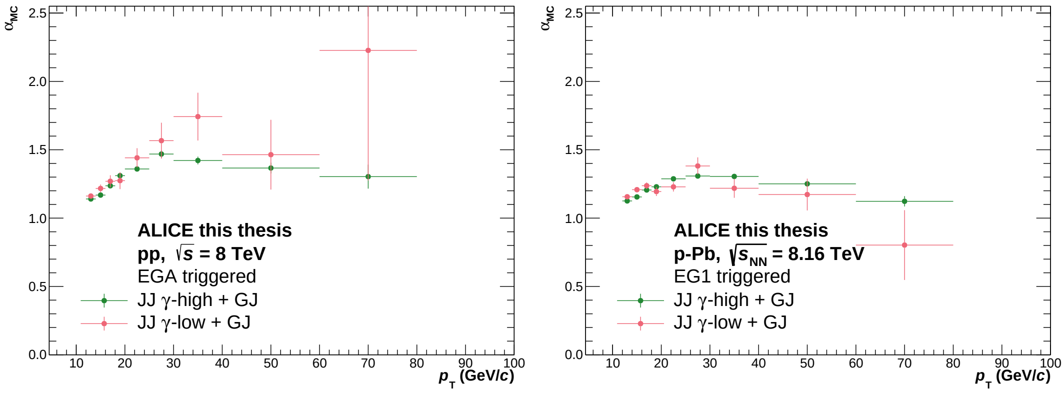

(a) pp collisions (b) p–Pb collisions

Figure 8.7: Correction factors α_{MC} calculated according to Eq. 8.11 to account for the correlation of shower shape and isolation quantity. For clusters with $p_{\mathrm{T}} < 16\,\mathrm{GeV}/c$ the factors are obtained using the sum of GJ MC and JJ γ-low MC, whereas the respective JJ γ-high production is used above this threshold.

required, which is analogous to the correction of the background template introduced in Sec. 8.1.1. An improved purity estimate can be obtained using the relation:

$$\left(\frac{B_n^{\mathrm{iso}}/B_n^{\overline{\mathrm{iso}}}}{B_w^{\mathrm{iso}}/B_w^{\overline{\mathrm{iso}}}}\right)_{\mathrm{data}} = \left(\frac{B_n^{\mathrm{iso}}/B_n^{\overline{\mathrm{iso}}}}{B_w^{\mathrm{iso}}/B_w^{\overline{\mathrm{iso}}}}\right)_{\mathrm{MC}}, \tag{8.10}$$

where the MC is obtained as the sum of the JJ and GJ MCs scaled with their respective cross sections. It replaces the “naive” assumption given in Eq. 8.7 with the assumption:

ASSUMPTION 2B The correlation between shower shape and isolation energy is accurately captured by the used MC. In particular, Eq. 8.10 must be true.

Replacing *Assumption 2a* (Eq. 8.7) with *Assumption 2b* (Eq. 8.10), as well as using *Assumption 1*, one obtains the corrected purity:

$$\begin{aligned} P_{\mathrm{ABCD}} &= 1 - \left(\frac{N_n^{\overline{\mathrm{iso}}}/N_n^{\mathrm{iso}}}{N_w^{\overline{\mathrm{iso}}}/N_w^{\mathrm{iso}}}\right)_{\mathrm{data}} \times \left(\frac{B_n^{\mathrm{iso}}/N_n^{\overline{\mathrm{iso}}}}{N_w^{\mathrm{iso}}/N_w^{\overline{\mathrm{iso}}}}\right)_{\mathrm{MC}} \\ &= 1 - \left(\frac{N_n^{\overline{\mathrm{iso}}}/N_n^{\mathrm{iso}}}{N_w^{\overline{\mathrm{iso}}}/N_w^{\mathrm{iso}}}\right)_{\mathrm{data}} \times \alpha_{\mathrm{MC}}. \end{aligned} \tag{8.11}$$

The applied correction factors α_{MC} are shown in Fig. 8.7 for EGA/EG1 triggered pp and p–Pb collisions. The factors are obtained using the different JJ productions give compatible results within the statistical uncertainties, however, the JJ γ-low production does not have sufficient statistics at high cluster p_{T}. Therefore, the α_{MC} factors obtained using the sum of GJ and JJ γ-low are only used for clusters with $p_{\mathrm{T}} < 16\,\mathrm{GeV}/c$, whereas the JJ γ-high production is used above this threshold. The effect of this correction on the obtained purity is illustrated in Fig. 8.8, which shows the ratio of the MC corrected purities (Eq. 8.11) with respect to the fully data-driven purity given in (Eq. 8.9). The correction is at most in the order of about 30 % (40 %) for pp (p–Pb) collisions, which is compatible with the corrections obtained for the template fitting approach to account for the same effect (see. Fig. 8.5).

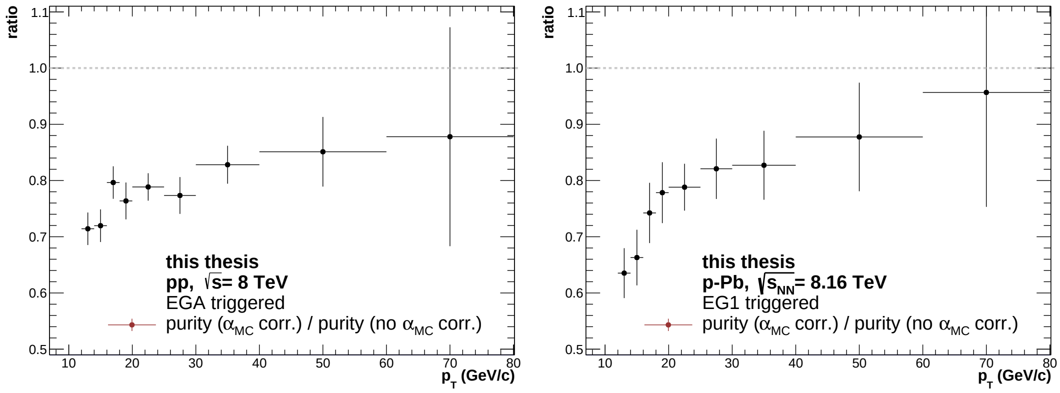

(a) pp collisions (b) p–Pb collisions

Figure 8.8: Ratios of the purity obtained with the ABCD method including a correction α_{MC} calculated according to Eq. 8.11 with respect to the fully data-driven purity given in Eq. 8.9.

8.2.1 *Accuracy of correlation description in MC*

In the previous section, the data-driven purity was corrected using an additional factor α_{MC}, which takes into account correlations of the shower shape and isolation energy. This correction is obtained from MC, and introduces *Assumption 2b*, i.e. that the underlying correlations are accurately captured by the used MC. As for the template fitting approach, this assumption is tested using the double ratio R_{shape}, which is defined in Eq. 8.5 and shown in an exemplary p_{T} interval for pp and p–Pb collisions in Fig 8.4. While the double ratio is flat for most p_{T} intervals within the statistical uncertainties, some residual slopes can be observed in some p_{T} intervals. It is important to recall that the absolute scale of this double ratio is not crucial, since the assumption stated in Eq. 8.10 is formulated in terms of double ratios: It is not required that the MC accurately captures the ratio $N^{\mathrm{iso}}/N^{\overline{\mathrm{iso}}}$. Instead, one only needs to rely on that fact that the dependence of this ratio on the shower shape is captured by the MC. The latter is reflected in the observed slope for R_{shape}. More precisely, since the ABCD method only considers regions in the σ^2_{long}-isolation phasespace, a statement about the accurate description of the shower shape dependence simplifies to a statement about the ratio $N^{\mathrm{iso}}/N^{\overline{\mathrm{iso}}}$ in the "narrow cluster" ($N_n^{\mathrm{iso}}/N_n^{\overline{\mathrm{iso}}}$) and "wide cluster" ($N_w^{\mathrm{iso}}/N_w^{\overline{\mathrm{iso}}}$) regions. In the absence of any residual slopes, one would therefore find:

$$\frac{R_{\mathrm{shape}}\left(\sigma^2_{\mathrm{long,n}}\right)}{R_{\mathrm{shape}}\left(\sigma^2_{\mathrm{long,w}}\right)} = 1 \qquad (8.12)$$

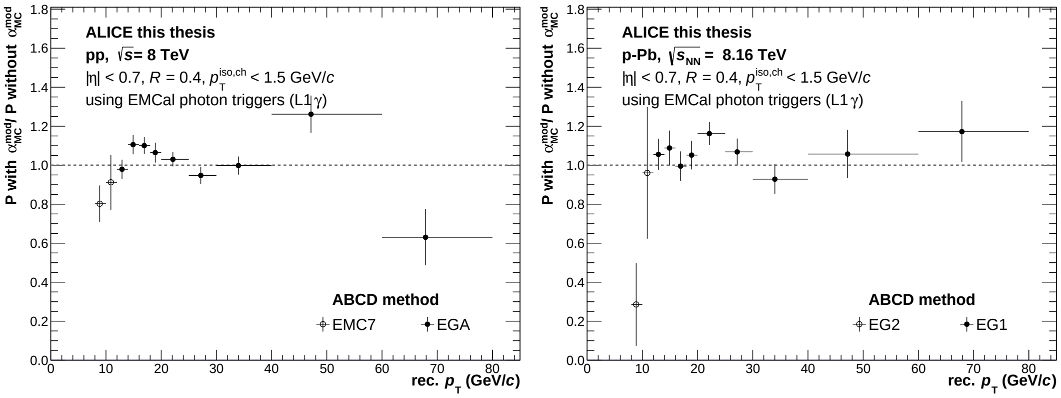

(a) pp collisions (b) p–Pb collisions

Figure 8.9: Impact of a modified correction $\alpha_{\mathrm{MC}}^{\mathrm{mod}}$ given in Eq. 8.13 on the purity estimate using the ABCD method. The purity ratio with and without this additional correction is shown for the pp and p–Pb sample, respectively, where the used EMCal triggers are denoted in the legend.

Therefore, in order to check the impact of any residual slopes on the purity estimate, a revised correction $\alpha_{\mathrm{MC}}^{\mathrm{mod}}$ replacing α_{MC} can be constructed, which is given by:

$$\begin{aligned}\alpha_{\mathrm{MC}}^{\mathrm{mod.}} &= \left(\frac{B_n^{\mathrm{iso}}/N_n^{\overline{\mathrm{iso}}}}{N_w^{\mathrm{iso}}/N_w^{\overline{\mathrm{iso}}}}\right)_{\mathrm{MC}} \times \left(\frac{R_{\mathrm{shape}}\left(\sigma^2_{\mathrm{long,n}}\right)}{R_{\mathrm{shape}}\left(\sigma^2_{\mathrm{long,w}}\right)}\right)\\ \alpha_{\mathrm{MC}}^{\mathrm{mod.}} &= \alpha_{\mathrm{MC}} \times \left(\frac{p_0 + \mathrm{med}(\sigma^2_{\mathrm{long,n}}) \cdot p_1}{p_0 + \mathrm{med}(\sigma^2_{\mathrm{long,w}}) \cdot p_1}\right),\end{aligned} \tag{8.13}$$

where $\mathrm{med}(\sigma^2_{\mathrm{long,n}})$ and $\mathrm{med}(\sigma^2_{\mathrm{long,w}})$ denote the median values of narrow $(0.1 \leq \sigma^2_{\mathrm{long}} \leq 0.3)$ or wide $(0.4 \leq \sigma^2_{\mathrm{long}} \leq 2.0)$ clusters, respectively. The parameters p_0 and p_1 are obtained from the first-order polynomial fit of the double ratio. The medians serve as a proxy for the average probed cluster shape in the "narrow" and "wide" cluster regions.

Fig. 8.9 shows the impact of the modified correction $\alpha_{\mathrm{MC}}^{\mathrm{mod}}$ on the purity estimate. Significant deviations from unity are observed for $p_{\mathrm{T}} \lesssim 12\,\mathrm{GeV}$, especially for the p–Pb sample. For reference, Fig. 8.10 shows the corresponding double ratios R_{shape} in both collision systems, which were used to extract $\alpha_{\mathrm{MC}}^{\mathrm{mod}}$ in the lowest covered momentum interval of $8\,\mathrm{GeV}/c \leq p_{\mathrm{T}} \leq 10\,\mathrm{GeV}/c$. Both collision systems showcase a residual slope with low statistical significance, which seems to be driven especially by the data points with $\sigma^2_{\mathrm{long}} \lesssim 0.9$. While the observed slopes are small, they have a significant impact on the purity determination at low p_{T}: As illustrated later in Fig. 8.11, the signal purity is below 20 % for $p_{\mathrm{T}} \lesssim 12\,\mathrm{GeV}/c$. In this region, small changes of α_{MC} result in big relative changes of the determined purity. For example, for an assumed signal purity of 15 %, a relative change of α_{MC} by only about 5 % would result in a relative change of almost 30 % on the determined purity, where α_{MC} enters via $P = 1 - (\cdots \times \alpha_{\mathrm{MC}})$.

The previously outlined studies showcase that the validity of *Assumption 2b* becomes increasingly important at low-p_{T}, where even small differences between data and MC can lead to significant modifications of the determined signal purity. However, even though

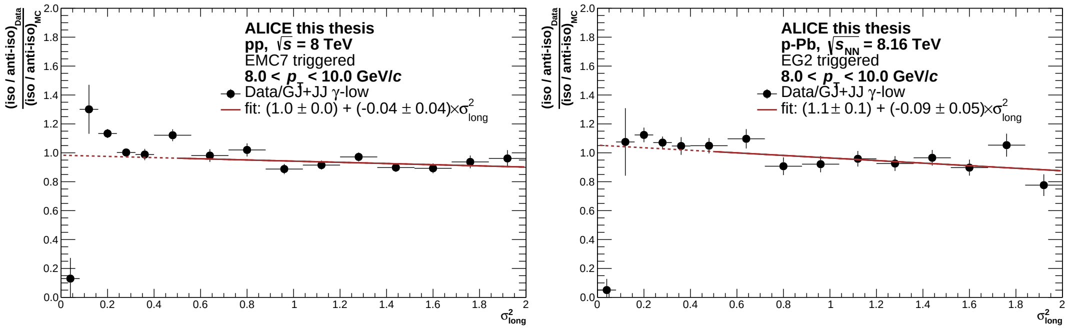

(a) pp collisions

(b) p-Pb collisions

Figure 8.10: Double ratio calculated according to Eq. 8.5 for the lowest covered p_{T}-interval for pp (left) and p–Pb (right) collisions. A first-order polynomial fit is indicated by a red line, where the solid part of the line indicates the fit region. A slope of ≈ 0 indicates agreement between data and MC in their description of the isolation dependence of the shower shape parameter.

the additional correction introduced in Eq. 8.13 allowed to showcase a potentially large impact of any mismatch on the extracted purity, the implementation of this correction for the "default" purity estimate used in this work is challenging. As illustrated in Fig. 8.10 determination of the slope parameter p_1 is highly impacted by statistical fluctuations, which is reflected in the quoted statistical uncertainty of the fit parameter. Instead, the impact of any residual slopes on the purity determination are considered as a systematic uncertainty, which is discussed in detail in Sec. 9. The steeply increasing uncertainty at low-p_{T} attributed to the residual slopes then reflects the observation that *Assumption 2b* becomes increasingly important for low purities, as well as the fact that one can only demonstrate the validity of *Assumption 2b* with limited accuracy.

8.3 PURITY RESULTS

The isolated prompt photon purities obtained using the template fitting approach and the ABCD method are shown in Fig. 8.11 for pp and p–Pb collisions at $\sqrt{s_{\mathrm{NN}}} = 8\,\mathrm{TeV}$ and 8.16 TeV, respectively. Both purity estimates have been corrected for the correlation of shower shape and isolation quantity, as discussed in the previous sections, and vertical bars and boxes denote the statistical and systematic uncertainties, respectively. In order to account for the finite width of the p_{T} bins [235], the bin centres are shifted in the p_{T}-direction according to the mean p_{T} value of the prompt photon cross section in the respective interval, which are obtained from the parametrizations given in Fig. 11.1 and Fig. 11.2. In both collision systems the purity is found to be rising from about 15 % at $p_{\mathrm{T}} \approx 10\,\mathrm{GeV}/c$ up to about $60-70\,\%$ for the largest covered momenta. Overall, the signal purity is found to be slightly smaller in p–Pb collisions with respect to pp collisions, which can most likely be attributed to the effects discussed in Sec. 7.3 as well as the larger UE. Agreement between both purity estimation methods is observed within the statistical and systematic uncertainties (see. Sec. 9), which serves as an important cross-check of the validity of both approaches. The purity estimates for the EMC7 and EG2 triggers in pp and p–Pb collisions, respectively, are indicated by open markers and in agreement with the estimates for the highest EMCal photon triggers. No purity could

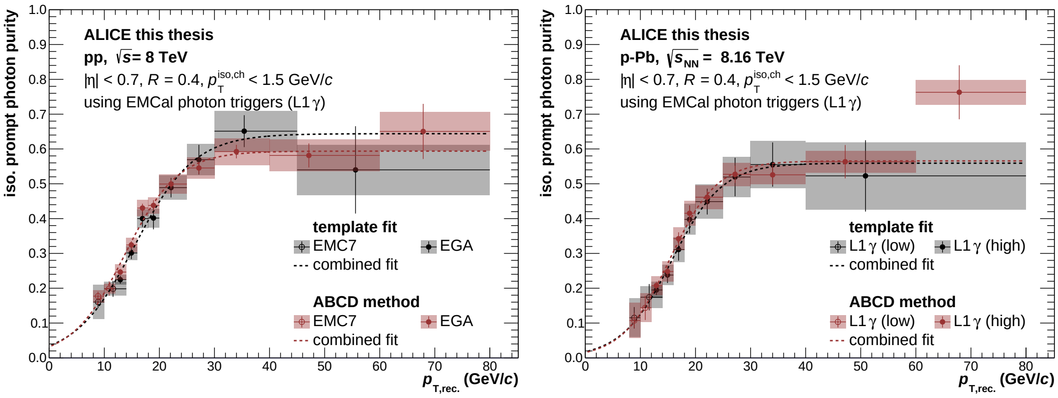

(a) pp collisions

(b) p–Pb collisions

Figure 8.11: Fully corrected purities obtained using the template fit method (black) and the ABCD method (red) in pp (left) and p–Pb (right) collision data. The vertical bars and boxes respectively denote the statistical and systematic uncertainties of the estimate (see Sec. 9). The purities of each method are fitted using a function given in Eq. 8.14, which takes into account the purities obtained using both triggers in each system.

be determined for even lower p_{T} in the MB samples, where the purity is expected to be $\lesssim 10\,\%$. For large transverse momenta, the measurement is limited by the available statistics, allowing for a purity determination for clusters with $p_{\mathrm{T}} \leq 80\,\mathrm{GeV}/c$. A wider p_{T} bin width is used for the template fitting approach at high p_{T}, in order to improve the stability of the fit. A finer p_{T}-binning could be achieved using the ABCD method, which only considers count integrals in each region rather than the shape of the σ^2_{long} distribution (see Sec. 8.5).

In order to reduce the impact of statistical fluctuations, the obtained purities are each fitted with a Sigmoid function:

$$P_{\mathrm{fit}} = \frac{a_0}{\exp\left(-a_1 \cdot (p_{\mathrm{T}} - a_2)\right)}, \tag{8.14}$$

where a_1, a_2 and a_3 denote the free parameters of the fit. The used functional form is motivated by the purity observed in MC and was found to well describe the purity in data. A variation of the parametrization, as well as the uncertainty of the fit parameters are taken into account in the evaluation of the systematic uncertainties (Sec. 9).

8.4 MONTE CARLO CLOSURE

In order to check the validity of both approaches, a so-called MC closure check is performed. Using the sum of GJ and JJ γ-high MC, where each production is scaled according to its cross section, purity estimates are obtained for each method, which are shown in Fig. 8.12 for the highest EMCal photon trigger in each collision system. The MC is treated in the same way as the data sample, and all previously discussed corrections are applied. The available information from the MC event generator allows to obtain a "true" reference purity, which is indicated by red open markers in the respective figures. For the ABCD method (green), the obtained purity agrees exactly with the reference purity, which is true "by construction" as illustrated when replacing the first term in

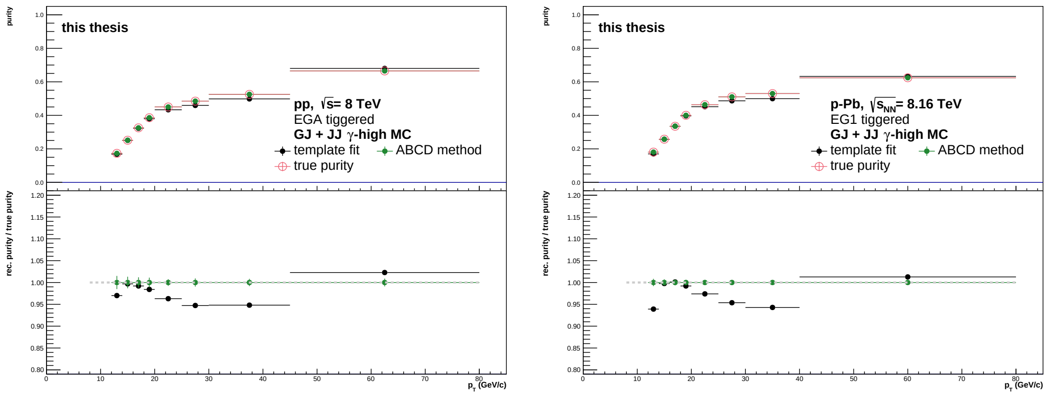

(a) pp collisions

(b) p–Pb collisions

Figure 8.12: Purities obtained from the sum of the GJ and JJ γ-high sample using both purity estimation techniques. The purities are compared to the purity obtained using information from the MC event generators.

Eq. 8.11 with the one obtained from the GJ+JJ MC. The perfect agreement between the ABCD estimate and reference purity serves as an important check for the validity of the implementation of the method in the analysis code. For the template fit, agreement is not expected by construction, as the results depend on the convergence of the fit and the discriminatory power of the shape of the σ^2_{long} distributions rather than their absolute integrals in a given region. The template fit estimate is found to agree within 5 % with the reference purity, where deviations could be mainly attributed to the shower shape binning of $\Delta\sigma^2_{\mathrm{long}} = 0.01$ in the signal region, which affects the convergence of the fit as well as the accuracy of the bin-by-bin integration. This is illustrated in Fig. 8.13, which shows the closure check in pp collision data for various choices of $\Delta\sigma^2_{\mathrm{long}}$. One finds that the observed discrepancies for the template fit closure check can be recovered using a finer σ^2_{long}, as illustrated in Fig. 8.13d. However, this smaller binning was found to not be feasible for the template fit method in data, which is limited by the statistical precision.

8.5 REMARKS ON ABCD METHOD VS. TEMPLATE FIT METHOD

As illustrated in Fig. 8.11, both purity estimation techniques allow to obtain the signal purity in a mostly data-driven way for the whole covered transverse momentum range. Furthermore, both purity estimates are compatible with each other within the experimental uncertainties. Nonetheless, as mentioned at the beginning of this chapter, the ABCD method is used as the default method to obtain the signal purity, whereas the template fitting approach is merely used as a cross-check. This section briefly outlines the key differences between both methods and why the ABCD method was chosen over the template fitting approach.

Both methods determine the purity in a data driven way using the same information: the shower shape and the isolation energy. However, both methods use this information in different ways, which has consequences for the stability of the purity determination. The ABCD method uses double ratios of *integrated counts* in the three background dominated control regions in order to obtain an estimate for the purity in the signal

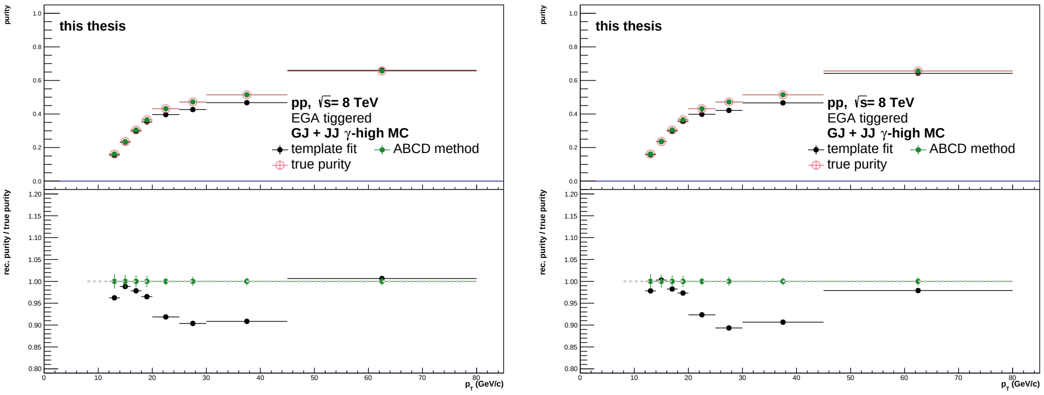

(a) $\delta\sigma^2_{\text{long}} = 0.02$ (b) $\delta\sigma^2_{\text{long}} = 0.04$

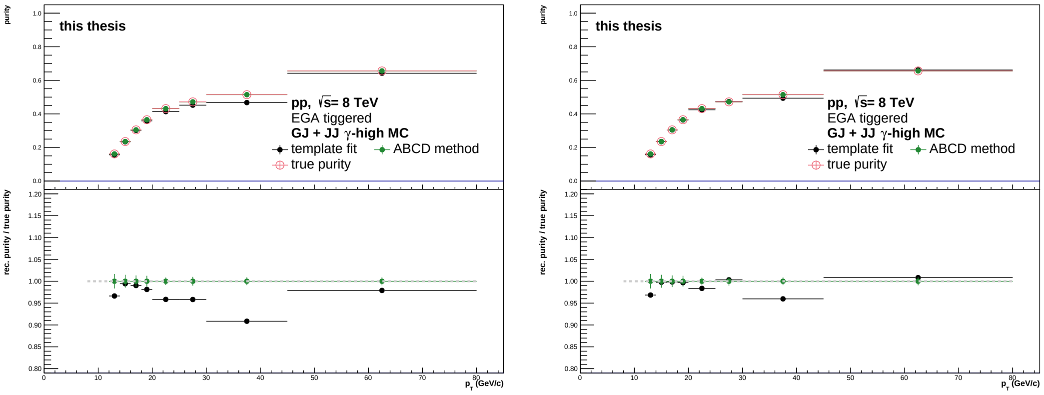

(c) p_{T} dependent $\delta\sigma^2_{\text{long}}$ (d) $\delta\sigma^2_{\text{long}} = 0.005$

Figure 8.13: Closure check for the purity estimates shown for different $\delta\sigma^2_{\text{long}}$ binnings.

region. The template fit on the other hand is inspecting the shape of the distributions in different regions, rather than using integrals. This makes the template fit more susceptible to statistical fluctuations, which may affect the convergence of the fitting procedure and the fit stability. Furthermore, the fitting procedure introduces uncertainties for the purity estimate, such as for example from the choice of the shower shape resolution $\delta\sigma^2_{\text{long}}$, which has been demonstrated in the previous section. It was therefore decided to use the ABCD method as the default method in this work to estimate the signal purity, as it was found to be more robust and stable compared to the template fitting approach.

Nonetheless, both approaches have limitations, which become especially evident at low p_{T}: As the opening angle between the photons from $\pi^0 \rightarrow \gamma\gamma$ decays increases, the long shower shape axis looses discriminatory power because the probability to observe merge clusters decreases. In addition, the signal purity becomes small at low-p_{T}, making it increasingly challenging to obtain an accurate data-driven determination. This is reflected in the large systematic uncertainties at low-p_{T}, which are presented in Sec. 9 and the purity determination ultimately limits the low-p_{T} reach of this measurement. For future analyses, new improved purity determination approaches could be considered that hopefully allow to extend the low-p_{T} reach of the measurement. For example, one could calculate the invariant mass of all photon pairs in a given event that include the isolated photon candidate, allowing to identify pairs with masses in the vicinity of the nominal π^0 and η meson masses (see also Sec. 12.2). This information could then be used as an additional variable carrying information for the purity determination. The determination could be performed using e.g. two-dimensional template fits or novel machine learning approaches using boosted decision trees. In addition, rather than attempting to obtain the signal purity in the low-p_T regime, one can also consider statistical approaches, where known background distributions are subtracted from the isolated prompt photon yield, as done for direct photon measurements [60]. However, the latter would require novel techniques to consider the impact of the isolation requirement, which is not imposed for direct photon measurements.

9

SYSTEMATIC UNCERTAINTIES

The systematic uncertainties of the measurement are identified and evaluated by varying the selection criteria discussed in the previous sections. The evaluation is performed for each trigger and collision system on the level of the isolated prompt photon cross sections (see. Eq. 11.1). As discussed in Sec. 8, the ABCD method is used as the default method to determine the purity of measurement, whereas the template fit method is used as a semi-independent cross-check. Therefore, the following discussion focusses on the systematic uncertainties using the ABCD method for the purity determination. Exceptions are the systematic uncertainties shown for the purity in Fig. 8.11, which are discussed separately at the end of this section. For a given source of systematic uncertainty (e.g. from the $\sigma^2_{\rm long}$ selection), the uncertainty is estimated using the relative change of the cross section as a function of photon $p_{\rm T}$ for multiple variations of the selection criterium. In order to remove statistical fluctuations, the obtained deviations are fitted with an appropriate functional form. It is chosen to describe the observed $p_{\rm T}$ dependence and a constant is used in cases where no such dependence is found. For the nuclear modification factor (see. Sec. 11.2) the uncertainties are evaluated directly on the ratio, by simultaneous variation of a given selection in both collision systems. This allows to take into account any present correlations between the systematic uncertainties of both systems.

An overview of all uncertainties for the isolated photon cross section in pp and p–Pb collisions, as well as for the nuclear modification factor $R_{\rm pA}$ is given in Tab. 9.1. In addition, Fig. 9.1 gives a graphical overview of the $p_{\rm T}$ dependence of all uncertainty sources for the studied observables. The total systematic uncertainty of the measurement in each $p_{\rm T}$ interval is given by the quadratic sum of the uncertainties from all identified sources, assuming that the sources are not correlated among each other in a given collision system. Overall, the systematic uncertainties are dominated by sources related to the purity determination, as well the identification of photon candidates using the shape of the electromagnetic shower in the calorimeter. In particular, the uncertainty of the purity parametrization, as well as the correction for residual correlations between shower shape and isolation energy dominate the uncertainties of the measurement. While the overall uncertainties are below 14 % (22 %) for the cross section in pp (p–Pb) collisions for $p_{\rm T} \gtrsim 12\,\mathrm{GeV}$, a steep increase of the uncertainties is observed below this threshold, reaching up to 61 % for the cross section in p–Pb collisions at the lowest covered $p_{\rm T}$. This steep increase is driven by the aforementioned purity determination, which becomes increasingly challenging for small signal purities. The systematic uncertainty of the $R_{\rm pA}$ is smaller than 23 % for $p_{\rm T} \gtrsim 12\,\mathrm{GeV}$, however, it likewise drastically increases for the lowest covered $p_{\rm T}$. In the following, each source of systematic uncertainty and its evaluation is described.

Table 9.1: Overview of the systematic uncertainties of the isolated prompt photon production cross section in pp and p–Pb collisions at $\sqrt{s_{\mathrm{NN}}} = 8\,\mathrm{TeV}$ and 8.16 TeV, respectively, as well as the nuclear modification factor R_{pA}. The uncertainties are given in percent for three exemplary momentum ranges. The total systematic uncertainty is given as the quadratic sum of the uncertainties from the given sources. Sources labelled with the "†" symbol are considered in addition for the systematic uncertainty of the purity, given by boxes in Fig. 8.11.

Name	cross section pp			cross section p–Pb			R_{pA}		
	9 GeV/c	13 GeV/c	50 GeV/c	9 GeV/c	13 GeV/c	50 GeV/c	9 GeV/c	13 GeV/c	50 GeV/c
anti-isolation†	3.0 %	0.9 %	0.9 %	4.0 %	1.2 %	0.4 %	5.0 %	2.0 %	2.0 %
M02 signal	4.9 %	4.9 %	4.9 %	5.0 %	7.0 %	7.0 %	6.0 %	6.0 %	6.0 %
track matching	2.9 %	0.1 %	0.6 %	3.5 %	1.1 %	1.1 %	1.1 %	1.0 %	1.0 %
distance to BC†	2.5 %	2.6 %	3.4 %	3.0 %	3.0 %	3.0 %	3.0 %	0.7 %	0.7 %
UE estimation	5.6 %	0.6 %	0.6 %	13.1 %	3.5 %	3.5 %	6.1 %	2.9 %	2.9 %
GJ mixing-ratio†	2.0 %	0.1 %	4.5 %	2.0 %	1.0 %	3.5 %	0.2 %	0.7 %	0.7 %
NLM selection	3.0 %	3.0 %	3.0 %	11.8 %	3.0 %	3.0 %	15.3 %	3.0 %	3.0 %
M02 background†	3.7 %	2.0 %	2.0 %	3.6 %	2.0 %	2.0 %	4.2 %	1.9 %	1.9 %
cross talk emulation†	2.8 %	2.9 %	4.1 %	2.7 %	2.7 %	4.8 %	0.1 %	0.3 %	0.7 %
purity function	21.3 %	10.1 %	6.1 %	35.8 %	15.5 %	9.2 %	41.6 %	18.5 %	11.0 %
slope correction†	8.8 %	4.0 %	4.0 %	44.2 %	10.2 %	1.7 %	38.9 %	8.0 %	0.0 %
trigger mimic†	0.4 %	0.2 %	2.2 %	7.4 %	3.0 %	5.3 %	8.4 %	3.5 %	3.0 %
energy scale†	1.1 %	1.0 %	3.6 %	1.7 %	1.1 %	2.2 %	3.0 %	3.0 %	3.0 %
material budget	2.1 %	2.1 %	2.1 %	2.1 %	2.1 %	2.1 %	3.0 %	3.0 %	3.0 %
trigger RF	0.1 %	2.8 %	2.8 %	2.1 %	2.2 %	2.2 %	2.1 %	2.2 %	2.2 %
total	25.6 %	13.6 %	13.1 %	60.9 %	21.4 %	15.8 %	60.8 %	22.4 %	14.7 %

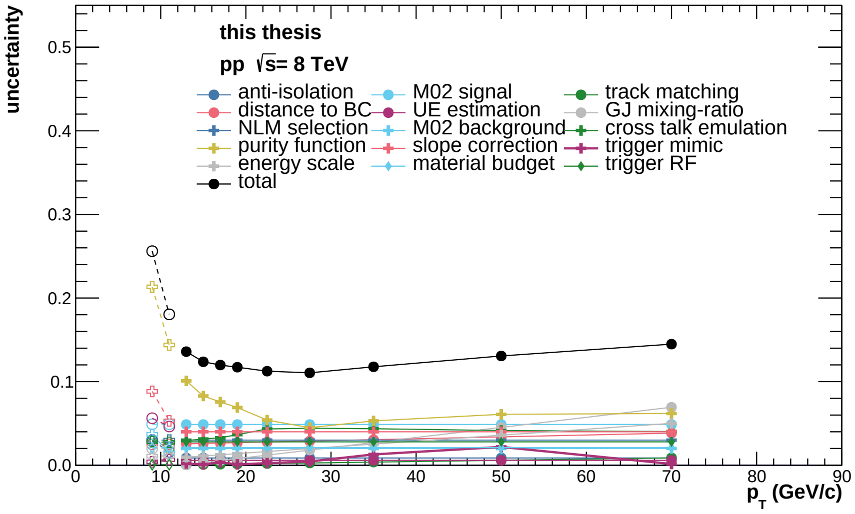

(a) cross section pp collisions at $\sqrt{s} = 8\,\text{TeV}$

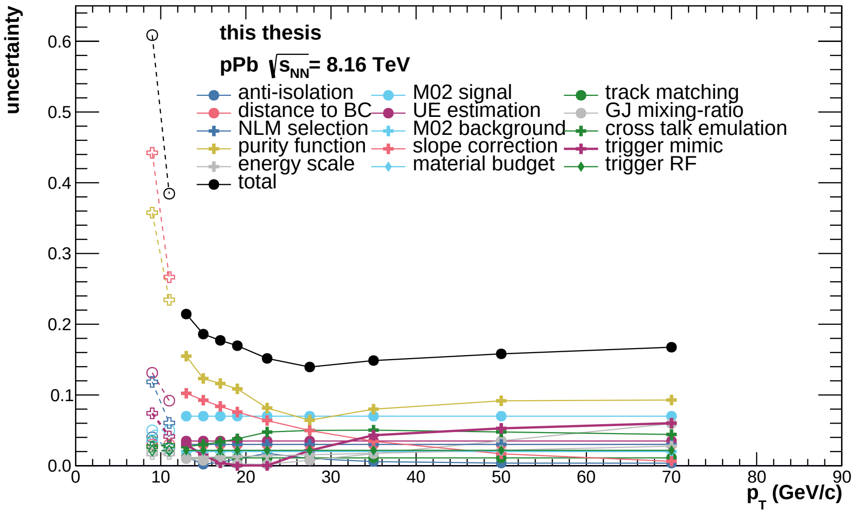

(b) cross section p–Pb collisions at $\sqrt{s_{\text{NN}}} = 8.16\,\text{TeV}$

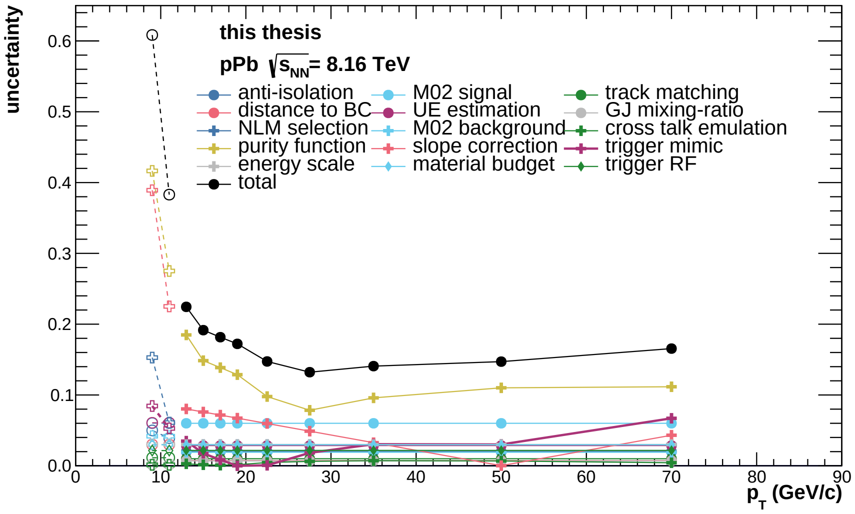

(c) nuclear modification factor R_{pA}

Figure 9.1: Overview of the p_{T}-dependence of the relative systematic uncertainties for the cross section measurement in the respective collision systems, as well as the R_{pA}. The closed markers denote the uncertainties obtained for the cross section measurements using the respective high threshold EMCal-γ triggers (EGA and EG1). The open markers denote that the low threshold triggers have been used.

SHOWER SHAPE SELECTION Several systematic effects related to the electromagnetic shower shape have been identified:

1. The signal shower shape requirement $(0.1 < \sigma^2_{\text{long}} < 0.3)$
2. The background cluster selection $(0.4 < \sigma^2_{\text{long}} < 2.0)$ used for the purity determination with the ABCD method.
3. The cross talk emulation, which affects the accuracy of the shower shape description in MC.

The shower shape signal selection uncertainty is estimated using four variations of the selection criterium, resulting in a systematic uncertainty of about 5 % and 7 % in pp and p–Pb collisions, respectively. A moderate cancellation of this uncertainty is observed on the R_{pA}, where one finds a systematic uncertainty of about 6 %. The impact of the shower shape selection for background clusters, which is used in the purity determination of the ABCD method has been evaluated using two variations of the lower σ^2_{long} threshold. One finds an uncertainty smaller than for the signal shower shape selection of at most 2 % for the highest trigger in both collision systems. A small increase of this uncertainty is observed below $p_{\text{T}} \approx 12\,\text{GeV}$, resulting in an uncertainty of up to 4 % at $p_{\text{T}} \approx 9\,\text{GeV}$. The systematic uncertainty arising from the cross talk emulation (see. Sec 5.4) is evaluated by performing the analysis without any cross talk emulation in both collision systems. Without any cross talk emulation in MC, the cross section is found to be lower by up to 10 % for $p_{\text{T}} \gtrsim 20\,\text{GeV}$. A smaller reduction of about 5 % is found for lower p_{T}. Since cross-talk between EMCal channels does exist and has been confirmed in the laboratory [184], using no cross-talk emulation is not correct, and the observed deviation of up to 10 % on the cross section can only serve as an upper bound of the systematic uncertainty association with the emulation in MC. Instead, half of the observed deviation in each p_{T} interval is considered as systematic uncertainty arising from the cross-talk emulation. The uncertainty is found to almost fully cancel for the R_{pA}, where one finds a remaining uncertainty of below 1 % for the full covered momentum range.

ENERGY SCALE UNCERTAINTY As outline in Sec. 5.2.4, the nonlinearity of the EMCal energy response is determined using test-beam data, as well as a correction of the absolute energy scale of each cell using a comparison the invariant mass of π^0 candidates. Good agreement of the energy response in data and MC is ensured using the *cluster energy fine-tuning*, which corrects for residual differences in the energy response in data and MC using $\pi^0 \rightarrow \gamma\gamma$ decays, where the two photons are measured using the calorimeter and the PCM. The systematic uncertainty of this evaluation is obtained through several variations[1] of the procedure outline in Sec. 5.2.4:

1. Variation of the photon reconstruction method: EMC (both photons reconstructed using the calorimeter) and PCM-EMC (one photon reconstructed using the PCM, one photon reconstructed with the EMCal)
2. Variation of the functional form of the parametrization used to correct the cluster energy

---

[1] I want to thank Joshua König and Nicolas Schmidt, who determined the energy fine-tuning for the used Run 1 and Run 2 dataset and provided me with different parametrizations used to determine the systematic uncertainty.

The uncertainty of the energy scale is found to increase with increasing p_{T}, reaching at most 4 % for the highest covered transverse momenta in both collision systems. The energy scale uncertainty is found to partially cancel for the R_{pA}, where one finds an uncertainty of about 3 %.

ISOLATION & UNDERLYING EVENT DESCRIPTION The isolation requirement fulfils multiple purposes in this analysis: Not only is it used to suppress the decay photon background and furthermore to determine the purity using it in conjunction with the shower shape, it is also part of the signal definition itself. The cross section is given as a fiducial *isolated* prompt photon cross-section, where the choice of isolation requirement impacts the size of the contributions from fragmentation photons. Therefore, a variation of the isolation requirement $p_{\mathrm{T}}^{\mathrm{iso}} \leq 1.5\,\mathrm{GeV}$ is not possible to assess the systematic uncertainty arising from the isolation determination. Instead, the impact of the isolation determination is quantified by studying the impact of the choice of the anti-isolation region on the data-driven purity determination. The chosen anti-isolation cut will not affect the purity in the signal region, and should therefore only be sensitive to possible systematic biases in the purity determination. Four variations of the anti-isolation selection are performed in both collision systems. Overall, one finds a small impact of this selection in both collision systems, which is at most about 4 % for the lowest covered p_{T} of $8\,\mathrm{GeV}/c$. The uncertainty is found to be mostly uncorrelated between both collision systems, and one obtains a similar uncertainty on the level of the R_{pA}.

The systematic uncertainty associated with the determination of the UE in the isolation cone is determined by using a k_{T}-jet finder instead of the perpendicular cone method for the UE determination, as outlined in Sec. 6.2. In pp collisions, the systematic impact of the UE determination is found to be negligible for $p_{\mathrm{T}} > 12\,\mathrm{GeV}/c$, with an increase toward lower p_{T} to up to about 5 %. A larger uncertainty is found for the p–Pb data, where the overall UE is also expected to be larger. One finds a systematic uncertainty ranging from about 13 % at low-p_{T} to about 3.5 % at high-p_{T}. This uncertainty partially cancels for the R_{pA}, ranging from 6 % to 3 %.

RESIDUAL CORRELATION OF SHOWER SHAPE AND ISOLATION One of the key assumptions made for the data-driven purity determination using the ABCD method is the absence of any correlation between the shower shape and the isolation energy. As outlined in Sec. 8.1.1, this assumption is not correct, thus making an additional correction using MC necessary to determine the purity. The validity of this MC correction is tested using the double ratio shown in Fig. 8.4, where an absence of a residual slope indicates that the correlation between shower shape and isolation energy is accurately captured by the used MC. However, small[2] residual slopes are observed in the double ratio, which indicate small remaining correlations not fully captured by the MC. To estimate the systematic uncertainty associated with these residual correlations, the obtained purity using the ABCD method is corrected for any residual slopes using Eq. 8.13. As for the “default” purity, the corrected purity is fitted using a Sigmoid function, in order to suppress statistical fluctuations. For $p_{\mathrm{T}} \geq 12\,\mathrm{GeV}$ one finds a moderate systematic uncertainty of up to 12 % in p–Pb collisions, which decreases with increasing p_{T}. However, a steep increase of the systematic uncertainty is observed for low-p_{T}, where

---

[2] Not all p_{T} intervals show statistically significant residual slopes. While the residual slope is small in all studies p_{T} intervals, only for some intervals the deviation is large enough to be considered statistically significant.

one finds deviations of up to 44 % on the level of the fully corrected cross section in p-Pb collisions at $p_{\mathrm{T}} \approx 9\,\mathrm{GeV}/c$. As shown in Fig. 8.11, the purity for $p_{\mathrm{T}} \leq 12\,\mathrm{GeV}$ is small and in the order of $10 - 20\,\%$. In this regime, even small corrections introduced in Eq. 8.13 can lead to significant relative changes of the purity, which is reflected in the steeply increasing systematic uncertainties. The performed studies indicate that the purity estimate becomes increasingly sensitive to the underlying assumptions for small purities. No significant correlation of this uncertainty source between both collision systems is observed, which can be attributed to the fact that the correlation of shower shape and isolation energy (driven by e.g. shower overlaps) is different in pp and p–Pb environments. While the uncertainty only slowly changes as a function of transverse momentum for $p_{\mathrm{T}} > 12\,\mathrm{GeV}/c$, the quick and steep rise of the uncertainty below this threshold indicates that the purity determination is especially challenging for $p_{\mathrm{T}} < 12\,\mathrm{GeV}/c$. Future studies are necessary to improve the purity estimate in this region in order to allow for competitive uncertainties in the low-x regime. These studies could include refined purity determination techniques using boosted decision trees or novel statistical approaches that replace the data-driven purity determination with a statistical subtraction of the decay photon background, similar to those employed by direct photon analyses [60].

GJ AND JJ MIXING RATIO The correction of the correlation between shower shape and isolation energy introduced in Sec. 8.1.1 is obtained from MC for the ABCD method and the template fitting approach. The MC is obtained using the sum of the GJ and JJ sample, weighted with their respective cross sections given by the Pythia event generator. The fraction of GJ processes in the overall MC sample therefore depends on the cross section predicted by Pythia, which are obtained using matrix elements at LO [77]. The systematic uncertainty associated with the so-called *mixing ratio* of the GJ and JJ sample is estimated by artificially increasing and decreasing the contribution of the GJ sample by a factor of two. This results in moderate systematic uncertainty on the cross section, which is increasing with increasing p_{T} up to at most 5 % in both collision systems. The uncertainties are found to be fully correlated between both collision systems, resulting in a negligible uncertainty on the level of the R_{pA}.

TRACK MATCHING The systematic uncertainty of the cluster track matching, which is used to remove clusters originating from charged tracks, is evaluated by studying four variations of the track matching criterium, including p_{T}-dependent variation of the $\Delta\varphi$-$\Delta\eta$ matching window. The uncertainty is found to be at most 1 % in both collision systems for $p_{\mathrm{T}} \gtrsim 12\,\mathrm{GeV}/c$.

PURITY FIT FUNCTION The data-driven purities shown in Fig. 8.11 are parametrized using a Sigmoid function in order to reduce statistical fluctuations. This introduces two potential systematic uncertainties:

1. The choice of the parametrizations functional form is arbitrary. For example, an error function could have been chosen to describe the purity instead of a Sigmoid function.
2. The free parameters of the parametrization themselves have an associated uncertainty.

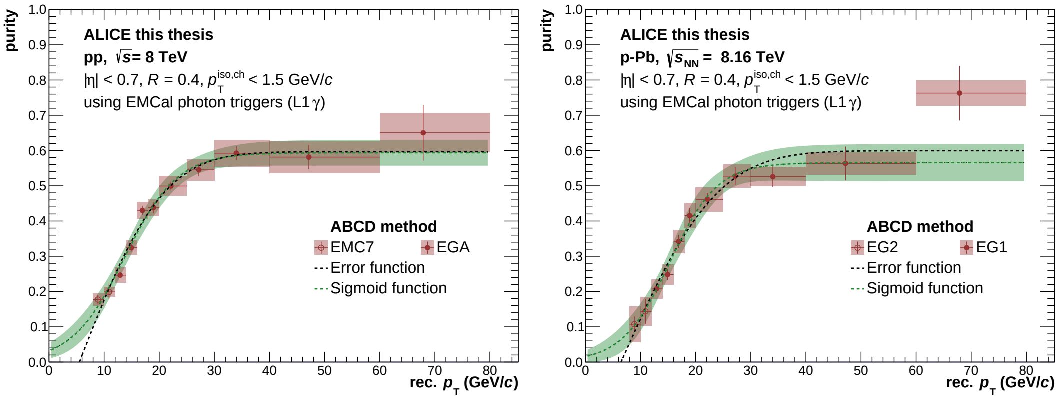

(a) pp at $\sqrt{s} = 8\,\text{TeV}$ (b) p–Pb at $\sqrt{s_{\text{NN}}} = 8.16\,\text{TeV}$

Figure 9.2: Purity obtained using the ABCD method shown together with different purity parametrizations. The fit using a Sigmoid function (green), which is used as the default parametrization in this analysis, is shown together with band, which reflects the uncertainties of the fit parameters at 90 % CL. The boxes denote the systematic uncertainty of the data-driven purity determination.

Fig. 9.2 shows the purities obtained using the ABCD method for the pp and p–Pb data, respectively. The purity parametrization using a Sigmoid function is shown together with a band, reflecting the uncertainties of the fit parameters at 90 % CL. In addition, an alternative parametrization of the purity using the error function is denoted by a black dashed line. Within the covered p_{T} range, one finds good agreement between both parametrization for both collision systems. Since the alternative parametrization is covered by the uncertainties of the Sigmoid fit, only the shown uncertainty band is used as the systematic uncertainty of the purity fit, in order to avoid double counting. This uncertainty is the dominant uncertainty of the measurement, and found to be decreasing with increasing photon p_{T}. It is largest for the cross section in p–Pb with about 36 % at $p_{\text{T}} = 9\,\text{GeV}/c$. However, it quickly decreases to below 15 % for $p_{\text{T}} \gtrsim 12\,\text{GeV}/c$. This uncertainty is assumed to be fully uncorrelated between both collision systems, and therefore added in quadrature to obtain the systematic uncertainty on the level of the R_{pA}.

TRIGGER REJECTION FACTOR & TRIGGER MIMICKING The determination of the trigger rejection factor is discussed in detail in Sec. 4.2 and 4.3.1 and relies on fits of cluster spectra ratios of the respective triggers in the high-p_{T} plateau region. A small systematic uncertainty is introduced by the choice of the high-p_{T} fit range, which has been estimated via multiple variations of the p_{T} region used for the fit. In addition, corrections for the trigger efficiency are introduced, which rely on mimicking the TRU response in MC. The systematic uncertainty arising from potential inaccuracies of the trigger mimicking in MC is estimated using the following variations:

1. The analysis is performed using no trigger mimicking at all. This means the trigger rejection factor is not corrected for any trigger inefficiencies and furthermore it is not taken into account in the signal efficiency.

2. The analysis is performed only correcting the trigger rejection factor for inefficiencies using MC, however, it is not taken into account in the determination of the signal efficiency

As for the cross-talk emulation uncertainty, the uncertainty arising from the used trigger mimicking is conservatively estimated using half of the deviations observed for the fully corrected cross sections and the R_{pA}. The impact of the chosen fit range for the trigger rejection factor determination is found to be small – at most 3 % for the cross section in pp data. The impact of the trigger mimicking is largest for the p–Pb data, where it reaches up to about 7.5 % for the lowest covered photon p_{T}.

OTHER CLUSTER SELECTIONS Of the cluster selection criteria given in Tab. 5.1, only the *number of local maxima* (*NLM*) selection and the requirement on the *minimum distance to a bad channel* were found to have a none-negligible impact on the isolated prompt photon cross section. Both selections impact the observed shower shape, which impacts the purity estimation. Three variations are performed for the selection according to the number of local maxima of the cluster, resulting in an uncertainty of about 3 % at high-p_{T} for both collision systems. For the p–Pb data, a steep increase of the uncertainty is observed for $p_{\mathrm{T}} < 12\,\mathrm{GeV}/c$ up to about 11 %, which propagates to an uncertainty of about 15 % on the R_{pA}. The systematic uncertainty associated with the distance to bad channel selection was found to be at most 3.5 %.

MATERIAL BUDGET For measurements of photons using the EMCal calorimeter, a small systematic uncertainty is introduced due to the so-called *outer material budget*, which refers to the detector material present directly in front of the calorimeter. In particular, the material of the TRD and TOF detector systems, as well as the outer wall of the TPC. This material leads to additional photon conversions, which impact the achievable energy resolution of the calorimeter. While these effects are considered in the used MCs, where the material in front of the EMCal is implemented in GEANT, the accuracy of this implementation is limited by the precision of our knowledge of the exact distribution of each material present in front of the calorimeter. To estimate the impact of a potential mismatch between the material budget in data and MC, studies were performed using $\pi^0 \rightarrow \gamma\gamma$ decays in pp collision data at $\sqrt{s} = 8\,\mathrm{TeV}$ [236]: Since at the time not all TRD modules were yet installed, the π^0 spectrum was measured separately for EMCal super modules with and without TRD modules in front of them. The studies concluded that the outer-material introduces a 2.1 % systematic uncertainty per photon, independent of the photons transverse momentum. This uncertainty includes the material of the TOF and TRD, which were assumed to contribute to this uncertainty equally and independently. Therefore, a 2.1 % material budget uncertainty is assigned for the isolated prompt photon cross section in both collision systems. As the material budget should be slightly different in the pp and p–Pb data (due to the aforementioned difference in the number of installed TRD modules), the systematic uncertainty is conservatively treated as fully uncorrelated on the level of the R_{pA} and added in quadrature.

PILEUP While out-of-bunch pileup can be effectively suppressed using the timing information of the EMCal detector (see Fig. 5.6), the employed selections do not remove in-bunch-pileup, where multiple collisions may occur within the same crossing of

LHC bunches. As outlined in Sec. 4.1, in-bunch pileup is removed in the analysis by rejecting events with multiple reconstructed primary vertices, that each have at least 3 contributing vertices and a separation of at least 8 mm in the SPD. Using this selection, one finds that at most about 3.5 % of the MB events can be attributed to in-bunch pileup in both collision systems. Using this value as an upper bound of the pileup present in the MB collisions events and assuming the event selection would reject none of these events, the probability that a MB event contains in-bunch pileup is at most 3.5 %. This analysis is performed using high-p_{T} observables in EMCal triggered events, where the rejection of the triggers has been determined in Sec. 4.2. The probability to find a in-bunch pileup event in the triggered sample is therefore given by the product $3.5\,\% \times 1/\mathrm{RF}$, which amounts to at most 0.01 % for the analysed data. The impact of in-bunch pileup on the measurement is therefore negligible and not further considered.

UNCERTAINTY OF THE PROMPT PHOTON PURITY All previously outlined uncertainty sources are evaluated directly on the level of the fully corrected isolated prompt photon cross section in both collision systems, as well as on the level of the R_{pA} to allow for the cancellation of correlations between uncertainties from both collision systems. For illustrative purposes, systematic uncertainties are also shown for the purity estimates shown in Fig. 8.11. These uncertainties are obtained by studying the relative change of the purity for the aforementioned variations of the used selection criteria. However, only uncertainty sources that are not expected to directly affect the signal purity are considered. The considered sources are marked with a '†' symbol in Tab. 9.1, and e.g. do not include the variation of the signal shower shape selection. In this way, the shown uncertainties express the systematic uncertainty of the purity *estimation* rather than showcasing the impact of various selection criteria on the true signal purity.

Fig. 9.3 shows the thus obtained relative systematic uncertainties of the different purity estimates in the pp and p–Pb collision data. The systematic uncertainty arising from the purity fit function is not included, as the fit is only performed in a later stage of the analysis. Similar trends as for the fully corrected cross sections are observed, where one finds that the purity estimate is dominated by the uncertainty of residual correlations of shower shape and isolation quantity, resulting in a steep rise of the uncertainty in p–Pb collisions for $p_{\mathrm{T}} \lesssim 12\,\mathrm{GeV}/c$. Comparing the two purity estimation techniques, one finds slightly larger systematic uncertainties for the template fit method, where in particular a stronger sensitivity to the used cross talk emulation is observed. This can be attributed to the fact that the template fitting approach is directly sensitive to the shape of the σ^2_{long} distributions, whereas the ABCD method only considers the double ratios of integrals. Furthermore, the dependence of the template fit estimate on the chosen σ^2_{long} bin-width (see Sec. 8.5) introduces an additional uncertainty in the order of a few percent. For pp collisions, the systematic uncertainty of the template fit purity estimate is significantly larger than the one obtained with the ABCD method for $p_{\mathrm{T}} \lesssim 12\,\mathrm{GeV}/c$. In principle, both purity estimates should be equally affected by the underlying correlations of shower shape and isolation quantity. However, investigation showed that for the template fit method the Sigmoid function, which is used to suppress statistical fluctuations and fitted over the whole covered p_{T} range, tends to prefer overall smaller purity values for these two bins, resulting in the observed deviation of up to 30 %. This showcases again the previously mentioned sensitivity of the purity estimate

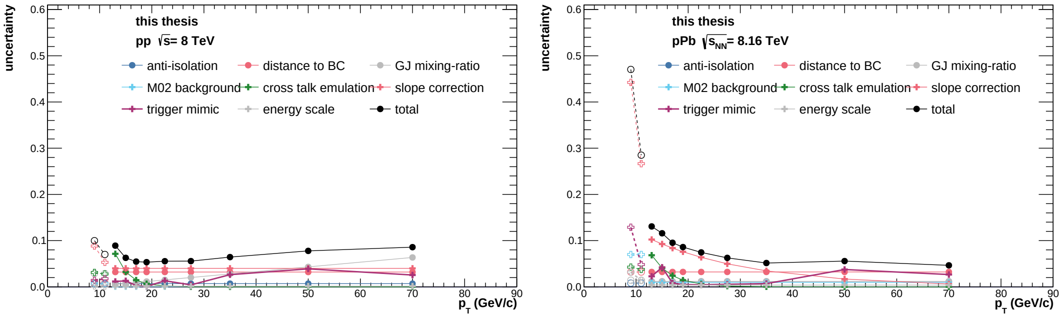

(a) ABCD method (pp collisions) (b) ABCD method (p–Pb collisions)

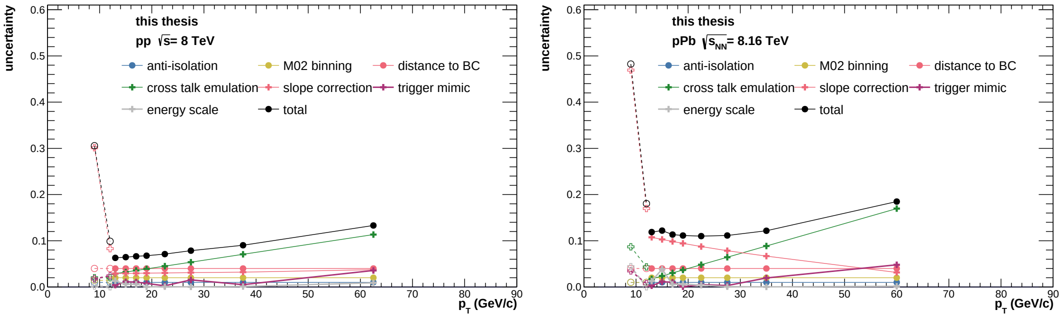

(c) temp. fit method (pp collisions) (d) temp. fit method (p-Pb collisions)

Figure 9.3: Overview of the p_T-dependence of the relative systematic uncertainties for the isolated prompt photon purity. The used purity estimation technique as well as the collision system are given in the respective figure caption. The closed markers denote the uncertainties obtained for the cross section measurements using the respective high threshold EMCal-γ triggers (EGA and EG1). The open markers denote that the low threshold triggers have been used.

for $p_T < 12\,\text{GeV}/c$, which is reflected in the sizable systematic uncertainties of the cross sections in this region.

In summary, one finds that the systematic uncertainties of the measurement are dominated by systematic uncertainty sources related to the purity estimation, mainly from the correction for the correlation of isolation energy and shower shape as well as the chosen fit parametrization to describe the purity. In particular, this results in a steeply increasing uncertainty for $p_T < 12\,\text{GeV}/c$ which illustrates the challenging purity extraction in this regime. Following the discovery of other effects at low-p_T, which are discussed in the following section, it was decided to only report the isolated prompt photon production cross sections in pp and p–Pb collisions for $p_T > 12\,\text{GeV}/c$ in this work, and the shown uncertainties below this threshold serve as a reference for future studies.

10

COMBINATION OF TRIGGERS

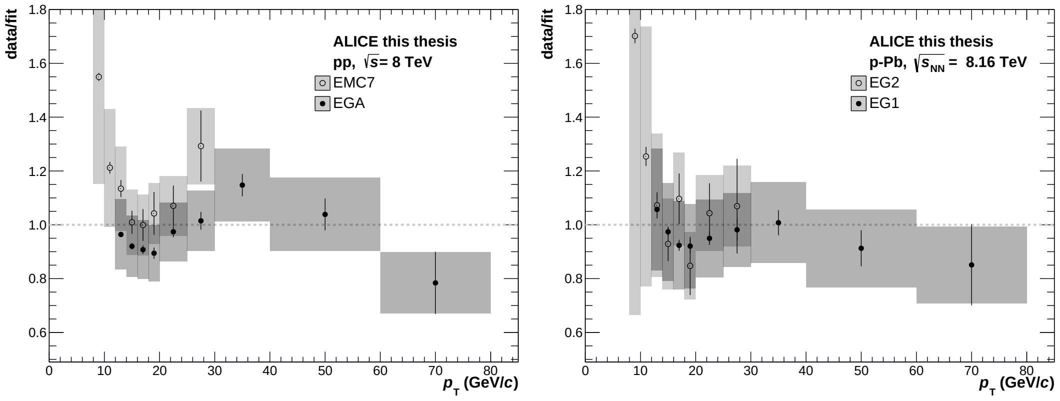

(a) pp collisions

(b) p–Pb collisions

Figure 10.1: Ratio of the fully corrected isolated prompt photon cross section to a modified power law fit (Eq. 10.1) for different EMCal photon triggered samples denoted in the respective legends. The fit is performed taking into account the cross section from the low-threshold EMCal triggers for $p_{\mathrm{T}} < 12\,\mathrm{GeV}/c$ and only the points from the high-threshold triggers for $p_{\mathrm{T}} \geq 12\,\mathrm{GeV}/c$.

As discussed in Sec. 4.2, the measurement is performed in each collision system using the EMCal L0 and L1 photon triggers in order to maximize the integrated luminosity for the studied high-p_{T} observable. The raw isolated prompt photon spectra as well as all corrections have been determined separately for each trigger sample and one obtains the corresponding fully corrected cross sections according to Eq. 11.1. In order to study the agreement of the measurements performed using the respective EMCal triggers, the cross sections are first fitted using a common modified power law function:

$$f_{\mathrm{fit}}(p_{\mathrm{T}}) = a_0 \cdot \left(1 + \frac{p_{\mathrm{T}}}{a_1}\right)^{-n}, \tag{10.1}$$

where a_0, a_1 and n are free parameters of the fit. The fit is performed taking into account the cross section from the low-threshold EMCal triggers (EMC7 and EG2) for $p_{\mathrm{T}} < 12\,\mathrm{GeV}/c$ and only the points from the high-threshold triggers (EGA and EG1) for $p_{\mathrm{T}} \geq 12\,\mathrm{GeV}/c$. The experimental uncertainties are taken into account in the fitting procedure, where in particular the quadratic sum of the statistical and systematic uncertainties is considered. Fig. 10.1 shows the ratio of the cross sections obtained with each EMCal photon trigger with respect to the aforementioned fit parametrization. The statistical and systematic uncertainties are denoted with vertical lines and filled boxes, respectively. For the p–Pb collision data (Fig. 10.1b), good agreement is observed between the EG1 and EG2 triggered sample within the uncertainties. Furthermore, both cross sections are in agreement with the combined fit within the uncertainties. However, increasing deviations between fit and data are observed for $p_{\mathrm{T}} < 12\,\mathrm{GeV}$, where the large systematic uncertainties of the EG2 triggered cross section do not provide significant

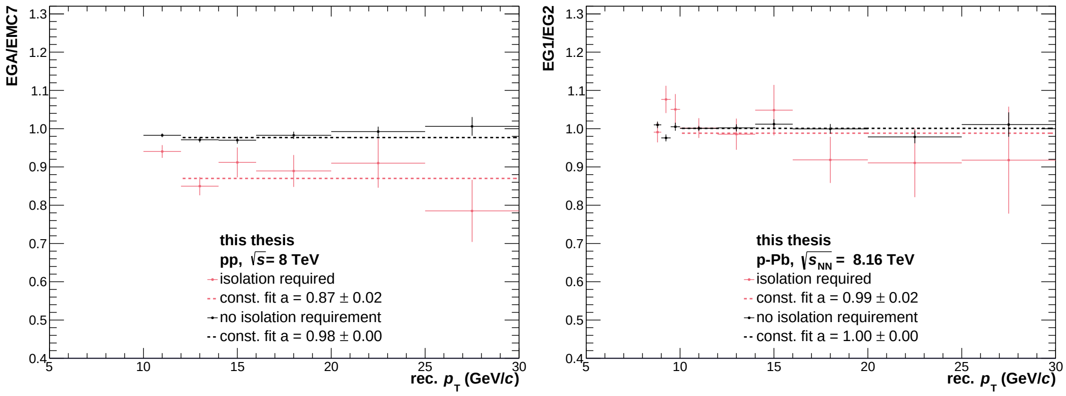

(a) pp collisions

(b) p–Pb collisions

Figure 10.2: Ratios of event-normalized raw cluster spectra from the highest available EMCal photon trigger with respect to the lower threshold trigger.

constrains for the fitting procedure. A different picture emerges for the measurement in pp collisions: Even though the cross sections using the EMC7 and EGA triggered sample are in agreement within the experimental uncertainties, the cross section from the EMC7 triggered sample tends to be systematically 10 % higher than for the EGA trigger in the overlap region between $p_T = 12\,\mathrm{GeV}/c$ and $30\,\mathrm{GeV}/c$. This deviation not expected. Several studies have been performed so far to investigate this issue, which will be outlined in the following.

10.1 INVESTIGATION OF TRIGGER NORMALIZATION

First, the event-normalized cluster spectra measured for both trigger samples in the respective collision systems have been compared. Only minimal cluster selection criteria are imposed, in particular the shower shape is required to fulfil $\sigma^2_{\mathrm{long}} > 0.1$ and the exoticity F_+ is required to be below 0.97. Furthermore, a selection on the cluster time of $-30\,\mathrm{ns} \leq t_{\mathrm{clus}} \leq 35\,\mathrm{ns}$ is imposed in order to remove out-of-bunch pileup contributions. Only a correction for the trigger efficiency outlined in Sec. 4.3.1 and *no* purity or reconstruction efficiency corrections are applied. The obtained cluster spectra are then scaled with the rejection factor of the respective EMCal trigger (see Sec. 4.2) and compared by calculating the ratio of the spectra obtained with the high threshold trigger with respect to the lower threshold. These ratios are shown as black markers for both collision systems in Fig. 10.2. As indicated by the constant fit, the raw cluster spectra ratios are in good agreement with unity for both collision systems. This is expected, considering that the same cluster selection criteria as for the rejection factor determination have been used. Next, the same ratios are determined for isolated clusters, i.e. only clusters that fulfil in addition $p_T^{iso} < 1.5\,\mathrm{GeV}/c$ in a cone with $R = 0.4$. The corresponding ratio is indicated by red markers in Fig. 10.2. While good agreement between both triggers is observed for the p–Pb collision data, significant deviations are observed in pp collisions. These deviations are of similar size as to those observed on the level of fully corrected cross sections in Fig. 10.1. This indicates that the imposed isolation requirement has a different impact on the measurement using the EMC7 trigger with respect to the EGA triggered sample. This effect seems to not be captured by the applied corrections

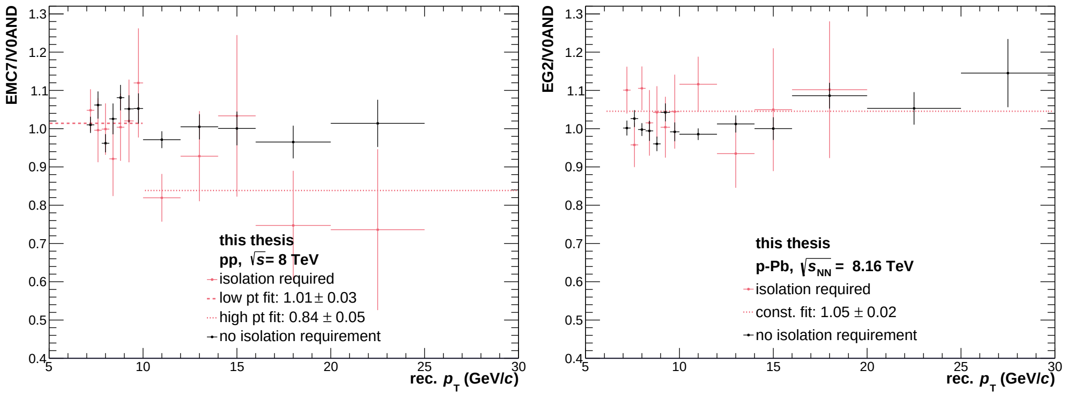

(a) pp collisions

(b) p–Pb collisions

Figure 10.3: Ratios of event-normalized raw cluster spectra from the low threshold EMCal photon trigger with respect to the cluster spectra measured in the MB sample.

and propagates to the fully corrected cross section ratio. Furthermore, the same ratios were calculated for the low threshold trigger with respect to the MB sample (V0AND), which is shown in Fig. 10.3. For the p–Pb collision data, the cluster spectrum obtained using the EG2 trigger is consistent within the statistical uncertainties with the corresponding spectrum in the MB sample – independent of the imposed isolation criterium. Drawing meaningful conclusions for the spectrum measured using the EMC7 trigger in pp collisions was found to me more challenging. While good agreement between the EMC7 and MB spectra is observed when no isolation requirement is imposed, no definitive conclusion can be made at this point about the agreement when the isolation requirement is included. At low-p_{T}, there seems to be good agreement between EMC7 and the MB sample, however, the agreement deteriorates for $p_{\mathrm{T}} \gtrsim 10\,\mathrm{GeV}/c$. While definite conclusions are challenging given the statistical uncertainties of the isolated cluster spectra, it is interesting to note that the observed underestimation is of similar magnitude than what is observed in Fig. 10.2.

From the previous studies it became clear that the observed disagreement between EGA and EMC7 trigger is in some form related to the isolation criterium, which imposes strict requirements on the event topology in the vicinity of the studied cluster. Furthermore, no such disagreement is observed for the EG1 and EG2 triggers, which are used for the measurement in p–Pb collisions. Comparing the trigger configurations used for the two datasets given in Tab. 4.2, one key difference between the used triggers is that the EMC7 trigger is the only EMCal L0 trigger used in this work, and that it furthermore was operated with a very low trigger threshold of 2 GeV. This might indicate that the operation with this low threshold introduces some form of trigger bias in the measurement, which is not covered by the applied corrections. This is in line with the observation that inconsistencies only seem to arise for this particular trigger when an isolation requirement is applied. The dependence on the trigger threshold hints at some sensitivity to the UE, which may modify the photon purity in the sample. In addition, to exclude any error in the analysis code, the fully corrected isolated prompt photon cross section obtained using the EGA trigger in pp collisions at $\sqrt{s} = 8\,\mathrm{TeV}$ has been compared to preliminary results [237, 238] obtained in the same collision system using an independent analysis framework. Good agreement is observed within the uncertainties.

10.2 CONCLUSIONS

Overall, the fully corrected isolated prompt photon cross sections obtained using the respective EMCal photon triggers are in agreement with each other within the systematic uncertainties in both collision systems. However, a difference of about 10 % is observed between the cross sections obtained using the EGA and EMC7 triggers in pp collisions at $\sqrt{s} = 8$ TeV. Further investigations showed that this difference might arise from potential biases in the EMC7 triggered sample. In particular, it is speculated that there may be an interplay of the isolation requirement and the low trigger threshold of 2 GeV, that introduces unaccounted sensitivity of the trigger to the UE. However, the exact cause of this deviation has not been found as of writing this work. The EMC7 trigger is the only L0 EMCal trigger used in this work, and the measurements using the L1 triggers operated at higher trigger thresholds don't seem to be sensitive to this effect.

Even though all fully corrected cross sections in the respective collision system are in agreement within the systematic uncertainties, it was therefore decided to not use the EMC7 trigger for the pp cross section presented in this work until the origin of this effect is fully understood. This slightly reduces the low-p_T reach of the measurement in pp collisions at $\sqrt{s} = 8$ TeV from 8 GeV/c to 12 GeV/c. This conservative approach was presented to the ALICE Physics Board, and the results were accepted as ALICE Preliminary [239]. Further investigations will be performed to better understand the aforementioned effects to also provide the measurement in pp collisions down to $p_\mathrm{T} = 8$ GeV/c for a final publication. Even though these effects are not observed for the p–Pb collision data, the cross section in this system is also presented only for the slightly reduced transverse momentum coverage of 12 GeV/$c \leq p_\mathrm{T} \leq 80$ GeV/c, which likewise has been accepted as an ALICE Preliminary figure [239].

11

RESULTS

This section presents the results of this work: The p_T-differential isolated prompt photon production cross section in pp and p–Pb collisions at $\sqrt{s_\mathrm{NN}} = 8\,\mathrm{TeV}$ and $8.16\,\mathrm{TeV}$, respectively, is presented and compared to pQCD calculations at NLO. The measurements cover photon p_T down to $12\,\mathrm{GeV}/c$ – extending the low-p_T reach of previous measurements in the same collision systems by the ATLAS collaboration [113, 114] by almost a factor of two. Furthermore, the nuclear modification factor R_pA is presented, which is confronted with theoretical calculations as well as the measurement by ATLAS in the same collision system. Finally, the impact of the measurement on existing nPDFs is estimated using a Bayesian reweighting procedure.

11.1 CROSS SECTIONS

The isolated prompt photon production cross section is calculated via

$$\frac{\mathrm{d}^2\sigma^\gamma}{\mathrm{d}p_\mathrm{T}^\gamma\,\mathrm{d}y} = \frac{1}{\mathcal{L}_\mathrm{int}} \cdot \frac{\mathrm{d}^2N_\mathrm{n}^\mathrm{iso}}{\mathrm{d}p_\mathrm{T}^\gamma\,\mathrm{d}y} \cdot \frac{P}{\epsilon \cdot A} \quad , \tag{11.1}$$

where the individual components are given by:

- $N_\mathrm{n}^\mathrm{iso}$ is the uncorrected isolated photon yield, which is given by the count of clusters at a given p_T fulfilling all selections outlined in the previous sections.
- $\mathcal{L}_\mathrm{int}$ is the integrated luminosity calculated according to Eq. 3.1
- A denotes the acceptance of the used calorimeters. It is obtained from geometrical considerations and given by the ratio of the area covered by the calorimeter with respect to the full azimuth at mid-rapidity $(2\pi \times (2 \cdot 0.7))$. One finds $A_\mathrm{pp} \approx 0.26$ and $A_\mathrm{pPb} \approx 0.40$ for the measurement in pp and p–Pb collisions, respectively.
- ϵ denotes the signal reconstruction efficiency (Sec. 7)
- P denotes the signal purity which is obtained using the ABCD method (Sec. 8)
- $\mathrm{d}p_\mathrm{T}{}^\gamma$ denotes the p_T bin width normalization
- $\mathrm{d}y$ is given by the width of the reported rapidity region of the measurement, i.e. $\mathrm{d}y = 2 \cdot 0.7 = 1.4$

Fig. 11.1 and 11.2 show the isolated prompt photon production cross section in pp and p-Pb collisions at $\sqrt{s_\mathrm{NN}} = 8\,\mathrm{TeV}$ and $8.16\,\mathrm{TeV}$, respectively[1]. The cross sections are obtained at mid-rapidity ($|\eta| < 0.7$) using a charged-only isolation $p_\mathrm{T,iso}^\mathrm{ch.} < 1.5\,\mathrm{GeV}/c$ in a cone with radius $R = 0.4$. The central values of the cross section in each p_T interval are denoted by black markers, where the vertical bars and boxes denote respectively the statistical and systematic uncertainties.

---

[1] The shown results have been published as ALICE preliminary figures and can be found in Ref. [239].

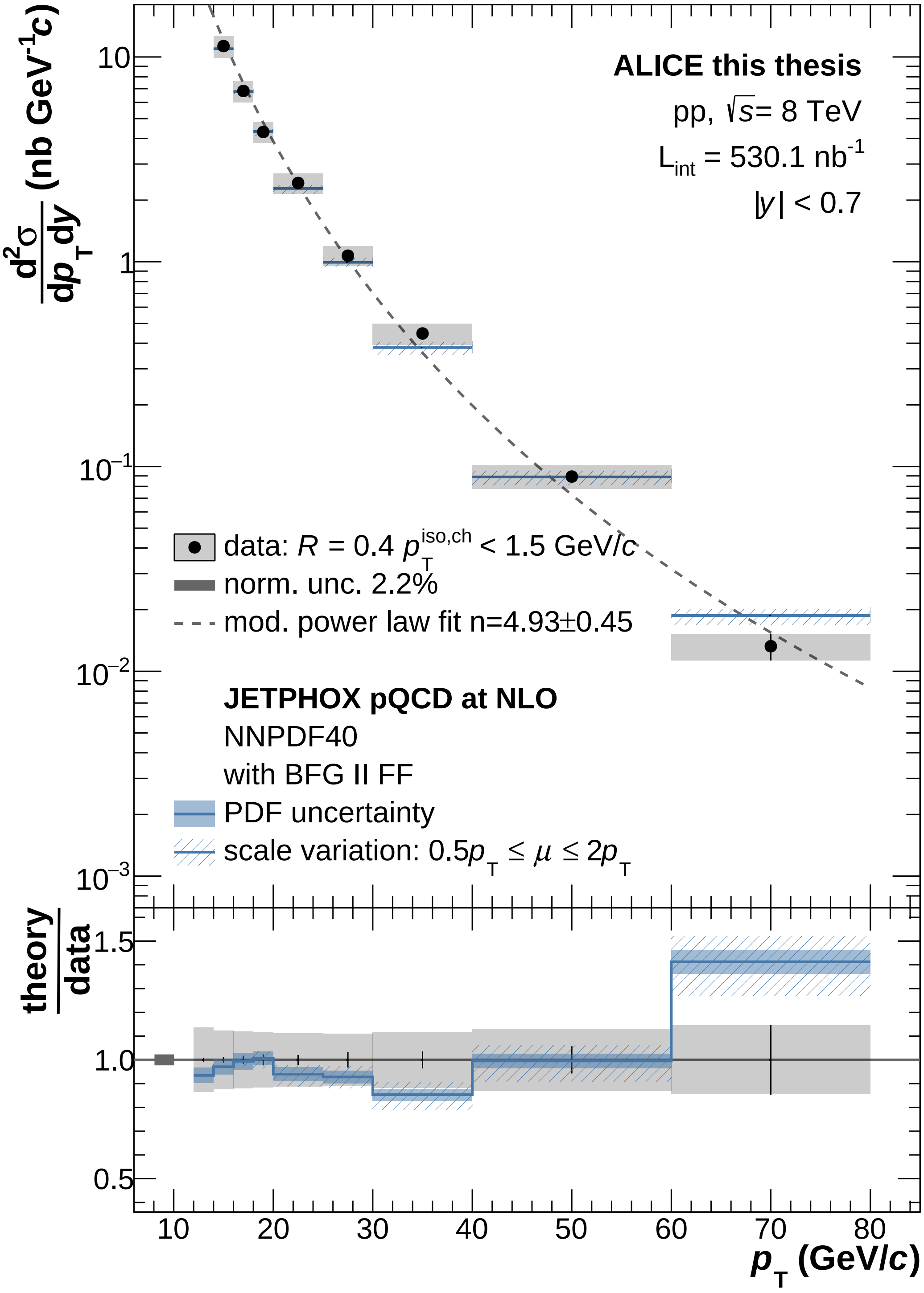

Figure 11.1: Isolated prompt photon production cross section in pp collisions at $\sqrt{s} = 8\,\text{TeV}$. The measurement is denoted by black markers, where the vertical bars and boxes denote the statistical and systematic uncertainties of the measurement, respectively. The blue solid lines denote the JetPhox pQCD calculation at NLO using the PDFs and fragmentation function denoted in the legend and a full isolation of $p_{\text{T,iso}}^{\text{full}} < 2\,\text{GeV}/c$ in a cone of $R = 0.4$. The dashed blue bands denote the theoretical scale uncertainty given by the variation of all scales according to $0.5p_{\text{T}} \leq \mu_R, \mu, \mu_f \leq 2p_{\text{T}}$. The solid shaded bands denote the PDF uncertainty at 90 % CL. The bottom panel shows the ratio of the pQCD prediction with respect to the measurement.

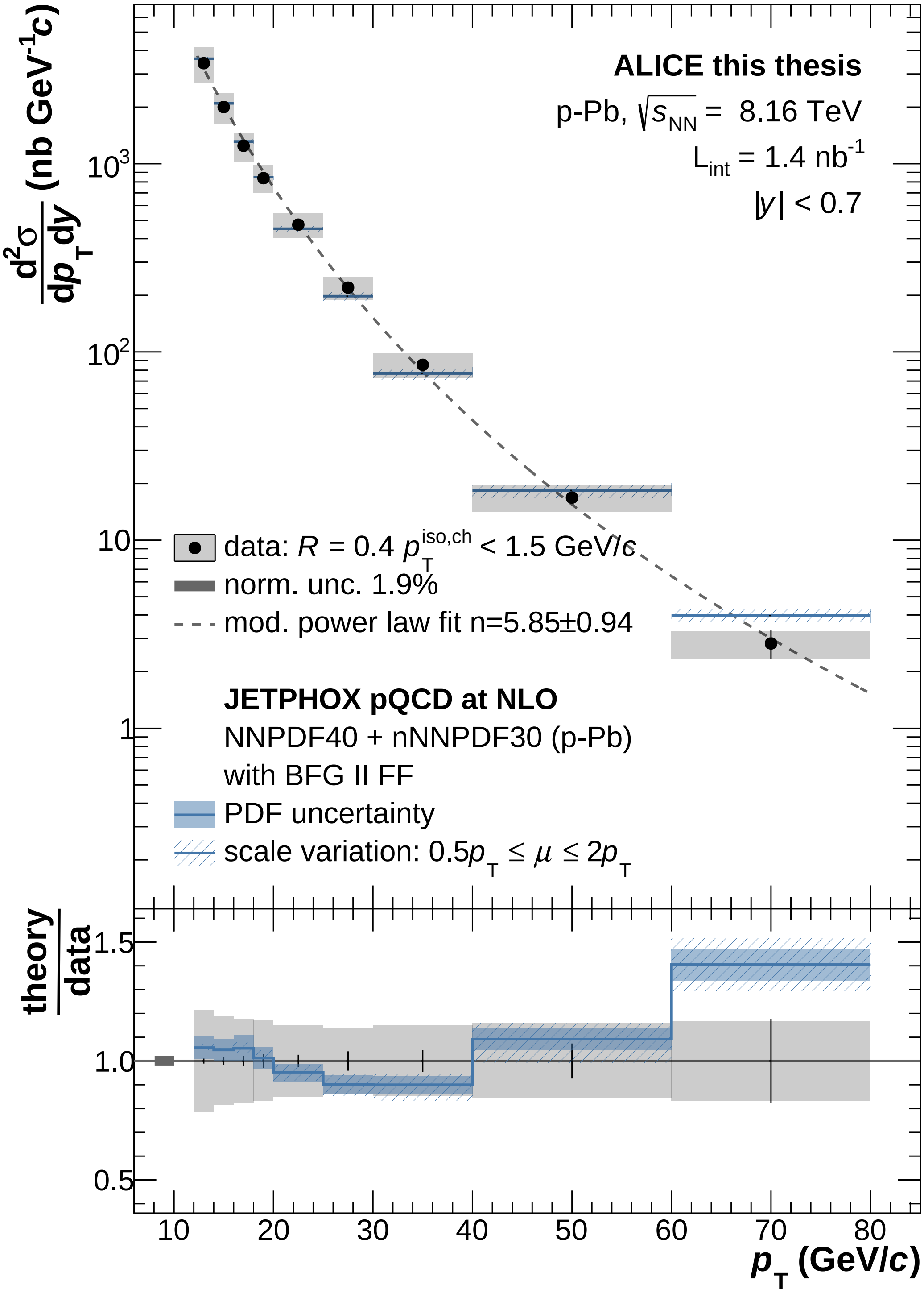

Figure 11.2: Isolated prompt photon production cross section in p–Pb collisions at $\sqrt{s_{\mathrm{NN}}}$ = 8.16 TeV. The measurement is denoted by black markers, where the vertical bars and boxes denote the statistical and systematic uncertainties of the measurement, respectively. The blue solid lines denote the JetPhox pQCD calculation at NLO using the PDFs and fragmentation function denoted in the legend and a full isolation of $p_{\mathrm{T,iso}}^{\mathrm{full}} < 2\,\mathrm{GeV}/c$ in a cone of $R = 0.4$. The dashed blue bands denote the theoretical scale uncertainty given by the variation of all scales according to $0.5p_{\mathrm{T}} \leq \mu_R, \mu, \mu_f \leq 2p_{\mathrm{T}}$. The solid shaded bands denote the PDF uncertainty at 90 % CL. The bottom panel shows the ratio of the pQCD prediction with respect to the measurement.

Overall, the measurements in both collision systems cover a photon transverse momentum range of $12\,\text{GeV}/c \leq p_\text{T} \leq 80\,\text{GeV}/c$ and are well described by a modified power law fit (Eq. 10.1), which is denoted by a grey dashed line.

The measurement is confronted with pQCD calculations at NLO, which are obtained using the JetPhox [73] program and denoted by blue lines. The calculations are performed assuming the respective collision energy and require a full (charged+neutral) isolation of $p^\text{full}_\text{T,iso} < 2\,\text{GeV}/c$ in a cone of $R = 0.4$, where the threshold is chosen to allow for a comparison to the measurement performed with a charged-only isolation of $p^\text{ch.}_\text{T,iso} < 1.5\,\text{GeV}/c$ according to Eq. 6.7. The calculation uses the NNPDF4.0 [24] proton PDF as well as the nNNPDF3.0 [66] nPDF, which are the most recent parametrizations provided by the NNPDF collaboration. The PDF uncertainties are evaluated by performing the NLO calculation for each member[2] of the respective PDF set and denoted by blue shaded bands. Calculations of the fragmentation component are performed using the BFG II [81] parton-to-photon fragmentation function. The renormalization scale μ_R, factorization scale μ and fragmentation scale μ_f are chosen to coincide with the photon p_T. The theoretical uncertainty arising due to this scale choice are evaluated through simultaneous two-point variation of all scales according to $0.5p_\text{T} \leq \mu_R, \mu, \mu_f \leq 2p_\text{T}$ and denoted by blue dashed bands. The bottom panels of Fig. 11.1 and Fig. 11.2 show the ratio of the theoretical predictions to the respective measurement: Good agreement between the calculations and experimental data is observed over almost the full covered transverse momentum range within the experimental and theoretical uncertainties, showcasing the ability of NLO calculations to adequately describe the experimental data in the inspected phasespace. Slight tension is observed for $p_\text{T} = 70\,\text{GeV}/c$, where both experimental and theoretical uncertainties are the largest. The presented results corroborate the observations in the previously published ALICE measurement of isolated prompt photon production in pp collisions at $\sqrt{s} = 7\,\text{TeV}$ [112], where likewise good agreement between data and pQCD calculations at NLO is observed within the experimental uncertainties.

As discussed in Sec. 2.4.4, the ATLAS collaboration performed measurements of the isolated prompt photon production cross section in the same collision systems: The measurement in pp collisions at $\sqrt{s} = 8\,\text{TeV}$ [113] covers a transverse momentum range down to $p_\text{T} = 25\,\text{GeV}/c$. At mid-rapidity ($|\eta| < 0.6$) an underestimation by a JetPhox pQCD calculation at NLO between 10 %-15 % is reported. No significant deviation of this magnitude could be observed within the uncertainties for the measurement presented in this work in the overlapping p_T region of $25\,\text{GeV}/c \leq p_\text{T} \leq 80\,\text{GeV}$[3]. However, several differences between the measurement in this work and the one presented in Ref. [113] have to be considered, mainly the less strict isolation requirement of $E^\text{iso}_\text{T} < 4.8\,\text{GeV} + 4.2 \times 10^{-3} E^\gamma_\text{T}$ in a cone of $R = 0.4$ used in the measurement by ATLAS. As illustrated in Fig. 2.22, this choice should lead to an increased fragmentation contribution to the prompt photon cross section. This could impact the comparison to pQCD calculations, as it leads to an increased dependence on the used parton-to-photon fragmentation functions, which are not as well constrained as PDFs and rely on old experimental data from e^+e^- colliders [81]. A similar underestimation is observed for isolated prompt photon production in p–Pb collisions at $\sqrt{s_\text{NN}} = 8.16\,\text{TeV}$ reported in

---

[2] The used PDF sets are accessed using the LHAPDF interface [240].

[3] Unfortunately, no direct comparison of both measurement in the same figure is possible, which would be beneficial for the reader. At the time of writing this thesis, the data over theory ratios from both ATLAS measurements have not been made publicly available on `hepdata`.

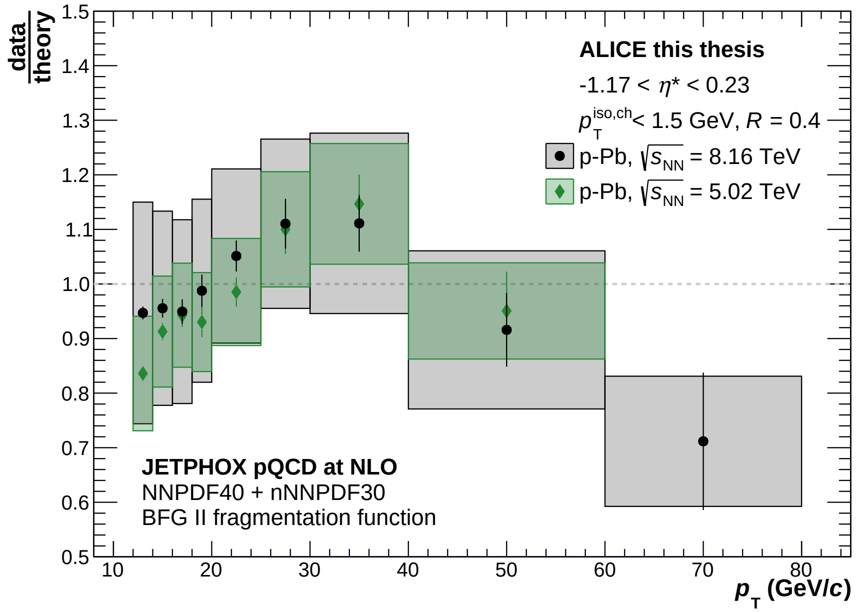

Figure 11.3: Ratio of the isolated prompt photon production cross section measurement in p–Pb collisions at $\sqrt{s_{\mathrm{NN}}} = 8.16\,\mathrm{TeV}$ and 5.02 TeV [241] with respect to pQCD calculations at NLO. Note: The measurement in p–Pb collisions at $\sqrt{s_{\mathrm{NN}}} = 5.02\,\mathrm{TeV}$ has preliminary status and is not yet part of an ALICE paper. The factor κ_{MC} is given in Eq. 7.7.While it is included in the signal efficiency for the measurement at $\sqrt{s_{\mathrm{NN}}} = 8.16\,\mathrm{TeV}$, it is instead used as a scaling for the NLO calculation for the measurement at $\sqrt{s_{\mathrm{NN}}} = 5.02\,\mathrm{TeV}$.

Ref. [114] by ATLAS using the same isolation criterium as used in Ref. [113], in a larger pseudorapidity region of $-1.84 < \eta^* < 0.91$ ($|\eta| < 1.375$). While no such deviation is observed in the measurement presented in this work, the same previously discussed difference between both measurements apply.

The measurement of the isolated prompt photon cross section in p–Pb collisions at $\sqrt{s_{\mathrm{NN}}} = 8.16\,\mathrm{TeV}$ is furthermore compared to a preliminary ALICE measurement of the same observable in p–Pb collisions at $\sqrt{s_{\mathrm{NN}}} = 5.02\,\mathrm{TeV}$ [241]. The comparison is performed on the level of the data/NLO ratio, which is shown in Fig. 11.3 for both collision energies. Both measurements use the same charged isolation requirement and cover the same acceptance of $|\eta| < 0.7$. The reference NLO calculations are obtained for both measurements with the JetPhox program using the same PDFs and fragmentation function, and only differ in the assumed collision energy. The comparison to theoretical calculations is in good agreement between both measurements within the experimental uncertainties[4], showcasing the ability of pQCD calculations at NLO to describe the isolated prompt photon production cross section for both collision energies.

For future studies, it would be interesting to confront the measurements presented in this work with pQCD calculations beyond NLO, were e.g. Ref. [113] and Ref. [91] showcase an improved description of the ATLAS isolated prompt photon data when incorporating higher-order effects in the calculation (e.g. using NNLOJet [123] or

---

[4] The systematic uncertainties of the preliminary measurement at $\sqrt{s_{\mathrm{NN}}} = 5.02\,\mathrm{TeV}$ are observed to be significantly smaller than those presented in this work. This is attributed to an overall more conservative systematic uncertainty evaluation presented in this work. For example, some uncertainty sources, such as the purity fit uncertainty, have not been considered for the preliminary results presented in Ref. [241].

PeTeR [121, 122] program). In addition, these calculations allow for reduced scale uncertainties, which can improve the sensitivity of the calculation to the used PDFs [91]. Furthermore, pQCD calculations at NLO that incorporate parton showers from Pythia to describe photon fragmentation are a promising approach to reduce the dependency on weakly constrained photon fragmentation functions (see e.g. Ref. [80]) and should be confronted with the presented experimental data in the future[5]. This would be especially interesting, considering that the presented pQCD calculations using photon-fragmentation functions describe the data rather well within the experimental uncertainties, whereas sizeable underestimations are observed for the ATLAS measurement [113]. In particular, confronting theoretical calculations incorporating Pythia parton showers with both measurements using different isolation thresholds could provide valuable insights into a possible dependence on the fragmentation description.

11.2 NUCLEAR MODIFICATION FACTOR

In order to quantify initial-state nuclear effects, the previously presented production cross sections are compared using the so-called nuclear modification factor R_{pA}, which is given as [37]:

$$R_{\mathrm{pA}} = \frac{\mathrm{d}^2 N^{\gamma}_{\mathrm{pA}} \big/ \mathrm{d}p_{\mathrm{T}}\,\mathrm{d}y^*}{\langle T_{\mathrm{pA}}\rangle \cdot \mathrm{d}^2\sigma^{\gamma}_{\mathrm{pp}} \big/ \mathrm{d}p_{\mathrm{T}}\,\mathrm{d}y^*} = \frac{\mathrm{d}^2\sigma^{\gamma}_{\mathrm{pA}} \big/ \mathrm{d}p_{\mathrm{T}}\,\mathrm{d}y^*}{A_{\mathrm{Pb}} \cdot \mathrm{d}^2\sigma^{\gamma}_{\mathrm{pp}} \big/ \mathrm{d}p_{\mathrm{T}}\,\mathrm{d}y^*} \quad \text{with} \quad \langle T_{\mathrm{pA}}\rangle = \frac{A_p \cdot A_{Pb}}{\sigma^{\mathrm{inel.}}_{\mathrm{pPb}}}, \tag{11.2}$$

where $\mathrm{d}^2\sigma^{\gamma} \big/ \mathrm{d}p_{\mathrm{T}}\,\mathrm{d}y^*$ are the double-differential isolated prompt photon production cross sections in pp and p-Pb collisions evaluated at the same centre-of-mass energy and rapidity y^* in the centre-of-mass reference frame. To account for the fact that even in the absence of any other nuclear effects more collisions between nucleons occur on average in a p–Pb collision compared to a pp collision, the production cross section obtained in pp collisions is scaled using the number of nucleons in lead $A_{\mathrm{pPb}} = 208$.

In addition to the aforementioned binary collision scaling, additional differences between both collision systems have to be taken into account: The collision energy for p–Pb collision is slightly higher than for pp collisions, i.e. $\sqrt{s_{\mathrm{NN}}} = 8.16\,\mathrm{TeV}$ and $8\,\mathrm{TeV}$, respectively. This difference arises because for this p–Pb dataset the LHC was operated with a beam energy of $E_p = 6.5\,\mathrm{TeV}$, where the (by design) equal magnetic field in both acceleration rings yields a total energy for the Pb beam of $E_{\mathrm{Pb}} = Z \cdot E_p = 533\,\mathrm{TeV}$ or about 2.76 TeV per nucleon. This asymmetry of beam energies per nucleon results in a centre-of-mass energy of [242]:

$$\sqrt{s_{\mathrm{NN}}} \approx 2 \cdot E_p \sqrt{\frac{Z_1 Z_2}{A_1 A_2}} \approx 8.16\,\mathrm{TeV} \quad \text{for} \quad E_p = 6.5\,\mathrm{TeV} \quad \text{in p-Pb collisions} \tag{11.3}$$

---

[5] I thank Prof. Klaasen and Alexander Neuwirth for the fruitful discussion regarding this topic. Even though the mentioned calculations for pp and p–Pb collisions at $\sqrt{s} = 8\,\mathrm{TeV}$ could not be included here within the timeframe of this work, they will definitely be considered for a future publication.

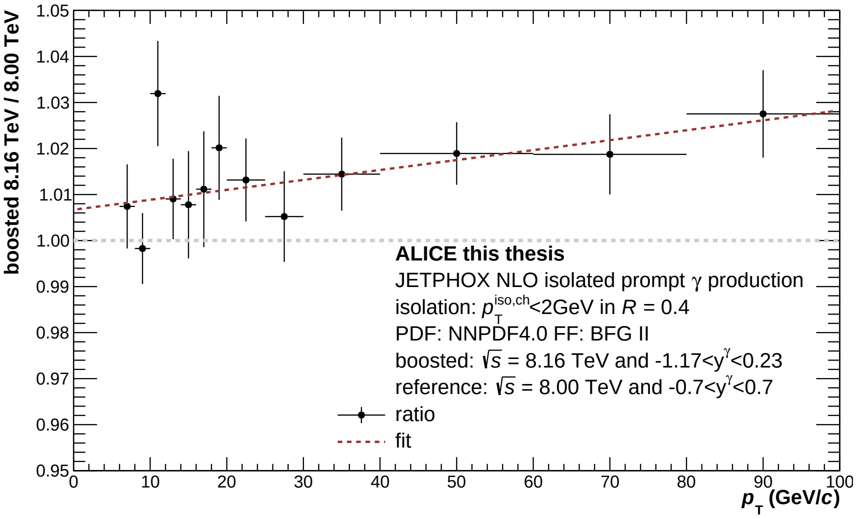

Figure 11.4: Ratio of isolated prompt photon cross section in pp collisions at $\sqrt{s} = 8.16\,\text{TeV}$ for $-1.17 < y^{\gamma} < 0.23$ with respect to pp collisions at $\sqrt{s} = 8\,\text{TeV}$ for $-0.7 < y^{\gamma} < 0.7$. The cross sections are obtained using the JetPhox program at NLO using the NNPDF3.0 proton PDF and BFG II fragmentation function. All scales are set to coincide with the photon momentum and an isolation of $p_{\rm T,\,iso}^{\rm full} < 2\,\text{GeV}$ in $R = 0.4$. The scaling relation is obtained using a first-order polynomial fit of the ratio and is given in Eq. 11.5.

Furthermore, the asymmetry of the beam energy leads to a rapidity shift, where the rapidity y measured for a particle in the laboratory frame is shifted with respect to the rapidity in the centre-of-mass frame y^* by

$$\Delta y \approx \frac{1}{2}\ln\left(\frac{Z_1 A_2}{A_1 Z_1}\right) \overset{\text{p-Pb}}{\approx} 0.46. \tag{11.4}$$

In order to correctly account for these difference, the pp collisions reference at $\sqrt{s} = 8\,\text{TeV}$ is scaled to the same centre-of-mass energy and rapidity window using a scaling relation determined using JetPhox at NLO: Fig. 11.4 shows the ratio of isolated prompt photon cross section in pp collisions at $\sqrt{s} = 8.16\,\text{TeV}$ for $-1.17 < y^{\gamma} < 0.23$ with respect to pp collisions at $\sqrt{s} = 8\,\text{TeV}$ for $-0.7 < y^{\gamma} < 0.7$. The scaling relation $\kappa_{\rm boost}$ is obtained by fitting a first-order polynomial to the obtained ratio, which is given by:

$$\kappa_{\rm boost}(p_{\rm T}) = (0.02 \pm 0.01)\,\% \cdot p_{\rm T} + (100.67 \pm 0.42)\,\%, \tag{11.5}$$

resulting in a correction of the pp cross section of at most 2.4 % in the covered transverse momentum range.

The thus obtained nuclear modification factor $R_{\rm pA}$ of isolated prompt photon production at $\sqrt{s_{\rm NN}} = 8.16\,\text{TeV}$ is shown in Fig. 11.5. The measurement is indicated by black markers, where the vertical bars and boxes denote the statistical and systematic uncertainties of the measurement. While the statistical uncertainties of both measurements entering the ratio are assumed to be fully uncorrelated and added in quadrature, correlations of the systematic uncertainties are taken into account, as discussed in Sec. 9. The isolated prompt photon $R_{\rm pA}$ is in agreement with unity within the uncertainties, in line with the findings by ATLAS in the same collision system at mid-rapidity [114] for $E_{\rm T} > 25\,\text{GeV}$. However, the low-$p_{\rm T}$ reach of the measurement presented in this work

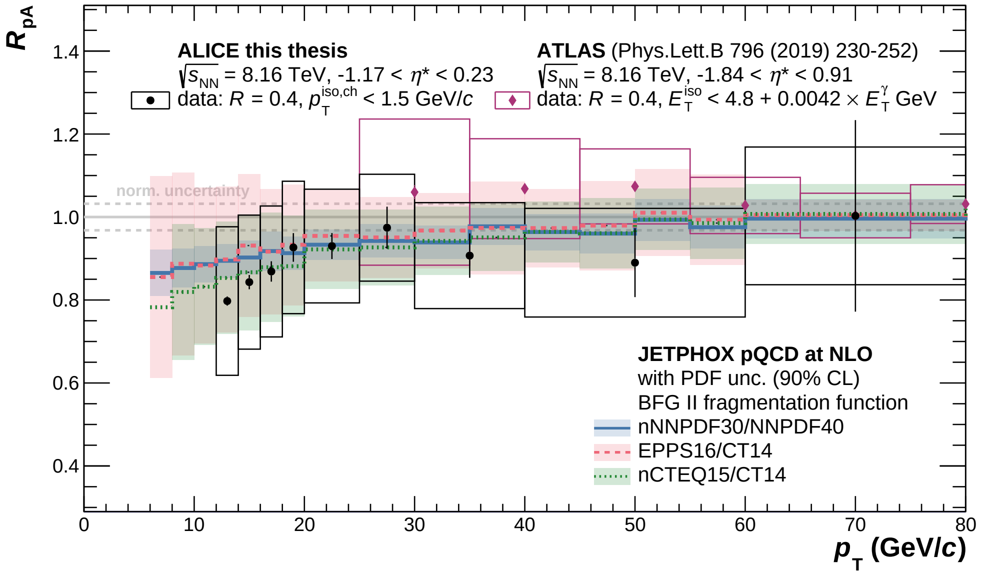

Figure 11.5: Nuclear modification factor (R_{pA}) of isolated prompt photon production in p–Pb collisions at $\sqrt{s_{NN}} = 8.16\,\text{TeV}$. The vertical error bars and boxes denote the statistical and systematic uncertainties, respectively. The dashed grey lines indicate the normalization uncertainty of 3.2 %. The measurement is compared to various pQCD calculations at NLO, where the used (n)PDFs and fragmentation function are given in the legend. The shown theory uncertainty bands are the respective nPDF uncertainties. The theory scale uncertainties were found to be fully correlated between both collision systems and are therefore negligible and not shown.

reveals a hint of an increasing suppression for $p_T < 25\,\text{GeV}/c$ of up to 20 %, which is however not (yet) significant within the experimental uncertainties. As of writing this work, the presented nuclear modification factor offers the lowest p_T reach of any prompt photon R_{pA} measured so far.

The measured R_{pA} is confronted with various pQCD calculations at NLO, which were obtained using the JetPhox[73] program. The used nPDFs are denoted in the legend and include cold nuclear matter effects such as gluon shadowing, as discussed in Sec. 2.3.3. While the theory scale uncertainties were found to mostly cancel on the level of the R_{pA}, the uncertainties of the nPDF dominate the theoretical uncertainties and are denoted by coloured bands. The nPDF uncertainties[6] correspond to a 90 % confidence level, and were calculated using LHAPDF [240] framework, taking into account if the members of the nPDF are given as a MC replica representation (nNNPDF3.0) or Hessian representation (EPPS16 and nCTEQ15). The theory predictions well describe the data for all three nPDFs within the experimental and theoretical uncertainties, displaying a similar suppression pattern leading to a modification of the isolated prompt photon production cross section of up to 20 % at $p_T \approx 12\,\text{GeV}/c$. This suppression is often attributed to low-x shadowing of gluons inside the lead nucleus [66]. A more detailed discussion of the nPDF uncertainties and the potential of this measurement to improve them is given the following section.

---

[6] It is important to note that more recent versions of the nPDFs for EPPS and nCTEQ have become available, which were not yet used for the presented calculations. In particular EPPS21 [243] and nCTEQ15HQ [244] offer overall reduced uncertainties of the gluon PDF through the inclusion of new experimental data. Updated calculations using these two nPDFs will be provided for the final publication.

11.3 IMPACT OF THE MEASUREMENT ON EXISTING NUCLEAR PDFS

As discussed in Sec. 2.2.3, PDFs are determined through a fitting procedure, i.e. the optimization of a set of free parameters of the used parametrizations that minimize a given χ^2 function quantifying how well the parametrization describes the included experimental data [23]. The uncertainties of these parametrizations are commonly determined using either a Hessian method [245] or a MC method [24], resulting in an ensemble of N so-called PDF members. These ensembles form a proper representation of the probability distribution of the PDF, given the included experimental data [246]. The fitting procedure is complex and time-consuming and requires theoretical calculations for each included observable as well as careful consideration of the experimental uncertainties, theoretical uncertainties, as well as the exact definition of the χ^2 function by the experts of the respective collaborations. Inclusion of the new experimental data presented as part of this thesis in this complex procedure is not a feasible approach to estimate the impact of this data on the existing parametrizations. Furthermore, additional challenges in the global fitting procedure may arise for isolated prompt photon observables due to the slowness of the JetPhox calculation, as was pointed out by David d'Enterria in Ref. [75].

Instead, the effect of new data on existing PDFs can be estimated using Bayesian inference, following a reweighting procedure outlined in Ref. [246] and [247], which can be easily applied to PDF sets that use the MC method to determine the PDF uncertainties. In this work, the implementation of this approach described in Ref. [248] is used, where the code has been provided by C. Loizides and M. van Leeuwen. The study is performed using the nuclear modification factor R_{pA} presented in Fig. 11.5, as the ratio offers the advantage of a partial cancellation of experimental and theoretical uncertainties between both collision systems. First, the calculation of the isolated prompt photon R_{pA} is performed using the JetPhox program for each replica of the nNNPDF30 nPDF set, where the results falling within the 90 % confidence level were previously denoted by the blue shaded band in Fig. 11.5. For each replica k, the agreement between data and prediction is quantified via:

$$\chi_k^2 = \frac{1}{N_{\mathrm{dat}}} \sum_{i=1}^{N_{\mathrm{dat}}} \frac{\left(R_i^{(\mathrm{th}),(k)} - R_i^{(\mathrm{exp})}\right)^2}{\Delta_{\mathrm{tot}}^2}, \tag{11.6}$$

where $R_i^{(\mathrm{exp})}$ is the measured R_{pA} in p_{T} bin i and $R_i^{(\mathrm{th}),(k)}$ is the corresponding theoretical prediction using replica k. The total experimental uncertainty of the N_{dat} data points is denoted by Δ_{tot} and is given by the quadratic sum of the statistical and systematic uncertainties, as well as the absolute normalization uncertainty. The fact that the normalization uncertainty is fully correlated from point to point is neglected here for simplicity, but can be included, as is for example done in Eq. 2 of Ref. [248]. The posterior probability P_k^{new} of replica k to observe the new data points can be obtained using Bayes' theorem as [248]:

$$P_k^{\mathrm{new}} = \frac{1}{N_{\mathrm{rep}}} \frac{P_k(\mathrm{data}|R^{(\mathrm{th}),(k)})}{\sum_k P_k(\mathrm{data}|R^{(\mathrm{th}),(k)})}, \tag{11.7}$$

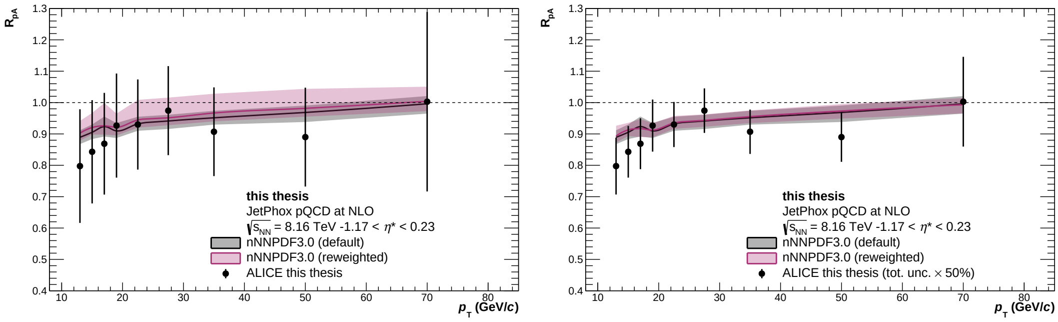

(a) full exp. uncertainties (b) 50 % exp. uncertainties

Figure 11.6: Reweighting study of potential constraints for the nNNPDF30 nPDF using the isolated prompt photon production R_{pA} at $\sqrt{s_{\mathrm{NN}}} = 8.16\,\mathrm{TeV}$ presented in this work. The ALICE data is denoted by black markers, where the vertical lines denote the total experimental uncertainties, including the normalization uncertainty added in quadrature. The right panel showcases a hypothetical scenario, where the experimental uncertainties have been reduced by a factor of 0.5. The data is shown together with JetPhox predictions using the nNNPDF30 to describe the lead nucleus, where shaded bands denote the 90 % CL PDFs uncertainties. The red bands denote the uncertainty taking into account the new experimental data in a Bayesian reweighting procedure, which is outlined in the text.

where $1/N_{\mathrm{rep}}$ is the equal probability before reweighting for each of the replicas and N_{rep} is the total number of replicas ($N_{\mathrm{rep}} = 201$ for nNNPDF30). The probability $P_k(\mathrm{data}|R^{(\mathrm{th}),(k)})$ can be expressed as:

$$P_k(\mathrm{data}|R^{(\mathrm{th}),(k)}) = \frac{1}{2^{\frac{N_{\mathrm{dat}}}{2}}\,\Gamma\!\left(\frac{N_{\mathrm{dat}}}{2}\right)}\left(\chi_k^2\right)^{\frac{N_{\mathrm{dat}}}{2}-1} e^{-\frac{\chi_k^2}{2}}, \tag{11.8}$$

where N_{dat} is the number of data points and χ_k^2 is given in Eq. 11.6. Finally, the confidence intervals of the thus reweighted ensemble of PDF members is obtained by calculating the sum of the reweighted probabilities $\sum_k P_k^{\mathrm{new}}$ until reaching 0.05 and 0.95 to determine the lower and upper bound of the 90 % CL, respectively.

Fig. 11.6 shows the results of the thus performed reweighting study. The black markers denote the measurement of the R_{pA} at $\sqrt{s_{\mathrm{NN}}} = 8.16\,\mathrm{TeV}$ presented in this work, which is compared to the corresponding JetPhox calculation at NLO using the nNNPDF30 nPDF set for the Pb beam. The relative PDF uncertainty of the prediction prior to any reweighting is already small and in the order of 5 % at 90 % CL, as indicated by the grey shaded band. This is significantly smaller than the total experimental uncertainties, which are about 24 % at $p_{\mathrm{T}} = 12\,\mathrm{GeV}$. As a consequence, the re-weighted results (red shaded band) that take into account the data presented in this work do not show an improvement of the nNNPDF30 uncertainties. The contrary is the case, and one even observes an increase of the PDF uncertainties, which is an artefact of the large difference between experimental and prior PDF uncertainty entering the reweighting procedure. Clearly improvements of the experimental uncertainties of the measurement are desirable in order to provide constraints for state-of-the art nPDF. This is further illustrated in Fig. 11.6b, which shows the same reweighting procedure using experimental uncertainties that have been artificially reduced by 50 %: A reduction of

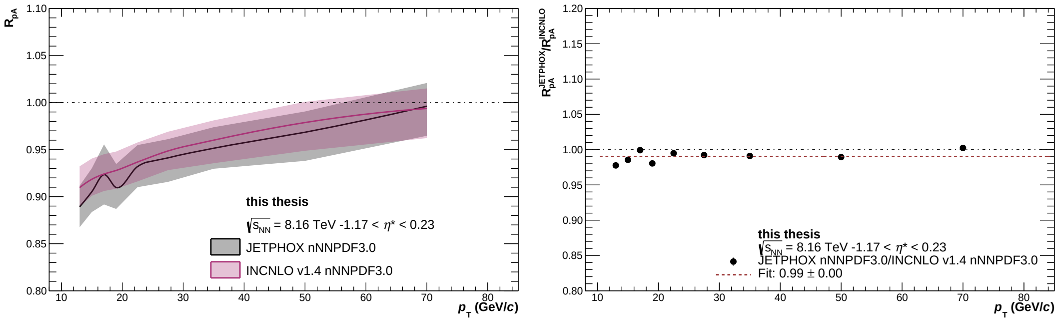

(a) Nuclear modification factor R_{pA}

(b) Ratio JETPHOX/INCNLO

Figure 11.7: **Left:** Calculation of the prompt photon R_{pA} at NLO using the JetPhox [73] and INCNLO [251–255] programs for $\sqrt{s_{NN}} = 8.16$ TeV. Both calculations use the NNPDF40 proton and nNNPDF30 nuclear PDFs, as well as the BFG II [81] fragmentation function. An isolation requirement of $p_T^{iso} < 2\,\text{GeV}/c$ in $R = 0.4$ is used for the JetPhox calculation, whereas no such requirement is available for INCNLO. The shaded band denotes the nPDF uncertainty at 90 % CL. **Right:** Ratio of median R_{pA} calculated using JetPhox with respect to the INCNLO prediction.

the nNNPDF30 uncertainties by about 10 % over almost the full covered momentum range is observed, showcasing that a precision measurement in this kinematic region can provide meaningful constraints.

For educational purposes, the impact of the measurement is also studied for older nPDFs provided by the NNPDF collaboration, i.e. nNNPDF20 (2020) [249] and nNNPDF10 (2019) [250], which use $N_{dat} = 1467$ and $N_{dat} = 451$ experimental datapoints in the fitting procedure, respectively. This is significantly less than what has been used for the most recent nNNPDF30 [66], which includes a total of $N_{dat} = 2188$ datapoints. As each nPDF contains several hundred MC replicas that allow to calculate the prior PDF uncertainty for the R_{pA}, additional challenges arose due to the high computing demands of the JetPhox program. In particular, the calculation of the direct- and fragmentation contribution of the isolated prompt photon production cross section required about 7 hours of computing time for each replica of the respective PDF set on a local computing cluster. This was acceptable for the predictions presented in Fig. 11.5, however, it was not feasible for the additional reweighting studies using nNNPDF20 and nNNPDF10, which would have required calculations for a total of $N_{rep} = 500$ replicas. Instead, the INCNLO code [251–255] is used, which allows to calculate the direct- and fragmentation prompt photon contribution with pQCD at NLO *without* any isolation requirement. These calculations were found to be significantly faster than those obtained using the JetPhox program. Even though INCNLO does not include any isolation requirement, the predictions were found to agree on the level of the prompt photon R_{pA} with those obtained using the JetPhox program *including* isolation. This agreement is illustrated in Fig. 11.7, which shows the prompt photon R_{pA} at $\sqrt{s_{NN}} = 8.16$ TeV calculated with both programs using nNNPDF30 for the lead nucleus. The central values of the R_{pA} were found to agree within about 3 % for both programs. This also indicates that the isolation requirement and fragmentation contribution are of less importance on the level of the R_{pA}, making it a robust observable for inclusion in global PDF fits. The latter point is also illustrated in Ref. [249], where the NNPDF collaboration explicitly encourages the inclusion of relative observables

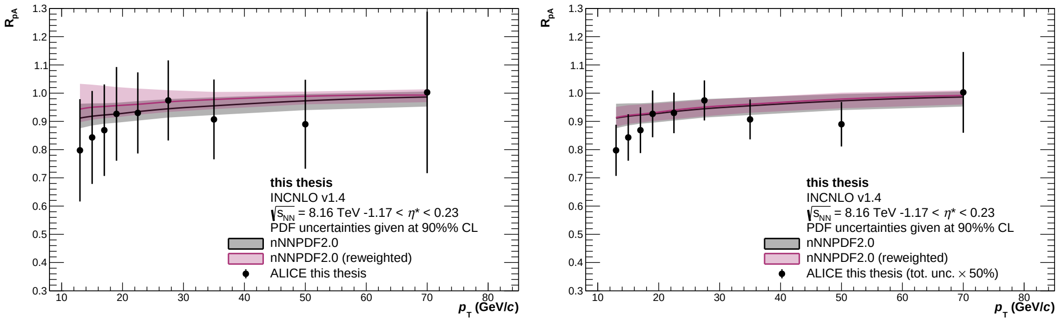

(a) nNNPDF20 and 100 % exp. uncertainties (b) nNNPDF20 and 50 % exp. uncertainties

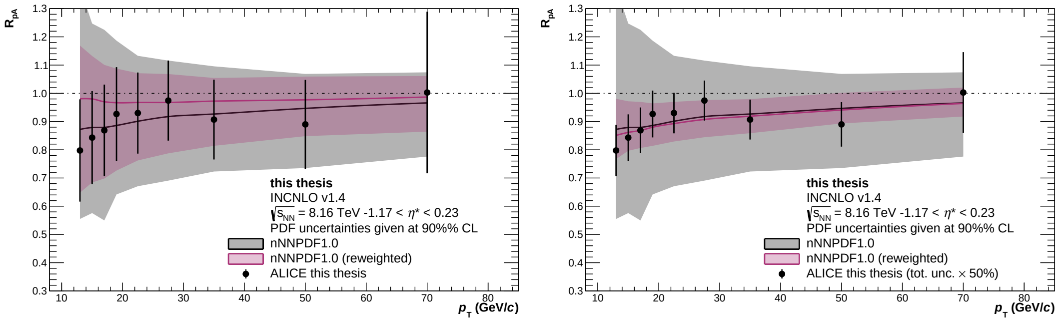

(c) nNNPDF10 and 100 % exp. uncertainties (d) nNNPDF10 and 50 % exp. uncertainties

Figure 11.8: Impact of the experimental data on nNNPDF20 (top) and nNNPDF10 (bottom) obtained using a reweighting study, analogous to what is shown in Fig. 11.6 for nNNPDF30. The INCNLO program is used to obtain the theoretical predictions of the prompt photon R_{pA}, where the predictions were found to be compatible to JetPhox predictions of the *isolated* prompt photon R_{pA} (see. Fig. 11.7).

like the prompt photon R_{pA} in global PDF fits after observing tension between theory and experiment for the isolated prompt photon production cross section measured by the ATLAS collaboration [113]. Furthermore, both programs yield similar nPDF uncertainties, which are denoted by shaded bands and agree with each other within 15 %. This showcases that the INCNLO program can be used as a reasonable proxy for further reweighting studies.

Finally, Fig. 11.8 showcases the impact of the measured isolated prompt photon R_{pA} on the nNNPDF20 and nNNPDF10 nPDFs. As for nNNPDF30, no significant improvements of the nPDF uncertainties are observed when including the experimental data using the full experimental uncertainties, whereas a moderate improvement of up to 19 % is observed when assuming 50 % reduced experimental uncertainties. Significant improvements of the nPDF uncertainties could be observed for nNNPDF10 from 2019, where an inclusion of the presented experimental data leads to a reduction of the PDF uncertainties on the R_{pA} by about 40 % for the full covered transverse momentum range. In addition, a reduction of the experimental uncertainties by 50 % further increases the constraining power of the measurement, where the reweighting study indicates an overall reduction of the nPDF uncertainties by up to 74 %.

In summary, the reweighting studies showcase that the presented measurement of the isolated prompt photon R_{pA} could significantly constrain older nPDFs such as nNNPDF10, however, further reductions of the experimental uncertainties of about 50 % are required in order to provide meaningful constraints for state-of-the-art nPDFs such as nNNPDF30. Nonetheless, these studies just serve as a guideline and solely showcase the potential impact of the measurement on the PDF uncertainties for predictions of isolated prompt photon production. The findings should explicitly not lead to the conclusion that there is no merit in including the presented measurement in global PDF fits. On the contrary: Since the inclusion of hadronic observables such as e.g. forward production of D mesons [130] – an observable sensitive to fragmentation and potential other final state effects – recently provided significant constraints for low-x gluons nPDFs, the measurement of independent observables becomes more important than ever. The measurement of isolated prompt photon production is highly relevant, also for global PDF fits, as it provides a robust probe for cold nuclear matter effects that is insensitive to the QGP and furthermore offers a highly suppressed sensitivity to fragmentation functions. Inclusion of prompt photon data in global PDF can therefore offer valuable insights for the study of gluon shadowing and provide additional context for other observables already included in the fitting procedure. In addition, measurements of prompt photon in a less-constrained phasespace, e.g. their measurement at very forward rapidities, can provide significant constraints of the gluon PDF at very low x, as discussed in the following section.

Part III

OUTLOOK: ISOLATED PROMPT PHOTON MEASUREMENTS WITH THE FORWARD CALORIMETER (FOCAL)

12

FUTURE PROSPECTS OF ISOLATED PHOTON MEASUREMENTS WITH THE FOCAL

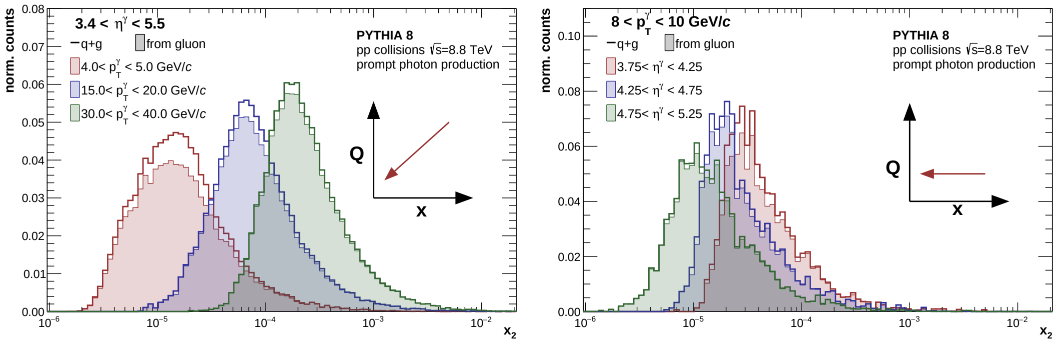

(a) variation of photon p_{T}

(b) variation of photon η

Figure 12.1: Bjorken x_2 probed by photons produced in the Compton process (qg→qγ) for various selections on the photon p_{T} and rapidity within the FoCal acceptance. The distributions are obtained using the PYTHIA event generator to simulate the Compton process for pp collisions at $\sqrt{s} = 8.8\,\mathrm{TeV}$. The sketches in the top right corner illustrate the probed region in the x-Q phasespace.

This section serves as an outlook of this work, exploring future measurements of isolated prompt photon production with the ALICE Forward Calorimeter (FoCal) (see Sec. 3.2.13). As illustrated in Fig. 12.1, such measurements performed at forward rapidities ($3.4 < \eta < 5.5$) will allow probing QCD evolution at low Bjorken-x of smaller than $x \sim 10^{-5}$. This is over two orders of magnitude lower than the x probed by the measurement at mid-rapidity presented in this work and the lowest x reach of any current or near-future experimental facility. Imposing selection criteria on the photon p_{T} and pseudorapidity within the FoCal acceptance, allows to further constrain the region probed in the x-Q phasespace, which is illustrated by the sketches in the respective panels. The key motivation for prompt photon measurements in this low-x region are the exploration of non-linear QCD dynamics, i.e. the process of gluon fusion resulting in a regime of saturated gluons at low x and Q (see Sec. 2.2.3). While the saturation scale Q_s is not precisely known, theoretical studies [256] indicate $Q_s \gg \Lambda_{\mathrm{QCD}}$ at $x \sim 10^{-5}$. The sensitivity of prompt photon production to the partonic distribution of gluons, their lack of final-state interaction and hadronisation, as well as their low-x reach make prompt photon measurements an ideal candidate to explore saturation in a perturbative regime. Experimental observation of saturation effects would be milestone for our understanding of the strong interaction, and measurements at forward rapidities with the FoCal will play an important role in this quest, complementing DIS measurements at a future Electron Ion Collider (EIC) [257].

This section compiles several studies of the expected performance for isolated prompt photon measurements using the FoCal. The studies were carried out using MC event generators in combination with an implementation of the FoCal detector in GEANT3 [186]. The studies were performed over the course of this PhD in order to provide estimates for the FoCal Letter-of-Intent (LOI) [72][1], as well as the upcoming Technical Design Report (TDR). Section 12.1 discusses the response of the detector to photons, including a brief outline of the employed clusterization algorithm used for these studies. Isolation capabilities using the FoCal-E and FoCal-H, which can be used to enhance the prompt photon signal are discussed in Sec. 12.2. In addition, so-called π^0 tagging is discussed, which can be used as an additional criterium to increase the signal-to-background ratio of the measurement. First attempts to employ the ABCD method to obtain the purity of the measurement are presented in Sec. 12.3. A study of the expected isolated prompt photon yields in the FoCal acceptance during LHC Run 4 using pQCD calculations at NLO is presented in Sec. 12.4, allowing to obtain a rough estimate of expected statistical uncertainties of the measurement. Finally, the obtained yields in combination with an estimate of the systematic uncertainties can be used to quantify the potential impact of such a measurement on existing nPDFs, which is presented in Sec. 12.5.

12.1 PHOTON RECONSTRUCTION

The response of the FoCal-E detector for photons is studied using the `AliGenBox` generator, which is distributed as part of the `AliRoot` [202] framework and allows generating single particles in a given phasespace. The generator is used to generate 200k events, each containing a single photon with $3.0 < \eta^{\gamma} < 5.8$ and $0 < p < 1.5\,\text{TeV}$. In contrast to a normally steeply falling photon production cross section as a function of p_{T}, the photons used for this study are generated using a flat momentum distribution in order to ensure sufficient statistics for the covered momentum range.

12.1.1 *Detector Simulation*

Each generated event is further processed using GEANT3[186], which simulates the interaction of the produced particles with active and passive material. This does not only include an implementation of the FoCal detector, but also other detectors and material present in Run 4 of LHC operation. The FoCal is implemented according to the detector description provided in Sec. 3.2.13 and is positioned $z = 7\,\text{m}$ from the interaction point, covering approximately $3.4 < \eta < 5.5$ in pseudorapidity. A coverage of up to $\eta \approx 5.8$ is reached with reduced azimuth angle coverage. The two pixel layers are implemented with an individual pixel size of $50 \times 50\,\mu\text{m}^2$ and a thickness of $30\,\mu\text{m}$. The 18 pad layers are implemented with a size of $1 \times 1\,\text{cm}^2$ and thickness of $500\,\mu\text{m}$ for the sensitive layers. All 20 layers of the FoCal-E are grouped into 6 segments, where for each tower in a segment the signal is calculated as the sum of the signals from the respective layers. The signal of each detector segment is purely based on the information from GEANT3, i.e. the information about shower development and the energy depositions in active detector material. In particular, the energy depositions in the pad layers are used directly as the signal of these layers, whereas the depositions in the pixel layers are only counted

---

[1] The work on the study of the isolation of prompt photons in the FoCal is largely based on macros and work by Marco van Leeuwen done before 2020. Since then, the tools were further modified, and this work presents updated figures using the most recent FoCal geometry and code improvements. I would like to use this opportunity to thank him for helping me get familiar with his code and letting me continue his past studies for the upcoming TDR!

as a hit above a given threshold. No additional simulation of the detector response and energy smearing has been implemented so far, however, its effects are expected to be negligible for high energy particles at forward rapidities [72].

The simulation currently only includes a simple implementation of the FoCal-H detector, consisting of 34 Pb layers with a thickness of 3 cm, which alternate with scintillator layers with a thickness of 0.2 cm that serve as the sensitive detector material. The detector is further divided into individual towers with a transverse segmentation of $2.5 \times 2.5\,\mathrm{cm}^2$ and the signal in each tower is obtained by summing the GEANT3 energy depositions in the longitudinal direction. At the time of writing this thesis, work is ongoing to implement a more realistic model of the FoCal-H detector. In particular, implementations of a so-called "Spaghetti" geometry are almost finished, which consists of a stack of copper tubes with inserted scintillation fibres – a promising design which has been used in multiple test beams setups in 2022.

12.1.2 *Clusterization*

In order to reconstruct the energy of photons and hadrons, a cluster finding algorithm is used, which takes into account the signals from the pad and pixel layers of the FoCal-E and is described in detail in Ref. [72]. The algorithm searches for seed signals above a given threshold in each segment, and then proceeds to add digits within a given radius around the seed tower to the cluster. In a second stage, additional requirements and weights are imposed that further merge or split the found clusters, where the weights were optimized using the simulation of single photons [72]. The thus obtained clusters from each segment are combined to clusters for all pad and pixel segments separately. In a final step the clusters for the full FoCal-E are obtained by combining clusters found for the pads and pixels, using a geometrical matching to associate clusters from the pads with highly granular pixel layers. If multiple pixel clusters are found within the same area as a pad cluster, the pad clusters are split according to the found pixel clusters. This procedure demonstrates the advantage of using two sensor technologies of differing granularity, where the usage of two highly granular pixel layers allows disentangling merged clusters in the less granular pad layers. The final cluster position is then calculated as the average positions from the two pixel layers.

12.1.3 *Response of the FoCal-E to single photons*

The reconstruction efficiency for photons in the FoCal-E acceptance is shown in Fig. 12.2a as a function of true photon energy for various pseudorapidity ranges. The efficiencies were obtained using the aforementioned simulation containing a single photon in each event. A cluster is associated with a generator level photon via a geometrical matching, where a cluster within $\Delta R = \sqrt{\Delta x^2 + \Delta y^2} < 0.2$ is considered to be produced by the given photon. One finds a photon reconstruction efficiency of about 90 % over almost the full covered energy range up to 1.5 TeV. This includes efficiency losses due multiple small gaps of about 8 mm between FoCal-E modules, which are required to accommodate cooling plates for the readout electronics. These gaps are visible as horizontal stripes in Fig. 12.3, which shows the $x - y$ position of photon clusters reconstructed in the FoCal-E detector. The cooling support has not yet been implemented for the studies performed for the LOI [72], where a photon reconstruction efficiency of

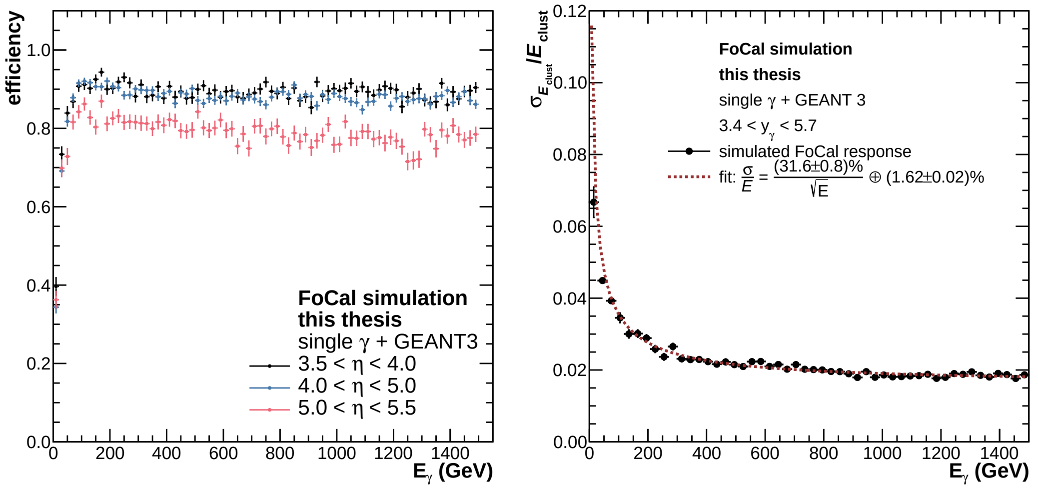

(a) efficiency

(b) energy resolution

Figure 12.2: **Left:** Photon reconstruction efficiency of the FoCal-E for various pseudorapidity intervals obtained from simulations. **Right:** Energy resolution of the FoCal-E as a function of photon energy E_γ.

$\approx 100\,\%$ is reported for $E_\gamma \gtrsim 100\,\mathrm{GeV}/c$. An increasing efficiency loss is observed for $E_\gamma \lessapprox 100\,\mathrm{GeV}/c$, which is still under investigation. It most likely originates from the selection criteria used by the clusterisation algorithm, which were optimized for larger photon energies and tuned to reduce cluster splitting effect for single photons. The impact of photon conversions on the reconstruction efficiency was found to be minor. This can be attributed to the small opening angle of the conversion electrons in the highly-boosted forward region, allowing to reconstruct the energy of both electrons in a single cluster, essentially recovering the energy of the converted photon. Comparison of the reconstruction efficiency for different pseudorapidity regions shows no strong dependence of the efficiency on the photon pseudorapidity. However, an efficiency loss of about 10 % is observed for the most forward studied pseudorapidity region ($5 < \eta < 5.5$). This loss can be attributed to an acceptance effect rather than a loss of photon reconstruction efficiency: While a projection of a pseudorapidity selection onto the xy plane of the FoCal-E surface results in circular selection, the surface of the FoCal-E is rectangular. This is illustrated in Fig. 12.3, which shows the $x-y$ position distribution of photon clusters in the FoCal-E. For very forward rapidities ($\eta > 5.3$), the acceptance of the detector is limited by the rect-

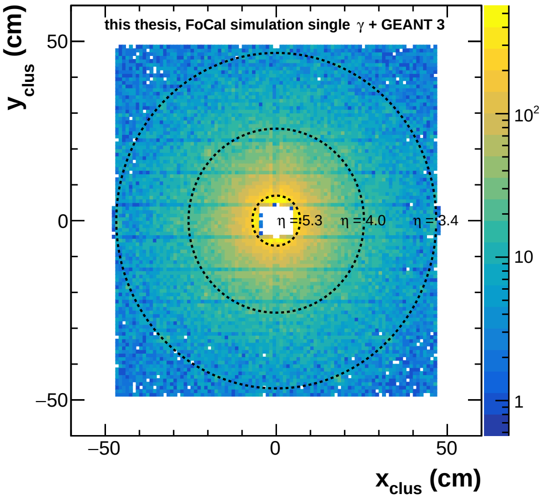

Figure 12.3: Position of photon clusters in the FoCal-*E* obtained from simulation of single photon events propagated through GEANT3. Circles of varying sizes illustrate various pseudorapidity selections.

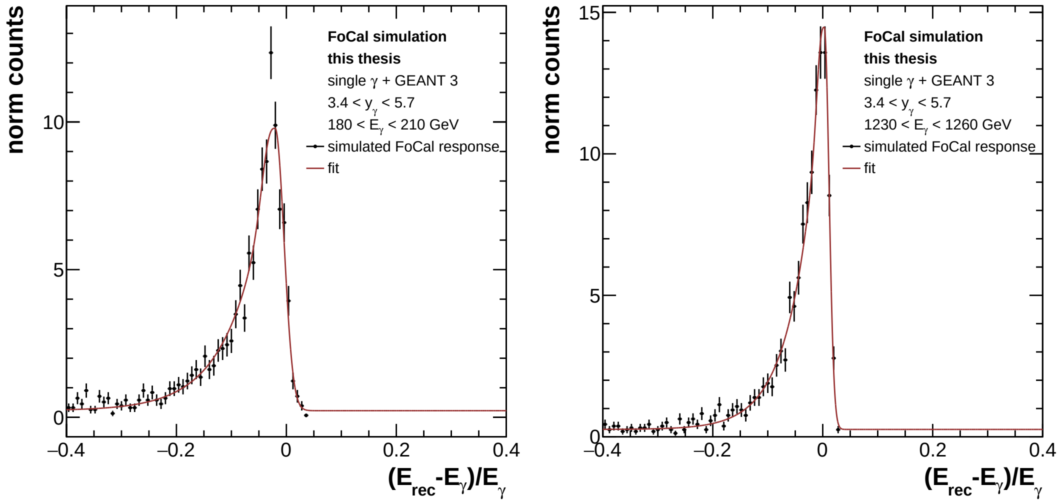

(a) low photon energy

(b) high photon energy

Figure 12.4: Energy response of the FoCal-E detector to photons obtained from MC simulations propagated through the detector geometry implemented in GEANT3. The response is given in two exemplary intervals of true photon energy (E_γ), and quantified as the relative difference of reconstructed and true photon energy. The response is fitted using a Gaussian with an exponential tail on the left side, as indicated by the red line. The energy resolution in the given energy slice is obtained using the Full Width at Half Maximum (FWHM) of the distribution converted to one standard deviation.

angular empty space in the middle of the detector, which is required for the beampipe, resulting in the observed efficiency loss.

In addition to the photon reconstruction efficiency, the energy resolution is a key-quantity for any calorimeter. Fig. 12.2b shows the expected energy resolution ($\sigma_{E_\mathrm{clust}}/E_\mathrm{clust}$) of the FoCal-E detector as a function of photon energy E_γ. The resolution is obtained using the aforementioned MC simulation of single photons: The relative difference of the reconstructed cluster energy and true photon energy $(E_\mathrm{clus} - E_\gamma)/E_\gamma$ is studied in slices of photon energy E_γ, as illustrated for two exemplary energy intervals in Fig. 12.4. The energy response of the detector is then fitted using a Gaussian with an exponential tail on the left side, denoted by the red line. The energy resolution in each E_γ slice is then given as the FWHM of the fit function converted to one standard deviation σ. Finally, the photon energy dependence of the resolution is fitted, and one obtains:

$$\frac{\sigma}{E} = \frac{(31.6 \pm 0.8)\,\%}{\sqrt{E}} \oplus (1.62 \pm 0.02)\,\% \tag{12.1}$$

where $\oplus$ denotes the addition in quadrature and the energy is given in units of GeV. This energy resolution is only based on the simulations with GEANT3 and therefore should only be considered as a rough estimate of the expected performance. Additional factors, such as channel-to-channel variations of the gain, linearity and electronic noise are expected to worsen the constant term of the resolution for a real detector [72]. Experimental determination of the energy resolution is currently ongoing using data collected with a FoCal prototype in electron and hadron beams of varying energy at

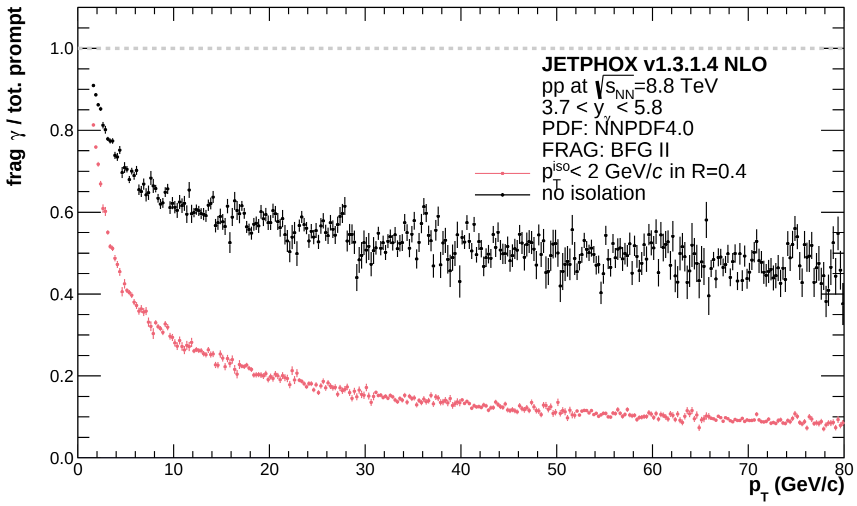

Figure 12.5: Contribution of fragmentation photons to the prompt photon cross section at forward rapidities ($3.7 < y < 5.8$). The calculation is obtained using the `JetPhox` [73] program at NLO for pp collisions at $\sqrt{s} = 8.8\,\text{TeV}$. All scales are chosen to coincide with the transverse momentum of the photon.

the PS and SPS. Nonetheless, even a larger constant term of up to 5 % is not expected to significantly impact physics analyses involving photons [72].

12.2 PROMPT PHOTON IDENTIFICATION

12.2.1 *Isolation*

As discussed in Sec. 6, isolation requirements are an important tool to suppress the large background of decay photons, as well as contributions from fragmentation photons. The latter is illustrated in Fig. 12.5, which shows the contribution of fragmentation photons to the prompt photon cross section. The ratios are obtained using the `JetPhox` program at NLO, assuming a collision energy of $\sqrt{s} = 8.8\,\text{TeV}$ and requiring the prompt photon to be produced within $3.7 < y < 5.8$. The used proton PDF and fragmentation function are given in the legend. Similar to the findings in Sec. 2.4.2 at mid-rapidity, one finds that an isolation requirement of $p_{\mathrm{T}}^{\mathrm{iso}} < 2\,\text{GeV}/c$ in a cone with $R = 0.4$ significantly suppresses the contribution of fragmentation photons, where in particular its contribution gets suppressed from about 60 % to 20 % at $p_{\mathrm{T}} \approx 20\,\text{GeV}/c$[2].

Since no tracking detectors are present at forward rapidities in ALICE, the implementation of an isolation criterium for the measurement of prompt isolated photons with the FoCal can only rely on quantities measured in the FoCal-E and FoCal-H. To study the expected performance of an isolation requirement, full simulations of MB pp collision events at the highest foreseen collision energy of $\sqrt{s} = 14\,\text{TeV}$ are performed with `Pythia6` and propagated through the detector geometry implemented in Geant3. In addition, a signal enhanced sample is simulated that only includes the GJ processes in `Pythia`. Fig. 12.5 shows the isolation energy ($E_{\mathrm{T,\,iso}}$) for all FoCal clusters

---

[2] As already noted in Sec. 2.4.2, this figure and the shown fractions should only be taken as an illustration of the impact of the isolation criterium. The definition of what is considered as the fragmentation contribution depends on the choice of the fragmentation scale.

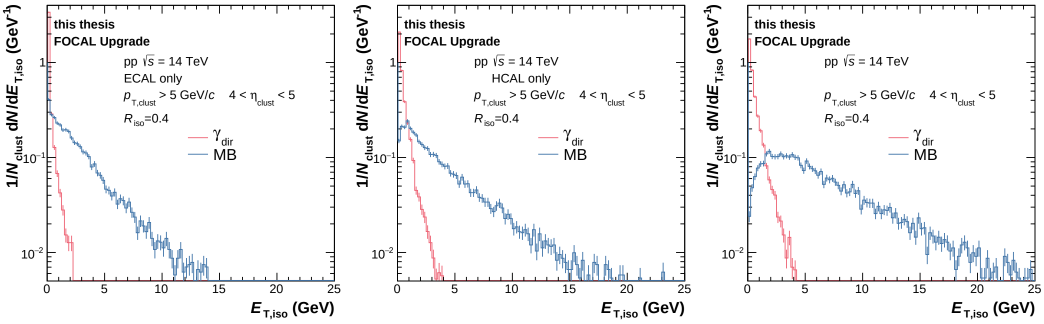

(a) FoCal-E only (b) FoCal-H only (c) FoCal-E + FoCal-H

Figure 12.6: Isolation energy ($E_{\mathrm{T,\,iso}}$) for all FoCal clusters with $p_{\mathrm{T,\,clust}} > 5\,\mathrm{GeV}$ found within $4 < \eta < 5$, calculated in a cone with $R = 0.4$ around the given cluster. The isolation energy is calculated using the detectors given in the respective caption. The different colours indicate the processes included in the `Pythia` simulation of pp collisions at $\sqrt{s} = 14\,\mathrm{TeV}$, resulting in a prompt photon signal dominated sample (red) and decay photon dominated sample (blue).

with $p_{\mathrm{T,\,clust}} > 5\,\mathrm{GeV}/c$ found within $4 < \eta < 5$. The isolation energy is calculated as the sum of the transverse energy of all clusters found within a cone of radius $R = 0.4$ around the respective cluster. Since no clusterization algorithm is currently implemented for the FoCal-H, energy deposits in each of its towers are considered as a cluster. Comparing the signal dominated GJ sample (red) with the background dominated MB sample (blue), a clear separation between signal and background is observed, similar to the findings at mid-rapidity in Sec. 6.

To quantify the effect of different isolation criteria on the signal extraction, the ratio of signal and background efficiency ($\epsilon_{\mathrm{sig.}}/\epsilon_{\mathrm{bkg.}}$) is studied as a function of the isolation threshold ($E_{\mathrm{T,iso,cut}}$) and is presented in Fig. 12.7. To obtain a first estimate, simplified definitions[3] of the signal and background efficiency are used, which are given by the fraction of clusters from the signal and background dominated sample, respectively, that fulfil a given isolation requirement. As illustrated in Fig. 12.7, employing an isolation criterium significantly improves the signal-to-background ratio, which increases with an increasingly strict isolation threshold. Furthermore, inclusion of the hadronic signal from FoCal-H further improves the sensitivity of the isolation cut, motivating the usage of the combined signal from FoCal-E and FoCal-H for photon isolation. The following studies will use an isolation requirement of $E^{\mathrm{H+E}}_{\mathrm{T,iso}} < 2\,\mathrm{GeV}$ in FoCal-E and FoCal-H, which increases the signal-to-background ratio by about a factor of 5 without introducing a significant loss of signal efficiency, which was found to be above 95 % using this threshold. In addition, the signal-to-background efficiency ratios have been studied for p–Pb collisions at the expected centre-of-mass energy of $\sqrt{s_{\mathrm{NN}}} = 8.8\,\mathrm{TeV}$, and are presented in Fig. 12.7b. The simulations are obtained by embedding Pythia pp collision events into p–Pb events generated using the Hijing [212] event generator, which are then propagated through Geant3. The performance is comparable to the one from pp collisions, however, one finds overall slightly higher signal-to-background

---

[3] These definitions are strictly speaking only correct if the GJ sample only contains clusters from prompt photons and the background sample does not contain any prompt photons. However, since the GJ is dominated by prompt photons these definitions are expected to be sufficient to obtain a first estimate of the isolation performance. Future studies should include more sophisticated definitions as given in Sec. 7.

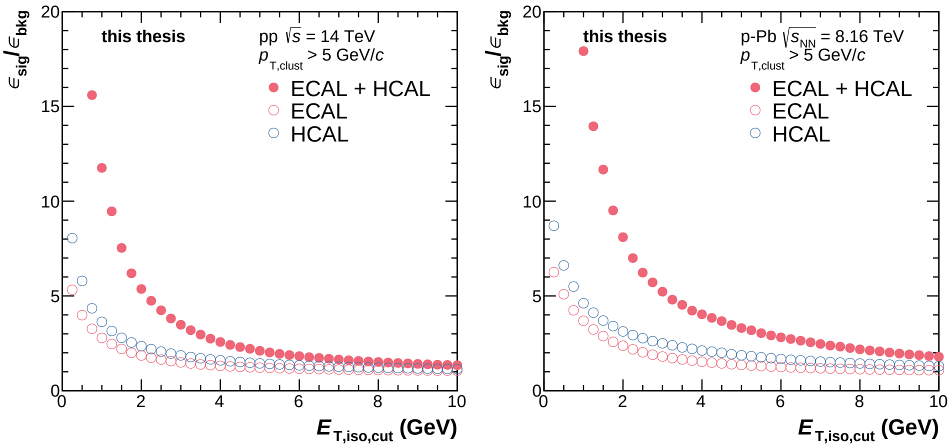

(a) pp collisions at $\sqrt{s} = 14\,\text{TeV}$ (b) p–Pb collision at $\sqrt{s_{\text{NN}}} = 8.8\,\text{TeV}$

Figure 12.7: Signal-to-background efficiency ratio ($\epsilon_{\text{sig.}}/\epsilon_{\text{bkg.}}$) shown as a function of isolation energy. Different markers indicate the calorimeters used to obtain the isolation energy. The ratios are shown for pp collision events at $\sqrt{s} = 14\,\text{TeV}$ obtained with PYTHIA (left) and p–Pb collisions at $\sqrt{s_{\text{NN}}} = 8.8\,\text{TeV}$ obtained from PYTHIA events embedded into p–Pb events from the HIJING event generator.

efficiency ratios, which can be attributed to the lack of an UE subtraction (see Sec. 6.2). The studies for p–Pb collisions therefore use a modified isolation requirement of $E_{\text{T,iso}}^{\text{H+E}} < 3\,\text{GeV}$ in the following, which compensates for the lack of UE subtraction and leads to a signal-to-background ratio comparable to the one observed in pp collisions ($S/B \approx 5.2$).

12.2.2 *Invariant mass tagging and shower shape*

In addition to the isolation requirement, other techniques are available to suppress the decay photon background in the prompt photon measurement:

1. Rejection of photons originating from π^0 decays using the invariant mass of photon clusters.
2. Rejection of elongated clusters originating from two decay photons with small opening angle.

The potential of both approaches to increase the signal-to-background ratio of the measurement has been studied using the simulation of pp and p–Pb collision events at $\sqrt{s_{\text{NN}}} = 14$ and $8.8\,\text{TeV}$, respectively, propagated through the realistic implementation of the Run4 ALICE geometry in Geant3. The collision events are simulated using PYTHIA6 (and HIJING) and divided into a signal and background dominated sample, as outlined in the previous section.

In order to reject photons originating from π^0 decays, the invariant mass $m_{\gamma\gamma}$ of all cluster pairs in a given event is calculated, requiring for each cluster an energy above 2 GeV. The cluster pair with an invariant mass closest to the nominal π^0 mass of $\approx 134\,\text{MeV}/c$ is then assigned as the invariant mass associated with a given cluster. If a cluster belongs to a pair with an invariant mass of $70\,\text{MeV}/c^2 < m_{\gamma\gamma} < 180\,\text{MeV}/c^2$,

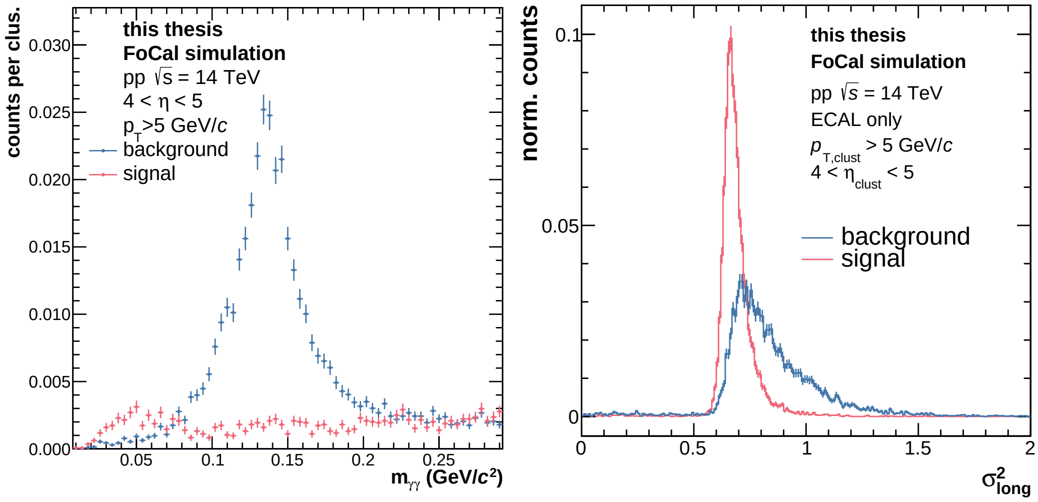

(a) π^0 tagging (b) shower shape

Figure 12.8: **Left:** Invariant mass of cluster pairs closest to the nominal π^0 mass ($134\,\text{MeV}/c^2$) shown for the signal and background dominated Pythia sample in pp collisions at $\sqrt{s} = 14\,\text{TeV}$. **Right:** Shower shape parameter σ^2_{long} for clusters with $p_{\text{T}} > 5\,\text{GeV}/c$ in the same collision system.

the cluster is "tagged" to originate from a π^0 decay and rejected as background. Fig. 12.8a shows the thus obtained invariant mass distribution for all signal and background cluster with $p_{\text{T}} > 5\,\text{GeV}/c$ in simulated pp collision events at $\sqrt{s} = 14\,\text{TeV}$. While the distribution of clusters from the background dominated sample (blue) displays a clear peak in the vicinity of the nominal π^0 mass on top of a small combinatorial background, no such peak is visible for clusters associated with a prompt photon, illustrating the discriminatory power of the π^0 tagging method.

Fig. 12.8b shows the shower shape of all clusters with $p_{\text{T}} > 5\,\text{GeV}/c$ in pp collisions at $\sqrt{s} = 14\,\text{TeV}$, where the signal and background dominated Pythia samples are denoted with different colours, as given in the legend. The shower shape is first calculated according to Eq. 5.7 for each FoCal-E pad segment contributing to a given cluster. Next, a single shower shape parameter σ^2_{long} is assigned to the full cluster given by the sum of the shape parameter from each pad segment weighted with the respective energy of the segment. As illustrated in Fig. 12.8b, clusters from the background dominated sample are overall more elongated than cluster from the signal sample, which can be attributed to $\pi^0 \rightarrow \gamma\gamma$ decays where the two photons are reconstructed as a single elongated cluster (see Sec. 5.3.2). The shower shape therefore contains information that allows for a distinction between signal and background photons and a shower shape selection of $\sigma^2_{\text{long}} < 0.7$ is incorporated in the prompt photon analysis to improve the signal-to-background ratio. In contrast to the π^0 tagging approach, which relies on a good shower separation provided by the pixel layers, shower merging is beneficial and even necessary to allow for a discrimination of signal and background using the shower shape.

Fig. 12.9 shows the signal and background efficiency in pp collisions at $\sqrt{s} = 14\,\text{TeV}$ as a function of cluster p_{T} for the various selection criteria discussed in this section. The reconstruction efficiency for the decay photon background is shown in the left

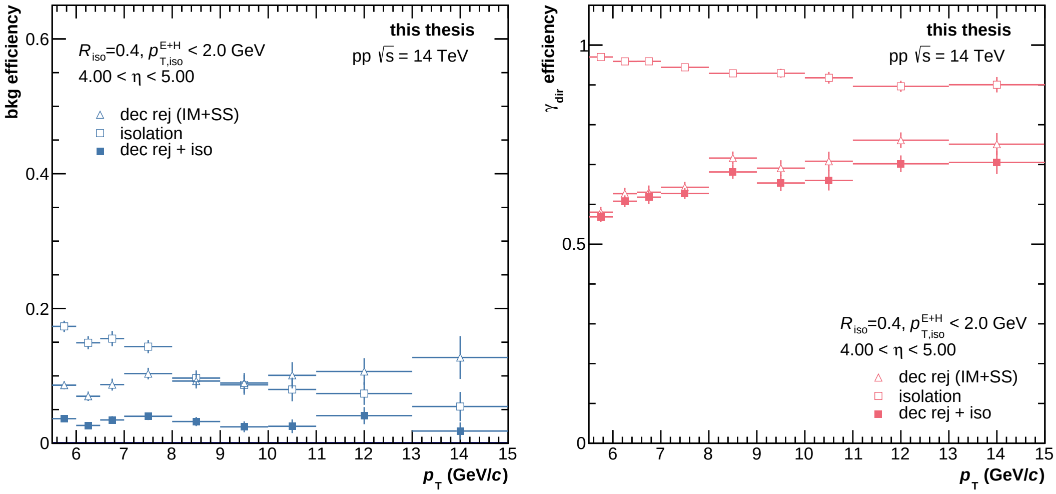

(a) background efficiency

(b) signal efficiency

Figure 12.9: **Left:** Reconstruction efficiency for background clusters in pp collisions at $\sqrt{s}$ = 14 TeV obtained using Pythia6 and full detector simulation in Geant3 for various selections, which are outlined in the text. **Right:** Reconstruction efficiency for signal photons in the same collision systems. A low reconstruction efficiency for the background sample and a high efficiency for the signal sample are desirable.

panel of the figure, where a low efficiency is desirable and corresponds to a large background rejection. One finds that the invariant mass rejection (IM) and shower shape selection (SS) remove about 87 % of all background photons for the studied p_{T} range up to 15 GeV/c. The isolation requirement is most efficient as higher transverse momenta, and removes up to 91 % of all background at $p_{\mathrm{T}} = 14$ GeV/c. Combining all criteria (dec. rej. + iso) an overall rejection of up to 97 % is achieved.

Fig. 12.9b shows the corresponding prompt photon signal efficiency, which is obtained using Pythia direct photon events. Both the SS and IM rejection remove between about 30 % and 50 % of the signal, which can be attributed to the overlap of the shower shape distributions of signal and background (Fig. 12.8b), as well as random cluster pairs falling within the π^0 invariant mass window (Fig. 12.8a). The inefficiency introduced by the isolation criterium is small and found to be below 10 % for the studied p_{T} range.

The signal and background efficiency for p–Pb collisions at $\sqrt{s_{\mathrm{NN}}} = 8.8$ TeV is shown in Fig. A.8. While the signal-to-background ratio is comparable to the one in pp collisions, one observes overall stronger suppressions of both signal and background contributions. Using all aforementioned selections, the background efficiency is in the order of a few percent, indicating an excellent suppression of background contributions. However, the selections also impact the signal efficiency, which is found to be between 10 % and 20 % for the studied transverse momentum range. In the future, these studies will be repeated using the perpendicular cone method to estimate the UE on an event-by-event basis.

Finally, 12.10a shows the fraction of all clusters produced by a direct prompt photon, where the ratio is obtained from a combined Pythia sample of pp collisions at $\sqrt{s}$ = 14 TeV consisting of MB and direct prompt photon processes weighted with their respective cross sections. Without any selections, the signal fraction is low, ranging from only 2 % at $p_{\mathrm{T}} = 5$ GeV/c to up to 4 % at $p_{\mathrm{T}} = 14$ GeV/c. The imposed selection criteria

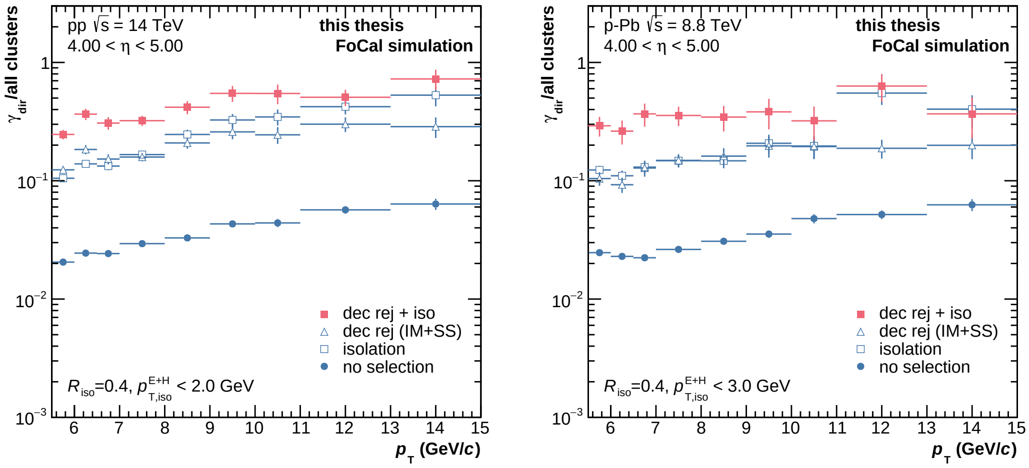

(a) pp collisions, $\sqrt{s} = 14\,\text{TeV}$ (b) p–Pb collisions, $\sqrt{s_{\text{NN}}} = 8.8\,\text{TeV}$

Figure 12.10: Fraction of clusters produced by direct prompt photons with respect to all clusters produced in pp and p–Pb collisions at $\sqrt{s_{\text{NN}}} = 14\,\text{TeV}$ and 8.8 TeV, respectively. The ratios are obtained using Pythia simulations, where MB and direct prompt photon processes are weighted with their respective cross sections. Several background rejection criteria are given in the legend, which significantly improve the fraction of direct prompt photon clusters in the sample.

significantly improve this fraction, especially at low-p_{T}, where a signal fraction of up to 37 % is observed when applying all selection criteria, corresponding to an improvement by a factor of 18. Similar improvements are observed for the simulated p–Pb collision sample, where the corresponding signal fractions are shown in Fig. 12.10b.

12.3 PURITY

As discussed in Sec. 8, several approaches are available to obtain the signal purity in a data-driven way, exploiting the discriminatory power of shower shape and isolation energy. Fig. 12.11 shows the isolation energy $E_{\text{T, iso}}$ as a function of shower shape parameter σ^2_{long} for the background (left) and signal dominated sample (right) measured with the FoCal-E and FoCal-H. Both samples are obtained using Pythia and Geant, as outlined in the previous sections. A clear difference is observed between both samples, where in particular signal photons tend to be narrow and isolated. In order to study the feasibility of a data-driven purity extraction with the FoCal detector, both samples shown in Fig. 12.11 are scaled according to their respective cross section from Pythia and added in order to obtain a sample containing signal and background processes. This sample is then treated as FoCal pseudo data and the purity is calculated using the ABCD method (see Sec. 8.2), where the used selections[4] for the four regions are given in Tab. 12.1.

The black markers in Fig. 12.12a show the prompt photon signal purity calculated according to Eq. 8.11 as a function of cluster p_{T} in pp collisions at $\sqrt{s} = 14\,\text{TeV}$ and $4 < \eta < 5$. The signal candidates are required to fulfil an isolation requirement of $p_{\text{T}}^{\text{H+E}} <$

---

[4] The selections for p–Pb collisions at $\sqrt{s_{\text{NN}}} = 8.8\,\text{TeV}$ are adapted to account for the differing isolation requirement. In particular, $E_{\text{iso}}^{\text{H+E}} \leq 3\,\text{GeV}$ and $E_{\text{anti-iso}}^{\text{H+E}} \geq 6\,\text{GeV}$ are used.

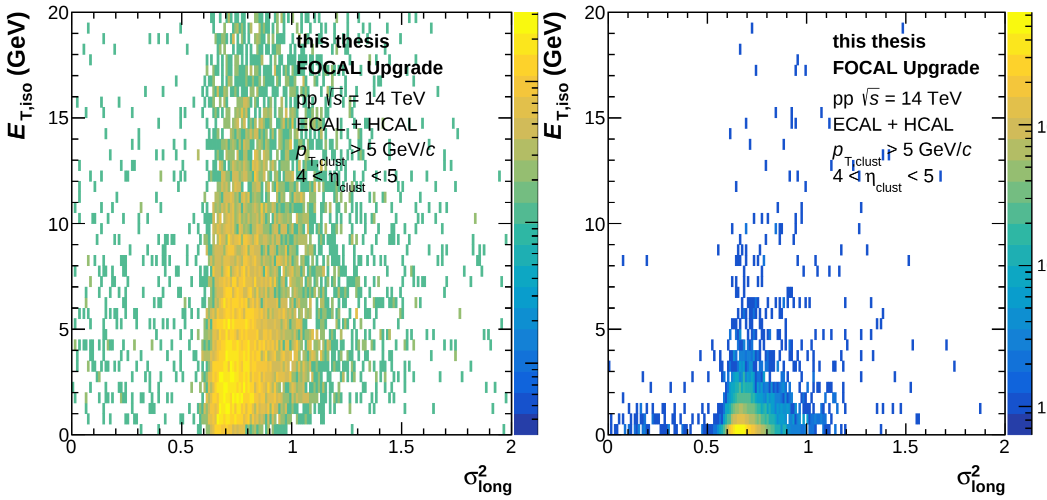

(a) background dominated

(b) signal dominated

Figure 12.11: Isolation energy $E_{\mathrm{T,\,iso}}$ as a function of shower shape parameter σ^2_{long} for PYTHIA MB events (left) and GJ events (right) propagated through the detector geometry using GEANT3.

2 GeV/c, as well as the decay photon tagging according to the invariant mass, which was discussed in the previous section. The purity is found to increase with increasing p_{T}, up to a signal purity of more than 70 % at 14 GeV/c. Furthermore, the purity determined using the ABCD method is in excellent agreement with the true signal purity (red markers). However, as discussed in Sec. 8.4, this perfect agreement arises "by construction" as a direct consequence of Eq. 8.11 for the case where data and MC are the same sample. For future measurements with the FoCal detector, the purity will be determined in a data driven way, where only the additional factor α_{MC} is determined using information from MC event generators, as discussed in Sec. 8.2. Fig. 12.12b shows the ratios of the purities determined with and without the α_{MC} correction, illustrating the impact of this correction on the purity estimates. One finds that neglecting underlying correlations leads to a significant overestimation of the signal purity of up to about 60 % at $p_{\mathrm{T}} \sim 6$ GeV/c. This shows that underlying correlations between shower shape and isolation energy have a sizeable impact on the purity determination, and therefore an accurate description of these correlations by the used MCs is essential for an accurate purity estimate for future FoCal measurements. However, as outlined in Sec. 8.2, the ability of the used MC productions to describe the correlations observed in data can be tested using the double ratio given in Eq. 8.5. Following a similar procedure for future FoCal

Table 12.1: Selections used for the different regions of the ABCD method for a FoCal measurement. The purity in the signal region $\mathbb{A}$ is estimated using the background dominated control regions $\mathbb{B}$, $\mathbb{C}$ and $\mathbb{D}$ as described in Sec. 8.2. The values in brackets denote the used thresholds for the p–Pb sample.

Region	Iso. (GeV/c)	Shower shape
$\mathbb{A}$	$\leq 2(3)$	$\sigma^2_{\mathrm{long}} \leq 0.7$
$\mathbb{B}$	$\leq 2(3)$	$\sigma^2_{\mathrm{long}} \geq 0.9$
$\mathbb{C}$	$\geq 5(6)$	$\sigma^2_{\mathrm{long}} \leq 0.7$
$\mathbb{D}$	$\geq 5(6)$	$\sigma^2_{\mathrm{long}} \geq 0.9$

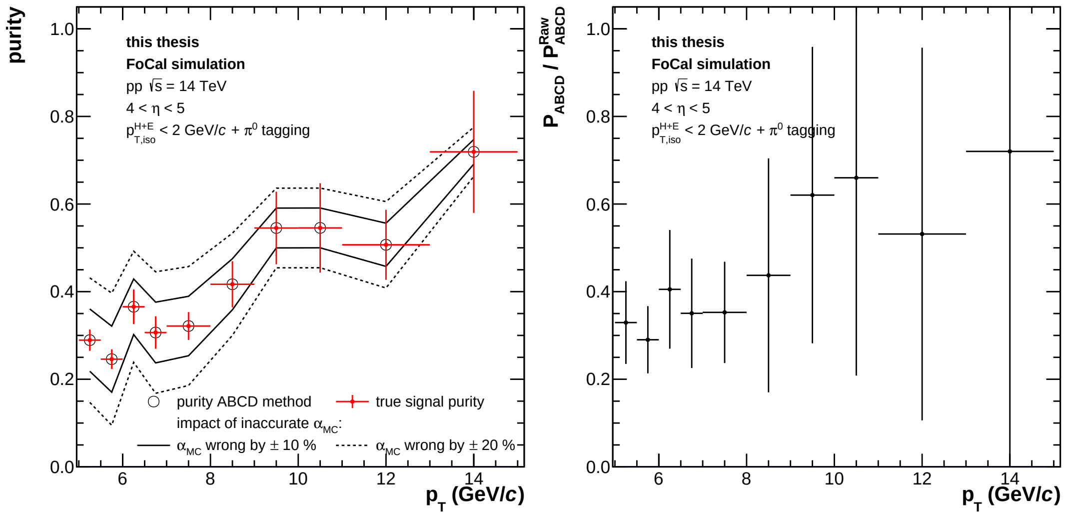

(a) Purity estimate

(b) Impact of α_{MC} correction

Figure 12.12: **Left:** Isolated prompt signal purity for clusters measured with the FoCal in $4 < \eta < 5$ in simulated pp collision events at $\sqrt{s} = 14\,\text{TeV}$. A purity estimate using the ABCD method according to Eq. 8.11 (black markers) is in agreement with the true signal purity of the MB+GJ Pythia sample. Dashed and solid lines indicate the impact of a potential wrong determination of α_{MC} on the purity estimate, which may arise if the used MC do not accurately describe the correlation of shower shape and isolation energy in data. **Right:** Ratio of the purity estimate obtained with and without the aforementioned α_{MC} correction.

measurements will allow determining and (if needed) adjust the MC description to obtain an accurate estimate of α_{MC}. Nonetheless, the impact of a potential mismatch between future data and the corresponding MC description on the purity determination is illustrated in Fig. 12.12a by dashed and solid lines. In particular, overestimation of the underlying correlations by 10 % leads to a relative modification of about 20 % for the purity estimate at $p_T \approx 6\,\text{GeV}/c$, decreasing to about 5 % at $p_T \approx 14\,\text{GeV}/c$. The same studies have been performed for p–Pb collisions at $\sqrt{s_{NN}} = 8.8\,\text{TeV}$ with adapted isolation thresholds given in Tab. 12.1, and the obtained purities are shown in Fig. A.9. The purities are mostly consistent with those from the pp reference within the statistical uncertainties of the simulation, however, an overall slightly smaller purity is observed at high-p_T.

Overall, the performed studies indicate the feasibility to determine the purity of future isolated prompt photon measurements using the ABCD method. The selections outlined in the previous sections result in a signal purity of above 20 % for both collision systems. This is of similar size compared to the purities observed in pp and p–Pb collision at $\sqrt{s_{NN}} = 8\,\text{TeV}$ and $8.16\,\text{TeV}$ (see Fig. 8.11) for $p_T > 8\,\text{GeV}/c$, where a successful purity determination has been demonstrated using "real" EMCal data. While Fig. 12.12b shows that corrections for the correlation between shower shape and isolation energy are important for future purity determinations in FoCal measurements, it is expected that the double ratio given in Eq. 8.5 will allow to test and control the MC description of the underlying correlations.

This study merely serves as a starting point, and several future studies should be conducted that fully exploit the potential of the FoCal detector. For example, the indi-

Table 12.2: Projected plan for LHC Run 4 operation (2029-2032). Estimates obtained from internal communications with C. Loizides.

system	collision energy $\sqrt{s_{\mathrm{NN}}}$	duration	luminosity $\mathcal{L}_{\mathrm{int}}$
pp	8.8 TeV	1 week	$4\,\mathrm{pb}^{-1}$
pp	14 TeV	18 months	$150\,\mathrm{pb}^{-1}$
p–Pb	8.8 TeV	3 weeks	$300\,\mathrm{nb}^{-1}$
Pb–Pb	5.02 TeV	3 months	$7\,\mathrm{nb}^{-1}$

vidual readout of all FoCal-E pad and pixel layers allows for three-dimensional shower tracking, providing addition information for purity determination techniques. Novel machine-learning approaches could be implemented, which could allow for a classification of signal and background using the full three-dimensional shower profile and isolation energy, as well as information from the invariant mass determined for showers in the highly granular pixel layers. Furthermore, statistical methods should be explored that do not rely on the determination of the signal purity but rather on statistical subtraction of background sources from an inclusive isolated photon spectrum – similar to the approaches used to measure direct (thermal) photons [60].

12.4 ESTIMATION OF PROMPT PHOTON YIELDS

In order to get an estimate of the statistical precision that can be achieved with the FoCal detector during Run 4 of LHC operation, the expected yields for various key observables have been calculated in this work, using the expected integrated luminosities $\mathcal{L}_{\mathrm{int}}$ given in Tab. 12.2. The LHC is expected to provide pp, p–Pb and Pb–Pb collisions at various centre-of-mass energies, where especially measurements of prompt photon production in p–Pb collisions at $\sqrt{s_{\mathrm{NN}}} = 8.8\,\mathrm{TeV}$ are crucial to study saturation and constrain nPDFs. As can be seen by the given integrated luminosities, any measurement relying on comparison to pp data will be limited by the statistical precision of the pp reference data at $\sqrt{s_{\mathrm{NN}}} = 8.8\,\mathrm{TeV}$, which amounts to about $4\,\mathrm{pb}^{-1}$ of data collected over 1 week. Fig. 12.13 shows the expected cumulative yields above a given p_{T} threshold for several inclusive p_{T} spectra at forward rapidities of $3.4 < y < 5.5$ in pp and p-Pb collisions at $\sqrt{s_{\mathrm{NN}}} = 8.8\,\mathrm{TeV}$. The inclusive isolated prompt photon production cross sections are obtained with JETPHOX at NLO[5] using recent (n)PDFs and the BFG II fragmentation function assuming $\sqrt{s_{\mathrm{NN}}} = 8.8\,\mathrm{TeV}$. An isolation requirement of $p_{\mathrm{T}}^{\mathrm{iso}} < 2\,\mathrm{GeV}/c$ in a cone of $R = 0.4$ is used to suppress fragmentation photon contributions. The cross sections are converted to yield estimates using the integrated luminosities of $\mathcal{L}_{\mathrm{int}} = 1\,\mathrm{pb}^{-1}$ and $100\,\mathrm{nb}^{-1}$ for pp and p–Pb collisions, respectively[6]. In addition, the p–Pb cross section has been multiplied by $A = 208$ to account for the expected number of collisions between

---

[5] I would like to thank Werner Vogelsang for the discussions and additional NLO calculations at this collision energy that helped me to validate the cross sections I obtained using the JetPhox program. In addition, calculations using the GRV fragmentation function show no significant modification of the isolated prompt photon cross section. Furthermore, cross sections at LO were found to be about a factor 2 below NLO, indicating the importance of higher order corrections especially in this kinematic region.

[6] The given luminosities don't exactly match those given in Tab. 12.2. This was done on purpose to allow for easy scaling to any integrated luminosity.

nucleons. As can be seen in the figure, even for the pp reference, inclusive isolated prompt photon measurements are expected to be feasible up to transverse momenta of about 50 GeV/c. With over one million counts for $p_{\mathrm{T}} \gtrsim 5$ GeV, the statistical uncertainty of the measurement is expected to be negligible, even taking into account efficiency losses quantified in Fig. 12.9b. More than one order of magnitude higher yields are estimated for isolated prompt photon production in p–Pb collisions at $\sqrt{s_{\mathrm{NN}}} = 8.8$ TeV. Furthermore, primary π^0 and jet production have been studied at LO using the PYTHIA8 event generator with the Monash 2013 [78] tune [7]. The jets in a given event are obtained using the FASTJET [258] program, which clusterises the charged and neutral particles generated by PYTHIA using the anti-k_{T} algorithm [259] and a resolution parameter of $R = 0.4$. Both observables, π^0 mesons and jets, are found to be abundantly produced in the FoCal acceptance in both collisions systems for the given integrated luminosities.

---

[7] In particular, the helper classes provided by Hendrik Poppenborg at https://github.com/hpoppenb/Delphi have been used, which were incredibly useful to obtain Pythia predictions for various probes.

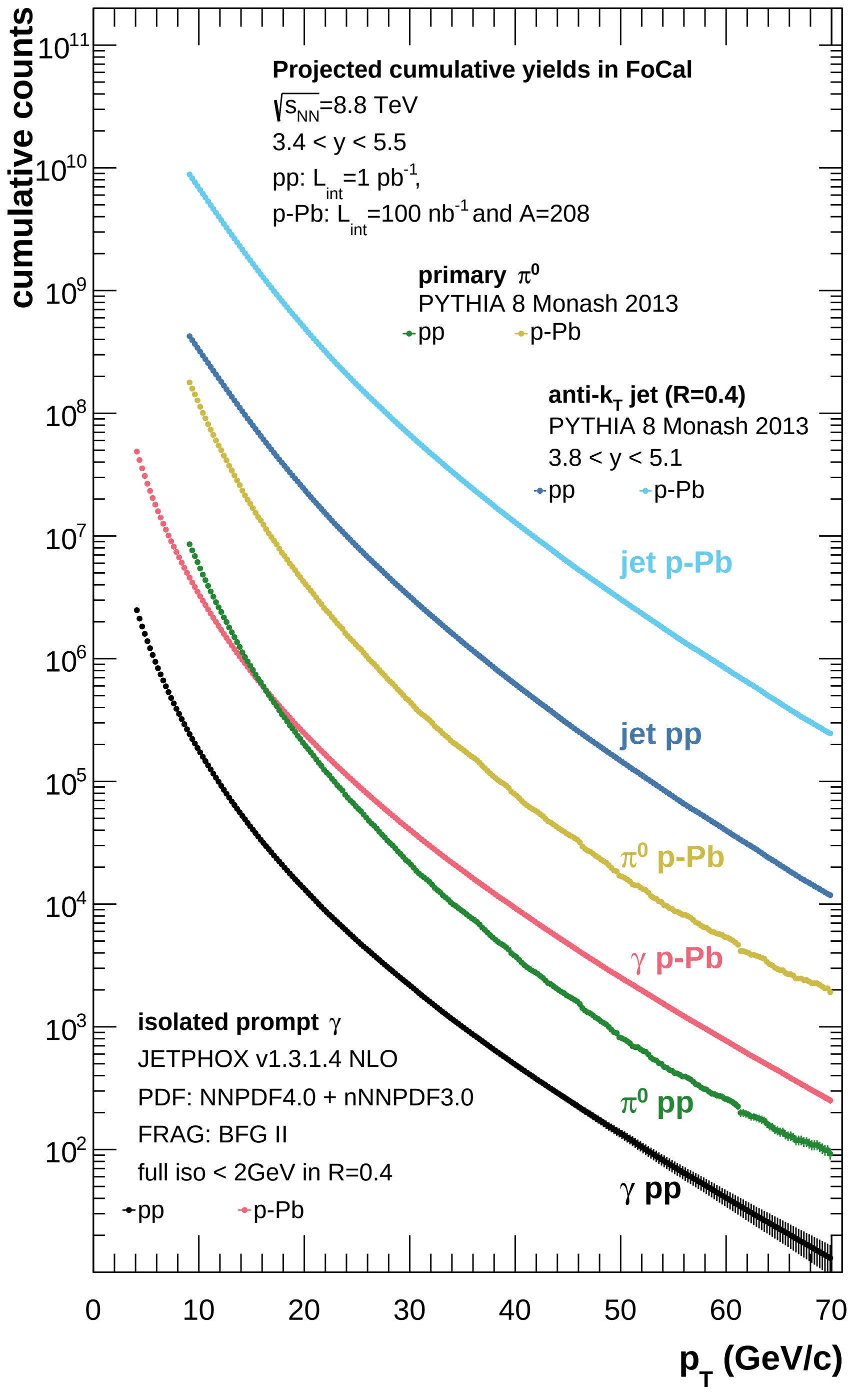

Figure 12.13: Expected cumulative yields of various observables above a given p_T in pp and p-Pb collisions at $\sqrt{s_{NN}} = 8.8$ TeV. The cross sections are obtained using the programs given in the respective legend and converted to yield estimates using the integrated luminosities $\mathcal{L}_{int}$ given in the top legend.

12.5 IMPACT ON NUCLEAR PDFS

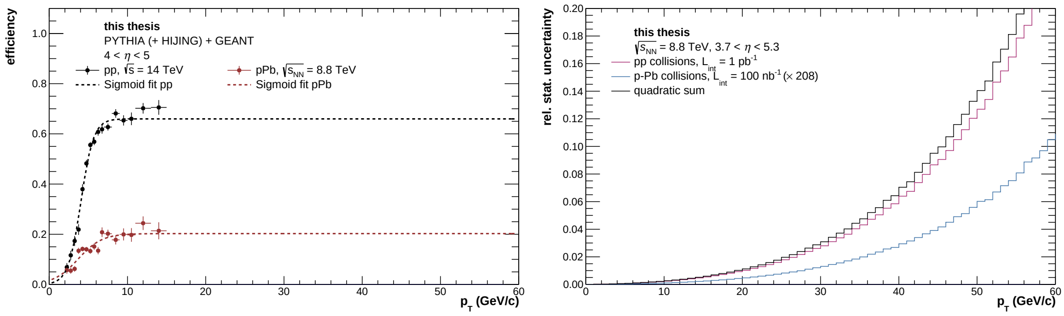

(a) signal rec. efficiency (b) expected stat. unc.

Figure 12.14: **Left:** Prompt photon signal efficiency for pp and p–Pb collisions at $\sqrt{s_{\mathrm{NN}}} = 14\,\mathrm{TeV}$ and $8.8\,\mathrm{TeV}$, respectively, obtained from Pythia (+ HIJING) collision events propagated through a GEANT3 description of the FoCal detector. The obtained efficiencies are fitted using a Sigmoid function to extrapolate the efficiency towards large transverse momenta. **Right:** Relative statistical uncertainties expected for a future measurement in pp and p–Pb collisions at $\sqrt{s_{\mathrm{NN}}} = 8.8\,\mathrm{TeV}$. The expected yields are obtained using JetPhox pQCD calculations at NLO, assuming integrated luminosities of $\mathcal{L} = 1\,\mathrm{pb}^{-1}$ and $100\,\mathrm{nb}^{-1}$ for the pp and p–Pb datasets, respectively.

The previous sections outlined the expected performance of isolated prompt photon measurements using the ALICE FoCal detector. In order to estimate the potential impact of future FoCal measurements of prompt photon production on existing nPDFs, the findings of the previous sections are combined with pQCD calculations at NLO to construct FoCal pseudo data. In particular, a pseudo measurement of the isolated prompt photon R_{pA} is obtained which is then used to perform a Bayesian reweighting study of nPDFs, following the procedure outline in Sec. 11.3. The following sections outline how the pseudo data is constructed, including the assumed statistical and systematic uncertainties, as well as the results of the reweighting study.

12.5.1 *Statistical uncertainties*

The expected statistical precision of a future prompt photon measurement is estimated using JetPhox predictions of the isolated prompt photon production cross section in pp and p–Pb collisions at $\sqrt{s_{\mathrm{NN}}} = 8.8\,\mathrm{TeV}$, which are converted to the expected signal yield in each system, as discussed in Sec. 12.4. The thus obtained yields are multiplied with the expected signal efficiency, which is determined for clusters fulfilling the isolation requirement, shower shape selection and π^0 mass tagging discussed in Sec. 12.2. The signal efficiency is again shown for both collision systems in Fig. 12.14a. A fit using a Sigmoid function (see Eq. 8.14) is performed to extrapolate the efficiencies to large transverse momenta which have not yet been covered in the presented performance studies. The expected statistical uncertainty for each p_{T} interval is then simply obtained as $\sigma = \sqrt{N}$, where N is the number of counts in the respective interval. Fig. 12.14b shows the expected relative statistical uncertainties for the measurement in pp and p–Pb collisions at $\sqrt{s_{\mathrm{NN}}} = 8.8\,\mathrm{TeV}$, respectively. In addition, the quadratic sum of the statistical uncertainties is shown, which corresponds to the expected statistical uncertainty

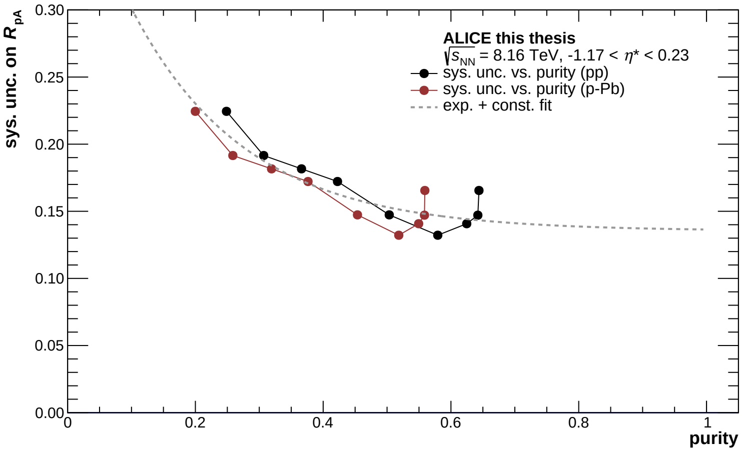

Figure 12.15: Relative systematic uncertainty of the measured isolated prompt photon R_{pA} presented in Fig. 11.5 as a function of the signal purity (see Fig. 8.11). For the black curve, the purity from the pp collision sample is considered, whereas the red curve shows the relative uncertainty as a function of the purity for the measurement in p–Pb collisions. The grey dashed line denotes a fit using an exponential function given in Eq. 12.2.

on the level of the R_{pA} assuming uncorrelated statistical uncertainties between both collision systems. One finds statistical uncertainties of less than 2 % for $p_{\mathrm{T}} \lesssim 25\,\mathrm{GeV}/c$, showcasing that a future measurement will most likely not be limited by the achievable statistical precision.

12.5.2 *Systematic uncertainties*

Estimation of the expected systematic uncertainties is challenging since no real data is available that would allow for a careful evaluation of all uncertainty sources as done in Sec. 9. These evaluations can not be performed accurately using only simulated data because systematic effects often arise due to detector effects that are not fully captured by used MCs. In order to still obtain a rough estimate of the expected systematic uncertainties, a pragmatic and conservative approach is used that considers the systematic uncertainties of the measurement at mid-rapidity presented in Sec. 9 as a baseline. The uncertainties on the level of the R_{pA} are shown in Fig. 9.1c and are dominated by uncertainties related to the purity determination. Under the assumption that a future measurement will employ the same method of purity determination, i.e. the ABCD method, it is reasonable to assume that the systematic uncertainties will likely be dominated by the purity determination procedure. As can be seen in Fig. 9.1c, the uncertainty measurement at mid-rapidity increases with decreasing photon transverse momentum. This is a consequence of the overall decreasing signal purity which results in an increasingly challenging data driven purity extraction. In order to “translate” the systematic uncertainty of the measurement at mid-rapidity to a phasespace of a future measurement using the FoCal, the relative systematic uncertainty of the R_{pA} is first displayed as a function of the signal purity. This is shown in Fig. 12.15, where the black and red points showcase the relative systematic uncertainty of the R_{pA} as a function of the signal purity in pp and p–Pb collisions, respectively. The aforementioned trend of an increasing systematic uncertainty for decreasing purity can be clearly observed. This

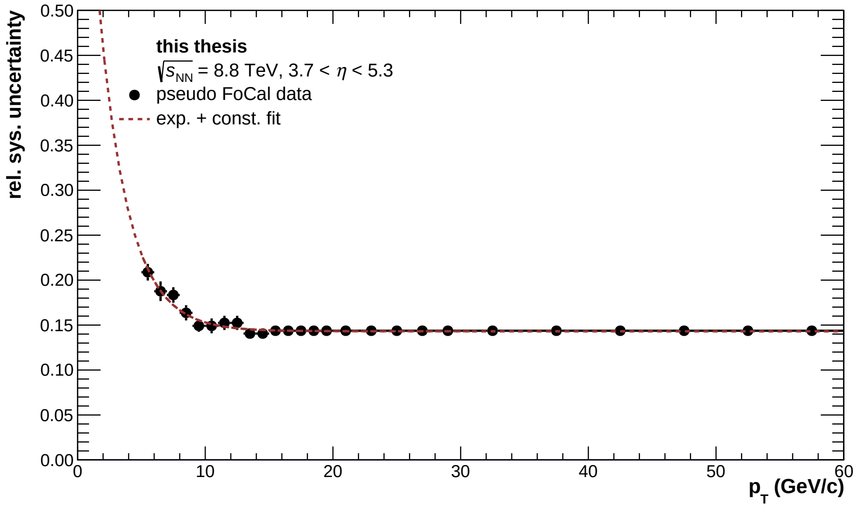

Figure 12.16: Conservative estimate of the expected relative systematic uncertainties of the isolated prompt photon R_{pA}, measured with the FoCal detector in $3.7 < \eta < 5.3$ at $\sqrt{s_{\mathrm{NN}}} = 8.8\,\mathrm{TeV}$. The grey dashed line denotes an exponential fit, where the used parametrization is given in Eq. 12.2.

observation is independent of whether the purity from the pp or p–Pb data sample is used, where the slighly lower purity in p–Pb collisions results in a slight shift with respect to the curve obtained using the purity from the pp sample. To resolve some ambiguity in the choice of reference purity and to allow for an extrapolation for all possible purities, both curves are fitted simultaneously using an exponential function:

$$f(p_{\mathrm{T}}) = a_0 \cdot \exp(a_1 p_{\mathrm{T}}) + a_2, \tag{12.2}$$

where a_{0-2} are free parameters of the fit.

Using the expected signal purities for a future FoCal measurement obtained from the simulation studies presented in Sec. 12.3, one can obtain a conservative estimate of the relative systematic uncertainty of a prompt photon R_{pA} measured with the FoCal detector. This is done by obtaining the FoCal signal purity for each photon p_{T} using Fig. 12.12a. As the FoCal signal purities are found to be similar in pp and p–Pb collisions, the purity in pp collisions is used as it offers a higher statistical precision. Furthermore, the purity is assumed to be constant for $p_T > 14\,\mathrm{GeV}$ where no data from the performance studies is available. This purity is then used to obtain the corresponding relative systematic uncertainty on the R_{pA} according to the fitted function shown in Fig. 12.15. The resulting *conservative* systematic uncertainty estimates for a future measurement of the isolated prompt photon R_{pA} using the FoCal detector is shown in Fig. 12.16. The vertical lines denote the statistical uncertainty, which is propagated from the purity estimates shown in Fig. 12.12a and driven by the number of used MC events. The systematic uncertainty is estimated to be about 20 % at $p_{\mathrm{T}} = 5\,\mathrm{GeV}/c$, decreasing to about 15 % for $p_{\mathrm{T}} > 14\,\mathrm{GeV}$. In order to reduce statistical fluctuations, the relative systematic uncertainty is fitted using an exponential function (Eq. 12.2), which is denoted by a red dashed line.

Considering the capabilities of the FoCal detector, which is explicitly designed to provide good shower separation and isolation capabilities required for prompt photon measurements, we assume that for a given signal purity, the systematic uncertainties of a future prompt photon measurement will be not worse than what is presented in

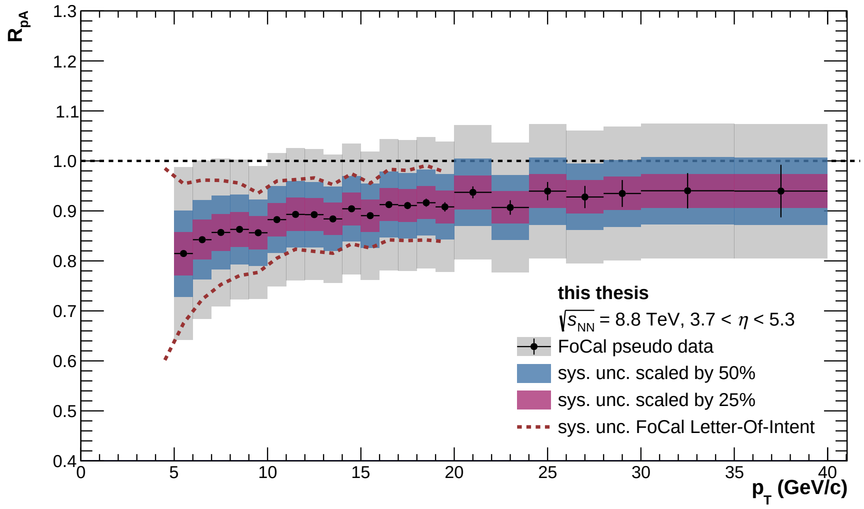

Figure 12.17: Focal pseudo data of the isolated prompt photon nuclear modification factor R_{pA} at $\sqrt{s_{\mathrm{NN}}} = 8.8\,\mathrm{TeV}$. The central values are calculated using the JetPhox program at NLO. The proton and lead beam are described using the CT18 [260] and nCTEQ15HQ [244] (n)PDFs, respectively. The estimation of the expected statistical and systematic uncertainties, denoted by vertical lines and shaded bands, respectively, is outlined in the text. The red dashed lines denote the systematic uncertainties obtained using an alternative approach, which is presented in Ref. [72] and outlined in the text.

Fig. 12.16. It is however important to stress that this is a very conservative estimate, which in particular neglects most of the detector improvements as well as possible future developments for the purity determination. The shown uncertainty merely serves as a conservative upper bound, and the reweighting studies presented in the following sections are performed considering several scenarios using improved systematic uncertainties.

12.5.3 *Construction of pseudo FoCal R_{pA}*

In order to obtain central values for the pseudo measurement of the isolated prompt photon R_{pA} the JetPhox program is used. In particular, calculations are performed at NLO for pp and p–Pb collisions at $\sqrt{s_{\mathrm{NN}}} = 8.8\,\mathrm{TeV}$ and photon rapidities of $3.7 < y < 5.3$, using an isolation requirement of $p_{\mathrm{T}}^{\mathrm{iso}} < 2\,\mathrm{GeV}/c$ in a cone of $R = 0.4$. As the reweighting studies presented in the following section use the nPDFs provided by the NNPDF collaboration, different PDFs are chosen for the JetPhox calculation in order to simulate pseudo experimental data that is slightly deviating from the expectations using nNNPDFs. In particular, the CT18 [260] PDF is used for the proton beam and the nCTEQ15HQ [244] nPDF for the lead nucleus. As for all previous calculations, the BFG II [81] fragmentation is used to describe the fragmentation photon contribution. Fig. 12.17 shows the thus obtained isolated prompt photon R_{pA}. The vertical lines denote the expected statistical uncertainties, as discussed in Sec. 12.5.1. In addition, the central values have been shifted randomly according to a Gaussian with a width corresponding to the statistical uncertainty in order to emulate statistical fluctuations of the measurement. Additional fluctuations larger than the size of the expected statistical precision of the measurement arise from statistical fluctuations of the JetPhox prediction, which are not included in the shown statistical uncertainty. The shaded bands denote the systematic uncertainty, which is obtained using the parametrization shown in Fig. 12.16. Three different scenarios are considered, which are denoted by the different colours of the bands. The grey band corresponds to the most conservative case, where the systematic uncertainties are considered to be comparable to those estimated for the measurement at mid-rapidity. The blue and red bands denote improved systematic uncertainties, which are obtained by scaling the conservative estimate by 50 % and 25 % respectively.

For reference, the red dashed lines denote an alternative estimation of the systematic uncertainties, which has been performed as part of the FoCal LOI and is described in Ref. [72]. The uncertainty of the prompt photon cross section at high-p_{T} is assumed to be dominated by the reconstruction efficiency and energy scale, where in particular an uncertainty of 5 % is assigned. At lower p_{T}, the systematic uncertainty is assumed to be dominated by the determination of the underlying background, which is mainly coming from $\pi^0 \rightarrow \gamma\gamma$ decays. Assuming a systematic uncertainty of 5 % for π^0 reconstruction efficiency, yield extraction and energy scale for the background yields, the signal-to-background ratios observed in simulation studies yield a propagated uncertainty on the signal yield of up to 20 % at $p_{\mathrm{T}} \sim 4\,\mathrm{GeV}/c$. The thus obtained uncertainties for the production cross section are added in quadrature to obtain the expected systematic uncertainties of the isolated prompt photon R_{pA}. As can be seen in the figure, the thus obtained systematic uncertainties are compatible with the upper bounds (grey) of the systematic uncertainties obtained as part of this work for $p_{\mathrm{T}} \sim 5\,\mathrm{GeV}/c$. For higher-$p_{\mathrm{T}}$, the systematic uncertainties presented in Ref. [72] approach the uncertainties corresponding to the scenario of the upper bounds scaled by 50 %. The following section outlines the impact of the thus constructed pseudo data on recent nPDFs for all previously considered scenarios of assumed systematic uncertainties.

12.5.4 *Reweighting studies*

The impact of the FoCal pseudo data on a selection of nPDFs is studied using the Bayesian reweighting approach outlined in Sec. 11.3. Following the previous pragmatic arguments of improved computation time, the INCNLO program is used to obtain predictions of the isolated prompt photon R_{pA} as well as the corresponding nPDFs uncertainties. However, the very small $x \sim 10^{-5}$ probed at forward rapidities caused numerical instabilities in the calculation, which required modifications[8] of the INCNLO source code that were provided by Ilkka Helenius.

BRIEF COMMENTS ON THE CHOICE OF THE FREE-PROTON BASELINE Fig. 12.18a shows the isolated prompt photon R_{pA} obtained using INCNLO pQCD calculations at NLO for photon rapidities of $3.7 < y < 5.3$ and $\sqrt{s_{\mathrm{NN}}} = 8.8\,\mathrm{TeV}$, where the nPDF uncertainties at 90 % CL are denoted by shaded bands. While nNNPDF30 [66] is used to describe the lead nucleus, different choices are made for the free proton PDF in order to illustrate an effect which has been previously not observed at mid-rapidity: Using NNPDF40 to describe the free-proton beam one observes a slightly increasing R_{pA} for $p_{\mathrm{T}} \lesssim 10\,\mathrm{GeV}/c$, which was not seen for the prediction using CT18 and nCTEQ15HQ (see Fig. 12.17).

---

[8] In particular, the `hadlib.f` file of INCNLO version 1.4 has been modified, where the modification can be provided on request by getting in touch with me or Marco van Leeuwen.

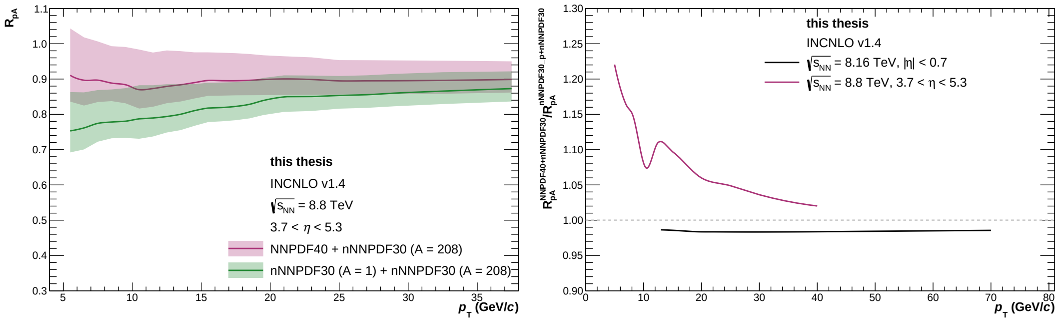

(a) Nuclear modification factor R_{pA} (b) R_{pA} double ratio

Figure 12.18: **Left:** Nuclear modification factor R_{pA} of prompt photon production at forward rapidities obtained using the INCNLO program [251] at NLO. The nNNPDF30 nPDF set is used to describe the lead beam, whereas two different PDFs are used to describe the proton beam, as given in the legend. The shaded bands denote the corresponding uncertainties of the nPDF at 90 % CL. **Right:** Ratio of the two R_{pA} predictions shown on the left. In addition, the ratio is shown for mid-rapidity ($|\eta| < 0.8$), where no significant differences are observed for the two free proton PDFs.

This increase is furthermore not present when using the implicit free-proton baseline contained in nNNPDF30 for $A = 1$, as illustrated by the green curve. Fig. 12.18b shows the ratio of the R_{pA} obtained using nNNPDF30 ($A = 208$) in combination with the NNPDF40 proton PDF with respect to the same observable using nNNPDF30 with $A = 1$ to describe the proton. The predicted R_{pA} is found to differ by up to 20 % at low-p_{T}, showcasing a substantial impact of the chosen proton reference. No such difference is observed at mid-rapidity ($|\eta| < 0.8$), where the predictions for both references agree within a few percent. This is interesting, considering that an explicit free proton boundary is used for nNNPDF30 to reproduce recent free proton PDFs for $A = 1$. In particular, the nNNPDF30 $A = 1$ has been constrained using the same experimental data used for the NNPDF40 [24] analysis, except those involving nuclear targets [66]. However, the fitting methodology of NNPDF3.1 [129] is used, which does not explicitly require positivity of the PDFs. This might indicate that the choice of fitting methodology becomes especially relevant in a weakly constrained phasespace, as is probed by measurements of prompt photon production at forward rapidities. To avoid the slight unphysical rise of the R_{pA}, the nNNPDF30 with $A = 1$ is used to describe the proton beam in the following studies, rather than the NNPDF40 used in the studies presented in Sec. 11.3.

BAYESIAN REWEIGHTING OF NNNPDF30 As illustrated by the shaded band in Fig. 12.18a, the uncertainties of the nNNPDF30 nPDF are small. In particular, they amount to about 12 % on the level of the prompt photon R_{pA} at forward rapidities, which inspects low Bjorken-x in the order of 10^{-5}. Experimental constraints in the phasespace of interest are dominated by the LHCb measurement of D^0 meson production in pp and p–Pb collisions at $\sqrt{s_{\mathrm{NN}}} = 5.02$ TeV [130] at forward and backward rapidities, which are included in the nNNPDF30 analysis via a combination of fitting and Bayesian reweighting [66]. In order to quantify the expected impact of a future FoCal measurement and compare it to the impact of the D^0 meson data, a special nNNPDF30 nPDF set that does *not* include the LHCb D^0 meson data is used as a prior for the reweighting studies. This nPDF set is referred to as nNNPDF30 (no LHCb D^0) in the following, and the corresponding prompt photon R_{pA}, which is calculated using INCNLO, is denoted by the black line and corresponding grey band in Fig. 12.19. The prediction including the LHCb D^0 meson data is illustrated by a blue line and shaded band, showcasing the significant reduction of the nPDF uncertainties achieved by inclusion of this experimental data.

For the FoCal pseudo data, three potential scenarios are considered:

1. The systematic uncertainties are equivalent to those presented in this work for the measurement of isolated prompt photon production for $|y| < 0.7$ in pp and p–Pb collisions at $\sqrt{s_{\mathrm{NN}}} = 8\,\mathrm{TeV}$ and $8.16\,\mathrm{TeV}$, respectively. Only adaptions for the expected signal purity of the FoCal measurement are taken into account, as discussed in Sec. 12.5.2.

2. The systematic uncertainties will be 50 % smaller than those achieved at mid-rapidity (which is compatible with the estimates provided in Ref. [72])

3. The uncertainties will be 75 % smaller than those achieved at mid-rapidity

The impact of the FoCal pseudo data is illustrated in Fig. 12.19 by a red line and shaded band, which shows the prompt photon R_{pA} obtained using the nNNPDF30 (no LHCb D^0) after Bayesian reweighting using the pseudo data. The three rows of figures correspond to the aforementioned three scenarios, differing in the assumed systematic uncertainty of the measurement. While the FoCal data does not provide any constraints for the used nPDF for the most conservative baseline, increasing constraints are observed for decreasing systematic uncertainties. Already for 50 % reduced systematic uncertainties (about 10 % systematic uncertainty at $p_{\mathrm{T}} = 5\,\mathrm{GeV}$) the FoCal pseudo data could provide a reduction of the nPDF uncertainties on the level of the R_{pA} by about 50 %. This scenario is in-line with the estimates for the expected systematic uncertainties provided in Ref. [72]. The size of the reduction is comparable to the constraints provided by the LHCb measurement of D^0 meson production at forward rapidities [130], as denoted by the blue lines and shaded bands. Furthermore, a reduction of the nPDF uncertainties of up to 80 % could be achieved assuming systematic uncertainties in the order of about 5 % at $p_{\mathrm{T}} = 5\,\mathrm{GeV}/c$. Depending on the size of the measured suppression of prompt photon production at forward rapidities, inclusion of the measurement can also impact the central values of the R_{pA} prediction, which are illustrated by solid lines and calculated as the median of all (weighted) nPDF members. This is particularly apparent in Fig. 12.19e, where the inclusion of the FoCal data leads to slightly higher central values than those predicted by the unweighted nNNPDF30. This highlights that future measurements could provide important quantitative insights into the suppression of the gluon PDF in the low-x regime.

In summary, a precise measurement of prompt photon production at forward rapidities ($3.7 < y < 5.3$) with the ALICE FoCal detector have the potential to provide significant constraints for recent nPDFs for unprecedented low x. The presented studies show that systematic uncertainties in the order of 10 % at $p_{\mathrm{T}} \sim 5\,\mathrm{GeV}$ are desirable to achieve a reduction of the nPDF uncertainties by more than 50 %, comparable to constraints provided by a measurement of D^0 meson production by LHCb [130]. The latter is currently the only measurement providing significant constraints for the gluon

PDF at $x \sim 10^{-5}$, where furthermore the relationship between the D^0 meson and gluon PDF is complicated by final-state interactions and the fragmentation process. A future measurement of isolated prompt photon production – where the impact of photon fragmentation and other final-state effects is highly suppressed – can provide important new information for global PDF fits. Depending on the size of the measured suppression of isolated prompt photon production in p–Pb collisions at forward rapidities, the new experimental findings might reveal tension with other experimental data or confirm them. This can provide important insights into the importance of the fragmentation process for existing measurements and furthermore gauge the robustness of the R_{pA} with respect to fragmentation. Furthermore, the FoCal measurement could be sensitive to gluon shadowing and/or gluon saturation, where both effects have to be disentangled in order to allow meaningful statements about non-linear QCD evolution. Definitive statements about gluon saturation may require *global* analyses of various experimental observables at various facilities, including prompt photon production, D^0 meson production and measurements at a future EIC [257].

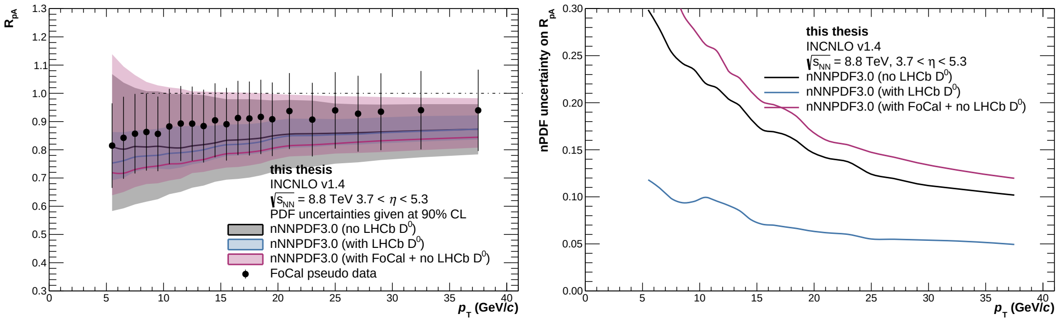

(a) conservative uncertainties (b) conservative uncertainties

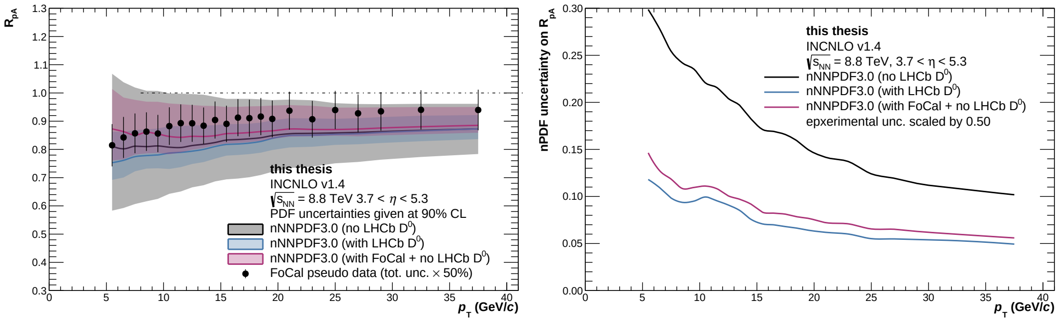

(c) 50 % exp. uncertainties (d) 50 % exp. uncertainties

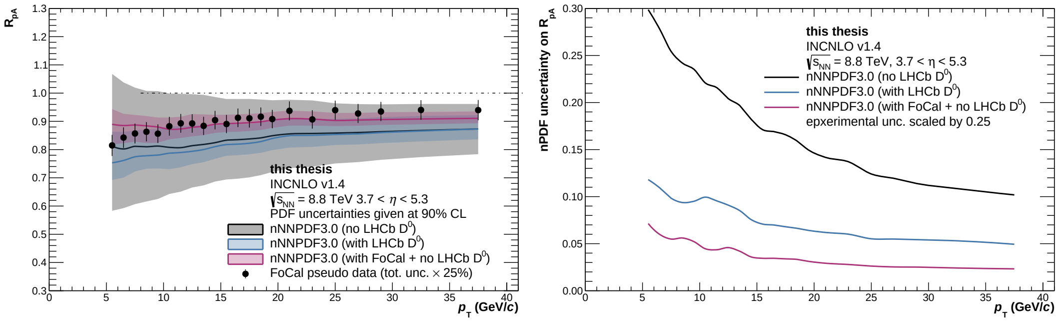

(e) 25 % exp. uncertainties (f) 25 % exp. uncertainties

Figure 12.19: Impact of the FoCal pseudo data on nNNPDF30 set when excluding the LHCb measurement of D^0 meson production [130] at forward rapidities. The impact is estimated on the level of the prompt photon R_{pA} using a Bayesian reweighting of the nPDF members. The R_{pA} for each member is obtained using INCNLO calculations at NLO, and the shaded bands denote the respective nPDF uncertainty at 90 % CL. The nNNPDF30 with $A = 1$ is used as the free-proton reference. Each row of figures illustrates the impact for different assumed systematic uncertainties of the pseudo data. The panels on the right show the respective relative nPDF uncertainties.

Part IV

SUMMARY & CONCLUSIONS

13

SUMMARY

Hadron colliders, such as the Large Hadron Collider (LHC), achieve large collision energies by colliding composite objects such as protons or even heavy nuclei. The unprecedented collision energies achieved at the LHC enable the exploration of a vast amount of interesting physics questions, and led for example to the experimental discovery of the Higgs boson by the ATLAS and CMS experiment in 2012 [137, 138]. Furthermore, the energy densities reached in the collision of e.g. two lead nuclei are so high, that ordinary matter undergoes a phase transition, resulting in a soup of quasi-free quarks and gluons known as the Quark-Gluon Plasma (QGP). The A Large Ion Collider Experiment (ALICE) detector – which is one of four main experiments at the LHC – is at the forefront of exploring this new state of matter which existed in our early universe mere microseconds after the Big Bang. Furthermore, the hadrons and nuclei used as projectiles in the accelerator are complicated and fascinating objects themselves, where a look inside the proton reveals a complex substructure of quarks and gluons – evolving with time and scale. This substructure is encoded in universal parametrizations known as Parton Distribution Functions (PDFs), which describe the probability densities of different parton species to carry a given momentum fraction of the proton's momentum. These PDFs can not be obtained from first principles, and rely on input from a vast amount of data from various experimental facilities and observables. Precise knowledge of these distributions is crucial, as they are needed as input for theoretical calculations of particles produced in hard scattering processes. In simple terms: What goes into the collision impacts what comes out of it. One of the key questions studied in this work is how these distributions inside the proton change when the proton itself is part of a bigger structure, e.g. a lead nucleus. Remarkably, previous experimental results indicate that the substructure of the proton is modified when part of a nucleus, where for example the probability density of the gluon is found to be suppressed [66] due to an effect known as "gluon shadowing". The gluon is furthermore interesting because one observes that the gluon's probability density is steeply increasing for decreasing momentum fractions carried by the gluon. This growth can not continue indefinitely and models such as the Colour-Glass Condensate (CGC) formalism predict the presence of a new regime where the growth is tamed by gluon fusion, resulting in a state of gluon saturated matter. No clear experimental evidence for gluon saturation is currently available, and its discovery would be a landmark in our understanding of the strong interaction.

The measurement of prompt photon production can provide experimental input for the previously outlined questions: How is the partonic substructure modified in nuclear environments and how does QCD – the underlying field theory of the strong interaction – behave in a novel non-linear regime of saturated gluons? Prompt photons are produced directly in the hard scattering of two partons, dominantly via the process $gq \rightarrow \gamma q$ at the LHC. This makes them especially sensitive to probability densities of the incoming gluons, which directly affect the production cross section of the outgoing photon. Since the photon does not carry so-called colour charge it does not participate in the strong interaction. This has the useful consequence that the photon will traverse the evolution of the collision almost unaffected – carrying the information of the incoming partons to the experimental apparatus. The measurement of prompt photons is however challenging, since most photons produced in a collision originate from particle decays rather than the hard scattering itself. Furthermore, prompt photons also get produced in the fragmentation process of an outgoing parton, which complicates the direct relationship between the prompt photon and the gluon. These effects necessitate experimental techniques such as *isolation*, which impose strict requirements on the energy deposited in the vicinity of the photon in order to significantly suppress decay- and fragmentation photons.

This thesis presents the measurement of the isolated prompt photon production cross section in pp and p–Pb collisions at $\sqrt{s_{\mathrm{NN}}} = 8\,\mathrm{TeV}$ and $8.16\,\mathrm{TeV}$, respectively. The measurement is performed using data recorded by the ALICE experiment in 2012 and 2016, where in particular the ElectroMagnetic Calorimeter (EMCal) is used to measure photons with pseudorapidities of $|\eta| < 0.7$. The activity in the vicinity of the photon, which is required for the aforementioned isolation requirement, is quantified using the transverse momentum (p_{T}) of charged tracks measured with the Inner Tracking System (ITS) and Time Projection Chamber (TPC) – the main tracking detectors of ALICE. In particular, the sum of the transverse momenta $\sum_i p_{\mathrm{T}}^i$ of all tracks within a cone of radius $R = 0.4$ around the photon is required to be below $1.5\,\mathrm{GeV}/c$, which allows removing about 70 % of the photons originating from background sources. However, as about 30 % of background photons fulfil the aforementioned selection, one of the key challenges of the measurement is to determine the signal purity in the remaining sample. In this work, two data-driven approaches that use the shape of the electromagnetic shower in combination with the measured isolation energy to determine the signal purity are presented. Both approaches give compatible signal purities, which are found to increase with the photon p_{T} and are in between about 20 % ($p_{\mathrm{T}} \approx 12\,\mathrm{GeV}/c$) and 65 % ($p_{\mathrm{T}} \approx 50\,\mathrm{GeV}/c$). The production cross sections of isolated prompt photon production is measured in both collision systems for $12\,\mathrm{GeV}/c \leq p_{\mathrm{T}} \leq 80\,\mathrm{GeV}/c$ and confronted with perturbative QCD (pQCD) calculations at Next-to-Leading Order (NLO) using the JetPhox [73] program. The calculations use the recent proton and nuclear PDFs NNPDF40[24] and nNNPDF30[66], as well as the BFG II [81] photon fragmentation function. Good agreement between the theoretical calculations and experimental data is observed in both collision systems within the theoretical and experimental uncertainties, showcasing the ability of NLO calculations to adequately describe the experimental data in the inspected phasespace. This corroborates previous findings by the ALICE collaboration in pp collisions at $\sqrt{s} = 7\,\mathrm{TeV}$ [112] and preliminary results in p–Pb collisions at $\sqrt{s_{\mathrm{NN}}} = 5.02\,\mathrm{TeV}$ [241], where likewise good agreement between data and theoretical predictions is observed.

In order to quantify possible modifications of the partonic substructure in nuclear environments, e.g. due to the presence of the aforementioned gluon shadowing, the so-called nuclear modification factor R_{pA} is constructed. This quantity is given as the ratio of the production cross section in p–Pb collisions with respect to a scaled reference measured in pp collisions, where a deviation from unity indicates the presence of nuclear effects. While the data is found to be in agreement with unity for the whole covered transverse momentum within the experimental uncertainties, a hint of a suppression is observed for photons with $p_{\mathrm{T}} \lesssim 20\,\mathrm{GeV}/c$. This is the first time the isolated prompt photon R_{pA} is presented for transverse momenta below $25\,\mathrm{GeV}/c$ – extending the low momentum reach of a previous measurement by the ATLAS collaboration [114] in the same collision system by a factor of two. Good agreement within the experimental uncertainties is observed between both measurements in the overlapping region of $25\,\mathrm{GeV}/c \leq p_\mathrm{T} \leq 80\,\mathrm{GeV}/c$. The measured R_pA is confronted with various pQCD calculations at NLO, which use nCTEQ15[23], EPPS16[65] and nNNPDF30[66] to describe parton distribution of protons inside the lead nucleus. The measurement is in good agreement with the theoretical predictions, which also indicate an increasing suppression of the prompt photon production for $p_\mathrm{T} \lesssim 20\,\mathrm{GeV}/c$ that is commonly attributed to gluon shadowing. In order to estimate the impact of the presented measurement on recent nuclear PDFs, the measured R_pA is used in a Bayesian reweighting study using the INCNLO [251] program. Significant constraining power is found for older nuclear PDFs such as nNNPDF10, where one observes a reduction if the nPDF uncertainty of about 40 % on the level of the R_pA. However, a reduction of the experimental uncertainties by about 50 % is required to provide meaningful constrains for more recent nuclear PDFs, such as nNNPDF30.

Explorations of non-linear QCD dynamics in a regime of saturated gluons require to inspect small Bjorken-x, where theoretical calculations [256] indicate that this medium is present below a saturation scale Q_s, which is predicted to be in a perturbative regime at $x \sim 10^{-5}$. However, Pythia studies using LO scattering kinematics indicate that the presented measurement probes $x \sim 10^{-3}$, which is most-likely not sufficient to probe gluons in a saturated regime. This motivates the second main part of the thesis, which outlines the feasibility of a measurement of isolated prompt photon production using the ALICE Forward Calorimeter (FoCal) [72]. This detector – proposed as an upgrade of the ALICE experiment for data taking in 2027-2029 – covers pseudorapidities of $3.4 < \eta < 5.5$, corresponding to a low-x reach down to $x \sim 10^{-6}$. Measuring isolated prompt photons at these forward rapidities therefore offers exciting opportunities to explore nonlinear QCD dynamics and furthermore allows constraining nPDFs in the low-x regime where experimental constrains are sparse. Consisting of two parts – an electromagnetic and hadronic calorimeter – the FoCal detector is well suited to perform measurements of prompt photons as well as the hadronic event activity in their vicinity. Furthermore, the use of a combination of pad and silicon pixel layers offers excellent possibilities to reject photons from particle decays, where in particular the small transverse size of 30 µm of the pixels allows achieving good shower separation to identify e.g. $\pi^0 \rightarrow \gamma\gamma$ decays. All key aspects of an isolated prompt photon analysis have been studied using simulated collision events from Pythia (and HIJING) propagated through a realistic implementation of the FoCal geometry in Geant3 for pp and p–Pb collisions at $\sqrt{s_\mathrm{NN}} = 14\,\mathrm{TeV}$ and $8.8\,\mathrm{TeV}$, respectively. Furthermore, simulations of single photons are used to obtain the energy resolution of the calorimeter as well as the photon reconstruction efficiency. The studies indicate a photon reconstruction efficiency of about 90 % for almost the full studied photon energies of up to 1.5 TeV. Several selections are explored to identify prompt photon candidates in full pp and p-Pb collision events, which showcase potential to significantly increase the signal-to-background ratio of the measurement. In particular, selections according to the isolation energy in the electromagnetic- and hadronic calorimeter, the tagging of π^0 candidates according to the invariant mass, as well as a shower shape selection improved the signal to background ratio by a factor of 18. In addition to the determination of signal and background efficiencies, the data-driven purity estimation technique used for the measurement at mid-rapidity is implemented. Overall, the signal purity in the simulated sample is found to be above 20 % in both collision systems, indicating the feasibility of a data-driven purity determination which was successfully used for the measurement at mid-rapidity for purities above 20 %.

In order to estimate the expected statistical precision of a future measurement of isolated prompt photon production with the FoCal detector, pQCD calculations at NLO are used in conjunction with the expected integrated luminosities for Run 4 of ALICE data taking. The studies indicate sufficient prompt photon yields in all collision systems for a measurement of up to $p_{\mathrm{T}} \sim 50\,\mathrm{GeV}/c$ with statistical uncertainties of less than 2 % for $p_{\mathrm{T}} \lesssim 25\,\mathrm{GeV}/c$. Furthermore, conservative assumptions are made about the expected systematic uncertainties by using information from the measurement at mid-rapidity as well as the presented performance studies. Theoretical predictions at next-to-leading order are then used to construct pseudo data of the nuclear modification factor of prompt photon production at forward rapidities $3.7 < y < 5.3$. Using Bayesian reweighting one finds that a prompt photon measurement with systematic uncertainties in the order of 10 % could provide significant constrains for recent nuclear PDFs – comparable to those provided by recent measurements of D^0 meson production by the LHCb experiment [130].

In summary, prompt photons are an exciting and robust probe for the initial state of nuclear collisions, in particular the momentum distribution of gluons bound inside the colliding proton. Measurements of prompt photon production in p–Pb collisions can offer insights into cold nuclear matter effects such as gluon shadowing, as well as non-linear QCD effects such as gluon saturation when measured at forward rapidities. They offer these insights in a robust way, mostly unaffected by final state effects such as fragmentation or interactions with a hot or cold medium. This work presented experimental findings on prompt photon production in pp and p–Pb collisions, probing the presence of cold nuclear matter effects using the nuclear modification factor. Performance studies for the future FoCal showcase the potential and feasibility of prompt photon measurements at forward rapidities exploiting the novel design of the calorimeter for prompt photon identification. I am convinced that isolated prompt photon measurements will also in the future play a crucial role in the exploration of the initial state of nuclear collisions and I hope that I can spark interest in these measurements – either performed using current experimental facilities or exciting upgrades such as the ALICE FoCal.

ZUSAMMENFASSUNG

Hadronische Beschleuniger, wie der Large Hadron Collider (LHC), erreichen große Kollisionsenergien, indem sie zusammengesetzte Objekte wie Protonen oder sogar schwere Kerne zur Kollision bringen. Die beispiellosen Kollisionsenergien, die am LHC erreicht werden, ermöglichen die Erforschung einer Vielzahl interessanter physikalischer Fragen und führten z.B. zur experimentellen Entdeckung des Higgs-Bosons durch das ATLAS- und CMS-Experiment im Jahr 2012 [137, 138]. Darüber hinaus sind die Energiedichten, die z.B. bei der Kollision zweier Bleikerne erreicht werden, so hoch, dass herkömmliche Materie in eine neue Phase übergeht, in der Quarks und Gluonen als quasi-freie Teilchen existieren. Diese „Ursuppe" wird als sogenanntes Quark-Gluon Plasma (QGP) bezeichnet. Das ALICE Experiment ist eines der führenden Experimente in der Erforschung dieses neuen Materiezustands, welcher in unserem frühen Universum nur wenige Mikrosekunden nach dem Urknall existierte. Darüber hinaus sind die Hadronen und Kerne, die im Beschleuniger als Projektile verwendet werden, selbst komplizierte und faszinierende Objekte, bei denen ein Blick ins Innere des Protons eine komplexe Substruktur aus Quarks und Gluonen offenbart, welche sich als Funktion der Zeit und der Impulsskala stetig verändert. Diese Substruktur wird mit universellen Parametrisierungen beschrieben – sogenannten Parton Distribution Functions (PDFs) – welche die Wahrscheinlichkeitsdichten der verschiedenen Partonarten beschreiben einen bestimmten Impulsanteil des Protonenimpulses zu tragen. Diese Parametrisierungen können nicht a priori theoretisch bestimmt werden, sondern beruhen auf einer großen Menge an experimentellen Daten aus einer Vielzahl an experimentellen Einrichtungen. Genaue Kenntnisse über diese Verteilungen sind von entscheidender Bedeutung, da sie für theoretische Berechnungen der Teilchenproduktion in harten Streuprozessen benötigt werden. In einfachen Worten: Was in die Kollision hineingeht wirkt sich auf das aus, was dabei herauskommt. Eine der Hauptfragen, die in dieser Arbeit untersucht werden, ist, wie sich diese Verteilungen ändern, wenn das Proton selbst Teil einer größeren Struktur ist, wie bspw. eines Bleikerns. Frühere experimentelle Ergebnisse deuten darauf hin, dass sich die Substruktur des Protons verändert, wenn es selbst Teil eines Kerns ist. So wurde z.B. festgestellt, dass die Wahrscheinlichkeitsdichte des Gluons aufgrund eines als "gluon shadowing" bekannten Effekts unterdrückt wird. Gluonen sind außerdem interessant, weil man beobachtet, dass ihre Wahrscheinlichkeitsdichte mit abnehmenden Impulsanteilen stark ansteigt. Dieses Wachstum kann nicht unbegrenzt anhalten, und Modelle wie der "Colour-Glass Condensate (CGC)" Formalismus sagen das Vorhandensein eines neuen Regimes voraus, in dem das Wachstum durch Gluonenfusion gebremst wird, was zu einem Zustand gluonengesättigter Materie führt. Derzeit gibt es keine eindeutigen experimentellen Beweise für die Existenz dieser Gluonensättigung, und ihre Entdeckung wäre ein Meilenstein für unser Verständnis der starken Wechselwirkung.

Die Messung der Produktion von prompten Photonen kann experimentellen Input für die zuvor skizzierten Fragen liefern: Wie wird die partonische Substruktur in nuklearen Umgebungen verändert, und wie verhält sich QCD – die zugrundeliegende Feldtheorie der starken Wechselwirkung – in einem neuartigen nichtlinearen Regime gesättigter Gluonen? Prompte Photonen werden direkt bei der harten Streuung von zwei Partonen erzeugt, hauptsächlich durch den Prozess $g\mathrm{q} \rightarrow \gamma\mathrm{q}$ am LHC. Das macht sie insbesondere sensitiv für die Wahrscheinlichkeitsdichte des Gluons, welches direkt den Wirkungsquerschnitt der prompten Photonen Produktion beeinflusst. Da das Photon keine sogenannte Farbladung trägt, nimmt es nicht an der starken Wechselwirkung teil. Dies hat die nützliche Konsequenz, dass das Photon die Entwicklung der Kollision nahezu unbeeinflusst durchläuft und die Information der eingehenden Partonen bis zur Versuchsapparatur transportiert. Herausforderungen bei der Messung von prompten Photon entstehen jedoch dadurch, dass die meisten bei der Kollision entstehenden Photonen nicht aus der harten Streuung selbst stammen, sondern aus Zerfällen von anderen Teilchen. Darüber hinaus werden prompte Photonen auch im Fragmentationsprozess eines ausgehenden Partons erzeugt, was die direkte Verbindung zwischen Gluon und Photon verkompliziert. Diese Effekte machen spezielle experimentelle Techniken wie die sogenannte *Isolation* erforderlich, welche die erlaubte deponierte Energie in der Nähe des Photons limitiert und so Anteile von Fragmentations- und Zerfallsphotonen signifikant unterdrückt.

In dieser Arbeit wird die Messung des Wirkungsquerschnitts der Produktion von isolierten prompten Photonen in pp und p–Pb Kollisionen bei Schwerpunktsenergien von $\sqrt{s_{\mathrm{NN}}} = 8\,\mathrm{TeV}$ bzw. $8.16\,\mathrm{TeV}$ vorgestellt. Die Messung erfolgt unter Verwendung von Daten des ALICE Experiments, welche in den Jahren 2012 und 2016 aufgezeichnet wurden. Hierbei wurde insbesondere das ElectroMagnetic Calorimeter (EMCal) zur Messung von Photonen mit Pseudorapiditäten von $|\eta| < 0,7$ verwendet. Die Aktivität in der Umgebung des Photons, die für die oben genannte Isolationsanforderungen erforderlich sind, wird anhand des Transversalimpulses (p_{T}) geladener Teilchenspuren quantifiziert, welche mit dem Inner Tracking System (ITS) und Time Projection Chamber (TPC) – die Hauptdetektoren für die Messung geladener Teilchen in ALICE – gemessen werden. Insbesondere muss die Summe aller Transversalimpulse $\sum_i p_{\mathrm{T}}^i$ von geladenen Teilchen in einem Kegel mit einem Radius $R = 0.4$ aufaddiert unter $1.5\,\mathrm{GeV}/c$ liegen, was es erlaubt, etwa 70 % der von Hintergrundquellen stammenden Photonen zu unterdrücken. Da jedoch etwa 30 % der Hintergrundphotonen die oben genannte Selektion erfüllen, besteht eine der größten Herausforderung der Messung darin, die Reinheit der verbleibenden Signalkandidaten zu bestimmen. In dieser Arbeit werden zwei datenbasierte Ansätze vorgestellt, welche die Form des Schauers im elektromagnetischen Kalorimeter mit der gemessenen Isolationsenergie kombinieren, um die Signalreinheit zu bestimmen. Beide Ansätze liefern vergleichbare Signalreinheiten, die mit dem Photon p_{T} ansteigen und zwischen etwa 20 % ($p_{\mathrm{T}} \approx 12\,\mathrm{GeV}/c$) und 65 % ($p_{\mathrm{T}} \approx 50\,\mathrm{GeV}/c$) liegen. Die Produktionswirkungsquerschnitte der isolierten prompten Photonen werden in beiden untersuchten Kollisionssystemen für $12\,\mathrm{GeV}/c \leq p_{\mathrm{T}} \leq 80\,\mathrm{GeV}/c$ gemessen und mit "perturbative QCD (pQCD)" Rechnungen bei "Next-to-Leading Order (NLO)" unter Verwendung des JetPhox Programms [73] verglichen. Die Berechnungen verwenden die aktuellen Protonen- und Kern-PDFs NNPDF40[24] und nNNPDF30[66], sowie die BFG II [81] Fragmentationsfunktion zur Beschreibung der Fragmentationsphotonen. Die theoretischen Berechnungen und experimentellen Daten sind in guter Übereinstimmung innerhalb der theoretischen und experimentellen Unsicherheiten für beide Kollisionssysteme. Dies zeigt die Eignung der Berechnungen bei NLO die experimentellen Daten im untersuchten Phasenraum adäquat zu beschreiben. Die präsentierten Resultate untermauern außerdem frühere Ergebnisse der ALICE Kollaboration in pp

Kollisionen bei $\sqrt{s} = 7\,\mathrm{TeV}$ [112] und vorläufige Ergebnisse in p–Pb Kollisionen bei $\sqrt{s_{\mathrm{NN}}} = 5.02\,\mathrm{TeV}$ [241], wo ebenfalls eine gute Übereinstimmung zwischen Daten und theoretischen Vorhersagen beobachtet wird.

Um mögliche Veränderungen der partonischen Substruktur in nuklearen Umgebungen zu quantifizieren, z.B. durch den oben genannten Effekts des "gluon shadowing", wird der sogenannte nukleare Modifikationsfaktor R_{pA} bestimmt. Diese Größe gibt das Verhältnis des Produktionswirkungsquerschnittes in p-Pb Kollisionen zu einer skalierten Referenz, die in pp Kollisionen gemessen wurde, an, wobei eine Abweichung von Eins auf das Vorhandensein von Kerneffekten hindeutet. Obwohl die Daten für den gesamten abgedeckten Transversalimpuls mit Eins übereinstimmen, wird dennoch ein Hinweis auf eine Unterdrückung des Produktionswirkungsquerschnitts prompter Photonen mit $p_{\mathrm{T}} \lesssim 20\,\mathrm{GeV}$ beobachtet. Dies ist das erste Mal, dass der prompte Photonen R_{pA} für Transversalimpulse unter $25\,\mathrm{GeV}/c$ bestimmt wurde und die präsentierten Resultate erweitern die Reichweite einer früheren Messung der ATLAS Kollaboration [114] für niedrige Transversalimpulse um einen Faktor Zwei. Zwischen beiden Messungen wird eine gute Übereinstimmung innerhalb der experimentellen Unsicherheiten im Überlappungsbereich von $25\,\mathrm{GeV}/c \le p_{\mathrm{T}} \le 80\,\mathrm{GeV}/c$ beobachtet. Der gemessene R_{pA} wird mit verschiedenen pQCD Rechnungen bei NLO konfrontiert, wobei die nCTEQ15[23], EPPS16[65] und nNNPDF30[66] PDFs zur Beschreibung der Partonenverteilung von Protonen im Inneren des Bleikerns verwendet wurden. Die Messung stimmt gut mit den theoretischen Vorhersagen überein, welche ebenfalls auf eine zunehmende Unterdrückung der Produktion isolierter prompter Photonen für $p_{\mathrm{T}} \lesssim 20\,\mathrm{GeV}/c$ hinweisen, welche üblicherweise "gluon shadowing" zugeordnet wird. Um die Bedeutung der vorgestellten Messung im Hinblick auf aktuelle nukleare PDFs abzuschätzen, werden eine Auswahl an nuklearen PDFs unter Berücksichtigung des gemessenen R_{pA} mithilfe von statistischer Rückschlüsse neu gewichtet. Dies geschieht mit der Verwendung von pQCD Rechnung bei NLO mit dem INCNLO [251] Programm. Für ältere nukleare PDFs wie z.B. nNNPDF10 wird eine signifikante Reduktion der PDF Unsicherheiten des R_{pA} von etwa 40 % unter Berücksichtigung der präsentierten Daten festgestellt. Nichtsdestotrotz sind eine Verringerung der experimentellen Unsicherheiten von ca. 50 % erforderlich um auch die Unsicherheiten des aktuellsten nuklearen PDF nNNPDF30 zu verbessern.

Die Erforschung der nichtlinearen Dynamik von QCD in einem Regime gesättigter Gluonen erfordert die Betrachtung kleiner Bjorken-x. Theoretische Berechnungen [256] deuten darauf hin, dass ein Medium gesättigter Gluonen unterhalb einer Sättigungsskala Q_s vorhanden ist, die in einem perturbativen Regime bei $x \sim 10^{-5}$ vorhergesagt wird. Durchgeführte Studien mit dem Pythia Programm unter Verwendung der Streuungskinematik bei LO zeigen jedoch, dass die vorgestellten Messung sensitiv zu $x \sim 10^{-3}$ ist, was wahrscheinlich nicht ausreicht, um Gluonen in einem gesättigten Bereich zu untersuchen. Dies motiviert den zweiten Hauptteil der Arbeit, der die Durchführbarkeit einer Messung der isolierten prompten Photonenproduktion mit dem ALICE Forward Calorimeter (FoCal) [72] demonstriert. Dieser Detektor, der als Upgrade des ALICE Experiments für die Datenaufnahme in den Jahren 2027-2029 vorgeschlagen wurde, deckt Pseudorapiditäten von $3.4 < \eta < 5.5$ ab, was einem niedrigen x-Bereich von bis zu $x \sim 10^{-6}$ entspricht. Die Messung isolierter prompter Photonen bei diesen Rapiditäten bietet daher aufregende Möglichkeiten die oben genannten nichtlinearen QCD Effekte zu erforschen, und ermöglicht darüber hinaus die verbesserte Bestimmung von nPDFs bei niedrigen x, für welchen Bereich nur wenige experimentelle Daten zur Verfügung stehen. Der aus zwei Teilen – einem elektromagnetischen und einem hadronischen Kalorimeter – bestehende FoCal Detektor ist gut geeignet, um Messungen von prompten Photonen sowie der hadronischen Aktivität in ihrer Umgebung durchzuführen. Darüber hinaus bietet die Verwendung einer Kombination aus Pad- und Silizium-Pixelschichten hervorragende Möglichkeiten, Photonen aus Teilchenzerfällen zu unterdrücken, wobei insbesondere die geringe Querschnittgröße von 30 μm der Pixel eine gute Separation mehrerer elektromagnetischen Schauer ermöglicht, um z.B. $\pi^0 \to \gamma\gamma$ Zerfälle zu identifizieren. Alle für die Messung prompter Photonen wichtigen Aspekte wurden anhand von simulierten Kollisionsereignissen aus PYTHIA (und HIJING) untersucht, die durch eine realistische Implementierung der FoCal Geometrie in GEANT3 für pp- und p–Pb-Kollisionen bei $\sqrt{s_{\mathrm{NN}}} = 14\,\mathrm{TeV}$ bzw. $8.8\,\mathrm{TeV}$ propagiert wurden. Darüber hinaus wurden Simulationen einzelner Photonen verwendet, um die Energieauflösung des Kalorimeters und die Effizienz der Photonenrekonstruktion zu bestimmen. Die Untersuchungen zeigen eine Photonenrekonstruktions-Effizienz von etwa 90 % für fast alle untersuchten Photonenenergien von bis zu 1.5 TeV. Zur Identifizierung von prompten Photonen Kandidaten in vollständigen pp- und p-Pb Kollisionsereignissen wurden verschiedene Signalselektionen untersucht, die das Signal-zu-Untergrund-Verhältnis der Messung deutlich erhöhen können. Insbesondere die Selektion anhand der im elektromagnetischen und hadronischen Kalorimeter gemessenen Isolationsenergie, die Identifizierung von π^0 Kandidaten anhand der invarianten Masse, sowie eine Selektion anhand der Form des elektromagnetischen Schauers verbesserten das Signal-Hintergrund-Verhältnis um einen Faktor von 18. Zusätzlich zur Bestimmung der Signal- und Hintergrund-Effizienz wurde eine datengetriebene Reinheitsschätzungstechnik implementiert, welche bereits für die Messung bei mittlerer Rapiditäten verwendet wurde. Die oben genannten Selektionen ermöglichen eine Signalreinheit von mehr als 20 % in den simulierten Kollisionsereignissen. Dies weist auf die Durchführbarkeit einer datengetriebenen Reinheitsbestimmung hin, welche bereits für die Messung bei mittlerer Rapiditäten für vergleichbare Reinheiten von über 20 % erfolgreich verwendet wurde.

Um die erwartete statistische Genauigkeit einer zukünftigen Messung des Produktionswirkungsquerschnitts von isolierten prompten Photonen mit dem FoCal Detektor abzuschätzen, werden pQCD Rechnungen bei NLO zusammen mit den erwarteten integrierten Luminositäten für “Run 4” der ALICE-Datenaufnahme verwendet. Die Studien zeigen ausreichende Photonenausbeuten in allen untersuchten Kollisionssystemen für eine Messung von bis zu $p_{\mathrm{T}} \sim 50\,\mathrm{GeV}/c$ mit statistischen Unsicherheiten von weniger als 2 % für $p_{\mathrm{T}} \lesssim 25\,\mathrm{GeV}/c$. Darüber hinaus werden konservative Annahmen über die zu erwartenden systematischen Unsicherheiten getroffen, indem Informationen aus der Messung bei mittlerem Rapiditäten sowie aus den vorgestellten Durchführbarkeitsstudien kombiniert werden. Dies erlaubt es mithilfe von pQCD Rechnungen bei NLO FoCal Pseudodaten des nuklearen Modifikationsfaktors der prompten Photonenproduktion bei Rapiditäten von $3.7 < \eta < 5.3$ zu konstruieren. Die so konstruierten Daten ermöglichen Neugewichtungsstudien der nuklearen PDFs und zeigen, dass eine Messung mit systematischen Unsicherheiten in der Größenordnung von 10 % signifikante Verbesserungen für die Unsicherheiten aktueller nuklearen PDFs liefern könnte - vergleichbar jüngsten Messungen der D^0 Mesonenproduktion durch das LHCb Experiment [130].

Zusammenfassend lässt sich sagen, dass prompte Photonen eine spannende und robuste Sonde für den Anfangszustand von Kernkollisionen sind, insbesondere für die Impulsverteilung der im kollidierenden Proton gebundenen Gluonen. Messungen der Produktion prompter Photonen in p-Pb Kollisionen können Einblicke in kalte Kernmaterieeffekte wie “gluon shadowing” sowie in nichtlineare QCD Effekte wie Gluonensättigung bieten, wenn sie bei großen Rapiditäten gemessen werden. Sie bieten diese Einblicke auf eine robuste Weise, weitgehend unbeeinflusst von Effekten wie Fragmentierung oder Wechselwirkungen mit einem heißen oder kaltem Medium. In dieser Arbeit wurden experimentelle Ergebnisse zur prompten Photonenproduktion in pp und p-Pb Kollisionen vorgestellt, wobei insbesondere das Vorhandensein von Effekten kalter Kernmaterie anhand des nuklearen Modifikationsfaktors untersucht wurde. Detaillierte Studien für das künftige FoCal zeigen das Potenzial und die Durchführbarkeit von Messungen prompter Photonen bei großen Rapiditäten unter Ausnutzung des neuartigen Designs des Kalorimeters, welches bestens zur Identifizierung von prompten Photonen geeignet ist. Ich bin überzeugt, dass Messungen isolierter prompter Photonen auch in Zukunft eine entscheidende Rolle bei der Erforschung des Anfangszustands von Kernkollisionen spielen werden. Ich hoffe, dass ich das Interesse an diesen Messungen wecken kann – entweder mit den derzeitigen experimentellen Einrichtungen oder mit spannenden Erweiterungen wie dem ALICE FoCal.

Part V

APPENDIX

A

ADDITIONAL FIGURES

A.1 EFFICIENCY

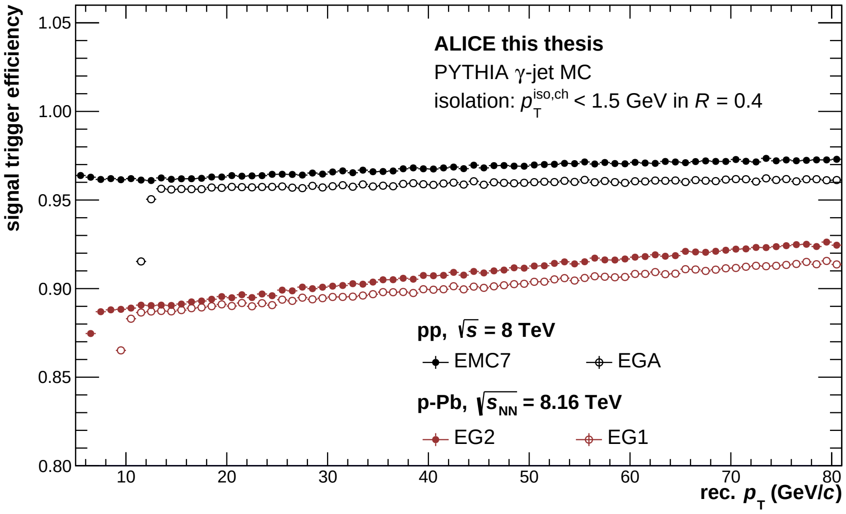

Figure A.1: Trigger efficiency for the isolated prompt photon signal from GJ MC in pp and p–Pb collisions at $\sqrt{s_{\mathrm{NN}}} = 8$ TeV and 8.16 TeV, respectively.

A.2 TEMPLATE FIT PURITY

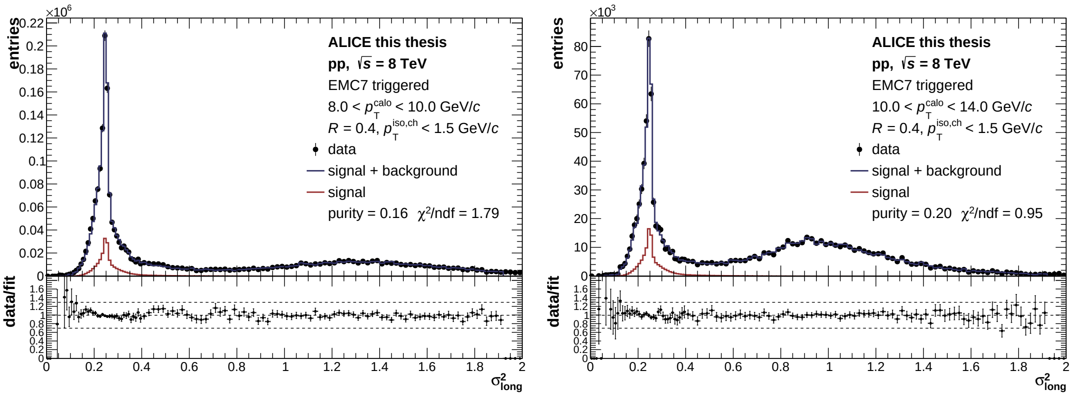

Figure A.2: Two-component template fit (Eq. 8.2) of the long axis σ^2_{long} of the shower shape ellipse in EMC7 triggered pp collisions at $\sqrt{s_{\mathrm{NN}}} = 8\,\mathrm{TeV}$ for different cluster p_{T} intervals. The signal and background templates are obtained from GJ MC and data, respectively, as outlined in the text. The purity is obtained in the photon signal region $0.1 \leq \sigma^2_{\mathrm{long}} \leq 0.3$ according to Eq. 8.3.

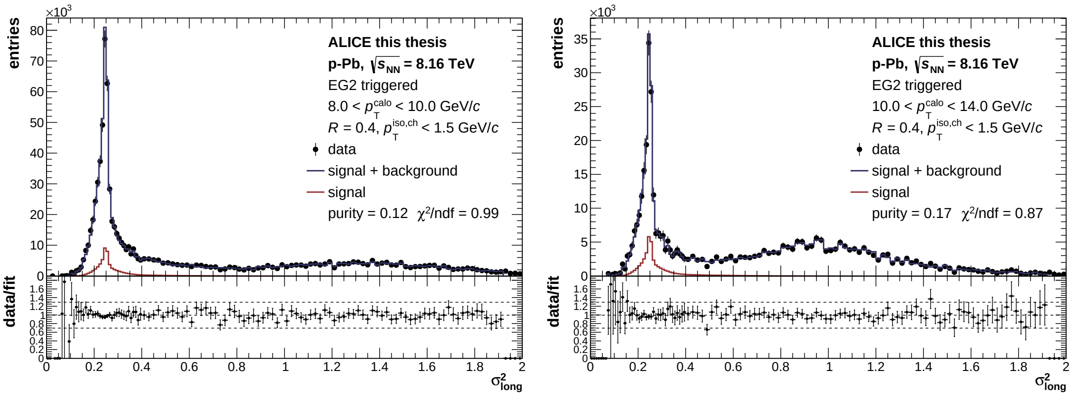

Figure A.3: Two-component template fit (Eq. 8.2) of the long axis σ^2_{long} of the shower shape ellipse in EG2 triggered p–Pb collisions at $\sqrt{s_{\mathrm{NN}}} = 8.16\,\mathrm{TeV}$ for different cluster p_{T} intervals. The signal and background templates are obtained from GJ MC and data, respectively, as outlined in the text. The purity is obtained in the photon signal region $0.1 \leq \sigma^2_{\mathrm{long}} \leq 0.3$ according to Eq. 8.3.

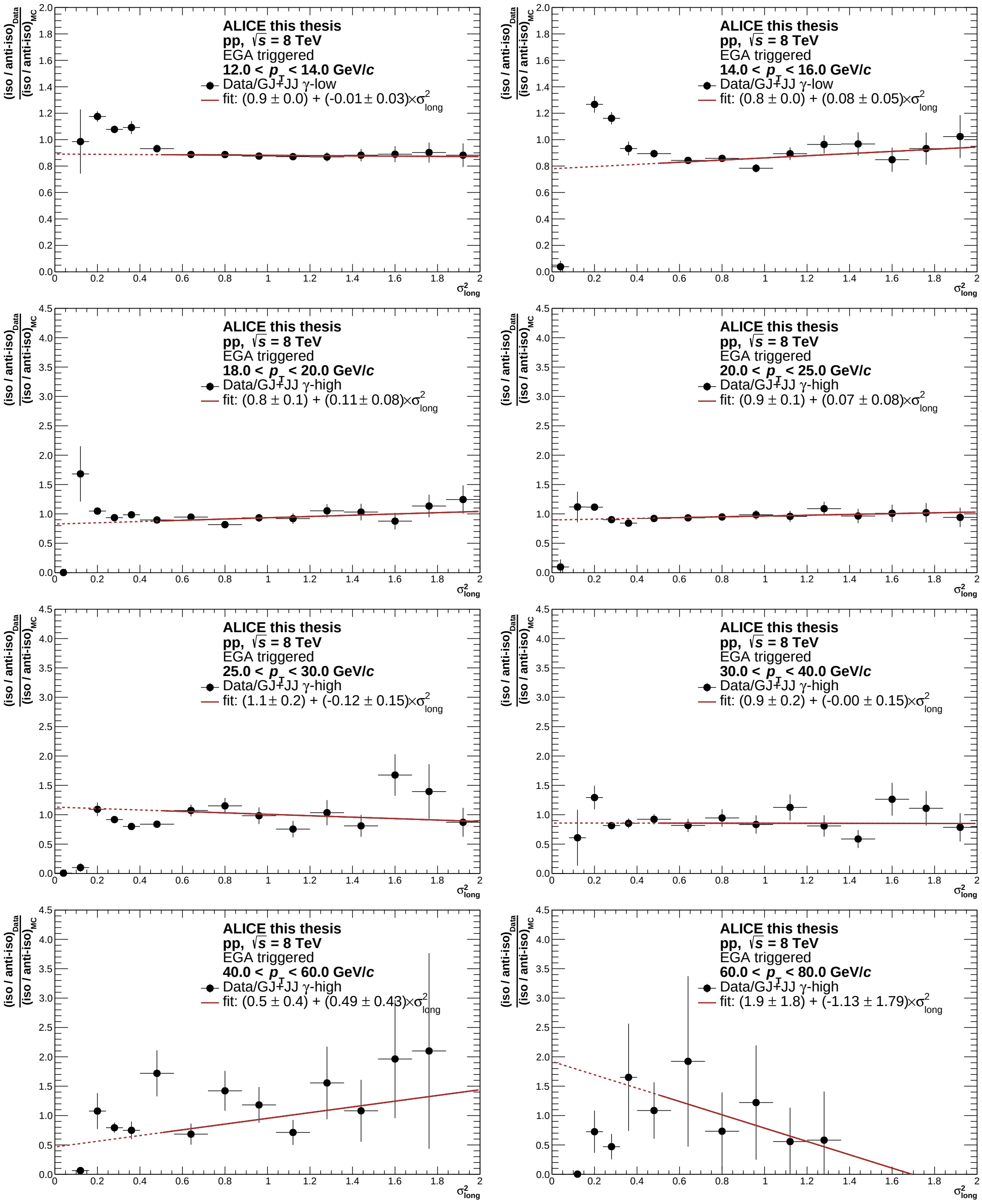

Figure A.4: Double ratio calculated according to Eq. 8.5 in various p_{T}-intervals for EGA triggered pp collisions at $\sqrt{s} = 8\,\mathrm{TeV}$. A first-order polynomial fit is indicated by a red line, where the solid part of the line indicates the fit region. A slope of ≈ 0 indicates agreement between data and MC in their description of the isolation dependence of the shower shape parameter.

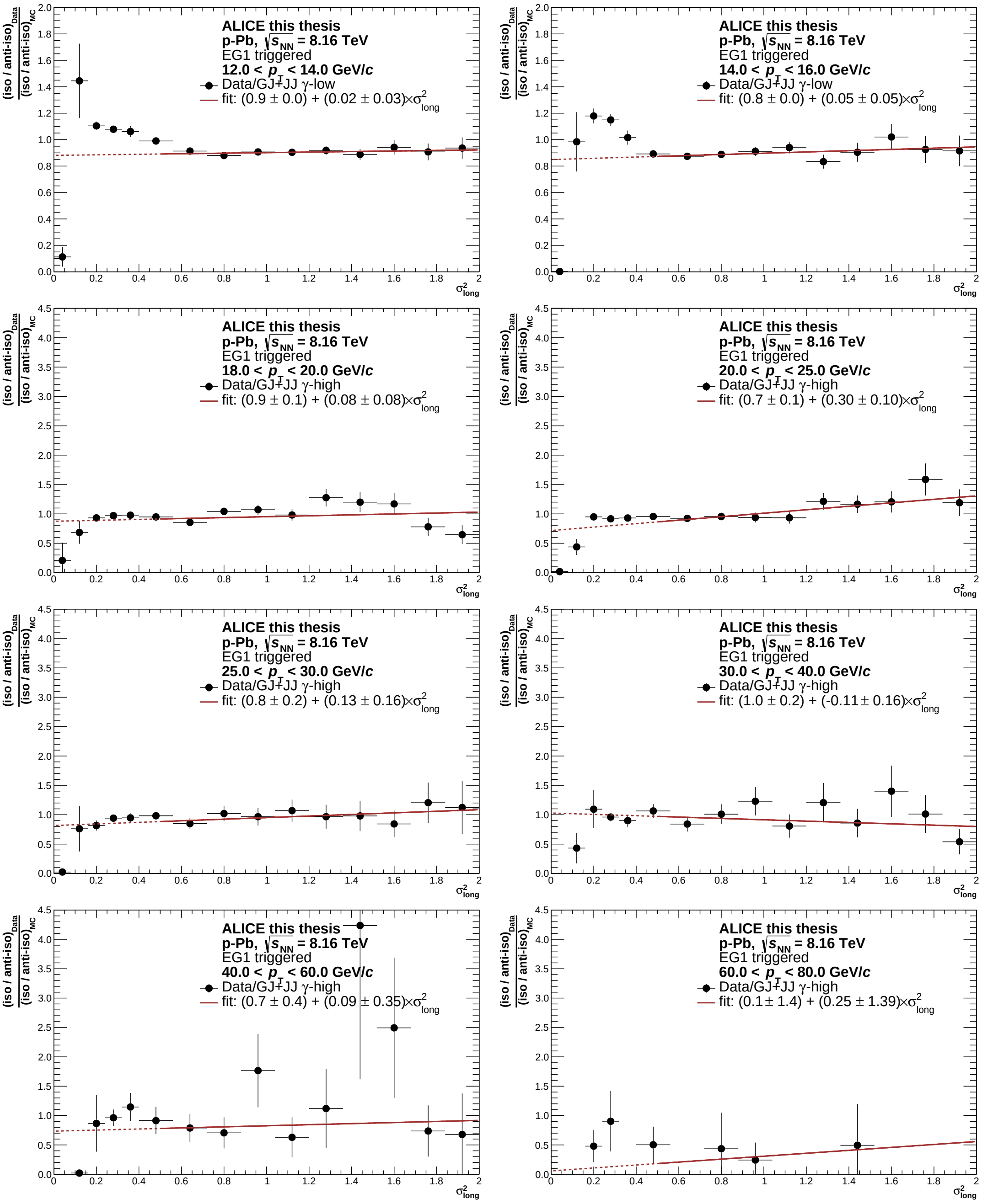

Figure A.5: Double ratio calculated according to Eq. 8.5 in various p_T-intervals for EG1 triggered p–Pb collisions at $\sqrt{s_{NN}}$ = 8.16 TeV. A first-order polynomial fit is indicated by a red line, where the solid part of the line indicates the fit region. A slope of ≈ 0 indicates agreement between data and MC in their description of the isolation dependence of the shower shape parameter.

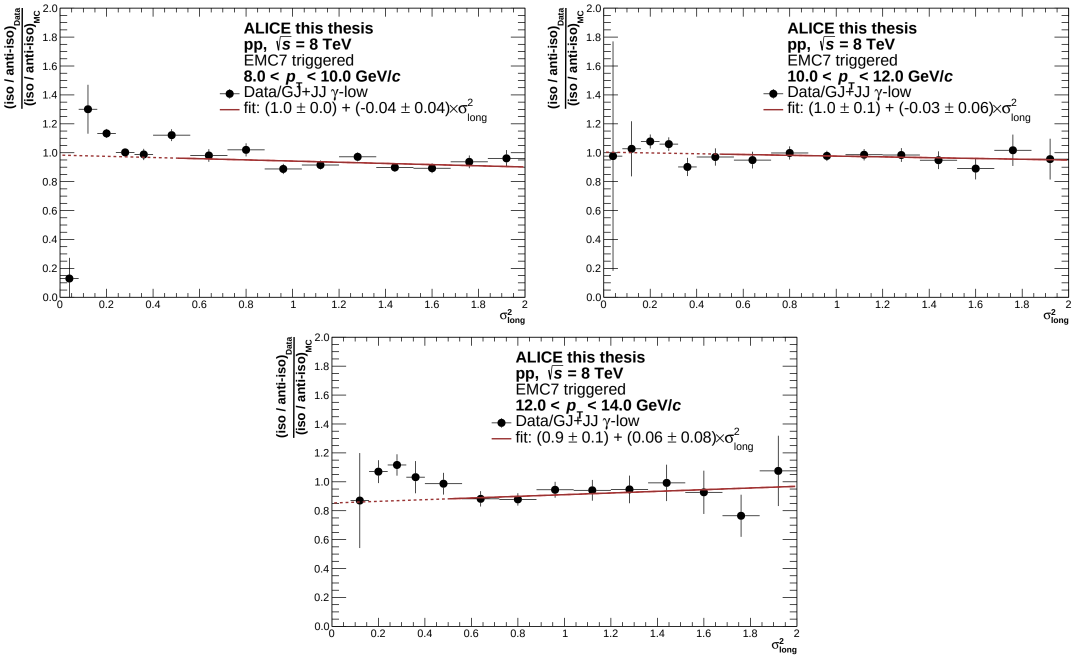

Figure A.6: Double ratio calculated according to Eq. 8.5 in various p_T-intervals for EMC7 triggered pp collisions at $\sqrt{s} = 8\,\text{TeV}$. A first-order polynomial fit is indicated by a red line, where the solid part of the line indicates the fit region. A slope of ≈ 0 indicates agreement between data and MC in their description of the isolation dependence of the shower shape parameter.

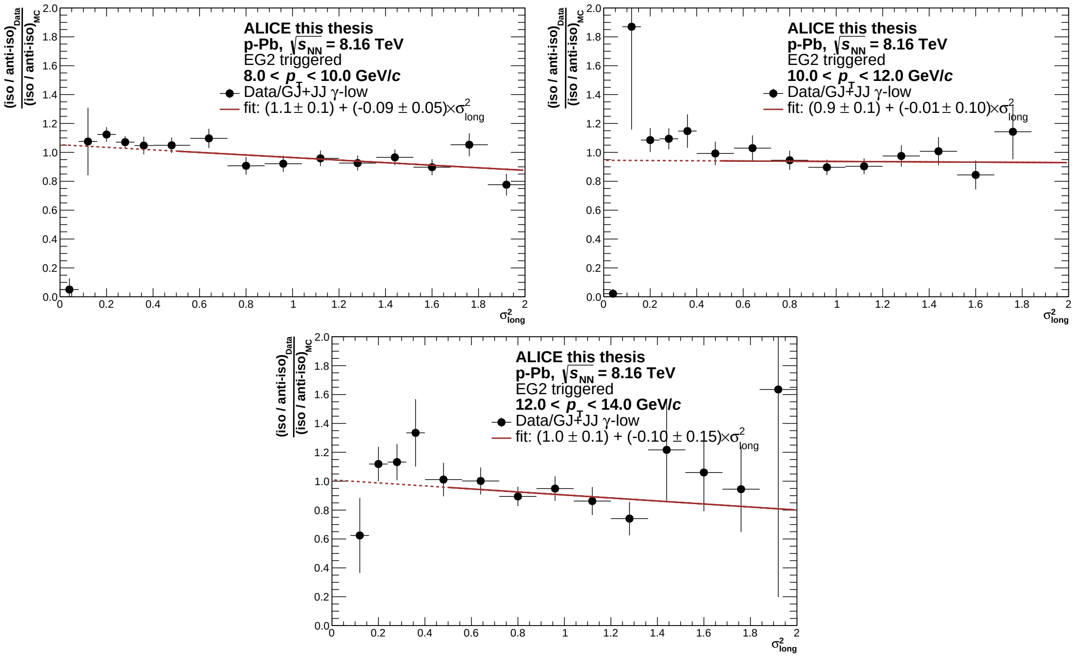

Figure A.7: Double ratio calculated according to Eq. 8.5 in various p_T-intervals for EG2 triggered p–Pb collisions at $\sqrt{s_{NN}} = 8.16\,\text{TeV}$. A first-order polynomial fit is indicated by a red line, where the solid part of the line indicates the fit region. A slope of ≈ 0 indicates agreement between data and MC in their description of the isolation dependence of the shower shape parameter.

A.3 ADDITIONAL FOCAL PERFORMANCE FIGURES

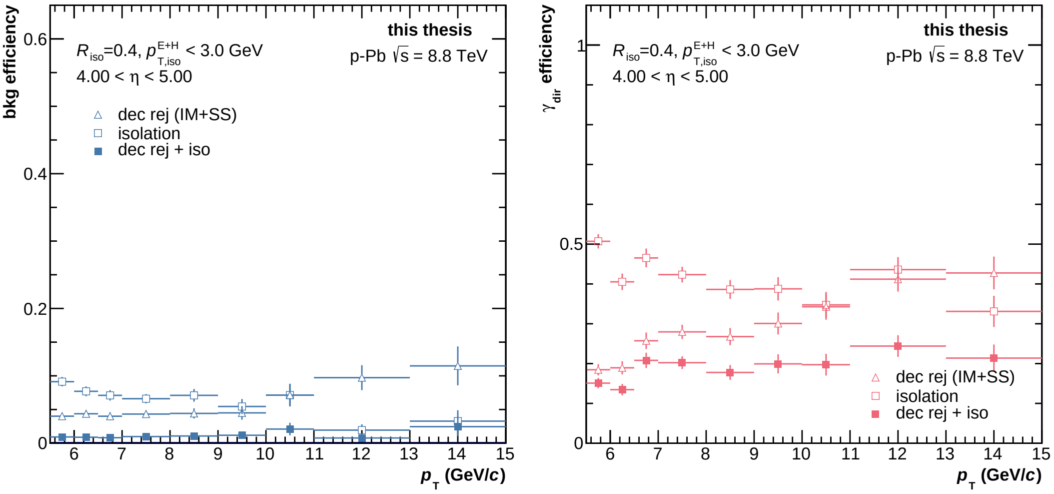

(a) background efficiency (b) signal efficiency

Figure A.8: **Left:** Reconstruction efficiency for background clusters in p–Pb collisions at $\sqrt{s_{\mathrm{NN}}} =$ 8.8 TeV obtained using PYTHIA6 and full detector simulation in GEANT3 for various selections, which are outlined in the text. **Right:** Reconstruction efficiency for signal photons in the same collision systems. A low reconstruction efficiency for the background sample and a high efficiency for the signal sample are desirable.

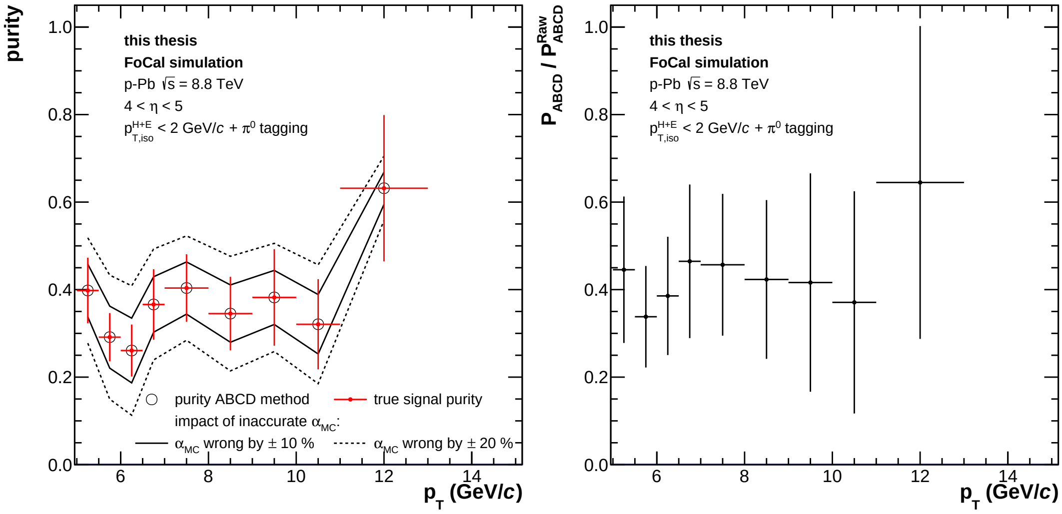

(a) Purity estimate

(b) Impact of α_{MC} correction

Figure A.9: **Left:** Isolated prompt photon signal purity for clusters measured with the FoCal within $4 < \eta < 5$ in simulated p–Pb collision events at $\sqrt{s_{\mathrm{NN}}} = 8.8\,\mathrm{TeV}$. A purity estimate using the ABCD method according to Eq. 8.11 (black markers) is in agreement with the true signal purity of the MB+GJ Pythia sample. Dashed and solid lines indicate the impact of a potential wrong determination of α_{MC} on the purity estimate, which may arise if the used MCs do not accurately describe the correlation of shower shape and isolation energy in data. **Right:** Ratio of the purity estimate obtained with and without the aforemention α_{MC} correction.

B

LIST OF ANALYSED RUNS

B.1 ANALYSED RUNS FOR PP COLLISIONS

Trigger MB

LHC12a: 176715, 176730, 176749, 176752, 176753, 176849, 176854, 176859, 176924, 176926, 176927, 176929, 177011
LHC12b: 177580, 177592, 177597, 177612, 177620, 177624, 177671, 177679, 177680, 177681, 177682, 177798, 177799, 177802, 177804, 177805, 177942
LHC12c: 179569, 179571, 179584, 179585, 179591, 179618, 179621, 179639, 179796, 179803, 179806, 179858, 179859, 179916, 179917, 179918, 179919, 179920, 180000, 180042, 180044, 180129, 180130, 180131, 180132, 180133, 180199, 180200, 180500, 180501, 180515, 180517, 180561, 180564, 180567, 180569, 180716, 180717, 180719, 180720, 182017, 182018, 182022, 182023, 182106, 182110, 182111, 182207, 182289, 182295, 182297, 182299, 182300, 182302, 182322, 182323, 182324, 182325, 182624, 182635, 182684, 182686, 182687, 182691, 182692, 182724, 182725, 182728, 182729, 182730, 182741, 182744
LHC12d: 183913, 183916, 183932, 183933, 183934, 183935, 183936, 183937, 183938, 183942, 183946, 184126, 184127, 184131, 184132, 184134, 184135, 184137, 184138, 184140, 184144, 184145, 184147, 184183, 184188, 184208, 184209, 184210, 184215, 184216, 184371, 184383, 184389, 184673, 184678, 184682, 184687, 184784, 184786, 185029, 185031, 185116, 185126, 185127, 185132, 185133, 185134, 185157, 185160, 185164, 185189, 185196, 185198, 185203, 185206, 185208, 185217, 185221, 185282, 185284, 185289, 185291, 185292, 185293, 185296, 185299, 185300, 185302, 185303, 185349, 185350, 185351, 185356, 185359, 185360, 185361, 185362, 185363, 185368, 185371, 185375, 185378, 185461, 185465, 185474, 185582, 185583, 185588, 185589, 185659, 185687, 185738, 185764, 185765, 185768, 185775, 185776, 185778, 185784, 186007, 186009, 186011, 186163, 186164, 186165, 186167, 186205, 186208, 186319, 186320
LHC12f: 186668, 186688, 186689, 186690, 186692, 186694, 186811, 186814, 186937, 186938, 186939, 186966, 186969, 186990, 186992, 186994, 187143, 187145, 187146, 187147, 187148, 187149, 187150, 187151, 187152, 187202, 187203, 187339, 187340, 187341, 187487, 187488, 187489, 187510, 187623, 187624, 187627, 187656, 187698, 187739, 187749, 187783, 187785, 187791, 187796, 188093, 188101
LHC12h: 189306, 189310, 189315, 189316, 189350, 189351, 189352, 189353, 189400, 189407, 189409, 189410, 189411, 189577, 189578, 189602, 189603, 189605, 189610, 189611, 189612, 189616, 189621, 189623, 189647, 189648, 189650, 189654, 189656, 189658, 189659, 189696, 189697, 189698, 190150, 190209, 190210, 190212, 190213, 190214, 190215, 190216, 190240, 190303, 190305, 190307, 190335, 190337, 190338, 190340, 190341, 190342, 190344, 190386, 190388, 190389, 190390, 190392, 190393, 190416, 190417, 190418, 190419, 190421, 190422, 190424, 190425, 190895, 190898, 190903, 190904, 190968, 190970, 190974, 190975, 190979, 190981, 190983, 190984, 191129, 191227, 191229, 191230, 191231, 191245, 191247, 191248, 191450, 191451, 192072, 192073, 192075, 192128, 192136, 192140, 192141, 192172, 192174, 192177, 192194, 192197, 192199, 192200, 192201, 192202, 192205, 192246, 192344, 192347, 192348, 192349, 192415, 192417, 192453, 192461, 192468, 192471, 192492, 192499, 192505, 192510, 192535, 192542, 192548, 192551, 192729, 192731, 192732
LHC12i 192772, 192775, 192778, 192779, 192820, 192822, 192824, 193004, 193005, 193007, 193008, 193010, 193011, 193014, 193047, 193049, 193051, 193092, 193093, 193094, 193097, 193148, 193155, 193156, 193187, 193188, 193189, 193194

Trigger EMC7

LHC12b: 177798, 177799
LHC12c: 179796, 179803, 179806, 179858, 179859, 179916, 179917, 179918, 179919, 179920, 180000, 180042, 180044, 180129, 180130, 180131, 180132, 180133, 180500, 180501, 180515, 180517, 180561, 180564, 180567, 180569, 180716, 180717, 180719, 180720, 182017, 182018, 182022, 182023, 182106, 182110, 182111, 182207, 182289, 182295, 182297, 182299, 182300, 182302, 182322, 182323, 182324, 182325, 182624, 182635, 182684, 182686, 182687, 182691, 182692, 182724, 182725, 182728, 182729, 182730, 182741, 182744
LHC12d: 183913, 183916, 183932, 183933, 183934, 183935, 183936, 183937, 183938, 183942, 183946, 184126, 184127, 184131, 184132, 184134, 184135, 184137, 184138, 184140, 184144, 184145, 184147, 184183, 184188, 184208, 184209, 184210, 184215, 184216, 184371, 184383, 184389, 184673, 184678, 184682, 184687, 184784, 184786, 185029, 185031, 185116, 185126, 185127, 185132, 185133, 185134, 185157, 185160, 185164, 185189, 185196, 185198, 185203, 185206, 185208, 185217, 185221, 185282, 185284, 185289, 185292, 185293, 185296, 185299, 185300, 185302, 185303, 185349, 185350, 185351, 185356, 185359, 185360, 185361, 185362, 185363, 185368, 185371, 185375, 185378, 185461, 185465, 185474, 185582, 185583, 185588, 185589, 185659, 185687, 185738, 185764, 185765, 185768, 185775, 185776, 185778, 185784, 186163, 186164, 186165, 186167, 186205, 186208, 186319, 186320
LHC12f: 186668, 186688, 186689, 186690, 186692, 186694, 186811, 186814, 186937, 186938, 186939, 186966, 186969, 186990, 186992, 186994, 187143, 187145, 187146, 187147, 187148, 187149, 187150, 187151, 187152, 187202, 187203, 187339, 187340, 187341, 187487, 187488, 187489, 187510, 187623, 187624, 187627, 187656, 187698, 187739, 187749, 187783, 187785, 187791, 187796, 188093, 188101
LHC12h: 190209, 190210, 190212, 190213, 190214, 190215, 190216, 190240, 190303, 190305, 190307, 190335, 190337, 190338, 190340, 190341, 190342, 190344, 190386, 190388, 190389, 190390, 190392, 190393, 190416, 190417, 190418, 190419, 190421, 190422, 190424, 190425, 191129, 191227, 191230, 191231, 191245, 191247, 191248, 191450, 191451, 192072, 192073, 192075, 192128, 192136, 192140, 192141, 192172, 192174, 192177, 192194, 192197, 192199, 192200, 192201, 192202, 192205, 192344, 192347, 192348, 192349, 192415, 192417, 192453, 192461, 192468, 192471, 192492, 192499, 192535, 192542, 192548, 192551, 192729, 192731, 192732
LHC12i: 192772, 192775, 192778, 192779, 192820, 192822, 192824, 193004, 193005, 193007, 193008, 193010, 193011, 193014, 193047, 193049, 193051, 193092, 193093, 193094, 193097, 193148, 193155, 193156, 193187, 193188, 193189, 193194

Trigger EGA

LHC12c: 179796, 179803, 179806, 179858, 179859, 179916, 179917, 179918, 179919, 179920, 180000, 180042, 180044, 180129, 180130, 180131, 180132, 180133, 180500, 180501, 180515, 180517, 180561, 180564, 180567, 180569, 180716, 180717, 180719, 180720, 182017, 182018, 182022, 182023, 182106, 182110, 182111, 182207, 182289, 182295, 182297, 182299, 182300, 182302, 182322, 182323, 182324, 182325, 182624, 182635, 182684, 182686, 182687, 182691, 182692, 182724, 182725, 182728, 182729, 182730, 182741, 182744
LHC12d: 183913, 183916, 183932, 183933, 183934, 183935, 183936, 183937, 183938, 183942, 183946, 184126, 184127, 184131, 184132, 184134, 184135, 184137, 184138, 184140, 184144, 184145, 184147, 184183, 184188, 184208, 184209, 184210, 184215, 184216, 184371, 184383, 184389, 184673, 184678, 184682, 184687, 184784, 184786, 185029, 185031, 185116, 185126, 185127, 185132, 185133, 185134, 185157, 185160, 185164, 185189, 185196, 185198, 185203, 185206, 185208, 185217, 185221, 185282, 185284, 185289, 185292, 185293, 185296, 185299, 185300, 185302, 185303, 185349, 185350, 185351, 185356, 185359, 185360, 185361, 185362, 185363, 185368, 185371, 185375, 185378, 185461, 185465, 185582, 185583, 185588, 185589, 185659, 185687, 185738, 185764, 185765, 185768, 185775, 185776, 185778, 185784, 186163, 186164, 186165, 186167, 186205, 186208, 186319, 186320
LHC12f: 186668, 186688, 186689, 186690, 186692, 186694, 186811, 186814, 186937, 186938, 186939, 186966, 186969, 186990, 186992, 186994, 187143, 187145, 187146, 187148, 187149, 187150, 187151, 187152, 187202, 187203, 187339, 187340, 187341, 187487, 187488, 187489, 187510, 187623, 187624, 187627, 187656, 187698, 187739, 187749, 187783, 187785, 187791, 187796, 188093, 188101
LHC12h: 189603, 189605, 189610, 189611, 189612, 189616, 189621, 189623, 189647, 189648, 189650, 189654, 189656, 189658, 189659, 189696, 189697, 189698, 190209, 190210, 190212, 190213, 190214, 190215, 190216, 190240, 190303, 190305, 190307, 190335, 190337, 190338, 190340, 190341, 190342, 190344, 190386, 190388, 190389, 190390, 190392, 190393, 190416, 190417, 190418, 190419, 190421, 190422, 190424, 190425, 191129, 191227, 191230, 191231, 191245, 191247, 191248, 191450, 191451, 192072, 192073, 192075, 192128, 192136, 192140, 192141, 192172, 192174, 192177, 192194, 192197, 192199, 192200, 192201, 192202, 192205, 192344, 192347, 192348, 192349, 192415, 192417, 192453, 192461, 192468, 192471, 192492, 192499, 192535, 192542, 192548, 192551, 192729, 192731, 192732
LHC12i: 192772, 192775, 192778, 192779, 192820, 192822, 192824, 193004, 193005, 193007, 193008, 193010, 193011, 193014, 193047, 193049, 193051, 193092, 193093, 193094, 193097

B.2 RUN NUMBERS FOR P–PB COLLISIONS

without SDD

LHC16r: 265698, 265700, 265701, 265705, 265709, 265713, 265714, 265741, 265742, 265744, 265756, 265788, 265789, 265795, 265797, 266034, 266081, 266083, 266084, 266085, 266086, 266117, 266187, 266189, 266193, 266196, 266197, 266208, 266304, 266316, 266317, 266318
LHC16s: 266437, 266438, 266439, 266441, 266543, 266549, 266881, 266882, 266883, 266886, 266944, 266993, 266994, 266997, 266998, 267070, 267072, 267077, 267081, 267110

FAST

LHC16r: 266318, 266317, 266316

LHC16s: 266998

LIST OF FIGURES

LIST OF TABLES

ACRONYMS

QFT	Quantum Field Theory
QED	Quantum Electro Dynamics
QCD	Quantum Chromodynamics
LO	Leading Order
NLO	Next-to-Leading Order
NNLO	Next-to-next-to-leading order
pQCD	perturbative QCD
DIS	Deep Inelastic Scattering
LHC	Large Hadron Collider
RHIC	Relativistic Heavy Ion Collider
PDF	Parton Distribution Function
MC	Monte Carlo
cm	centre-of-mass
DY	Drell–Yan
nPDF	nuclear PDF
CGC	Colour-Glass Condensate
ALICE	A Large Ion Collider Experiment
QGP	Quark-Gluon Plasma
CBM	Compressed Baryonic Matter
FAIR	Facility for Antiproton and Ion Research
FoCal	Forward Calorimeter
NNNLL	next-to-next-to-next-to-leading-logarithmic
CERN	Conseil Européen pour la Recherche Nucléaire
LEP	Large Electron-Positron collider
RF	radiofrequency
ECRIS	Electron Cyclotron Resonance Ion Source
PSB	Proton Synchrotron Booster
PS	Proton Synchrotron
SPS	Super Proton Synchrotron
LEIR	Low Energy Ion Ring
COMPASS	COmmon Muon Proton Apparatus for Structure and Spectroscopy
CMS	Compact Muon Solenoid
ATLAS	A Toroidal LHC Apparatus

LHCb	Large Hadron Collider beauty
CKM	Cabibbo-Kobayashi-Maskawa
TOTEM	TOTal Elastic and diffractive cross section Measurement
MoEDAL	Monopole and Exotics Detector At the LHC
LHCf	Large Hadron Collider forward
ITS	Inner Tracking System
SPD	Silicon Pixel Detector
SDD	Silicon Drift Detector
SSD	Silicon Strip Detector
TPC	Time Projection Chamber
TRD	Transition Radiation Detector
TOF	Time-Of-Flight
PHOS	Photon Spectrometer
EMCal	ElectroMagnetic Calorimeter
DCal	Di-Jet Calorimeter
MWPC	Multi-Wire Proportional Chamber
TR	Transition Radiation
GTU	Global Tracking Unit
MRPC	Multigap Resistive Plate Chamber
EM	electromagnetic
SM	supermodule
APD	Avalanche Photo Diode
TRU	Trigger Region Unit
STU	Summary Trigger Unit
CTP	Central Trigger Processor
L0	Level-0
L1	Level-1
L2	Level-2
APD	Avalanche Photo-Diode
CPV	Charged-Particle Veto
HMPID	High-Momentum Particle Identification Detector
RICH	Ring Imaging Cherenkov
ZDC	Zero Degree Calorimeter
PMD	Photon Multiplicity Detector
FMD	Forward Multiplicity Detector
MB	minimum bias
WLCG	Worldwide LHC Computing Grid

DAQ	Data Acquisition
HLT	High Level Trigger
O^2	Online-Offline Computing System
FLP	First Layer Processing
EPN	Event Processing Node
CTF	Compressed Time Frame
AOD	Analysis Data Object
MPI	Multi Parton Interaction
ISR	Initial-State Radiation
FSR	Final-State Radiation
JJ	Jet-Jet
GJ	Gamma-Jet
FEE	Front End Electronics
LED	Light-Emitting Diode
PCM	Photon Conversion Method
MIP	Minimum Ionizing Particles
UE	Underlying Event
DCA	Distances of Closest Approach
EIC	Electron Ion Collider
TDR	Technical Design Report
LOI	Letter-of-Intent
FWHM	Full Width at Half Maximum
Linac	Linear accelerator

LEBENSLAUF

FLORIAN JONAS

Geburtsdatum: 13.06.1995
Geburtsort: Hamm
Staatsangehörigkeit: Deutsch
Eltern: Andreas Jonas & Nicole Jonas (geb. Wilmsen)

BERUFSERFAHRUNG

Okt 2018 - heute	**Wissenschaftlicher Mitarbeiter** Insitut für Kernphysik Westfälische Wilhelms-Universität	Münster, DE/Genf, CH
Jul-Sep 2017	**Sommerstudent** European Organization for Nuclear Research (CERN)	Genf, CH
Jan-Mär 2016 & Jul+Sep 2016	**Wissenschaftliche Hilfskraft** Institut für Theoretische Physik Westfälische Wilhelms-Universität	Münster, DE
Jul 2012	**Praktikant** Deutsches Zentrum für Luft- und Raumfahrt	Köln, DE

SCHULAUSBILDUNG / STUDIUM

2018-heute	**Promotionsstudium (Physik)** Insitut für Kernphysik Westfälische Wilhelms-Universität Doktorarbeit: *Probing the initial state of heavy-ion collisions with isolated prompt photons* Betreuung: C. Klein-Boesing, A. Andronic; entsendet ans CERN in Zusammenarbeit mit Oak Ridge National Lab (ORNL)	Genf, CH
2016-2018	**Master of Science (Physik)** Insitut für Kernphysik Westfälische Wilhelms-Universität Masterarbeit: *Measurement of ω and η mesons via their three pion decay with ALICE in pp collisions at $\sqrt{s} = 7$TeV* Note: 1.0 (mit Auszeichnung)	Münster, DE
2013-2016	**Bachelor of Science (Physik)** Insitut für Kernphysik Westfälische Wilhelms-Universität Bachelorarbeit: *Simulations for optimization of ω-reconstruction at ALICE* Note: 2.0	Münster, DE
2005-2013	**Allgemeine Hochschulreife** Freiherr-vom-Stein Gymnasium Leistungskurs Mathematik und Physik Note: 1.4	Hamm, DE
Jul-Dez 2010	**Schüleraustausch** Otumoetai College	Tauranga, NZ

LIST OF PUBLICATIONS

- 2022 -

Performance of the ALICE Electromagnetic Calorimeter
ALICE Collaboration
arXiv:2209.04216 (submitted to JINST)

- 2021 -

Centrality dependence of electroweak boson production in PbPb collisions at the CERN Large Hadron Collider
F. Jonas and C. Loizides
Phys. Rev. C 104, 044905

- 2020 -

Production of ω mesons in pp collisions at $\sqrt{s} = 7\,\mathrm{TeV}$
ALICE Collaboration
Eur. Phys. J. C 80, 1130

Letter of Intent: A Forward Calorimeter (FoCal) in the ALICE experiment
ALICE Collaboration
CERN-LHCC-2020-009, LHCC-I-036

BIBLIOGRAPHY

[1] Mark Thomson. *Modern Particle Physics*. Cambridge University Press, 2013. DOI: 10.1017/CBO9781139525367.

[2] Steven Weinberg. "The Making of the Standard Model." In: *Eur. Phys. J. C* 34 (2003), 5–13. 21 p. URL: https://cds.cern.ch/record/799984.

[3] Wikimedia Commons. *Standard model of elementary particles*. 2019. URL: https://en.wikipedia.org/wiki/File:Standard_Model_of_Elementary_Particles.svg.

[4] Matthew D. Schwartz. *Quantum Field Theory and the Standard Model*. Cambridge University Press, 2013. DOI: 10.1017/9781139540940.

[5] Tom Lancaster and Stephen J. Blundell. *Quantum Field Theory for the Gifted Amateur*. Oxford University Press, 2014. ISBN: 978-0-19-969933-9.

[6] James Clerk Maxwell. *A Treatise on Electricity and Magnetism*. Vol. 1. Cambridge Library Collection - Physical Sciences. Cambridge University Press, 2010. DOI: 10.1017/CBO9780511709333.

[7] R. P. Feynman. "Space-Time Approach to Quantum Electrodynamics." In: *Phys. Rev.* 76 (6 Sept. 1949), pp. 769–789. DOI: 10.1103/PhysRev.76.769. URL: https://link.aps.org/doi/10.1103/PhysRev.76.769.

[8] Steven Weinberg. *The Quantum Theory of Fields*. Vol. 1. Cambridge University Press, 1995. DOI: 10.1017/CBO9781139644167.

[9] Meinard Kuhlmann. "Quantum Field Theory." In: *The Stanford Encyclopedia of Philosophy*. Ed. by Edward N. Zalta. Fall 2020. Metaphysics Research Lab, Stanford University, 2020.

[10] Michael E. Peskin and Daniel V. Schroeder. *An Introduction to Quantum Field Theory*. Reading, USA: Perseus Books, 1995. ISBN: 0-201-50397-2.

[11] Particle Data Group et al. "Review of Particle Physics." In: *Progress of Theoretical and Experimental Physics* 2020.8 (Aug. 2020). 083C01. ISSN: 2050-3911. DOI: 10.1093/ptep/ptaa104. eprint: https://academic.oup.com/ptep/article-pdf/2020/8/083C01/34673722/ptaa104.pdf. URL: https://doi.org/10.1093/ptep/ptaa104.

[12] Jeff Greensite. *An introduction to the confinement problem*. Vol. 821. 2011. DOI: 10.1007/978-3-642-14382-3.

[13] Daisuke Jido and Minori Sakashita. "Quark confinement potential examined by excitation energy of the Λ_c and Λ_b baryons in a quark–diquark model." In: *Progress of Theoretical and Experimental Physics* 2016.8 (Aug. 2016). 083D02. ISSN: 2050-3911. DOI: 10.1093/ptep/ptw113. eprint: https://academic.oup.com/ptep/article-pdf/2016/8/083D02/9621857/ptw113.pdf. URL: https://doi.org/10.1093/ptep/ptw113.

[14] *α_s(2019): Precision measurements of the QCD coupling*. July 2019. arXiv: 1907.01435 [hep-ph].

[15] Peter Skands. "Introduction to QCD." In: *Theoretical Advanced Study Institute in Elementary Particle Physics: Searching for New Physics at Small and Large Scales*. 2013, pp. 341–420. DOI: 10.1142/9789814525220_0008. arXiv: 1207.2389 [hep-ph].

[16] Cheuk-Yin Wong. *Introduction to High-Energy Heavy-Ion Collisions*. WORLD SCIENTIFIC, 1994. DOI: 10.1142/1128. eprint: https://www.worldscientific.com/doi/pdf/10.1142/1128. URL: https://www.worldscientific.com/doi/abs/10.1142/1128.

[17] John C. Collins, Davison E. Soper, and George F. Sterman. "Factorization of Hard Processes in QCD." In: *Adv. Ser. Direct. High Energy Phys.* 5 (1989), pp. 1–91. DOI: 10.1142/9789814503266_0001. arXiv: hep-ph/0409313.

[18] E Perez and E Rizvi. "The quark and gluon structure of the proton." In: *Reports on Progress in Physics* 76.4 (Mar. 2013), p. 046201. DOI: 10.1088/0034-4885/76/4/046201. URL: https://doi.org/10.1088/0034-4885/76/4/046201.

[19] V.N. Gribov and L.N. Lipatov. "Deep inelastic electron scattering in perturbation theory." In: *Physics Letters B* 37.1 (1971), pp. 78–80. ISSN: 0370-2693. DOI: https://doi.org/10.1016/0370-2693(71)90576-4. URL: https://www.sciencedirect.com/science/article/pii/0370269371905764.

[20] Gavin P. Salam. "An Introduction to leading and next-to-leading BFKL." In: *Acta Phys. Polon. B* 30 (1999). Ed. by A. Bialas and M. Praszalowicz, pp. 3679–3705. arXiv: hep-ph/9910492.

[21] Juan Rojo et al. "The PDF4LHC report on PDFs and LHC data: Results from Run I and preparation for Run II." In: *J. Phys. G* 42 (2015), p. 103103. DOI: 10.1088/0954-3899/42/10/103103. arXiv: 1507.00556 [hep-ph].

[22] Jacob J. Ethier and Emanuele R. Nocera. "Parton Distributions in Nucleons and Nuclei." In: *Annual Review of Nuclear and Particle Science* 70.1 (2020), pp. 43–76. DOI: 10.1146/annurev-nucl-011720-042725. eprint: https://doi.org/10.1146/annurev-nucl-011720-042725. URL: https://doi.org/10.1146/annurev-nucl-011720-042725.

[23] K. Kovarik et al. "nCTEQ15 - Global analysis of nuclear parton distributions with uncertainties in the CTEQ framework." In: *Phys. Rev. D* 93.8 (2016), p. 085037. DOI: 10.1103/PhysRevD.93.085037. arXiv: 1509.00792 [hep-ph].

[24] Richard D. Ball et al. "The Path to Proton Structure at One-Percent Accuracy." In: (Sept. 2021). arXiv: 2109.02653 [hep-ph].

[25] L. A. Harland-Lang, A. D. Martin, P. Motylinski, and R. S. Thorne. "Parton distributions in the LHC era: MMHT 2014 PDFs." In: *Eur. Phys. J. C* 75.5 (2015), p. 204. DOI: 10.1140/epjc/s10052-015-3397-6. arXiv: 1412.3989 [hep-ph].

[26] Sayipjamal Dulat, Tie-Jiun Hou, Jun Gao, Marco Guzzi, Joey Huston, Pavel Nadolsky, Jon Pumplin, Carl Schmidt, Daniel Stump, and C. P. Yuan. "New parton distribution functions from a global analysis of quantum chromodynamics." In: *Phys. Rev. D* 93.3 (2016), p. 033006. DOI: 10.1103/PhysRevD.93.033006. arXiv: 1506.07443 [hep-ph].

[27] H. Abramowicz et al. “Combination of measurements of inclusive deep inelastic $e^{\pm}p$ scattering cross sections and QCD analysis of HERA data.” In: *Eur. Phys. J. C* 75.12 (2015), p. 580. DOI: `10.1140/epjc/s10052-015-3710-4`. arXiv: `1506.06042 [hep-ex]`.

[28] S. Alekhin, J. Blümlein, S. Moch, and R. Placakyte. “Parton distribution functions, α_s, and heavy-quark masses for LHC Run II.” In: *Phys. Rev. D* 96.1 (2017), p. 014011. DOI: `10.1103/PhysRevD.96.014011`. arXiv: `1701.05838 [hep-ph]`.

[29] Pedro Jimenez-Delgado and Ewald Reya. “Delineating parton distributions and the strong coupling.” In: *Phys. Rev. D* 89.7 (2014), p. 074049. DOI: `10.1103/PhysRevD.89.074049`. arXiv: `1403.1852 [hep-ph]`.

[30] G. Altarelli and G. Parisi. “Asymptotic freedom in parton language.” In: *Nuclear Physics B* 126.2 (1977), pp. 298–318. ISSN: 0550-3213. DOI: `https://doi.org/10.1016/0550-3213(77)90384-4`. URL: `https://www.sciencedirect.com/science/article/pii/0550321377903844`.

[31] A.H. Mueller. “A simple derivation of the JIMWLK equation.” In: *Physics Letters B* 523.3 (2001), pp. 243–248. ISSN: 0370-2693. DOI: `https://doi.org/10.1016/S0370-2693(01)01343-0`. URL: `https://www.sciencedirect.com/science/article/pii/S0370269301013430`.

[32] T. Lappi and H. Mäntysaari. “Next-to-leading order Balitsky-Kovchegov equation with resummation.” In: *Phys. Rev. D* 93 (9 May 2016), p. 094004. DOI: `10.1103/PhysRevD.93.094004`. URL: `https://link.aps.org/doi/10.1103/PhysRevD.93.094004`.

[33] Javier L. Albacete and Cyrille Marquet. “Gluon saturation and initial conditions for relativistic heavy ion collisions.” In: *Prog. Part. Nucl. Phys.* 76 (2014), pp. 1–42. DOI: `10.1016/j.ppnp.2014.01.004`. arXiv: `1401.4866 [hep-ph]`.

[34] Francois Gelis, Edmond Iancu, Jamal Jalilian-Marian, and Raju Venugopalan. “The Color Glass Condensate.” In: *Annual Review of Nuclear and Particle Science* 60.1 (2010), pp. 463–489. DOI: `10.1146/annurev.nucl.010909.083629`. eprint: `https://doi.org/10.1146/annurev.nucl.010909.083629`. URL: `https://doi.org/10.1146/annurev.nucl.010909.083629`.

[35] B. Alver, M. Baker, C. Loizides, and P. Steinberg. “The PHOBOS Glauber Monte Carlo.” In: (May 2008). arXiv: `0805.4411 [nucl-ex]`.

[36] Wit Busza, Krishna Rajagopal, and Wilke van der Schee. “Heavy Ion Collisions: The Big Picture and the Big Questions.” In: *Annual Review of Nuclear and Particle Science* 68.1 (2018), pp. 339–376. DOI: `10.1146/annurev-nucl-101917-020852`. eprint: `https://doi.org/10.1146/annurev-nucl-101917-020852`. URL: `https://doi.org/10.1146/annurev-nucl-101917-020852`.

[37] David d’Enterria and Constantin Loizides. “Progress in the Glauber Model at Collider Energies.” In: *Annual Review of Nuclear and Particle Science* 71.1 (2021), pp. 315–344. DOI: `10.1146/annurev-nucl-102419-060007`. eprint: `https://doi.org/10.1146/annurev-nucl-102419-060007`. URL: `https://doi.org/10.1146/annurev-nucl-102419-060007`.

[38] B. Abelev, J. Adam, D. Adamová, A. M. Adare, M. M. Aggarwal, G. Aglieri Rinella, M. Agnello, A. G. Agocs, and Agostinelli. "Centrality determination of Pb-Pb collisions at $\sqrt{s_{NN}} = 2.76$ TeV with ALICE." In: *Phys. Rev. C* 88 (4 Oct. 2013), p. 044909. DOI: 10.1103/PhysRevC.88.044909. URL: https://link.aps.org/doi/10.1103/PhysRevC.88.044909.

[39] F. Gelis. "Color Glass Condensate and Glasma." In: *Int. J. Mod. Phys. A* 28 (2013), p. 1330001. DOI: 10.1142/S0217751X13300019. arXiv: 1211.3327 [hep-ph].

[40] Christian Klein-Bösing. "Study of the Quark-Gluon Plasma with Hard and Electromagnetic Probes." 2013. URL: https://cds.cern.ch/record/2729069.

[41] Jaroslav Adam et al. "Measurement of transverse energy at midrapidity in Pb-Pb collisions at $\sqrt{s_{\mathrm{NN}}} = 2.76$ TeV." In: *Phys. Rev. C* 94.3 (2016), p. 034903. DOI: 10.1103/PhysRevC.94.034903. arXiv: 1603.04775 [nucl-ex].

[42] Jean-Philippe Karr, Dominique Marchand, and Eric Voutier. "The proton size." In: *Nature Rev. Phys.* 2.11 (2020), pp. 601–614. DOI: 10.1038/s42254-020-0229-x.

[43] J. C. Collins and M. J. Perry. "Superdense Matter: Neutrons or Asymptotically Free Quarks?" In: *Phys. Rev. Lett.* 34 (21 May 1975), pp. 1353–1356. DOI: 10.1103/PhysRevLett.34.1353. URL: https://link.aps.org/doi/10.1103/PhysRevLett.34.1353.

[44] N. Cabibbo and G. Parisi. "Exponential hadronic spectrum and quark liberation." In: *Physics Letters B* 59.1 (1975), pp. 67–69. ISSN: 0370-2693. DOI: https://doi.org/10.1016/0370-2693(75)90158-6. URL: https://www.sciencedirect.com/science/article/pii/0370269375901586.

[45] Jonah E. Bernhard, J. Scott Moreland, Steffen A. Bass, Jia Liu, and Ulrich Heinz. "Applying Bayesian parameter estimation to relativistic heavy-ion collisions: Simultaneous characterization of the initial state and quark-gluon plasma medium." In: *Phys. Rev. C* 94 (2 Aug. 2016), p. 024907. DOI: 10.1103/PhysRevC.94.024907. URL: https://link.aps.org/doi/10.1103/PhysRevC.94.024907.

[46] Patrick Steinbrecher. "The QCD crossover at zero and non-zero baryon densities from Lattice QCD." In: *Nucl. Phys. A* 982 (2019). Ed. by Federico Antinori, Andrea Dainese, Paolo Giubellino, Vincenzo Greco, Maria Paola Lombardo, and Enrico Scomparin, pp. 847–850. DOI: 10.1016/j.nuclphysa.2018.08.025. arXiv: 1807.05607 [hep-lat].

[47] Peter Senger. "Exploring Cosmic Matter in the Laboratory—The Compressed Baryonic Matter Experiment at FAIR." In: *Particles* 2.4 (2019), pp. 499–510. ISSN: 2571-712X. DOI: 10.3390/particles2040031. URL: https://www.mdpi.com/2571-712X/2/4/31.

[48] Peter Braun-Munzinger and Johanna Stachel. "The quest for the quark-gluon plasma." In: *Nature* 448 (2007), pp. 302–309. DOI: 10.1038/nature06080.

[49] S. Acharya et al. "Neutral pion and η meson production at midrapidity in Pb-Pb collisions at $\sqrt{s_{NN}} = 2.76$ TeV." In: *Phys. Rev. C* 98 (4 Oct. 2018), p. 044901. DOI: 10.1103/PhysRevC.98.044901. URL: https://link.aps.org/doi/10.1103/PhysRevC.98.044901.

[50] J. Adam et al. "Centrality dependence of the nuclear modification factor of charged pions, kaons, and protons in Pb-Pb collisions at $\sqrt{s_{NN}} = 2.76$ TeV." In: *Phys. Rev. C* 93 (3 Mar. 2016), p. 034913. DOI: 10.1103/PhysRevC.93.034913. URL: https://link.aps.org/doi/10.1103/PhysRevC.93.034913.

[51] B. Abelev, J. Adam, D. Adamová, and M.M. Aggarwal. "Production of charged pions, kaons and protons at large transverse momenta in pp and Pb–Pb collisions at sNN=2.76 TeV." In: *Physics Letters B* 736 (2014), pp. 196–207. ISSN: 0370-2693. DOI: https://doi.org/10.1016/j.physletb.2014.07.011. URL: https://www.sciencedirect.com/science/article/pii/S0370269314004973.

[52] J. D. Bjorken. "Energy Loss of Energetic Partons in Quark - Gluon Plasma: Possible Extinction of High p(t) Jets in Hadron - Hadron Collisions." In: (Aug. 1982).

[53] A. Adare et al. "Suppression Pattern of Neutral Pions at High Transverse Momentum in Au+Au Collisions at $\sqrt{s_{NN}} = 200$ GeV and Constraints on Medium Transport Coefficients." In: *Phys. Rev. Lett.* 101 (23 Dec. 2008), p. 232301. DOI: 10.1103/PhysRevLett.101.232301. URL: https://link.aps.org/doi/10.1103/PhysRevLett.101.232301.

[54] Shreyasi Acharya et al. "Nuclear modification factor of light neutral-meson spectra up to high transverse momentum in p–Pb collisions at sNN=8.16 TeV." In: *Phys. Lett. B* 827 (2022), p. 136943. DOI: 10.1016/j.physletb.2022.136943. arXiv: 2104.03116 [nucl-ex].

[55] Serguei Chatrchyan et al. "Measurement of isolated photon production in *pp* and PbPb collisions at $\sqrt{s_{NN}} = 2.76$ TeV." In: *Phys. Lett. B* 710 (2012), pp. 256–277. DOI: 10.1016/j.physletb.2012.02.077. arXiv: 1201.3093 [nucl-ex].

[56] Serguei Chatrchyan et al. "Study of Z production in PbPb and pp collisions at $\sqrt{s_{\text{NN}}} = 2.76$ TeV in the dimuon and dielectron decay channels." In: *JHEP* 03 (2015), p. 022. DOI: 10.1007/JHEP03(2015)022. arXiv: 1410.4825 [nucl-ex].

[57] Serguei Chatrchyan et al. "Study of *W* boson production in PbPb and *pp* collisions at $\sqrt{s_{NN}} = 2.76$ TeV." In: *Phys. Lett. B* 715 (2012), pp. 66–87. DOI: 10.1016/j.physletb.2012.07.025. arXiv: 1205.6334 [nucl-ex].

[58] Jean-François Paquet, Chun Shen, Gabriel S. Denicol, Matthew Luzum, Björn Schenke, Sangyong Jeon, and Charles Gale. "Production of photons in relativistic heavy-ion collisions." In: *Phys. Rev. C* 93.4 (2016), p. 044906. DOI: 10.1103/PhysRevC.93.044906. arXiv: 1509.06738 [hep-ph].

[59] Charles Gale. "Photon Production in Hot and Dense Strongly Interacting Matter." In: *Landolt-Bornstein* 23 (2010). Ed. by R. Stock, p. 445. DOI: 10.1007/978-3-642-01539-7_15. arXiv: 0904.2184 [hep-ph].

[60] Jaroslav Adam et al. "Direct photon production in Pb-Pb collisions at $\sqrt{s_{NN}} = 2.76$ TeV." In: *Phys. Lett. B* 754 (2016), pp. 235–248. DOI: 10.1016/j.physletb.2016.01.020. arXiv: 1509.07324 [nucl-ex].

[61] A. Adare et al. "Enhanced production of direct photons in Au+Au collisions at $\sqrt{s_{NN}} = 200$ GeV and implications for the initial temperature." In: *Phys. Rev. Lett.* 104 (2010), p. 132301. DOI: 10.1103/PhysRevLett.104.132301. arXiv: 0804.4168 [nucl-ex].

[62] A. Adare et al. “Centrality dependence of low-momentum direct-photon production in Au + Au collisions at $\sqrt{s_{NN}} = 200\text{GeV}$.” In: *Phys. Rev. C* 91 (6 June 2015), p. 064904. DOI: 10.1103/PhysRevC.91.064904. URL: https://link.aps.org/doi/10.1103/PhysRevC.91.064904.

[63] Javier L. Albacete, Adrian Dumitru, and Cyrille Marquet. “The initial state of heavy-ion collisions.” In: *Int. J. Mod. Phys. A* 28 (2013), p. 1340010. DOI: 10.1142/S0217751X13400101. arXiv: 1302.6433 [hep-ph].

[64] Michele Arneodo. “Nuclear effects in structure functions.” In: *Physics Reports* 240.5 (1994), pp. 301–393. ISSN: 0370-1573. DOI: https://doi.org/10.1016/0370-1573(94)90048-5. URL: https://www.sciencedirect.com/science/article/pii/0370157394900485.

[65] Kari J. Eskola, Petja Paakkinen, Hannu Paukkunen, and Carlos A. Salgado. “EPPS16: Nuclear parton distributions with LHC data.” In: *The European Physical Journal C* 77.3 (Mar. 2017). arXiv: 1612.05741, p. 163. ISSN: 1434-6044, 1434-6052. DOI: 10.1140/epjc/s10052-017-4725-9. URL: http://arxiv.org/abs/1612.05741 (visited on 01/03/2022).

[66] Rabah Abdul Khalek, Rhorry Gauld, Tommaso Giani, Emanuele R. Nocera, Tanjona R. Rabemananjara, and Juan Rojo. “nNNPDF3.0: Evidence for a modified partonic structure in heavy nuclei.” In: (Jan. 2022). arXiv: 2201.12363 [hep-ph].

[67] N N Nicolaev and V I Zakharov. “Parton model and deep inelastic scattering on nuclei.” In: *Phys. Lett., B, v. 55, no. 4, pp. 397-399* (Mar. 1975). DOI: 10.1016/0370-2693(75)90368-8. URL: https://www.osti.gov/biblio/4235775.

[68] Nestor Armesto. “Nuclear shadowing.” In: *J. Phys. G* 32 (2006), R367–R394. DOI: 10.1088/0954-3899/32/11/R01. arXiv: hep-ph/0604108.

[69] J. J. Aubert et al. “The ratio of the nucleon structure functions $F2_n$ for iron and deuterium.” In: *Phys. Lett. B* 123 (1983), pp. 275–278. DOI: 10.1016/0370-2693(83)90437-9.

[70] P R Norton. “The EMC effect.” In: *Reports on Progress in Physics* 66.8 (July 2003), pp. 1253–1297. DOI: 10.1088/0034-4885/66/8/201. URL: https://doi.org/10.1088/0034-4885/66/8/201.

[71] P. Duwentäster, L. A. Husová, T. Ježo, M. Klasen, K. Kovařík, A. Kusina, K. F. Muzakka, F. I. Olness, I. Schienbein, and J. Y. Yu. “Impact of inclusive hadron production data on nuclear gluon PDFs.” In: *Phys. Rev. D* 104 (2021), p. 094005. DOI: 10.1103/PhysRevD.104.094005. arXiv: 2105.09873 [hep-ph].

[72] *Letter of Intent: A Forward Calorimeter (FoCal) in the ALICE experiment*. June 2020.

[73] S. Catani, M. Fontannaz, J. P. Guillet, and E. Pilon. “Cross-section of isolated prompt photons in hadron hadron collisions.” In: *JHEP* 05 (2002), p. 028. DOI: 10.1088/1126-6708/2002/05/028. arXiv: hep-ph/0204023.

[74] John M. Campbell, R. Keith Ellis, and Ciaran Williams. “Direct Photon Production at Next-to–Next-to-Leading Order.” In: *Phys. Rev. Lett.* 118.22 (2017). [Erratum: Phys.Rev.Lett. 124, 259901 (2020)], p. 222001. DOI: 10.1103/PhysRevLett.118.222001. arXiv: 1612.04333 [hep-ph].

[75] David d'Enterria and Juan Rojo. "Quantitative constraints on the gluon distribution function in the proton from collider isolated-photon data." In: *Nucl. Phys. B* 860 (2012), pp. 311–338. DOI: 10.1016/j.nuclphysb.2012.03.003. arXiv: 1202.1762 [hep-ph].

[76] Stephen Holmes, Ronald S. Moore, and Vladimir Shiltsev. "Overview of the Tevatron Collider Complex: Goals, Operations and Performance." In: *JINST* 6 (2011), T08001. DOI: 10.1088/1748-0221/6/08/T08001. arXiv: 1106.0909 [physics.acc-ph].

[77] Christian Bierlich et al. "A comprehensive guide to the physics and usage of PYTHIA 8.3." In: (Mar. 2022). arXiv: 2203.11601 [hep-ph].

[78] Peter Skands, Stefano Carrazza, and Juan Rojo. "Tuning PYTHIA 8.1: the Monash 2013 Tune." In: *Eur. Phys. J. C* 74.8 (2014), p. 3024. DOI: 10.1140/epjc/s10052-014-3024-y. arXiv: 1404.5630 [hep-ph].

[79] Richard D. Ball, Valerio Bertone, Stefano Carrazza, Luigi Del Debbio, Stefano Forte, Alberto Guffanti, Nathan P. Hartland, and Juan Rojo. "Parton distributions with QED corrections." In: *Nucl. Phys. B* 877 (2013), pp. 290–320. DOI: 10.1016/j.nuclphysb.2013.10.010. arXiv: 1308.0598 [hep-ph].

[80] Michael Klasen, Christian Klein-Bösing, and H. Poppenborg. "Prompt photon production and photon-jet correlations at the LHC." In: *JHEP* 03 (2018), p. 081. DOI: 10.1007/JHEP03(2018)081. arXiv: 1709.04154 [hep-ph].

[81] L. Bourhis, M. Fontannaz, and J.Ph. Guillet. "Quark and gluon fragmentation functions into photons." In: *Eur. Phys. J. C* 2.3 (1998), pp. 529–537. DOI: epjc/v2/p529(epjc708). URL: https://doi.org/epjc/v2/p529(epjc708).

[82] Raphaëlle Ichou and David d'Enterria. "Sensitivity of isolated photon production at TeV hadron colliders to the gluon distribution in the proton." In: *Phys. Rev. D* 82 (1 July 2010), p. 014015. DOI: 10.1103/PhysRevD.82.014015. URL: https://link.aps.org/doi/10.1103/PhysRevD.82.014015.

[83] P. Aurenche, J. Ph. Guillet, E. Pilon, M. Werlen, and M. Fontannaz. "Recent critical study of photon production in hadronic collisions." In: *Phys. Rev. D* 73 (9 May 2006), p. 094007. DOI: 10.1103/PhysRevD.73.094007. URL: https://link.aps.org/doi/10.1103/PhysRevD.73.094007.

[84] J. R. Andersen et al. "Les Houches 2013: Physics at TeV Colliders: Standard Model Working Group Report." In: (May 2014). arXiv: 1405.1067 [hep-ph].

[85] Stefano Frixione. "Isolated photons in perturbative QCD." In: *Phys. Lett. B* 429 (1998), pp. 369–374. DOI: 10.1016/S0370-2693(98)00454-7. arXiv: hep-ph/9801442.

[86] Stefano Frixione and Werner Vogelsang. "Isolated photon production in polarized *pp* collisions." In: *Nucl. Phys. B* 568 (2000), pp. 60–92. DOI: 10.1016/S0550-3213(99)00575-1. arXiv: hep-ph/9908387.

[87] Sayipjamal Dulat, Tie-Jiun Hou, Jun Gao, Marco Guzzi, Joey Huston, Pavel Nadolsky, Jon Pumplin, Carl Schmidt, Daniel Stump, and C. P. Yuan. "New parton distribution functions from a global analysis of quantum chromodynamics." In: *Phys. Rev. D* 93.3 (2016), p. 033006. DOI: 10.1103/PhysRevD.93.033006. arXiv: 1506.07443 [hep-ph].

[88] B. Ducloué, T. Lappi, and H. Mäntysaari. "Isolated photon production in proton-nucleus collisions at forward rapidity." In: *Phys. Rev. D* 97.5 (2018), p. 054023. DOI: `10.1103/PhysRevD.97.054023`. arXiv: `1710.02206 [hep-ph]`.

[89] M. McLaughlin et al. "Inclusive Production of Direct Photons in 200-GeV/c Collisions." In: *Phys. Rev. Lett.* 51 (1983), p. 971. DOI: `10.1103/PhysRevLett.51.971`.

[90] Morad Aaboud et al. "Measurement of the cross section for inclusive isolated-photon production in pp collisions at $\sqrt{s} = 13$ TeV using the ATLAS detector." In: *Phys. Lett. B* 770 (2017), pp. 473–493. DOI: `10.1016/j.physletb.2017.04.072`. arXiv: `1701.06882 [hep-ex]`.

[91] Georges Aad et al. "Measurement of the inclusive isolated-photon cross section in pp collisions at $\sqrt{s} = 13$ TeV using 36 fb^{-1} of ATLAS data." In: *JHEP* 10 (2019), p. 203. DOI: `10.1007/JHEP10(2019)203`. arXiv: `1908.02746 [hep-ex]`.

[92] Albert M Sirunyan et al. "Measurement of differential cross sections for inclusive isolated-photon and photon+jets production in proton-proton collisions at $\sqrt{s} =$ 13 TeV." In: *Eur. Phys. J. C* 79.1 (2019), p. 20. DOI: `10.1140/epjc/s10052-018-6482-9`. arXiv: `1807.00782 [hep-ex]`.

[93] W. Vogelsang and M. R. Whalley. "A Compilation of data on single and double prompt photon production in hadron hadron interactions." In: *J. Phys. G* 23 (1997), A1–A69. DOI: `10.1088/0954-3899/23/7A/001`.

[94] G. Aad et al. "Measurement of the inclusive isolated prompt photon cross section in pp collisions at $\sqrt{s} = 7$ TeV with the ATLAS detector." In: *Phys. Rev. D* 83 (2011), p. 052005. DOI: `10.1103/PhysRevD.83.052005`. arXiv: `1012.4389 [hep-ex]`.

[95] Georges Aad et al. "Measurement of the inclusive isolated prompt photon cross-section in pp collisions at $\sqrt{s} = 7$ TeV using 35 pb^{-1} of ATLAS data." In: *Phys. Lett. B* 706 (2011), pp. 150–167. DOI: `10.1016/j.physletb.2011.11.010`. arXiv: `1108.0253 [hep-ex]`.

[96] Serguei Chatrchyan et al. "Measurement of the Differential Cross Section for Isolated Prompt Photon Production in pp Collisions at 7 TeV." In: *Phys. Rev. D* 84 (2011), p. 052011. DOI: `10.1103/PhysRevD.84.052011`. arXiv: `1108.2044 [hep-ex]`.

[97] Vardan Khachatryan et al. "Measurement of the Isolated Prompt Photon Production Cross Section in pp Collisions at $\sqrt{s} = 7$~TeV." In: *Phys. Rev. Lett.* 106 (2011), p. 082001. DOI: `10.1103/PhysRevLett.106.082001`. arXiv: `1012.0799 [hep-ex]`.

[98] Serguei Chatrchyan et al. "Measurement of isolated photon production in pp and PbPb collisions at $\sqrt{s_{NN}} = 2.76$ TeV." In: *Phys. Lett. B* 710 (2012), pp. 256–277. DOI: `10.1016/j.physletb.2012.02.077`. arXiv: `1201.3093 [nucl-ex]`.

[99] C. Albajar, M.G. Albrow, O.C. Allkofer, A. Astbury, B. Aubert, T. Axon, C. Bacci, T. Bacon, N. Bains, J.R. Batley, et al. "Direct photon production at the CERN proton-antiproton collider." In: *Physics Letters B* 209.2 (1988), pp. 385–396. ISSN: 0370-2693. DOI: `https://doi.org/10.1016/0370-2693(88)90968-9`. URL: `https://www.sciencedirect.com/science/article/pii/0370269388909689`.

[100] J Alitti et al. “A measurement of single and double prompt photon production at the CERN pp collider.” In: *Physics Letters, Section B: Nuclear, Elementary Particle and High-Energy Physics* 288 (Aug. 1992).

[101] R. Ansari et al. “Direct Photon Production in $\bar{p}p$ Collisions at $\sqrt{s} = 630$-GeV.” In: *Z. Phys. C* 41 (1988), p. 395. DOI: 10.1007/BF01585623.

[102] D. Acosta et al. “Comparison of the isolated direct photon cross sections in $p\bar{p}$ collisions at $\sqrt{s} = 1.8$-TeV and $\sqrt{s} = 0.63$-TeV.” In: *Phys. Rev. D* 65 (2002), p. 112003. DOI: 10.1103/PhysRevD.65.112003. arXiv: hep-ex/0201004.

[103] V. M. Abazov et al. “The Ratio of the Isolated Photon Cross Sections at $\sqrt{s} = 630$ GeV and 1800 GeV.” In: *Phys. Rev. Lett.* 87 (2001). Ed. by Dezsõ Horváth, Péter Lévai, and András Patkós, p. 251805. DOI: 10.1103/PhysRevLett.87.251805. arXiv: hep-ex/0106026.

[104] D. Acosta et al. “Direct photon cross section with conversions at CDF.” In: *Phys. Rev. D* 70 (2004), p. 074008. DOI: 10.1103/PhysRevD.70.074008. arXiv: hep-ex/0404022.

[105] F. Abe et al. “A Precision measurement of the prompt photon cross-section in $p\bar{p}$ collisions at $\sqrt{s} = 1.8$ TeV.” In: *Phys. Rev. Lett.* 73 (1994). [Erratum: Phys.Rev.Lett. 74, 1891–1893 (1995)], pp. 2662–2666. DOI: 10.1103/PhysRevLett.73.2662.

[106] B. Abbott et al. “The isolated photon cross-section in $p\bar{p}$ collisions at $\sqrt{s} = 1.8$ TeV.” In: *Phys. Rev. Lett.* 84 (2000), pp. 2786–2791. DOI: 10.1103/PhysRevLett.84.2786. arXiv: hep-ex/9912017.

[107] S. Abachi et al. “Isolated photon cross-section in the central and forward rapidity regions in $p\bar{p}$ collisions at $\sqrt{s} = 1.8$ TeV.” In: *Phys. Rev. Lett.* 77 (1996), pp. 5011–5015. DOI: 10.1103/PhysRevLett.77.5011. arXiv: hep-ex/9603006.

[108] T. Aaltonen et al. “Measurement of the Inclusive Isolated Prompt Photon Cross Section in $p\bar{p}$ Collisions at $\sqrt{s} = 1.96$~TeV using the CDF Detector.” In: *Phys. Rev. D* 80 (2009), p. 111106. DOI: 10.1103/PhysRevD.80.111106. arXiv: 0910.3623 [hep-ex].

[109] V. M. Abazov et al. “Measurement of the isolated photon cross section in $p\bar{p}$ collisions at $\sqrt{s} = 1.96$-TeV.” In: *Phys. Lett. B* 639 (2006). [Erratum: Phys.Lett.B 658, 285–289 (2008)], pp. 151–158. DOI: 10.1016/j.physletb.2006.04.048. arXiv: hep-ex/0511054.

[110] S. S. Adler et al. “Measurement of direct photon production in p + p collisions at s**(1/2) = 200-GeV.” In: *Phys. Rev. Lett.* 98 (2007), p. 012002. DOI: 10.1103/PhysRevLett.98.012002. arXiv: hep-ex/0609031.

[111] Georges Aad et al. “Measurement of the inclusive isolated prompt photons cross section in pp collisions at $\sqrt{s} = 7$ TeV with the ATLAS detector using 4.6 fb^{-1}.” In: *Phys. Rev. D* 89.5 (2014), p. 052004. DOI: 10.1103/PhysRevD.89.052004. arXiv: 1311.1440 [hep-ex].

[112] Shreyasi Acharya et al. “Measurement of the inclusive isolated photon production cross section in pp collisions at $\sqrt{s} = 7$ TeV.” In: *Eur. Phys. J. C* 79.11 (2019), p. 896. DOI: 10.1140/epjc/s10052-019-7389-9. arXiv: 1906.01371 [nucl-ex].

[113] Georges Aad et al. “Measurement of the inclusive isolated prompt photon cross section in pp collisions at $\sqrt{s} = 8$ TeV with the ATLAS detector.” In: *JHEP* 08 (2016), p. 005. DOI: `10.1007/JHEP08(2016)005`. arXiv: `1605.03495 [hep-ex]`.

[114] Morad Aaboud et al. “Measurement of prompt photon production in $\sqrt{s_{\mathrm{NN}}} =$ 8.16 TeV p+Pb collisions with ATLAS.” In: *Phys. Lett. B* 796 (2019), pp. 230–252. DOI: `10.1016/j.physletb.2019.07.031`. arXiv: `1903.02209 [nucl-ex]`.

[115] Georges Aad et al. “Centrality, rapidity and transverse momentum dependence of isolated prompt photon production in lead-lead collisions at $\sqrt{s_{\mathrm{NN}}} = 2.76$ TeV measured with the ATLAS detector.” In: *Phys. Rev. C* 93.3 (2016), p. 034914. DOI: `10.1103/PhysRevC.93.034914`. arXiv: `1506.08552 [hep-ex]`.

[116] Francois Arleo, Stanley J. Brodsky, Dae Sung Hwang, and Anne M. Sickles. “Higher-Twist Dynamics in Large Transverse Momentum Hadron Production.” In: *Phys. Rev. Lett.* 105 (2010), p. 062002. DOI: `10.1103/PhysRevLett.105.062002`. arXiv: `0911.4604 [hep-ph]`.

[117] A. Guffanti. “NNPDF2.1: Including heavy quark mass effects in NNPDF fits.” In: *AIP Conference Proceedings* 1369.1 (2011), pp. 21–28. DOI: `10.1063/1.3631514`. eprint: `https://aip.scitation.org/doi/pdf/10.1063/1.3631514`. URL: `https://aip.scitation.org/doi/abs/10.1063/1.3631514`.

[118] G. Alverson et al. “Production of direct photons and neutral mesons at large transverse momenta by π^- and p beams at 500-GeV/c.” In: *Phys. Rev. D* 48 (1993), pp. 5–28. DOI: `10.1103/PhysRevD.48.5`.

[119] L. Apanasevich et al. “Evidence for parton k_T effects in high p_T particle production.” In: *Phys. Rev. Lett.* 81 (1998), pp. 2642–2645. DOI: `10.1103/PhysRevLett.81.2642`. arXiv: `hep-ex/9711017`.

[120] L. Apanasevich et al. “Measurement of direct photon production at Tevatron fixed target energies.” In: *Phys. Rev. D* 70 (2004), p. 092009. DOI: `10.1103/PhysRevD.70.092009`. arXiv: `hep-ex/0407011`.

[121] Thomas Becher, Christian Lorentzen, and Matthew D. Schwartz. “Precision Direct Photon and W-Boson Spectra at High p_T and Comparison to LHC Data.” In: *Phys. Rev. D* 86 (2012), p. 054026. DOI: `10.1103/PhysRevD.86.054026`. arXiv: `1206.6115 [hep-ph]`.

[122] Matthew D. Schwartz. “Precision direct photon spectra at high energy and comparison to the 8 TeV ATLAS data.” In: *JHEP* 09 (2016), p. 005. DOI: `10.1007/JHEP09(2016)005`. arXiv: `1606.02313 [hep-ph]`.

[123] Xuan Chen, Thomas Gehrmann, Nigel Glover, Marius Höfer, and Alexander Huss. “Isolated photon and photon+jet production at NNLO QCD accuracy.” In: *JHEP* 04 (2020), p. 166. DOI: `10.1007/JHEP04(2020)166`. arXiv: `1904.01044 [hep-ph]`.

[124] Enrico Bothmann et al. “Event Generation with Sherpa 2.2.” In: *SciPost Phys.* 7.3 (2019), p. 034. DOI: `10.21468/SciPostPhys.7.3.034`. arXiv: `1905.09127 [hep-ph]`.

[125] Zhong-Bo Kang, Ivan Vitev, and Hongxi Xing. "Effects of cold nuclear matter energy loss on inclusive jet production in $p+A$ collisions at energies available at the BNL Relativistic Heavy Ion Collider and the CERN Large Hadron Collider." In: *Phys. Rev. C* 92 (5 Nov. 2015), p. 054911. DOI: `10.1103/PhysRevC.92.054911`. URL: `https://link.aps.org/doi/10.1103/PhysRevC.92.054911`.

[126] Alan D. Martin, R. G. Roberts, W. James Stirling, and R. S. Thorne. "Parton distributions and the LHC: W and Z production." In: *Eur. Phys. J. C* 14 (2000), pp. 133–145. DOI: `10.1007/s100520050740`. arXiv: `hep-ph/9907231`.

[127] Alan D. Martin, R. G. Roberts, W. James Stirling, and R. S. Thorne. "Parton distributions: A New global analysis." In: *Eur. Phys. J. C* 4 (1998), pp. 463–496. DOI: `10.1007/s100520050220`. arXiv: `hep-ph/9803445`.

[128] John M. Campbell, Juan Rojo, Emma Slade, and Ciaran Williams. "Direct photon production and PDF fits reloaded." In: *Eur. Phys. J. C* 78.6 (2018), p. 470. DOI: `10.1140/epjc/s10052-018-5944-4`. arXiv: `1802.03021 [hep-ph]`.

[129] Richard D. Ball et al. "Parton distributions from high-precision collider data." In: *Eur. Phys. J. C* 77.10 (2017), p. 663. DOI: `10.1140/epjc/s10052-017-5199-5`. arXiv: `1706.00428 [hep-ph]`.

[130] Roel Aaij et al. "Study of prompt D^0 meson production in pPb collisions at $\sqrt{s_{\mathrm{NN}}} = 5$ TeV." In: *JHEP* 10 (2017), p. 090. DOI: `10.1007/JHEP10(2017)090`. arXiv: `1707.02750 [hep-ex]`.

[131] Albert M Sirunyan et al. "Study of jet quenching with isolated-photon+jet correlations in PbPb and pp collisions at $\sqrt{s_{_{\mathrm{NN}}}} = 5.02$ TeV." In: *Phys. Lett. B* 785 (2018), pp. 14–39. DOI: `10.1016/j.physletb.2018.07.061`. arXiv: `1711.09738 [nucl-ex]`.

[132] Shreyasi Acharya et al. "Measurement of isolated photon-hadron correlations in $\sqrt{s_{\mathrm{NN}}} = 5.02$ TeV pp and p-Pb collisions." In: *Phys. Rev. C* 102.4 (2020), p. 044908. DOI: `10.1103/PhysRevC.102.044908`. arXiv: `2005.14637 [nucl-ex]`.

[133] Georges Aad et al. "Measurement of isolated-photon pair production in pp collisions at $\sqrt{s} = 7$ TeV with the ATLAS detector." In: *JHEP* 01 (2013), p. 086. DOI: `10.1007/JHEP01(2013)086`. arXiv: `1211.1913 [hep-ex]`.

[134] "Measurement of the production cross-section of isolated photon pairs in pp collisions at 13 TeV with the ATLAS detector." In: (July 2020).

[135] G. Arnison et al. "Experimental observation of isolated large transverse energy electrons with associated missing energy at s=540 GeV." In: *Physics Letters B* 122.1 (1983), pp. 103–116. ISSN: 0370-2693. DOI: `https://doi.org/10.1016/0370-2693(83)91177-2`. URL: `https://www.sciencedirect.com/science/article/pii/0370269383911772`.

[136] M. Banner et al. "Observation of single isolated electrons of high transverse momentum in events with missing transverse energy at the CERN pp collider." In: *Physics Letters B* 122.5 (1983), pp. 476–485. ISSN: 0370-2693. DOI: `https://doi.org/10.1016/0370-2693(83)91605-2`. URL: `https://www.sciencedirect.com/science/article/pii/0370269383916052`.

[137] Georges Aad et al. “Observation of a new particle in the search for the Standard Model Higgs boson with the ATLAS detector at the LHC.” In: *Phys. Lett. B* 716 (2012), pp. 1–29. DOI: 10.1016/j.physletb.2012.08.020. arXiv: 1207.7214 [hep-ex].

[138] S. Chatrchyan et al. “Observation of a new boson at a mass of 125 GeV with the CMS experiment at the LHC.” In: *Physics Letters B* 716.1 (2012), pp. 30–61. ISSN: 0370-2693. DOI: https://doi.org/10.1016/j.physletb.2012.08.021. URL: https://www.sciencedirect.com/science/article/pii/S0370269312008581.

[139] “LHC Machine.” In: *JINST* 3 (2008). Ed. by Lyndon Evans and Philip Bryant, S08001. DOI: 10.1088/1748-0221/3/08/S08001.

[140] Jorg Wenninger. “LHC status and performance.” In: *PoS* CHARGED2018 (2019), p. 001. DOI: 10.22323/1.339.0001.

[141] Michaela Schaumann et al. “First Xenon-Xenon Collisions in the LHC.” In: *9th International Particle Accelerator Conference*. June 2018. DOI: 10.18429/JACoW-IPAC2018-MOPMF039.

[142] Ewa Lopienska. “The CERN accelerator complex, layout in 2022. Complexe des accélérateurs du CERN en janvier 2022.” In: (Feb. 2022). General Photo. URL: https://cds.cern.ch/record/2800984.

[143] M A Hone. *The duoplasmatron ion source for the new CERN Linac preinjector*. Tech. rep. Geneva: CERN, Nov. 1979. URL: https://cds.cern.ch/record/2640736.

[144] P. Sortais, J.L. Bouly, N. Chauvin, J.C. Curdy, R. Geller, T. Lamy, P. Sole, and J.L. Vieux-Rochaz. “ECRIS as ion source and charge breeder.” In: *Nuclear Physics A* 701.1 (2002). 5th International Conference on Radioactive Nuclear Beams, pp. 537–549. ISSN: 0375-9474. DOI: https://doi.org/10.1016/S0375-9474(01)01641-4. URL: https://www.sciencedirect.com/science/article/pii/S0375947401016414.

[145] E. Boltezar, H. Haseroth, W. Pirkl, G. Plass, T. Sherwood, U. Tallgren, P. Tetu, D. Warner, and M. Weiss. “THE NEW CERN 50-MEV LINAC.” In: *10th International Linear Accelerator Conference*. 1980, S2–2.

[146] E. Boltezar, H. Haseroth, W. Pirkl, G. Plass, T. R. Sherwood, U. Tallgren, P. Tetu, D. Warner, and M. Weiss. “PERFORMANCE OF THE NEW CERN 50-MeV LINAC.” In: *IEEE Trans. Nucl. Sci.* 26 (1979), pp. 3674–3676. DOI: 10.1109/TNS.1979.4330576.

[147] K. H. Reich. “The CERN Proton Synchrotron Booster.” In: *IEEE Trans. Nucl. Sci.* 16 (1969), pp. 959–961. DOI: 10.1109/TNS.1969.4325414.

[148] N. Angert et al. “CERN heavy ion facility design report.” In: (Apr. 1993). DOI: 10.5170/CERN-1993-001.

[149] M. Chanel. “LEIR: The low energy ion ring at CERN.” In: *Nucl. Instrum. Meth. A* 532 (2004). Ed. by T. Katayama and T. Koseki, pp. 137–143. DOI: 10.1016/j.nima.2004.06.040.

[150] “The CERN proton synchrotron.” In: (Jan. 1962). Ed. by E. Regenstreif. DOI: 10.5170/CERN-1962-003.

[151] Jean-Paul Burnet et al. *Fifty years of the CERN Proton Synchrotron: Volume 1*. CERN Yellow Reports: Monographs. Geneva: CERN, 2011. DOI: `10.5170/CERN-2011-004`. URL: `https://cds.cern.ch/record/1359959`.

[152] W P C Mills. “The present performance of the SPS.” In: *IEEE Trans. Nucl. Sci.* 26 (Mar. 1979), 3176–3178. 3 p. DOI: `10.1109/TNS.1979.4329975`. URL: `https://cds.cern.ch/record/133232`.

[153] L. Gatignon. “Physics at the SPS.” In: *Review of Scientific Instruments* 89.5 (2018), p. 052501. DOI: `10.1063/1.5016162`. eprint: `https://doi.org/10.1063/1.5016162`. URL: `https://doi.org/10.1063/1.5016162`.

[154] P. Abbon et al. “The COMPASS experiment at CERN.” In: *Nucl. Instrum. Meth. A* 577 (2007), pp. 455–518. DOI: `10.1016/j.nima.2007.03.026`. arXiv: `hep-ex/0703049`.

[155] D. Banerjee et al. “Dark matter search in missing energy events with NA64.” In: *Phys. Rev. Lett.* 123.12 (2019), p. 121801. DOI: `10.1103/PhysRevLett.123.121801`. arXiv: `1906.00176 [hep-ex]`.

[156] G. Aad et al. “The ATLAS Experiment at the CERN Large Hadron Collider.” In: *JINST* 3 (2008), S08003. DOI: `10.1088/1748-0221/3/08/S08003`.

[157] S. Chatrchyan et al. “The CMS Experiment at the CERN LHC.” In: *JINST* 3 (2008), S08004. DOI: `10.1088/1748-0221/3/08/S08004`.

[158] A. Augusto Alves Jr. et al. “The LHCb Detector at the LHC.” In: *JINST* 3 (2008), S08005. DOI: `10.1088/1748-0221/3/08/S08005`.

[159] G. Anelli et al. “The TOTEM experiment at the CERN Large Hadron Collider.” In: *JINST* 3 (2008), S08007. DOI: `10.1088/1748-0221/3/08/S08007`.

[160] James Pinfold et al. “Technical Design Report of the MoEDAL Experiment.” In: (June 2009).

[161] B. Acharya et al. “The Physics Programme Of The MoEDAL Experiment At The LHC.” In: *Int. J. Mod. Phys. A* 29 (2014), p. 1430050. DOI: `10.1142/S0217751X14300506`. arXiv: `1405.7662 [hep-ph]`.

[162] O. Adriani et al. “The LHCf detector at the CERN Large Hadron Collider.” In: *JINST* 3 (2008), S08006. DOI: `10.1088/1748-0221/3/08/S08006`.

[163] Arturo Tauro. “ALICE Schematics.” General Photo. May 2017. URL: `https://cds.cern.ch/record/2263642`.

[164] K. Aamodt et al. “The ALICE experiment at the CERN LHC.” In: *JINST* 3 (2008), S08002. DOI: `10.1088/1748-0221/3/08/S08002`.

[165] Betty Bezverkhny Abelev et al. “Performance of the ALICE Experiment at the CERN LHC.” In: *Int. J. Mod. Phys. A* 29 (2014), p. 1430044. DOI: `10.1142/S0217751X14300440`. arXiv: `1402.4476 [nucl-ex]`.

[166] G. Dellacasa et al. “ALICE technical design report of the inner tracking system (ITS).” In: (June 1999).

[167] C. Larionov. *dE/dx of charged particles vs their momentum for ITS pure standalone tracks measured in p-Pb collisions at 8.16 TeV*. `https://alice-figure.web.cern.ch/node/16718`. ALICE Performance Figure. 2018.

[168] B Abelev et al. “Technical Design Report for the Upgrade of the ALICE Inner Tracking System.” In: *J. Phys. G* 41 (2014), p. 087002. DOI: 10.1088/0954-3899/41/8/087002.

[169] Felix Reidt. “Upgrade of the ALICE ITS detector.” In: *Nucl. Instrum. Meth. A* 1032 (2022), p. 166632. DOI: 10.1016/j.nima.2022.166632. arXiv: 2111.08301 [physics.ins-det].

[170] J. Alme et al. “The ALICE TPC, a large 3-dimensional tracking device with fast readout for ultra-high multiplicity events.” In: *Nucl. Instrum. Meth. A* 622 (2010), pp. 316–367. DOI: 10.1016/j.nima.2010.04.042. arXiv: 1001.1950 [physics.ins-det].

[171] *Schematic of the ALICE Time Projection Chamber (TPC)*. https://www.physi.uni-heidelberg.de/~sma/research/tpc.php. Accessed: 2022-07-04.

[172] Ernst Hellbär. “The ALICE TPC: Optimization of the Performance in Run 2 and Developments for the Future.” In: *PoS* LHCP2019 (2019). Ed. by Pablo Roig Garcés, Irais Bautista Guzman, Arturo Fernández Téllez, and Mario Iván Martínez Hernández, p. 240. DOI: 10.22323/1.350.0240. arXiv: 1909.03746 [physics.ins-det].

[173] C. Lippmann. *dEdx figure for PDG review on TPCs - color version*. https://alice-figure.web.cern.ch/node/8731. ALICE Performance Figure. 2018.

[174] “First results of the ALICE detector performance at 13 TeV.” In: (Aug. 2015). URL: https://cds.cern.ch/record/2047855.

[175] B Abelev et al. “Upgrade of the ALICE Experiment: Letter Of Intent.” In: *J. Phys. G* 41 (2014), p. 087001. DOI: 10.1088/0954-3899/41/8/087001.

[176] A. Andronic and J. P. Wessels. “Transition Radiation Detectors.” In: *Nucl. Instrum. Meth. A* 666 (2012), pp. 130–147. DOI: 10.1016/j.nima.2011.09.041. arXiv: 1111.4188 [physics.ins-det].

[177] P. Cortese. “ALICE transition-radiation detector: Technical Design Report.” In: (2001).

[178] Shreyasi Acharya et al. “The ALICE Transition Radiation Detector: construction, operation, and performance.” In: *Nucl. Instrum. Meth. A* 881 (2018), pp. 88–127. DOI: 10.1016/j.nima.2017.09.028. arXiv: 1709.02743 [physics.ins-det].

[179] V. L. Ginzburg and I. M. Frank. “Radiation of a uniformly moving electron due to its transition from one medium into another.” In: *J. Phys. (USSR)* 9 (1945), pp. 353–362.

[180] J. Adolfsson et al. “The upgrade of the ALICE TPC with GEMs and continuous readout.” In: *JINST* 16.03 (2021), P03022. DOI: 10.1088/1748-0221/16/03/P03022. arXiv: 2012.09518 [physics.ins-det].

[181] Pavel Larionov. *TOF beta-p performance in p-Pb collisions at 8.16 TeV, LHC16r dataset*. https://alice-figure.web.cern.ch/node/16722. Accessed: 2022-07-10.

[182] G. Dellacasa et al. “ALICE technical design report of the time-of-flight system (TOF).” In: (Feb. 2000).

[183] P. Cortese et al. “ALICE electromagnetic calorimeter technical design report.” In: (Sept. 2008).

[184] "Performance of the ALICE Electromagnetic Calorimeter." In: (Sept. 2022). arXiv: 2209.04216 [physics.ins-det].

[185] J. Allen et al. "ALICE DCal: An Addendum to the EMCal Technical Design Report Di-Jet and Hadron-Jet correlation measurements in ALICE." In: (June 2010).

[186] R Brun, F Bruyant, M Maire, A C McPherson, and P Zanarini. "GEANT 3: user's guide Geant 3.10, Geant 3.11; rev. version." In: (1987). URL: https://cds.cern.ch/record/1119728.

[187] Christian Wolfgang Fabjan, L Jirdén, V Lindestruth, Lodovico Riccati, D Rorich, Pierre Van de Vyvre, O Villalobos Baillie, and Hans de Groot. *ALICE trigger data-acquisition high-level trigger and control system: Technical Design Report*. Technical design report. ALICE. Geneva: CERN, 2004. URL: https://cds.cern.ch/record/684651.

[188] G. Dellacasa et al. "ALICE technical design report of the photon spectrometer (PHOS)." In: (Mar. 1999).

[189] D. V. Aleksandrov et al. "A high resolution electromagnetic calorimeter based on lead-tungstate crystals." In: *Nucl. Instrum. Meth. A* 550 (2005), pp. 169–184. DOI: 10.1016/j.nima.2005.03.174.

[190] Nicolas Schmidt. "Direct photon and light neutral meson production in hadron collisions at the LHC with ALICE." Presented 31 May 2021. 2021. URL: https://cds.cern.ch/record/2779384.

[191] S. Evdokimov, V. Izucheev, Yu. Kharlov, E. Kondratyuk, S. Sadovsky, and A. Shangaraev. "The ALICE CPV Detector." In: *KnE Energ. Phys.* 3 (2018), pp. 260–267. DOI: 10.18502/ken.v3i1.1752.

[192] Dong Wang et al. "Level-0 trigger algorithms for the ALICE PHOS detector." In: *Nucl. Instrum. Meth. A* 629 (2011), pp. 80–86. DOI: 10.1016/j.nima.2010.11.111.

[193] S. Beole et al. "ALICE technical design report: Detector for high momentum PID." In: (Aug. 1998).

[194] G. Dellacasa et al. "ALICE technical design report of the zero degree calorimeter (ZDC)." In: (Mar. 1999).

[195] G. Dellacasa et al. "ALICE technical design report: Photon multiplicity detector (PMD)." In: (Sept. 1999).

[196] Shreyasi Acharya et al. "Direct photon elliptic flow in Pb-Pb collisions at $\sqrt{s_{\mathrm{NN}}}$ = 2.76 TeV." In: *Phys. Lett. B* 789 (2019), pp. 308–322. DOI: 10.1016/j.physletb.2018.11.039. arXiv: 1805.04403 [nucl-ex].

[197] P Cortese et al. "ALICE technical design report on forward detectors: FMD, T0 and V0." In: (Sept. 2004).

[198] J. Conrad, J. G. Contreras, and C. E. Jorgensen. "Minimum bias triggers in proton-proton collisions with VZERO and pixel detectors." In: (2005).

[199] E. Abbas et al. "Performance of the ALICE VZERO system." In: *JINST* 8 (2013), P10016. DOI: 10.1088/1748-0221/8/10/P10016. arXiv: 1306.3130 [nucl-ex].

[200] D. Acosta et al. "Results of Prototype Studies for a Spaghetti Calorimeter." In: *Nucl. Instrum. Meth. A* 294 (1990), pp. 193–210. DOI: `10.1016/0168-9002(90)91833-W`.

[201] R. Brun and F. Rademakers. "ROOT: An object oriented data analysis framework." In: *Nucl. Instrum. Meth. A* 389 (1997). Ed. by M. Werlen and D. Perret-Gallix, pp. 81–86. DOI: `10.1016/S0168-9002(97)00048-X`.

[202] ALICE collaboration. *AliRoot software*. URL: `https://github.com/alisw/AliRoot`.

[203] ALICE collaboration. *AliPhysics software*. URL: `https://github.com/alisw/AliPhysics`.

[204] *git: fast version control*. Accessed: 2022-07-20. URL: `https://git-scm.com/`.

[205] Ian Bird. "Computing for the Large Hadron Collider." In: *Annual Review of Nuclear and Particle Science* 61.1 (2011), pp. 99–118. DOI: `10.1146/annurev-nucl-102010-130059`. eprint: `https://doi.org/10.1146/annurev-nucl-102010-130059`. URL: `https://doi.org/10.1146/annurev-nucl-102010-130059`.

[206] I Bird et al. *Update of the Computing Models of the WLCG and the LHC Experiments*. Tech. rep. 2014. URL: `https://cds.cern.ch/record/1695401`.

[207] Christian Wolfgang Fabjan, L Jirdén, V Lindestruth, Lodovico Riccati, D Rorich, Pierre Van de Vyvre, O Villalobos Baillie, and Hans de Groot. *ALICE trigger data-acquisition high-level trigger and control system: Technical Design Report*. Technical design report. ALICE. Geneva: CERN, 2004. URL: `https://cds.cern.ch/record/684651`.

[208] R. Fruhwirth. "Application of Kalman filtering to track and vertex fitting." In: *Nucl. Instrum. Meth. A* 262 (1987), pp. 444–450. DOI: `10.1016/0168-9002(87)90887-4`.

[209] Nicolas Schmidt. *EMCal L1 triggered event display (ALI-PERF-349213)*. URL: `https://alice-figure.web.cern.ch/node/17820`.

[210] Stefan Roesler, Ralph Engel, and Johannes Ranft. "The Monte Carlo event generator DPMJET-III." In: *International Conference on Advanced Monte Carlo for Radiation Physics, Particle Transport Simulation and Applications (MC 2000)*. Dec. 2000, pp. 1033–1038. DOI: `10.1007/978-3-642-18211-2_166`. arXiv: `hep-ph/0012252`.

[211] T. Pierog, Iu. Karpenko, J. M. Katzy, E. Yatsenko, and K. Werner. "EPOS LHC: Test of collective hadronization with data measured at the CERN Large Hadron Collider." In: *Phys. Rev. C* 92.3 (2015), p. 034906. DOI: `10.1103/PhysRevC.92.034906`. arXiv: `1306.0121 [hep-ph]`.

[212] Xin-Nian Wang and Miklos Gyulassy. "HIJING: A Monte Carlo model for multiple jet production in p p, p A and A A collisions." In: *Phys. Rev. D* 44 (1991), pp. 3501–3516. DOI: `10.1103/PhysRevD.44.3501`.

[213] S. Agostinelli et al. "GEANT4–a simulation toolkit." In: *Nucl. Instrum. Meth. A* 506 (2003), pp. 250–303. DOI: `10.1016/S0168-9002(03)01368-8`.

[214] Alfredo Ferrari, Paola R. Sala, Alberto Fasso, and Johannes Ranft. "FLUKA: A multi-particle transport code (Program version 2005)." In: (Oct. 2005). DOI: `10.2172/877507`.

[215] F. Carminati and A. Morsch. "Simulation in ALICE." In: *eConf* C0303241 (2003), TUMT004. arXiv: physics/0306092.

[216] P. Buncic, M. Krzewicki, and P. Vande Vyvre. "Technical Design Report for the Upgrade of the Online-Offline Computing System." In: (Apr. 2015).

[217] Chiara Zampolli. "ALICE data processing for Run 3 and Run 4 at the LHC." In: *PoS* ICHEP2020 (2021), p. 929. DOI: 10.22323/1.390.0929. arXiv: 2012.04391 [physics.ins-det].

[218] ALICE collaboration. *O2Physics software*. URL: https://github.com/AliceO2Group/O2Physics.

[219] Daniel Mühlheim. "Measurement of Neutral Mesons and Direct Photons in pp Collisions with ALICE." Presented 2018. 2018. URL: https://www.uni-muenster.de/imperia/md/content/physik_kp/muehlheim2018.pdf.

[220] Vladislav Balagura. "Notes on van der Meer Scan for Absolute Luminosity Measurement." In: *Nucl. Instrum. Meth. A* 654 (2011), pp. 634–638. DOI: 10.1016/j.nima.2011.06.007. arXiv: 1103.1129 [physics.ins-det].

[221] "ALICE luminosity determination for pp collisions at $\sqrt{s} = 8$ TeV." In: (2017). URL: https://cds.cern.ch/record/2255216.

[222] "ALICE luminosity determination for p-Pb collisions at $\sqrt{s_{NN}} = 8.16$ TeV." In: (2018). URL: https://cds.cern.ch/record/2314660.

[223] Bo Andersson, G. Gustafson, and B. Soderberg. "A General Model for Jet Fragmentation." In: *Z. Phys. C* 20 (1983), p. 317. DOI: 10.1007/BF01407824.

[224] Torbjorn Sjostrand. "Jet Fragmentation of Nearby Partons." In: *Nucl. Phys. B* 248 (1984), pp. 469–502. DOI: 10.1016/0550-3213(84)90607-2.

[225] S.Yu. Shmakov, V.V. Uzhinskii, and A.M. Zadorozhny. "DIAGEN — Generator of inelastic nucleus-nucleus interaction diagrams." In: *Computer Physics Communications* 54.1 (1989), pp. 125–135. ISSN: 0010-4655. DOI: https://doi.org/10.1016/0010-4655(89)90038-6. URL: https://www.sciencedirect.com/science/article/pii/0010465589900386.

[226] H. J. Drescher, M. Hladik, S. Ostapchenko, T. Pierog, and K. Werner. "Parton based Gribov-Regge theory." In: *Phys. Rept.* 350 (2001), pp. 93–289. DOI: 10.1016/S0370-1573(00)00122-8. arXiv: hep-ph/0007198.

[227] J. Allen et al. "Performance of prototypes for the ALICE electromagnetic calorimeter." In: *Nucl. Instrum. Meth. A* 615 (2010), pp. 6–13. DOI: 10.1016/j.nima.2009.12.061. arXiv: 0912.2005 [physics.ins-det].

[228] Torbjörn Sjöstrand and Maria van Zijl. "A multiple-interaction model for the event structure in hadron collisions." In: *Phys. Rev. D* 36 (7 1987), pp. 2019–2041. DOI: 10.1103/PhysRevD.36.2019. URL: https://link.aps.org/doi/10.1103/PhysRevD.36.2019.

[229] T. Affolder et al. "Charged jet evolution and the underlying event in proton-antiproton collisions at 1.8 TeV." In: *Phys. Rev. D* 65 (9 2002), p. 092002. DOI: 10.1103/PhysRevD.65.092002. URL: https://link.aps.org/doi/10.1103/PhysRevD.65.092002.

[230] S. Catani, Yuri L. Dokshitzer, M. H. Seymour, and B. R. Webber. "Longitudinally invariant K_t clustering algorithms for hadron hadron collisions." In: *Nucl. Phys. B* 406 (1993), pp. 187–224. DOI: `10.1016/0550-3213(93)90166-M`.

[231] Shreyasi Acharya et al. "Measurement of charged jet cross section in *pp* collisions at $\sqrt{s} = 5.02$ TeV." In: *Phys. Rev. D* 100.9 (2019), p. 092004. DOI: `10.1103/PhysRevD.100.092004`. arXiv: `1905.02536 [nucl-ex]`.

[232] Jaroslav Adam et al. "Centrality dependence of charged jet production in p-Pb collisions at $\sqrt{s_{\rm NN}} = 5.02$ TeV." In: (Mar. 2016). DOI: `10.1140/epjc/s10052-016-4107-8`. arXiv: `1603.03402 [nucl-ex]`.

[233] ALICE collaboration. *TFractionFitter documentation*. URL: `https://root.cern.ch/doc/v606/classTFractionFitter.html`.

[234] Roger J. Barlow and Christine Beeston. "Fitting using finite Monte Carlo samples." In: *Comput. Phys. Commun.* 77 (1993), pp. 219–228. DOI: `10.1016/0010-4655(93)90005-W`.

[235] G. D. Lafferty and T. R. Wyatt. "Where to stick your data points: The treatment of measurements within wide bins." In: *Nucl. Instrum. Meth. A* 355 (1995), pp. 541–547. DOI: `10.1016/0168-9002(94)01112-5`.

[236] Shreyasi Acharya et al. "π^0 and η meson production in proton-proton collisions at $\sqrt{s} = 8$ TeV." In: *Eur. Phys. J. C* 78.3 (2018), p. 263. DOI: `10.1140/epjc/s10052-018-5612-8`. arXiv: `1708.08745 [hep-ex]`.

[237] S. Chandra. *Isolated photons measurement in pp collisions at $\sqrt{s} = 8$ TeV with the ALICE detector at LHC*. `https://alice-notes.web.cern.ch/node/1254`. ALICE Analysis Note (unpublished). 2021.

[238] S. Chandra. *Cross section: isolated photons cross section pp 8 TeV*. `https://alice-figure.web.cern.ch/node/22221`. ALICE Physics Preliminary Figure. 2021.

[239] F. Jonas. *Isolated prompt photon production cross section in pp and p-Pb collisions at 8.16 TeV*. `https://alice-figure.web.cern.ch/node/26260`. ALICE Physics Preliminary Figure. 2023.

[240] Andy Buckley, James Ferrando, Stephen Lloyd, Karl Nordström, Ben Page, Martin Rüfenacht, Marek Schönherr, and Graeme Watt. "LHAPDF6: parton density access in the LHC precision era." In: *Eur. Phys. J. C* 75 (2015), p. 132. DOI: `10.1140/epjc/s10052-015-3318-8`. arXiv: `1412.7420 [hep-ph]`.

[241] D. U. Dixit. *Ratio to JETPHOX of Isolated photon differential cross section measured in p-Pb collisions at $sqrt(s) = 5.02$ TeV*. `https://alice-figure.web.cern.ch/node/22280`. ALICE Physics Preliminary Figure. 2021.

[242] C. A. Salgado et al. "Proton-Nucleus Collisions at the LHC: Scientific Opportunities and Requirements." In: *J. Phys. G* 39 (2012), p. 015010. DOI: `10.1088/0954-3899/39/1/015010`. arXiv: `1105.3919 [hep-ph]`.

[243] Kari J. Eskola, Petja Paakkinen, Hannu Paukkunen, and Carlos A. Salgado. "EPPS21: a global QCD analysis of nuclear PDFs." In: *Eur. Phys. J. C* 82.5 (2022), p. 413. DOI: `10.1140/epjc/s10052-022-10359-0`. arXiv: `2112.12462 [hep-ph]`.

[244] M. Klasen et al. "Global analyses of nuclear PDFs with heavy-quark and neutrino data." In: *PoS* ICHEP2022 (2022), p. 443. DOI: `10.22323/1.414.0443`. arXiv: `2210.10284 [hep-ph]`.

[245] J. Pumplin, D. R. Stump, and W. K. Tung. "Multivariate fitting and the error matrix in global analysis of data." In: *Phys. Rev. D* 65 (2001), p. 014011. DOI: 10.1103/PhysRevD.65.014011. arXiv: hep-ph/0008191.

[246] Richard D. Ball, Valerio Bertone, Francesco Cerutti, Luigi Del Debbio, Stefano Forte, Alberto Guffanti, Jose I. Latorre, Juan Rojo, and Maria Ubiali. "Reweighting NNPDFs: the W lepton asymmetry." In: *Nucl. Phys. B* 849 (2011). [Erratum: Nucl.Phys.B 854, 926–927 (2012), Erratum: Nucl.Phys.B 855, 927–928 (2012)], pp. 112–143. DOI: 10.1016/j.nuclphysb.2011.03.017. arXiv: 1012.0836 [hep-ph].

[247] Richard D. Ball, Valerio Bertone, Francesco Cerutti, Luigi Del Debbio, Stefano Forte, Alberto Guffanti, Nathan P. Hartland, Jose I. Latorre, Juan Rojo, and Maria Ubiali. "Reweighting and Unweighting of Parton Distributions and the LHC W lepton asymmetry data." In: *Nucl. Phys. B* 855 (2012), pp. 608–638. DOI: 10.1016/j.nuclphysb.2011.10.018. arXiv: 1108.1758 [hep-ph].

[248] Marco van Leeuwen. "Constraining nuclear Parton Density Functions with forward photon production at the LHC." In: (Sept. 2019). arXiv: 1909.05338 [hep-ph].

[249] Rabah Abdul Khalek, Jacob J. Ethier, Juan Rojo, and Gijs van Weelden. "nNNPDF2.0: quark flavor separation in nuclei from LHC data." In: *JHEP* 09 (2020), p. 183. DOI: 10.1007/JHEP09(2020)183. arXiv: 2006.14629 [hep-ph].

[250] Rabah Abdul Khalek, Jacob J. Ethier, and Juan Rojo. "Nuclear parton distributions from lepton-nucleus scattering and the impact of an electron-ion collider." In: *Eur. Phys. J. C* 79.6 (2019), p. 471. DOI: 10.1140/epjc/s10052-019-6983-1. arXiv: 1904.00018 [hep-ph].

[251] INCNLO. *INCNLO-direct photon and inclusive hadron production code - INCNLO version 1.4*. 2002. URL: https://lapth.cnrs.fr/PHOX_FAMILY/readme_inc.html.

[252] F. Aversa, P. Chiappetta, Mario Greco, and J. P. Guillet. "QCD Corrections to Parton-Parton Scattering Processes." In: *Nucl. Phys. B* 327 (1989), p. 105. DOI: 10.1016/0550-3213(89)90288-5.

[253] P. Aurenche, R. Baier, M. Fontannaz, and D. Schiff. "Prompt Photon Production at Large p(T) Scheme Invariant QCD Predictions and Comparison with Experiment." In: *Nucl. Phys. B* 297 (1988), pp. 661–696. DOI: 10.1016/0550-3213(88)90553-6.

[254] P. Aurenche, M. Fontannaz, J. Ph. Guillet, Bernd A. Kniehl, E. Pilon, and M. Werlen. "A Critical phenomenological study of inclusive photon production in hadronic collisions." In: *Eur. Phys. J. C* 9 (1999), pp. 107–119. DOI: 10.1007/s100529900018. arXiv: hep-ph/9811382.

[255] P. Aurenche, M. Fontannaz, J. P. Guillet, Bernd A. Kniehl, and M. Werlen. "Large p(T) inclusive pi0 cross-sections and next-to-leading-order QCD predictions." In: *Eur. Phys. J. C* 13 (2000), pp. 347–355. DOI: 10.1007/s100520000309. arXiv: hep-ph/9910252.

[256] Krzysztof J. Golec-Biernat and M. Wusthoff. "Saturation effects in deep inelastic scattering at low Q**2 and its implications on diffraction." In: *Phys. Rev. D* 59 (1998), p. 014017. DOI: 10.1103/PhysRevD.59.014017. arXiv: hep-ph/9807513.

[257] A. Accardi et al. “Electron Ion Collider: The Next QCD Frontier: Understanding the glue that binds us all.” In: *Eur. Phys. J. A* 52.9 (2016). Ed. by A. Deshpande, Z. E. Meziani, and J. W. Qiu, p. 268. DOI: `10.1140/epja/i2016-16268-9`. arXiv: `1212.1701 [nucl-ex]`.

[258] Matteo Cacciari, Gavin P. Salam, and Gregory Soyez. “FastJet User Manual.” In: *Eur. Phys. J. C* 72 (2012), p. 1896. DOI: `10.1140/epjc/s10052-012-1896-2`. arXiv: `1111.6097 [hep-ph]`.

[259] Matteo Cacciari, Gavin P. Salam, and Gregory Soyez. “The anti-k_t jet clustering algorithm.” In: *JHEP* 04 (2008), p. 063. DOI: `10.1088/1126-6708/2008/04/063`. arXiv: `0802.1189 [hep-ph]`.

[260] Tie-Jiun Hou et al. “New CTEQ global analysis of quantum chromodynamics with high-precision data from the LHC.” In: *Phys. Rev. D* 103.1 (2021), p. 014013. DOI: `10.1103/PhysRevD.103.014013`. arXiv: `1912.10053 [hep-ph]`.

DECLARATION

Hiermit versichere ich, dass die vorliegende Arbeit über *Probing the initial state of heavy-ion collisions with isolated prompt photons* selbstständig verfasst worden ist, dass keine anderen Quellen und Hilfsmittel als die angegebenen benutzt worden sind und dass die Stellen der Arbeit, die anderen Werken – auch elektronischen Medien – dem Wortlaut oder Sinn nach entnommenen wurden, auf jeden Fall unter Angabe der Quelle als Entlehnung kenntlich gemacht worden sind.

Münster, Mai 2023

Florian Jonas

Ich erkläre mich mit einem Abgleich der Arbeit mit anderen Texten zwecks Auffindung von Übereinstimmungen sowie mit einer zu diesem Zweck vorzunehmenden Speicherung der Arbeit in eine Datenbank einverstanden.

Münster, Mai 2023

Florian Jonas

COLOPHON

This document was typeset using the typographical look-and-feel `classicthesis` developed by André Miede and Ivo Pletikosić. The style was inspired by Robert Bringhurst's seminal book on typography *"The Elements of Typographic Style"*.
`classicthesis` is available for both LaTeX and LyX:

`https://bitbucket.org/amiede/classicthesis/`

and distributed under the GNU General Public License.